



UNSW
SYDNEY

Australian Centre for Advanced Photovoltaics
Annual Report 2019
Appendix



ARENA



COLLABORATION GRANTS

ACAP's competitively selected Collaboration Grants, are reported online at <http://www.acap.net.au/annual-reports>.

6.35 A CASE STUDY OF THE DEGRADATION OF FLEXIBLE PHOTOVOLTAIC MODULES

Lead Partner

CSIRO

CSIRO Team

Dr Hasitha Weerasinghe, Régine Chantler, Dr Doojin Vak, Jyothi Ramamurthy, Andrew Faulks, Karl Weber, Fiona Glenn, Dr Andrew Scully

Interns: Rahul Banakar, Oscar Elsasser

Academic Partners

Australian Academy of Technology and Engineering (ATSE): Peter Pentland, Executive Manager ATSE Schools Program

Stanford University: Prof. Reinhold Dauskardt, Dept of Materials Science and Engineering

Funding Support

ACAP, CSIRO

Aims

The main objective of this project is to study the degradation of organic photovoltaic (OPV) modules due to prolonged handling by end-users. A secondary objective is to increase awareness of next generation solar technology by school students, who are acting as end-users for this study.

Progress

Following recruitment of schools (the participants in this program), the initial 100 printed modules were fabricated for evaluation. This work was outlined in the previous report.

The first quarter of 2019 was focused on the fabrication of 500 OPV modules, along with the mass production of the data acquisition system developed in 2018.

Preparation of 500 OPV modules

Over 100 m of printed solar film (PSF) was produced using roll-to-roll (R2R) deposition methods in ambient conditions. The architecture of this solar film is shown in Figure 6.35.1. Three layers of the PSF, that is the electron transport layer (ETL), active polymer layer and hole transport layer (HTL) were coated onto the flexible ITO-PET substrate. The top electrode was printed using screen printing.

Modules were encapsulated in a nitrogen filled glovebox following an intensive pre-conditioning step which removed the moisture and oxygen adsorbed on both the solar modules and encapsulation material.

During production and encapsulation three parameters of the final PSF modules were varied: the ETL layer, the active polymer material and the encapsulation architecture.

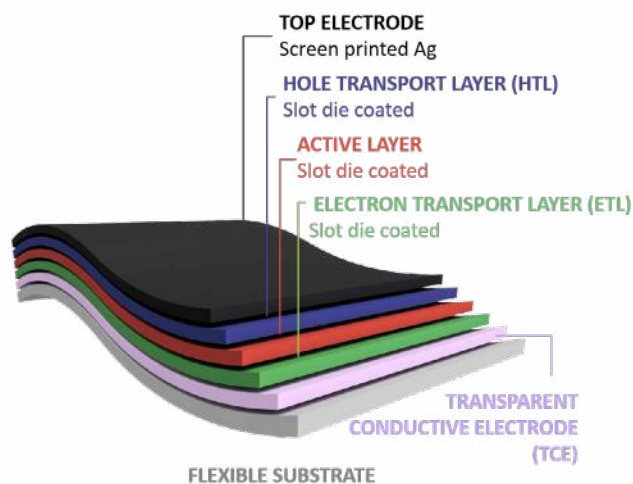


Figure 6.35.1: Schematic showing OPV module architecture.

Figure 6.35.2 illustrates the two different encapsulation architectures (complete and partial) used during this study. Table 6.35.1 further illustrates the four types of modules (based on different ETL layers, active polymer materials and encapsulation architectures) employed during this study.

Characterisation of OPV modules

Initial electrical performance (V_{oc} , J_{sc} , fill factor (FF) and power conversion efficiency (PCE)) of the modules was measured and recorded before they were sent to the schools (Figure 6.35.3). J-V curves were obtained using a CSIRO in-house solar simulator under one-sun illumination.

Further analysis such as electroluminescence and photocurrent mapping were conducted on the best performing modules.

School roll out and initiatives

Over 200 schools applied to participate in the program rollout organised by Peter Pentland from ATSE's STELR school education program. Using criteria such as geographic and demographic diversity, 100 schools were selected and received a flexible solar kit (contents shown in Figure 6.35.4)

So far over 25,000 students from Australia, New Zealand and Indonesia have been introduced to this new printed solar technology.

Two competitions were organised during National Science Week in August 2019 with the aim to encourage handling of the modules as well as exploring novel application of this flexible solar technology.

Highlights

- This program has been very popular among the participants, resulting in this study and OPV modules appearing in the headline news in Indonesia. The short documentary presents students from Bontang High School (Bontang, East Kalimantan, Indonesia) running experiments while teachers talked very positively about the program (see Figure 6.35.5).

- An article was published in August in the ATSE news website. Titled "The school scientists making solar shine", the article by Peter Pentland, highlights the scope of the project and what a positive impact it had on the school and students.
- Preliminary results of this project were presented at the 7th ACAP Conference and the 6th Asia-Pacific Solar Research Conference (Canberra, 2019). The project leader, Régine Chantler was rewarded for the best staff poster presented at the conference (see Highlight in Section 2 of this report).

Future Work

The key activities in the next six months include:

- Returning of the modules along with the data gathered and the completed questionnaires to the CSIRO laboratory.
- Preparation of samples for mechanical analysis (adhesion/ cohesion of coated and printed layers) by Professor Dauskardt's team at Stanford University.
- Further analysis of the effect of the modules' variations on their performance.
- Fabrication of the next batch of OPV modules to send to schools. The schools will then continue their experiments.
- Conclusion of the project and release of a paper.

Table 6.35.1: Overview of OPV module variations produced using different materials and encapsulation architectures.

MODULE VARIATIONS		#1	#2	#3	#4
ACTIVE LAYER	Commercial ink	✓	✓		✓
	P3HT: PCBM			✓	
ELECTRON TRANSPORT LAYER	ZnO				✓
	PEIE	✓	✓	✓	
ENCAPSULATION	Full		✓	✓	✓
	Partial	✓			

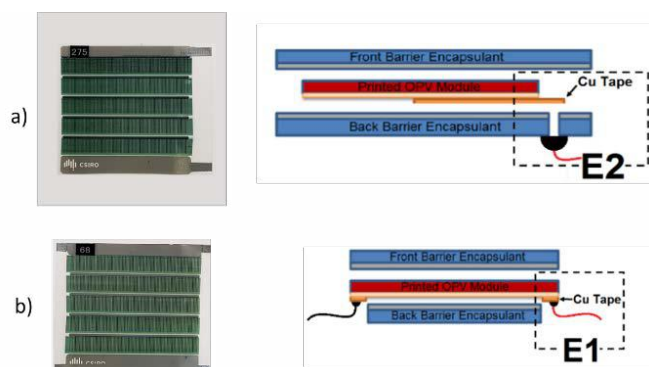


Figure 6.35.2: Images of OPV modules and corresponding structures of (a) complete encapsulation; and (b) partial encapsulation architectures.

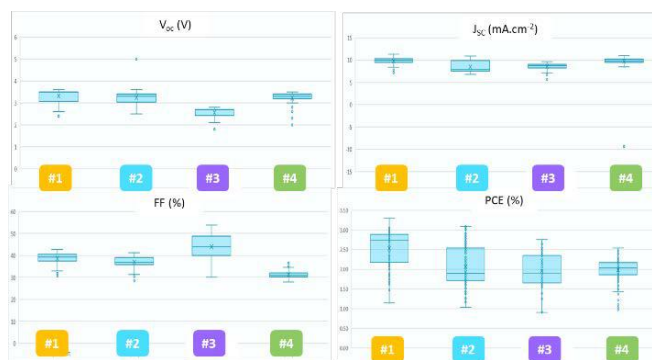


Figure 6.35.3: Overview of the module performances (V_{oc} , J_{sc} , FF and PCE) for each of the module types as per Table 6.35.1.



Figure 6.35.4: Image of the contents of the flexible solar kit received by the selected schools: four OPV modules, a load box, test leads, a return envelope and conductive tape. Schools are to supply their own multimeter to perform their own I-V curve.

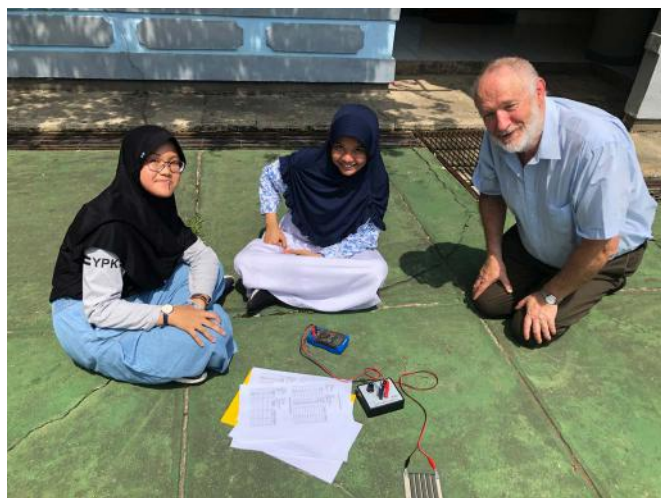


Figure 6.35.5: (a) Images of students from Bontang High School. (b) Student on the headline news in Indonesia. <https://eksposkaltim.com/berita-9914-pt-kni-monitoring-implementasi-stelr-stem-di-smp-negeri-2-bontang.html>.

References:

The school scientists making solar shine, 15 August, 2019, Peter Pentland ATSE News

<https://www.atse.org.au/news-and-events/article/the-school-scientists-making-solar-shine/>

6.36 LIFE CYCLE ASSESSMENT OF RECYCLING PROCESSES OF SILICON SOLAR MODULES

Lead Partner

UNSW

UNSW Team

Dr Marina Monteiro Lunardi, Dr Jose Bilbao, Dr Richard Corkish

Academic Partner

Federal University of Rio Grande do Sul (UFRGS) – Brazil: Dr Hugo Marcelo Veit, Dr Pablo Ribeiro Dia

Overview

The solar photovoltaic (PV) market is growing fast and estimates for the future are optimistic. Predictions show that in 2019 PV systems should reach more than 120 GW of solar installations worldwide (Nhede 2019), which represents a substantial growth compared to 2017 (93.9 GW per year), and even more significant if compared to 1997 (114.1 MW per year) (Mints 2018). Crystalline silicon (c-Si) technologies continue to lead the PV market (approximately 90%) (ITRPV 2019) and China remains the world's largest market (Bahar 2019).

The significant progress in solar energy usage is one of the main contributors in the search for a globally sustainable economy. Yet, solar modules don't last forever and the increase in PV installations will also produce a considerable amount of waste in the future when these panels reach their end-of-life (EoL). Estimates show that the number of EoL solar panels may account for up to 8.0 million tonnes per year by 2030 (Weckend et al. 2016). With this in mind, it is crucial to notice that the progress of the global PV market (and consequential waste) requires specific regulations and proper treatment/recycling processes to deal with this type of discarded material when the panels are not in use anymore.

The primary components of a standard c-Si module structure are aluminium (Al) frame, low-iron glass, encapsulant (usually ethylene vinyl acetate, EVA), c-Si solar cells interconnected by copper ribbon, polymer-based backsheet (commonly polyvinyl fluoride, Tedlar®) and a junction box (Dias et al. 2016). By weight, approximately 76% of a c-Si module is glass, but the rest of the module has some valuable materials to be recovered, such as polymer (encapsulant and backsheet foil, 10% of total weight), Al (mostly the frame, 8%), Si solar cells (5%), copper (Cu) interconnectors (1%), and silver (Ag) contact lines (about 0.1%) (Wambach et al. 2006; Sander & Politik 2007).

So far, reusing or recycling parts of EoL PV systems hasn't received much attention. Yet, results from recent environmental studies show that materials such as glass, Si, Al, Ag, Pb and Cu can be recovered from PV modules at sufficient quality for them to be re-introduced into the PV supply chain or this or other industries (Weckend 2016). The environmental and economic importance of recovering these materials is significant since some of the elements are valuable or scarce, such as Ag, for example (Weckend 2016; IEA-PVPS 2016).

Besides, PV waste presents a potential environmental and health-related hazard because of the presence of some toxic materials, such as lead. Most of the existing PV recycling processes involve large quantities of electricity and/or chemicals, creating some concerns around potential environmental impacts related to these methods.

Aim

Our project evaluated, with an environmental perspective, two different recycling processes for c-Si solar modules considering their sustainability through the life cycle assessment (LCA) approach. An LCA analysis collects and evaluates inputs and outputs such as energy, materials, wastes and emissions translating these values into potential environmental impacts. Most of the LCA studies about PV modules focus on the production and operation phases, assuming landfill as the EoL option. Most of the publications that consider recycling of PV modules are based on case studies (Vellini et al. 2017; Latunussa et al. 2016; Tao & Yu 2015).

Our project compared two different recycling approaches for solar modules (at a laboratory scale) and calculated the potential environmental impacts of these processes. The results from the experiments were analysed and discussed to understand the ecological benefits of these processes in terms of reduction of impacts from the recovery and reuse of materials from c-Si solar modules.

Progress

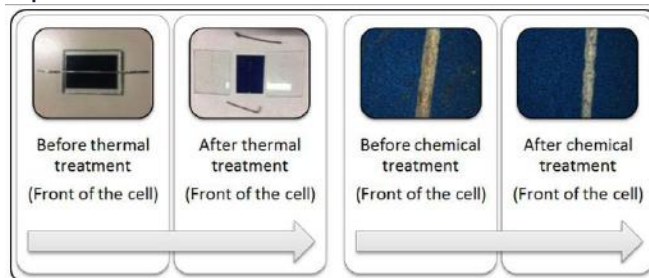
Experiment 1 started with the thermal method, as mentioned, which was used for the delamination of the module layers (EVA and backsheet) under high temperature. Then, HNO_3 was used to leach metals from the solar cells. The use of an ultrasonic bath was beneficial for promoting reaction speed (Zhang 2016). Apparent visual changes in the surface of the samples were observed after the chemical reaction using HNO_3 .

Experiment 1 confirmed that HNO_3 at high temperature and with the aid of an ultrasonic bath could successfully recover Ag, Al and Cu from used PV wafer (Zhang 2016). Comparisons with other methods of recycling were made, such as under normal conditions (without ultrasonic bath) and using a hot plate instead of the ultrasonic bath, but they were not as successful. Particularly for Ag, which has significant financial value (Weckend et al. 2016), the extraction rate with the ultrasonic bath was increased by one hundred times when compared with the extraction rate without it (Zhang 2016). The results for Experiment 2 show that, compared with Experiment 1, the module backsheets were also recovered, instead of being incinerated.

The experiments were conducted successfully in terms of recovering materials from EoL solar modules (Figure 6.36.1). During both experiments the LCA-required data was collected to build the life cycle inventory (LCI) used to calculate the environmental impacts from these processes. Experiment 1 confirmed the potential of recovering different metals from the cells through a chemical process. Experiment 2 demonstrated the possibility to separate most of the components from EoL solar modules, including valuable and rare materials. In both cases, the materials recovered could be used as raw

materials in the production of new solar cells and modules, resulting in a more environmentally friendly process (Ardente et al. 2019), or introduced to other industries.

Experiment 1



Experiment 2



Figure 6.36.1: Experiment 1 (left) – Considering the thermal and the chemical treatments. The left side of the image shows the separation of the module's parts (glass, cells, metals) and the right side of the image shows the recovery of metals from the chemical reaction. Experiment 2 (right) – Different PV components separated using an organic solvent (toluene).

The LCI for this study was built with the collection of data from both experiments, including material usage, energy consumption, emissions and wastes from each step of the recycling process. The LCA compared the recycling experiments described to assess which steps of these processes have the most significant impacts and how these impacts affect the overall life cycle of PV modules. The results are discussed, and suggestions to how these effects can be minimised are presented.

The results for the LCA are presented using the ReCiPe method in terms of three main effects (Human Health effects, Ecosystems impacts and Resources depletion). The results for Experiments 1 and 2 are shown in Figure 6.36.2, where, for Experiment 1, step 1 is the thermal separation, and step 2 is the chemical separation (nitric acid + ultrasonic bath).

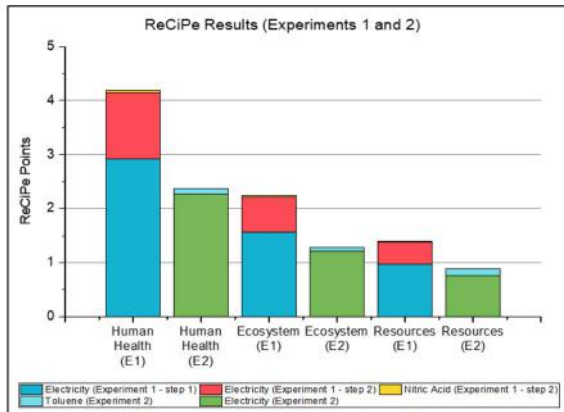


Figure 6.36.2: ReCiPe results (Human Health, Ecosystem and Resources) for Experiments 1 and Experiment.

The environmental analysis shows that electricity has the most significant impacts in all three ReCiPe impacts, due to the electricity mix being assumed for China, as it remains the biggest producer and customer for Si cells and modules (Hutchins 2018) and its electricity mix is approximately 70% based on fossil fuels (coal-based) (West 2017). The usage of fossil fuels has impacts in terms of global warming potential and human health, because of the burning process and the release of CO₂ and other greenhouse gas (GHG) emissions, and in resource depletion, as coal is a non-renewable material.

The use of chemicals also has some small but important environmental outcomes in all categories analysed. Considering HNO₃, the most significant ReCiPe impact is for human health, due to its high corrosivity, particularly to the eyes, skin, and mucous membranes in humans (an oral dose of 10 mL can be lethal (PUBCHEM DATABASE)). As well as for the results for HNO₃, the use of C₇H₈ has a much lower impact when compared with the electricity effects on all ReCiPe categories. However, this substance can affect humans' nervous systems (brain and nerves) causing headaches, dizziness, unconsciousness, memory loss, nausea, incoordination, cognitive impairment, and vision and hearing loss may become permanent with repeated exposure, as well as some other damages to the human brain. Additional human health effects of potential concern may include immune, kidney, liver and reproductive effects. The effects of C₇H₈ on animals are similar to those seen in humans (IRIS 2005).

Both experiments analysed in this study were able to recover some of the materials from the solar modules, as discussed. Recovering materials such as Ag, Al, Cu, Si and glass could be beneficial, as they might be re-introduced into the supply chain of solar modules or other industries. Besides, some of the materials are valuable and/or scarce (Weckend et al. 2016). The environmental benefits from the recovery of materials are also analysed via LCA and the results (also using the ReCiPe method) are shown in Figure 6.36.3.

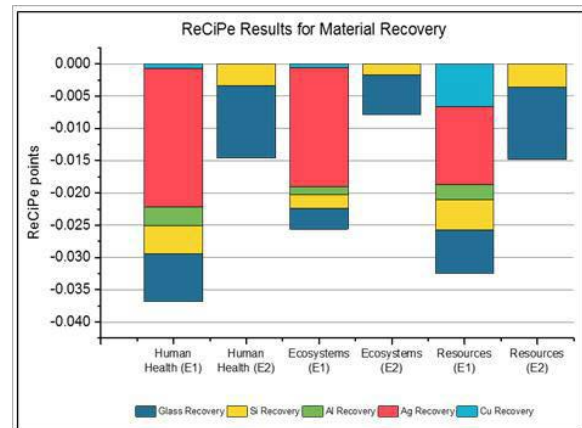


Figure 6.36.3: ReCiPe results for the recovery of glass, silicon (Si), aluminium (Al), silver (Ag) and copper (Cu), comparing Experiment 1 and Experiment 2.

The impacts of the materials recovery from Experiments 1 and 2 (respectively) have negative impacts for all categories, which means that the recovery process is environmentally beneficial. These results are mainly because Experiment 1 recovers a higher quantity of material compared with Experiment 2 (particularly Ag). However, the quality of these materials was not taken into consideration and it might affect the impacts of reusing elements such as Si and Ag, for example.

Glass recovery also has important environmental benefits. The main factor for this benefit is because glass represents about 76% of the modules' weight and is predicted to reach 80% of the modules' total weight by 2030 (Weckend et al. 2016). The environmental and economic benefits of recycling glass are related to the use of energy to produce this material, which is purified to be used in solar modules (low-iron glass), and also because glass requires significant space when disposed in landfill (Vellini & Savioli 2009; Kang et al. 2012).

Highlights

- The use of electricity from non-renewable sources causes the main ecological impacts from both experiments conducted.
- The use of chemicals should be taken into consideration, despite their smaller impacts, due to their harm to humans and the environment.
- In the near future, recycling plants specialising in PV waste need to increase treatment capacities and maximise revenues aiming for better output quality recovered resources and the capability to recycle a greater fraction of embodied materials.

Future Work

The project has been very successful in building collaboration between UNSW and UFRGS. In 2019 thermal and chemical experiments were conducted in LACOR – Brazil with the process steps documented to be part of the inventory data preparation. These experiments allowed us to conduct an LCA to analyse each process step and identify possible environmental issues to be addressed.

This project allowed us to build a good relationship with the Brazilian team, sharing our knowledge and complementing each other with different points of view about the same topic. We continue working together on other projects supporting both sides and building a comprehensive and reliable source of knowledge and data collection.

References

- ARDENTE, F., LATUNUSSA, C. E. & BLENGINI, G. A. 2019. Resource efficient recovery of critical and precious metals from waste silicon PV panel recycling. *Waste Management*, 91, 156-167.
- BAHAR, H. 2019. Solar PV: Tracking Clean Energy Progress. *International Energy Agency* The International Energy Agency.
- DIAS, P. R., BENEVIT, M. G. & VEIT, H. M. 2016. Photovoltaic solar panels of crystalline silicon: Characterization and separation. *Waste Management & Research*, 34, 235-245.
- HUTCHINS, M. 2018. Cell manufacturer ranking. *PV Magazine*.
- IEA-PVPS 2016. Snapshot of Global Photovoltaic Markets. *IEA Photovoltaic Power Systems Programme Report T1-29*.
- INTEGRATED RISK INFORMATION SYSTEM (IRIS), 2005. Toluene. Washington: U.S. Environmental Protection Agency – National Center for Environmental Assessment.
- ITRPV 2019. International Technology Roadmap for Photovoltaic – 2018 Results. In: EQUIPMENT, V. P. (ed.).
- KANG, S., YOO, S., LEE, J., BOO, B. & RYU, H. 2012. Experimental investigations for recycling of silicon and glass from waste photovoltaic modules. *Renewable Energy*, 47, 152-159.
- LATUNUSSA, C. E., ARDENTE, F., BLENGINI, G. A. & MANCINI, L. 2016. Life Cycle Assessment of an innovative recycling process for crystalline silicon photovoltaic panels. *Solar Energy Materials and Solar Cells*, 156, 101-111.
- MINTS, P. 2018. The solar flare, Issue 4. SPV Market Research.
- National Center for Biotechnology Information, Available: <https://pubchem.ncbi.nlm.nih.gov/compound/944> [Accessed 8 May 2019].
- NHEDE, N. 2019. Eight trends shaping 2019 global solar pv market. *Smart Energy International*. www.smart-energy.com.
- PUBCHEM DATABASE INFORMATION, N. C. F. B. Nitric acid [Online]. PubChem Database. U.S. National Library of Medicine.
- SANDER, K. & POLITIK, I. F. Ö. U. 2007. *Study on the Development of a Take Back and Recovery System for Photovoltaic Products*.
- TAO, J. & YU, S. 2015. Review on feasible recycling pathways and technologies of solar photovoltaic modules. *Solar Energy Materials and Solar Cells*, 141, 108-124.
- VELLINI, M., GAMBINI, M. & PRATTELLA, V. 2017. Environmental impacts of PV technology throughout the life cycle: Importance of the end-of-life management for Si-panels and CdTe-panels. *Energy*, 138, 1099-1111.
- VELLINI, M. & SAVIOLI, M. 2009. Energy and environmental analysis of glass container production and recycling. *Energy*, 34, 2137-2143.
- WAMBACH, K., SCHLENKER, S., MÜLLER, A., KLENK, M., WALLAT, S., KOPECEK, R. & WEFRINGHAUS, E. The Second Life of a 300 kW PV Generator Manufactured With Recycled Wafers From the Oldest German PV Power Plant. Abstract submitted to the 21st European Photovoltaic Solar Energy Conference and Exhibition, Dresden, Germany, 4-8 September 2006, 2006. Citeseer.
- WECKEND, S., WADE, A. & HEATH, G. 2016. End-of-life management Solar Photovoltaic Panels. IRENA and IEA-PVPS.
- WEST, B. 2017. Chinese coal-fired electricity generation expected to flatten as mix shifts to renewables. EIA's International Energy Outlook 2017.
- ZHANG, X. 2016. *Recycling of PV panels in Australia*. Bachelor of Engineering in Renewable Energy Engineering, The University of New South Wales.

6.37 IMPROVING UV STABILITY AND EFFICIENCY OF FOUR-TERMINAL PEROVSKITE-SILICON TANDEM SYSTEM WITH LUMINESCENT DOWNSHIFTING INCORPORATED ENCAPSULANT

Lead Partner

ANU

ANU Team

Dr The Duong, Prof. Kylie Catchpole, A/Prof. Thomas White

Academic Partners

Karlsruhe Institute of Technology (KIT): Prof. Bryce Richard, Dr Ulrich Paetzold

CSIRO Newcastle: Dr Benjamin Duck

Funding Support

ACAP

Aim

The objective of this project is to improve the UV stability of perovskite-silicon tandem solar cells using a luminescent downshifting (LDS) material. In the tandem systems, the LDS material will be incorporated into the front encapsulant to convert short wavelength light in the UV range to longer wavelength light to which the perovskite cell responds more efficiently. This will also enhance the stability of the perovskite cell due to the presence of the TiO₂ electron transport layer.

Progress

In order to make great progress in the project, Dr The Duong visited KIT for the second time from 4 October 2019 to 29 November 2019. During the visit, Dr Duong successfully incorporated the Lumogen F Violet V570 (BASF) into ethylene vinyl acetate (EVA) and fabricated large-area, durable LDS-incorporated EVA sheets. The following outlines the optimised procedure to produce high quality LDS-incorporated EVA sheets.

Step 1. Dissolve EVA pellets (Dupont PV1650) in dichloromethane with a concentration of 250 mg ml⁻¹, then stir for two hours on a hotplate at 90°C.

Step 2. Dissolve V570 dyes in dichloromethane with a concentration of 0.325 mg ml⁻¹, then stir for two hours at room temperature.

Step 3. Mix the two abovementioned solutions with a volume ratio of 1:1. This makes the dye concentration of 0.13% or 1300 ppm (relative to EVA). Stir the solution for two hours on a hotplate at 90°C.

Step 4. Take the solution off the hotplate and wait for it to cool down to room temperature. The solution is then poured on a mould and left to dry at 60°C inside a vacuum oven overnight.

Figure 6.37.1(a) shows a picture of a large-area LDS-incorporated EVA sheet on the left and a pure EVA sheet on the right. The thickness of the EVA sheets was controlled at 800 μm. Figure 6.37.1(b) shows the PLQY value close to 100% of the LDS-incorporated EVA sheet. The film also absorbs 100% of light at the wavelength of 375 nm. Different moulds were used to fabricate EVA sheets. To simplify the process, a textured silicon wafer was chosen as a mould to fabricate textured LDS-incorporated EVA sheets. Figure 6.37.1(c) and Figure 6.37.1(d) present the optical microscope images of a textured pure EVA sheet and a textured LDS-incorporated EVA sheet, respectively. The images clearly show the textured features on the foils with the size of 10–20 μm, which replicate the textured feature on the textured silicon wafer used as the mould.

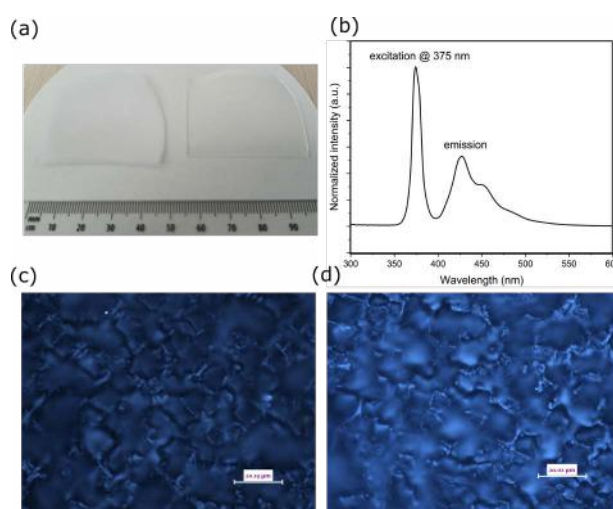


Figure 6.37.1: (a) Pictures of an LDS-incorporated EVA sheet and a pure EVA sheet. (b) PLQY of the LDS-incorporated EVA sheet. (c–d) Optical microscope images of the LDS-incorporated EVA sheet and the pure EVA sheet.

The textured LDS-incorporated EVA sheet was used on top of a perovskite-silicon tandem solar cell (Figure 6.37.2(a)). It serves multiple purposes in improving the performance of the systems. First, it converts UV light to green light, which improves the photocurrent response and UV stability of the perovskite top cell. Second, it acts as an anti-reflection coating layer to reduce the optical loss in the system. Third, it might work as a self-cleaning layer if the textured features and the property of the material can be optimised (Roslizar et al. 2019). Figure 6.37.2(b) shows the reflectance spectra of a semi-transparent perovskite solar cell with different anti-reflection structures. It clearly shows that the textured EVA sheets significantly reduce the reflectance from the device at the long wavelength region. At the short wavelength region, the reflectance is also reduced from 400 nm to 700 nm. However, the reflectance is higher in the samples with LDS-incorporated EVA sheets (both planar and textured) at the wavelengths from 280 nm to 400 nm. This is because the LDS dyes inside the sheets convert light in this UV wavelength range to green light and partially scatter it back to the detector. Nevertheless, the use of the textured LDS-incorporated EVA sheets results in higher transparency of the device at the long wavelength region (Figure 6.37.2(c)), which will improve the photocurrent of the silicon bottom cell in the tandem system.

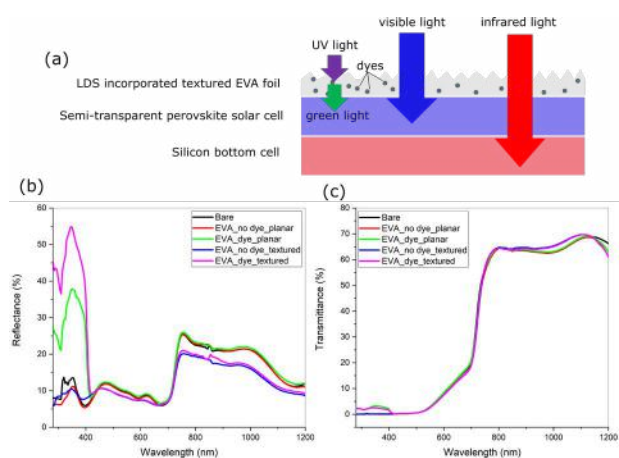


Figure 6.37.2: (a) Schematic of a perovskite-silicon tandem solar cell with an application of a textured LDS-incorporated EVA sheet. (b) Reflectance spectra of a semi-transparent perovskite solar cell with different anti-reflection structures. (c) Transmittance spectra of a semi-transparent perovskite solar cell with different anti-reflection structures.

Highlights

- Successfully fabricated durable and large-area LDS-incorporated EVA sheets.
- Used textured silicon wafers as moulds to fabricate textured LDS-incorporated EVA sheets.
- Applied the textured LDS-incorporated EVA sheets in perovskite-silicon tandem solar cells.

Future Work

- Characterise the J-V and EQE of the perovskite-silicon tandem solar cells with the application of textured LDS-incorporated EVA sheets.
- Measure the UV stability of the perovskite-silicon tandem solar cells with the application of textured LDS-incorporated EVA sheets.
- Prepare a manuscript on the work to submit to conferences and/or scientific journals.

References

ROSLIZAR, A., DOTTERMUSCH, S., VÜLLERS, F., KAVALENKA, M. N., GUTTMANN, M., SCHNEIDER, M., PAETZOLD, U. W., HÖLSCHER, H., RICHARDS, B. S. & KLAMPAFTIS, E. 2019. Self-cleaning performance of superhydrophobic hot-embossed fluoropolymer films for photovoltaic modules. *Solar Energy Materials and Solar Cells*, 189, 188-196.

6.38 NANOSCALE LOCALISATION OF DEFECTS IN SILICON AND CZTS VIA CATHODOLUMINESCENCE AND PHOTOLUMINESCENCE SPECTROSCOPY

Lead Partner

UNSW

UNSW Team

A/Prof. Ziv Hameiri, A/Prof. Xiaojing Hao, Dr Michael Pollard, Mr Robert Lee Chin.

Academic Partner

AMOLF: Prof. Albert Polman

Funding Support

ACAP Collaboration Grant, UNSW, UNSW RIS, AMOLF

Aims

The main goals of this project are:

- Development of cathodoluminescence (CL)-based measurement methods for silicon-based PV.
- Development of CL-based measurement methods for CZTS solar cells.
- Comparison between CL and micro-photoluminescence (μ PL) measurements. Identify the advantages and disadvantages of each method.
- Development of methods to extract injection-dependent lifetime using time-resolved PL and CL measurements.
- Establish a strong collaboration between UNSW and AMOLF.

Progress

In the last year, we have focused on development of a method to extract defect parameters from localised μ PL measurements. Sub-bandgap luminescence is characteristic of radiative transitions from defects in semiconductors. However, methods to extract defect-identifying parameters from this luminescence are lacking. We developed a method to extract these parameters from temperature- and intensity-dependent μ PL spectra. The initial "coarse" analysis determines the relevant radiative recombination mechanism by fitting the integrated defect PL spectra with phenomenological models for the temperature- and intensity-dependence. The subsequent "detailed" analysis fits the integrated defect PL spectra using rigorous physical models for the defect radiative recombination and spectral line-shape. From these fits the defect parameters are extracted, including the defect energy level(s). As we obtain these values directly from the defect luminescence, our method provides higher confidence than more traditional indirect methods, such as those involving band-to-band PL and photoconductance. The method was demonstrated on spatially non-uniform defects with radiative transitions in n-type monocrystalline silicon samples. It was shown that the defect PL

originates from a donor-acceptor pair recombination mechanism, involving a shallow acceptor and deeper donor energy level. The acceptor level is extracted from the temperature-dependent spectra, while the intensity-dependent spectra give the sum of acceptor and donor energies

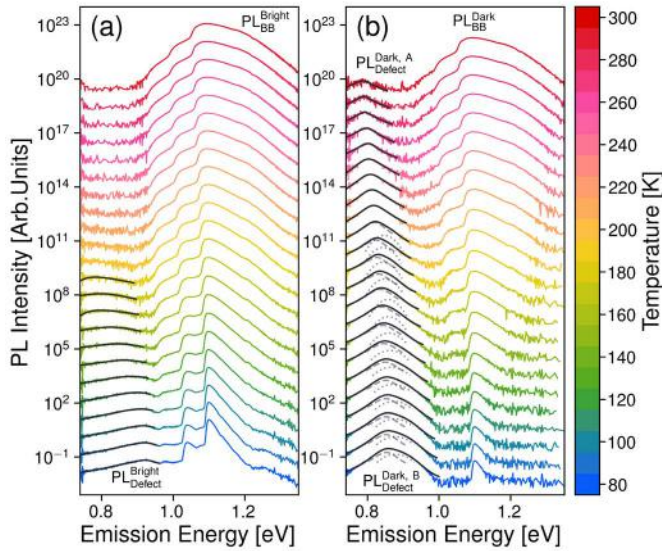


Figure 6.38.1: Temperature-dependent spectral PL including their fits for (a) high-quality silicon; and (b) low-quality silicon. All spectra are measured at a light intensity of 19.5 suns.

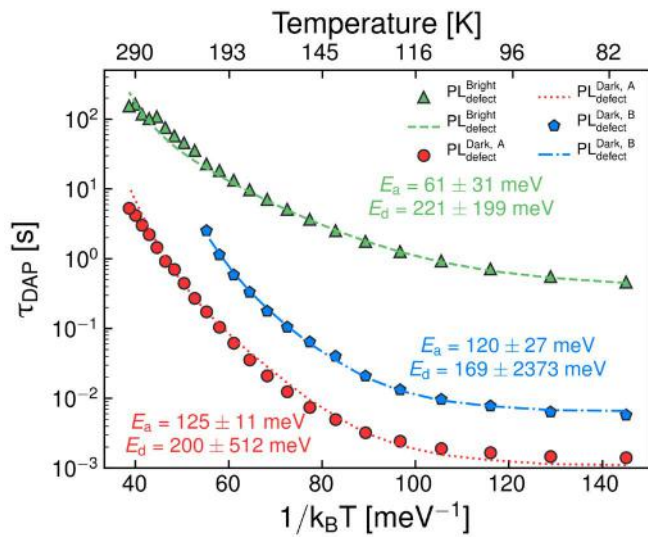


Figure 6.38.2: τ_{DAP} versus $1/k_B T$. The coloured lines are the fits using the physical model for donor-acceptor pair recombination.

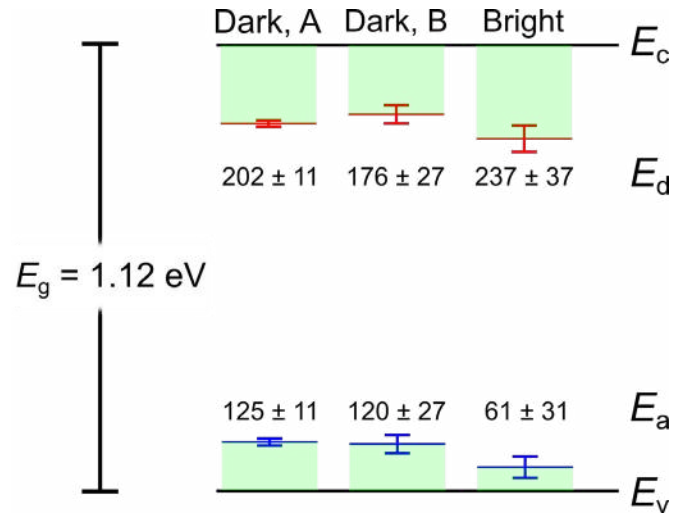


Figure 6.38.3: Band diagram showing the extracted defect energies (E_a and E_d). E_v and E_c represent the valence and conduction band-edges, respectively. The long horizontal lines represent the position of the defect energies and the short bars represent the standard error-bars. All values of the defect energies are in units of meV.

Highlights

- A visit to UNSW by Professor Albert Polman (February 2019; also planned for February 2020).
- Development of a method to extract defect parameters from localised μ PL measurements.
- One journal publication by Robert Lee Chin (SOLMAT, 2020).
- UNSW purchased a CL system (to be installed in March/April 2020).

Future Work

- Measurements of the metal-silicon interfaces.
- Extending the developed capabilities to map defect parameters.
- Comparison between μ PL and CL measurements.
- Continue measurements of CZTS samples.

References

LEE-CHIN, R., POLLARD, M., ZHU, Y & HAMEIRI, Z. 2020. Detailed analysis of radiative transitions from defects in n-type monocrystalline silicon using temperature- and light intensity-dependent spectral photoluminescence. *Solar Energy Materials and Solar Cells*, 208, 110376. DOI: 10.1016/j.solmat.2019.110376. (in press)

6.39 OPTIMISATION OF SILICON SOLAR CELL FABRICATION PROCESSES USING MACHINE LEARNING ALGORITHM

Lead Partner

UNSW

UNSW Team

A/Prof. Ziv Hameiri, Dr Rhett Evans, Mr Yoann Buratti,
Mr Caspre Eijkens (exchange student; Delft University of Technology)

Academic Partner

SERIS: Dr Shubham Duttagupta

Funding Support

ACAP Collaboration Grant, UNSW, SERIS

Aims

The main goals of this project are:

- Development of manufacturing optimisation method of silicon solar cell using machine learning.
- Assess the capability of the developed method to optimise a non-silicon photovoltaic fabrication process.
- Strengthen the collaboration between UNSW and SERIS.

Progress

The manufacturing of photovoltaic devices is a combination of consecutive processes that turns silicon, chemicals, gases and metals into a solar cell. Each process follows a recipe that needs to maximise the performance of the fabricated solar cells. The configuration of a process is a complex optimisation problem, since many interactions between process variables exist. Typically, process optimisation involves statistical modelling of experimental data using low order polynomials. However, polynomial functions struggle to fit many variables and non-linear patterns and can therefore only model a few processes. In this project, we address this problem by using machine learning (ML) algorithms, which can accurately model complex patterns in high dimensional data. ML simultaneously learns multiple processes and the interactions among their variables that normally remain unexplored. We tested the capacity to model manufacturing processes using simulated data for several ML algorithms. An artificial neural network was found to model a complete production line with 49 input variables, predicting cell efficiencies with a mean absolute error of 0.29%. Furthermore, using an optimisation algorithm, the neural network identified a new process configuration with a significantly better cell efficiency, demonstrating the advantage of ML models for PV manufacturing process optimisation.

Manufacturing data is simulated with the virtual production line (VPL) software that was developed in collaboration between UNSW and PV Lighthouse. VPL simulates the manufacturing of solar cells using ten fabrication processes and 49 input variables. The solar cells' electrical properties are modelled using PC1D. VPL includes many interactions to imitate the complexity of solar cell fabrication. In this

part of the project, we created three different data sets with different sets of equations (modes) to model the interconnections of the VPL processes. For each mode, 9,500 random process configurations are simulated for training and 500 for testing. For a fair comparison, each algorithm is evaluated to identify its optimal settings, such as the hidden layer structure for artificial neural network (ANN). Extra hidden layers increase the model's capacity for fitting complex patterns but needs more training data for good predictions.

The performance of the algorithms is assessed by predicting the photovoltaic cell efficiency based on the process variables and is measured with the root mean squared error (RMSE) and the coefficient of determination (R^2) in a five-fold cross-validation. The algorithm scoring the lowest RMSE is then trained on a balanced data set of 280,000 samples to test its capacity to model a complete production line. Finally, a genetic algorithm is used to optimise the selected model in order to identify the configuration of each process that achieves the highest PCE.

Results

After optimising the settings of the ML algorithms and the polynomial fitting (POLY), three differently simulated data sets are modelled with an ANN with two hidden layers (ANN2), three hidden layers (ANN3), POLY, support vector regression (SVR), random forests (RF) and AdaBoost. For each data set, the models are trained on 9,500 data points and tested on the remaining 500. The RMSE scores of these tests are shown in Figure 6.39.1(a). The respective performance of the methods is equivalent for the three data sets. ANN performed unanimously best as it scored the lowest RMSE in this comparison. This result suggests that ANN is most appropriate for modelling a complete PV manufacturing line.

Next, a balanced data set of 240,000 data points is modelled with ANN3 and its performance is assessed using the RMSE of 15,000 data points that were not seen before. A scatterplot of actual PCE versus predicted PCE is shown in Figure 6.39.1(b), scoring an RMSE of 0.29 and an R^2 of 0.99, which is an impressive result. This model is then optimised with a genetic algorithm and identifies a configuration that achieves a 1.6% increase in PCE compared to the maximum PCE that was included in the data. Since PV manufacturing lacks a broad variation in the data, future research will focus on combining the variance of DoE data with the size of production data.

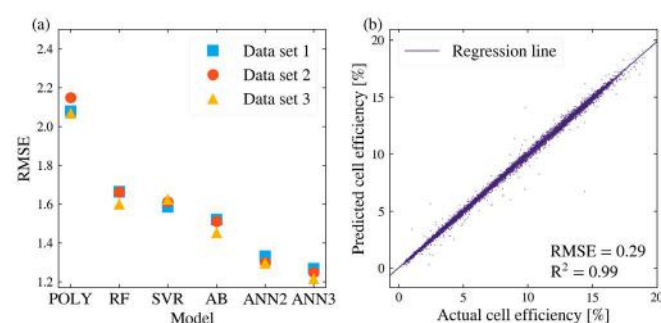


Figure 6.39.1: (a) Comparison of five ML regression models and polynomial fitting on three different data sets. (b) Scatterplot of actual versus predicted of 15,000 data points.

Highlights

- Employment of an exchange student (from Delft University of Technology).
- Development of machine learning algorithm to predict end-of-the-line efficiency based on processing setting.
- An invited talk by Associate Professor Hameiri at the Silicon Workshop (CO, USA).
- A talk by Associate Professor Hameiri at the 29th International PV Science and Engineering Conference (Xi'an, China).
- A poster presentation at the Asia-Pacific Solar Research Conference (Canberra, Australia).

Future Work

- Test the developed algorithm on SERIS data.
- Journal publication.

References

EIJKENS, C. A., BURATTI, Y. & HAMEIRI, Z. 2019. Multivariate process optimization of commercial solar cell manufacturing using machine learning, 29th International Photovoltaic Science and Engineering Conference, Xi'an, China, 4–8 November 2019.

6.40 ADVANCING THE PDS TECHNIQUE FOR ALL PHOTOVOLTAIC THIN FILMS

Lead Partner

UNSW

UNSW Team

Xiaojing Hao, Gavin Conibeer

UNSW Student

Xueyun Zhang

Academic Partners

Tokyo University: Prof. Masakazu Sugiyama, Prof. Yoshitaka Okada
Macquarie University: Dr Binesh Puthen Veetil

Industry Partner

Open Instruments: Henner Kampwerth, Michael Pollard

Funding Support

AUSIAPV, UNSW, Tokyo University

Aims

While dark energy losses, such as carrier thermalisation and defect recombination, are critically important parameters in photovoltaic (PV) device performance, they are some of the most difficult material parameters to measure. To minimise these detrimental properties, it is necessary to accurately monitor them during material and device development. Usually, these parameters are indirectly quantified via an energy balance equation. In this scheme, the illuminating photon energy must equal the sum of the electrical device output and the luminescent (bright) and thermalisation (dark) losses. While the first two can be directly measured, the "dark" component cannot, and must therefore be inferred as the "remainder" by subtraction of the others. However, the cumulative error from the electrical and luminescent measurements can often render "dark" values useless. Measurements on thin-film materials can be particularly difficult due to their weak signals from photo-absorption and spatially integrated and quantitative photoluminescence.

To directly measure these "dark" losses in thin-film photovoltaic devices, Professor Sugiyama suggested a concept based on a highly sensitive photothermal deflection spectrometer (PDS). The PDS system that was subsequently developed for this purpose is capable of measuring optical absorption with very high sensitivity, about 1000 times better than traditional $1-(R+T)$ absorption systems. The PDS system at UNSW has become a tool of choice for many researchers interested in sub-bandgap phenomena, such as trap states and Urbach tails in thin-film materials.

This collaborative project between Tokyo University, Open Instruments (2019) and UNSW capitalises on Professor Sugiyama's initial idea. It intends to (1) develop a new measurement technique that

can accelerate R&D for all ACAP members, (2) initiate a lasting international partnership in the field of characterisation, and (3) add further value to the PDS system that is being commercialised.

Progress

The system was initially developed at UNSW through an ARENA Fellowship during 2013–2015 and further developed towards commercialisation in stages with industrial collaborator Open Instruments and support from ACAP (ACAP Collaboration Grant Round 3) and ARENA (ARENA Commercialisation of R&D).

More details on the principle of the PDS measurement can be found in section PP3 of this report. The relevant detail for this project is that the instrument measures the heat that is generated by the photo-absorption of the sample. The heat signature represents the number of absorbed photons by assuming that all absorbed energy will recombine thermally (“dark” recombination).

A typical PDS measurement does not extract charge carriers via electrical contacts and radiative emission (photoluminescence) can be calibrated out. However, if the measurement sample is a photovoltaic device with electrical contacts, the measured “dark” recombination can be altered; new measurement modes become possible.

For contacted devices, “dark” energy losses due to shunt resistance, series resistance and defect recombination and thermalisation are of interest. While shunt and series resistance losses can be measured electrically (I-V curve), losses due to defects and thermalisation are extremely difficult to measure. It is here that the temperature-measuring PDS system comes into its own. With PDS, it is possible to measure all three of these components by modulating conditions that affect different loss mechanisms.

For this project, the latest laboratory PDS setup and first industrial setup, developed with ACAP support and in collaboration with Open Instruments, are used and shown in Figure 6.40.1. Both will be modified accordingly to allow electrical biasing.



Figure 6.40.1: The first commercial beta version of a PDS unit was presented at the Asia-Pacific Solar Research Conference (APSRC) at UNSW in December 2018.

Highlights

- An exciting new measurement capability of PDS, the measurement of dark carrier recombination, is being explored.

Future Work

This project will conclude at the end of 2020. Results will be summarised in the next annual report.

References

ACAP Collaboration Grant Round 3. Alignment-free PDS tool: From university to industry. (ACAP Collaboration Grant – Round 3 – (Funding: 1-SRI001, InfoEd: RG123662-Q)).

ARENA Commercialisation of R&D. “Launch of a Photothermal Absorption Spectrometer for Cost Reduction in PV Materials”, ARENA Commercialisation of R&D Funding Initiative Pilot Funding, (contract: 2019/CRD005).

OPEN INSTRUMENTS. 2019. <http://www.openinstruments.com>.

6.41 PASSIVATING TUNNEL CONTACTS ON SI BY Al_2O_3 -MONOLAYERS IN SiO_2 AND SI-RICH/NANOCRYSTALLINE SiO_x

Lead Partner

ANU

ANU Team

Dr Daniel Hiller

Academic Partner

Institute of Energy and Climate Research (IEK-5), Jülich Research Center, Germany: Dr Kaining Ding, Dr Manuel Pomaska, Malte Köhler

Funding Support

ACAP

Aim

The objective of this project is to investigate combinations of ultra-thin films of atomic layer deposited Al_2O_3 and SiO_2 or SiO_x as passivating hole-selective tunnel contacts on Si. The challenge is to achieve very good Si surface passivation with <2 nm SiO_2 or SiO_x layers and just (sub)-monolayers of Al_2O_3 , so that the whole stack thickness still allows for direct quantum mechanical charge carrier tunnelling. Such layer stacks are optically fully transparent and the materials are stable in firing.

Progress

The knowledge and understanding of the initial Al_2O_3 -growth during the first ALD-cycles is decisive for this passivating contact concept. Since ALD depends on the surface chemistry, the pre-treatments of the Si wafer dominate the initial deposition. A well-known example is the difference between hydrophilic wet-chemically oxidised surfaces (for example from RCA-solutions) and hydrophobic HF-last Si. Almost no Al_2O_3 deposition occurs during the initial cycles until the Si-H surface groups are gradually replaced by hydroxyl groups (Si-OH or Al-OH) that enable efficient trimethylaluminium (TMAI) chemisorption (Frank et al. 2003; Delabie et al. 2012). In contrast, efficient ALD-growth can be achieved on hydroxylated surfaces from the very first ALD-cycle on. Our previous research suggested that ultra-thin thermal tunnel- SiO_2 is a suitable surface for Si surface passivation with (sub)-monolayers of Al_2O_3 (König et al. 2017; Hiller et al. 2018; Hiller et al. 2019). Yet, the exact evolution of the deposition as a function of ALD-cycles was unknown. In collaboration with Dr Philipp Hönicke from the Physikalisch-Technische Bundesanstalt (PTB), Germany's national metrology institute, the Al-deposition of the initial ALD-cycles was studied using reference-free grazing incidence X-ray fluorescence (GIXRF) at the BESSY II synchrotron in Berlin. The results are shown in Figure 6.41.1. Whereas ALD- Al_2O_3 deposition on a fully hydroxylated RCA-2 oxide is almost perfectly ideal compared to typical steady-state ALD-growth, the initial 3 ALD-cycles on a thermal tunnel-oxide do not form a complete first ALD-monolayer (i.e. 4×10^{14} Al-atoms cm^{-2}). For ≥ 4 ALD-cycles the Al-deposition/cycle is increasing due to progressive hydroxylation of the surface. Steady-state deposition on thermal- SiO_2 is approached after 10 ALD-cycles.

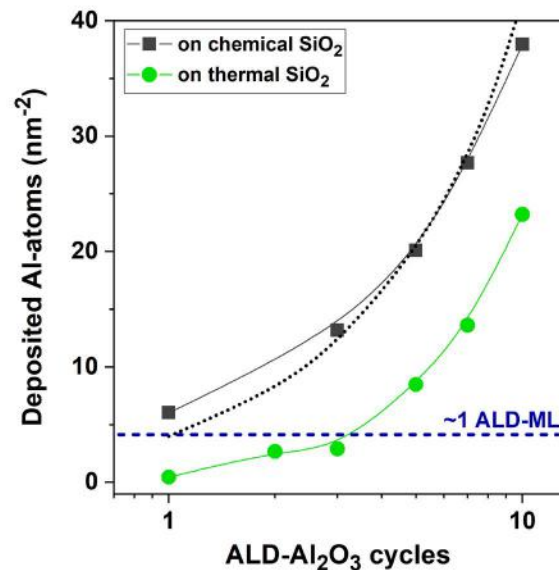


Figure 6.41.1: Al-deposition from GIXRF measurements as a function of ALD-cycles on a chemically grown tunnel-oxide (RCA-2, 1.2 nm thick) compared to a thermal tunnel-oxide (1.3 nm thick). The blue dashed line represents approximately 1 ALD- Al_2O_3 monolayer according to the typical steady-state deposition of 4×10^{14} Al-atoms cm^{-2} . The black dotted line shows idealised deposition of 4×10^{14} Al-atoms cm^{-2} /cycle.

Symmetrical lifetime samples with FZ-Si (n-type, 5 Ω -cm) were fabricated using different interfacial oxides and 0 to 30 ALD- Al_2O_3 cycles. The passivation has to be activated by rapid thermal annealing (RTA) in the temperature range of 800–850 °C for a couple of seconds in N_2 -atmosphere. It turned out that wet-chemically grown oxides (for example by boiling HNO_3) or ultra-thin oxides grown in situ in the ALD-reactor by prolonged exposure to H_2O -vapour or O_3 -gas provide, in conjunction with the ultra-thin ALD- Al_2O_3 film, just a moderate surface passivation quality with surface saturation current densities J_{0s} of 75 to 200 fAcm^{-2} . On 1.6 nm thick thermal.

tunnel oxides, however, $J_{0s} = 40 \text{ fAcm}^{-2}$ is observed even before a forming gas anneal (FGA), (Figure 6.41.2(a)). An additional FGA reduces the recombination further and at best $J_{0s} = 25 \text{ fAcm}^{-2}$ (corresponding to a surface recombination velocity $S_{\text{eff}} = 2.7 \text{ cm s}^{-1}$) is achieved. Remarkably, even for just one ALD- Al_2O_3 cycle (that is, 1/10 of an ALD-monolayer), around 30 fAcm^{-2} are measured after FGA. Similar surface passivation qualities are also found for p-type Si (2.5 Ω -cm).

Interestingly, it is mandatory to activate the passivation by RTA, which involves an intense irradiation with visible light (that is $h\nu > E_{\text{gap,Si}}$). Experiments with two clean dummy wafers that sandwich the lifetime sample during RTA but absorb all above-bandgap light showed one order of magnitude worse surface passivation. Tube furnace annealing using similar parameters as RTA allows for roughly 50% of the

surface passivation quality compared to RTA, which we attribute to the small component of visible light in the blackbody radiation of the furnace (that is the orange glow at around 800°C). The exact physical mechanism of the light-activated surface passivation could not be revealed yet.

In Figure 6.41.2(b) the contact resistivities (ρ_c) of stacks with 1.6 nm thermal-SiO₂ and a varying number of ALD-Al₂O₃ cycles is shown (on p-type Si for hole tunnelling). Very low values are measured without Al₂O₃, but the first ALD-cycle increases ρ_c already to ~0.2 mΩ·cm², a value which is still considered non-critical (Melskens et al. 2018). For 2-4 ALD-cycles ρ_c approaches critical values around 0.5 mΩ·cm², before it increases exponentially for thicker layers. Unfortunately, the Pd-contacts used for ρ_c -measurements strongly deteriorate the surface passivation as lifetime measurements with semitransparent ~7 nm thick Pd films revealed. Another high work function metal suitable for hole contacts (Ni) was also tested with the same result. Future work will have to identify other, maybe non-metal, contact materials that preserve the very good surface passivation and enable a low ρ_c .

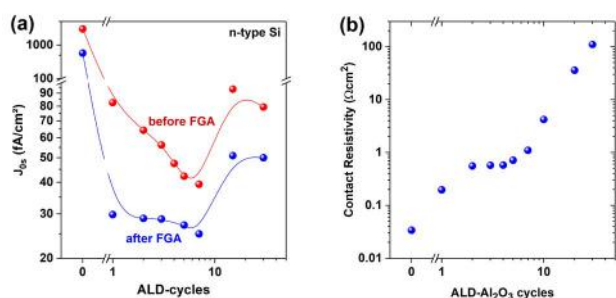


Figure 6.41.2: (a) Surface passivation quality of ALD-Al₂O₃ ultra-thin films on 1.6 nm thick thermal SiO₂ on n-type Si, before and after forming gas annealing (FGA). (b) Contact resistivities for holes of the same dielectric stacks with Pd contacts.

Highlights

- Understanding of initial ALD-growth on thermal tunnel-SiO₂ by precise quantification of Al-deposition via reference-free GIXRF: Sub-monolayer deposition of Al₂O₃ up to 3 ALD-cycles.
- Very good surface passivation with down to $J_{0s} = 25$ fAcm⁻² ($S_{eff} = 2.7$ cm s⁻¹) for ≤ 7 ALD-Al₂O₃ cycles on n-type Si (similar performance on p-type Si). Thermal tunnel-oxides were found to be superior over other oxides.
- Surface passivation requires thermal activation (~800°C, few seconds) and the additional irradiation with visible light from the RTA-lamps is decisive.
- Moderate contact resistivities for one ALD-cycle (0.2 mΩ·cm²), critically high for 2-4 ALD-cycles (~0.5 mΩ·cm²).
- Two invited talks by Dr Hiller at the MRS Fall Meeting 2019 (Symposium EN11), Boston, USA, and Silicon Days 2019, TU Freiberg, Germany.

- Visit by Dr Ding from Jülich Research Center to ANU and UNSW (February 2019).
- Visit to Jülich Research Center by Dr Hiller (June 2019).

Future Work

- Finding suitable (maybe non-metal) contact materials that maintain a good Si surface passivation, in contrast to the tested high work function metals (Pd, Ni), before fabrication of test cells together with the partners.

References

- DELABIE, A., SIONCKE, S., RIP, J., VAN ELSHOCHT, S., POURTOIS, G., MUELLER, M., BECKHOFF, B. & PIERLOOT, K. 2012. Reaction mechanisms for atomic layer deposition of aluminum oxide on semiconductor substrates. *Journal of Vacuum Science & Technology A*, 30.
- FRANK, M. M., CHABAL, Y. J. & WILK, G. D. 2003. Nucleation and interface formation mechanisms in atomic layer deposition of gate oxides. *Applied Physics Letters*, 82, 4758-4760.
- HILLER, D., GOTTLICHER, J., STEININGER, R., HUTHWELKER, T., JULIN, J., MUNNIK, F., WAHL, M., BOCK, W., SCHOENAERS, B., STESMANS, A. & KONIG, D. 2018. Structural Properties of Al-O Monolayers in SiO₂ on Silicon and the Maximization of their Negative Fixed Charge Density. *ACS Applied Materials & Interfaces*, 10, 30495-30505.
- HILLER, D., JORDAN, P. M., DING, K. N., POMASKA, M., MIKOLAJICK, T. & KONIG, D. 2019. Deactivation of silicon surface states by Al-induced acceptor states from Al-O monolayers in SiO₂. *Journal of Applied Physics*, 125.
- KONIG, D., HILLER, D., GUTSCH, S., ZACHARIAS, M. & SMITH, S. 2017. Modulation Doping of Silicon using Aluminium-induced Acceptor States in Silicon Dioxide. *Scientific Reports*, 7.
- MELSKENS, J., VAN DE LOO, B. W. H., MACCO, B., BLACK, L. E., SMIT, S. & KESSELS, W. M. M. 2018. Passivating Contacts for Crystalline Silicon Solar Cells: From Concepts and Materials to Prospects. *IEEE Journal of Photovoltaics*, 8, 373-388.

6.42 OUTDOOR STABILITY/DURABILITY ASSESSMENT OF TWO-TERMINAL PEROVSKITE-SILICON TANDEM CELLS

Lead Partner

UNSW

UNSW Team

A/Prof. Anita Ho-Baillie, Dr Jianghui Zheng, Mr Lei (Adrian) Shi

Academic Partner

CSIRO, Energy, Newcastle

Funding Support

ACAP

Aim

Monolithic integration of a perovskite-silicon tandem device in a two-terminal configuration, although an elegant approach, has inherent current matching limitations for such a series connected device. The aim of the project is to increase understanding of the effect of varying spectrum, angle of incidence and temperature when two-terminal perovskite-silicon cells operate under real outdoor conditions.

Progress

Due to unforeseen constraints imposed externally on the team fabricating perovskite/Si tandem solar cells none was available for testing under outdoor conditions. Effort was instead focused on preparing the necessary equipment and experimental procedures for applying a range of tests on the devices when they became available.

Dedicated source measure units with maximum power point tracking capability have been prototyped for control of device load in the field. A limitation of the previous system was the necessity of using a constant load (either a resistive or diode load) that was only successful at mimicking operating behaviour at a subset of the outdoor conditions. For example, a resistive load can be sized to work appropriately under standard test conditions (STC) equivalent conditions but will hold the device at an incorrect voltage under different irradiance and temperature conditions. The new dedicated units integrate with the existing control system allowing the device to be held at appropriate operating conditions that are adapted in real time while also allowing for the transfer of control to the bespoke I-V measuring system for periodic standard measurements.

Maximum power point tracking control software has been prepared for use in outdoor and indoor testing procedures. This will allow measurement of the optimal power due to changing operating conditions both external (irradiance, temperature etc) and internal (ion migration, degradation etc).

CSIRO's spectral response measurement system has been upgraded with additional bias light capability allowing for better selective control over measurement junctions. Sample rotation capability has also been added allowing measurement of the angle of incidence response of devices under controlled conditions.

A new stability measurement system has been developed for testing the impact of varying irradiance, spectrum, temperature and long-term exposure on the devices. The system is based on spectrally variable LED sources with temperature control and allows for long-term side-by-side comparison of multiple devices under variable operating conditions.

Highlights

- Improved outdoor measurement capability with individual load control and maximum power point tracking (MPPT).
- Indoor spectral response and angle of incidence measurement capability for measurement on tandem devices.
- Long-term indoor measurement capability with variable irradiance, spectrum and temperature.

Future Work

- Analyse cell performance taking into account climatic data due to multiple variables introduced by real outdoor conditions.
- Testing of devices with identical fabrication conditions both indoor and outdoor.
- Obtain field energy yield data accounting for the time of the day and day of the year.
- Assessment of cells at standard test conditions (STC) and nominal operating cell temperature (NOCT) equivalent conditions in an outdoor environment.

6.43 HIGH EFFICIENCY SPECTRUM SPLITTING CPV RECEIVER USING A TRIPLE-JUNCTION SOLAR CELL WITH INTERNAL BRAGG REFLECTOR

Lead Partner

UNSW

UNSW Team

Dr Yajie Jiang, Dr Mark Keevers, Scientia Prof. Martin Green

Industry Partners

AZUR SPACE Solar Power
RayGen Resources Pty Ltd

Funding Support

ACAP

Aim

UNSW has demonstrated a world record conversion efficiency of 40.6% with a spectrum splitting concentrator photovoltaic (CPV) submodule, using a 150-layer dielectric band-pass filter to divert the 900–1050 nm spectral band from a triple-junction solar cell (TJSC) to a Si cell. This project aims to develop a potentially lower cost and higher performance approach using a TJSC with an internal spectrum-splitting Bragg reflector, which can be implemented with little additional cost during manufacture, in contrast to fabrication of discrete dielectric filters.

Progress

The centralised power tower technology is regarded as one of the most promising approaches to CPV, which is being developed by Australian company RayGen Resources, consisting of a field of heliostats concentrating the sunlight to a single flat 1 m² PV array atop a mast (Figure 6.43.1). The cells used in the receiver are high performance GaInP/GaInAs/Ge TJSCs. One disadvantage of these TJSCs is the bottom Ge cell having a much lower bandgap, generating much more current than the other two cells. The extra current is wasted as heat within the cell, increasing challenges in maintaining low operating temperatures where the cells are most efficient.



Figure 6.43.1: RayGen's Central Receiver CPV power tower. Inset shows receiver.

Given this single large receiver, an efficient approach to solve this problem is using spectrum splitting by reflecting some of the excess photons reaching the Ge cell in the TJSC array onto a relatively inexpensive array of Si cells (Figure 6.43.2). This project proposed a novel approach by integrating an intermediate distributed Bragg reflector (DBR) during TJSC fabrication, optimised to function as a suitable band-reflect filter (Jiang et al. 2019). This approach shows potential practical application to CPV power tower technology by replacing the TJ array with a V-shaped spectrum splitting receiver, which combines the TJ array with spectrum splitting DBR + an additional Si array (Figure 6.43.3).

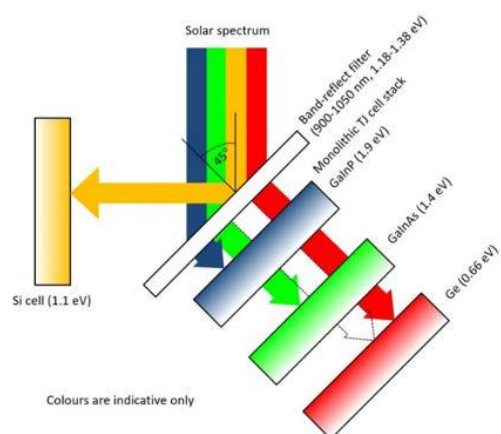


Figure 6.43.2: Schematic of the spectrum splitting concept used in this work.

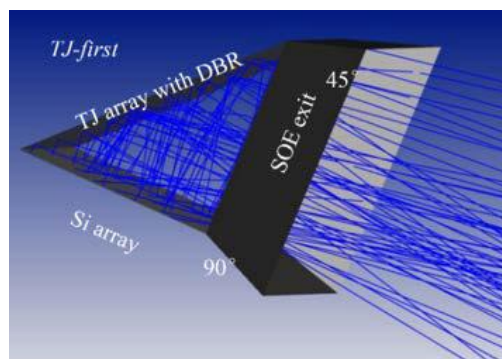


Figure 6.43.3: Schematic of a V-shaped spectrum splitting receiver.

A spectrum splitting DBR was implemented with little additional cost during manufacture of the commercial CPV product by our industrial partner AZUR SPACE. The spectrum splitting cell exhibits no visual difference compared to the baseline cell (Figure 6.43.4).

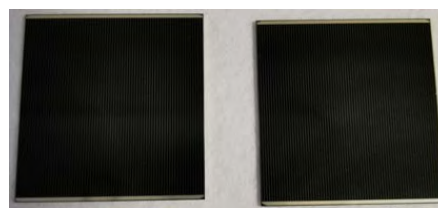


Figure 6.43.4: Images of baseline cell without DBR (left) and spectrum splitting cell with DBR (right).

Both baseline cells and spectrum splitting cells with DBR were fabricated. Light current-voltage (LIV) measurements were conducted on all the cells under AM1.5D spectrum (350x concentration) at 25°C. Spectrum splitting cells with DBR shows no major detriment to the cell performance compared with baseline cells (Figure 6.43.5).

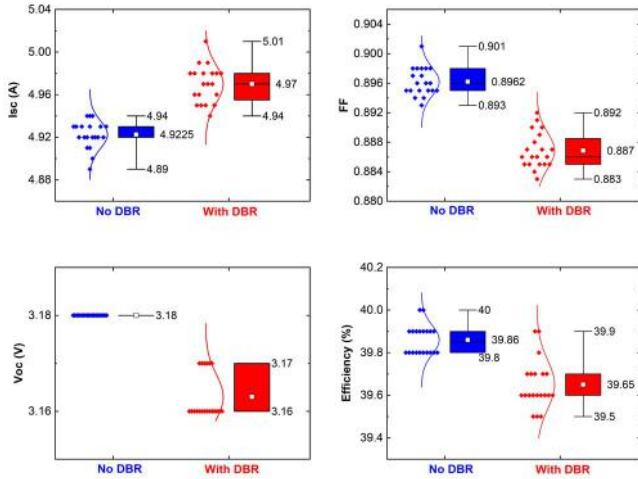


Figure 6.43.5: I_{sc} , V_{oc} , FF and efficiency distribution comparison between baseline cells and cells with spectrum splitting DBR.

The important distinguishment between these two types of cells are their reflection. The spectrum splitting DBR is integrated in the CPV cell to divert extra photons away from the Ge bottom sub-cell without detriment to the current-limiting sub-cells. Figure 6.43.6 shows the measured reflection of two TJSCs with/without DBR. A broad reflection band between 950 and 1050 nm is achieved with approximately 90% reflection for a CPV cell with DBR, demonstrating the feasibility of a DBR-assisted spectrum splitting approach.

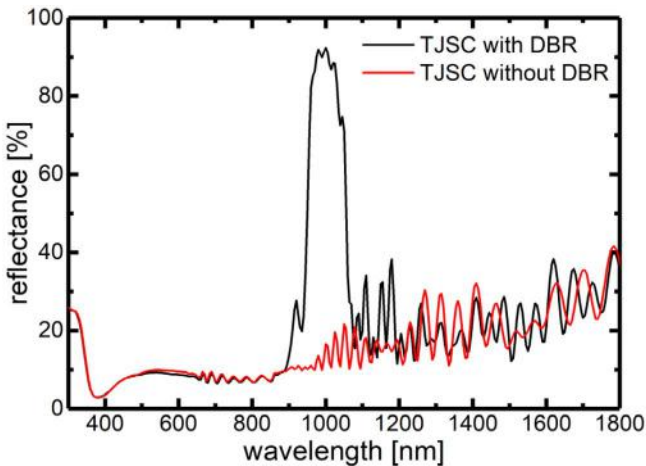


Figure 6.43.6: Reflectance measurements of two typical TJSCs with and without DBR.

The current densities and efficiencies were modelled using Solcore (Alonso-Álvarez et al. 2018), a Python-based integrated optical and electrical modelling framework for solar cells. The optical part of the simulations, calculating the reflected power and depth-dependent absorption/generation rate, was carried out using the built-in transfer matrix method (TMM) optical model, using the same optical constants

data which we used to fit the reflectance measurements. The external quantum efficiency (EQE) and LIV characteristics were calculated using the depletion approximation (Nelson 2003) as implemented in Solcore.

To simulate the performance of an integrated CPV receiver consisting of a TJSC and a Si cell, the reflectance and LIV characteristics of different TJSC structures were calculated assuming 5% shading loss, and an incident AM1.5D spectrum concentrated 350x incident at 45° AOI (angle of incidence) on the TJSC. Light reflected from the TJSC is incident normally on the Si cell, which is modelled on an Amonix concentrator cell.

The calculated sub-cell photocurrent densities of the TJSCs are shown in Table 6.43.1. The spectrum-splitting DBR designs have the desired effect of diverting photons away from the Ge bottom sub-cell without detriment to the top or current-limiting middle sub-cells. In the four-junction receiver, the corresponding Si cell efficiency and total spectrum splitting receiver efficiency shows a clear enhancement of 38.2%+3.2%=41.5% compared with the original TJSC structure of 39.1%.

Table 6.43.1: Calculated sub-cell photocurrent densities and LM TJSC + Si cell efficiencies.

Device structure	J _{sc} top sub-cell (mAcm ²)	J _{sc} middle sub-cell (mAcm ²)	J _{sc} bottom sub-cell (mAcm ²)	FF (%)	Efficiency LM TJSC (%)	Efficiency Si cell (%)	Efficiency Total (%)
Original T JSC @ 0° AOI	12.5	11.9	18.6	91.4	39.1	N/A	39.1
TJSC with spectrum splitting DBR @ 0° AOI	12.5	11.9	15.4	91.0	38.9	N/A	38.9
TJSC with spectrum splitting DBR @ 45° AOI	12.6	11.8	15.4	91.0	38.3	3.2	41.5

Note: The concentration on the TJSC at 45° is $350/\sqrt{2}=247\times$, the contribution from the Si cell is conservative because reflection from the metal on the TJSC is assumed lost and not captured by the Si cell.

The bottom sub-cell still has a much larger current density (15.4 mAcm⁻²) compared to the current-limiting middle cell (11.8 mAcm⁻²). Our next iteration will be targeted at broadening the spectrum splitting reflection band, to achieve closer to current matching conditions between three sub-cells in the TJSC, but leaves a sensible margin above the limiting current to avoid the Ge sub-cell excessively reducing the TJSC fill factor (Meusel et al. 2002).

Figure 6.43.7 shows the impact on EQE between original TJSC at 0° AOI and a four-junction spectrum splitting receiver with TJSC at 45° AOI plus an Si cell to capture the reflected light. The additional Si cell shows an effective EQE in the four-junction receiver.

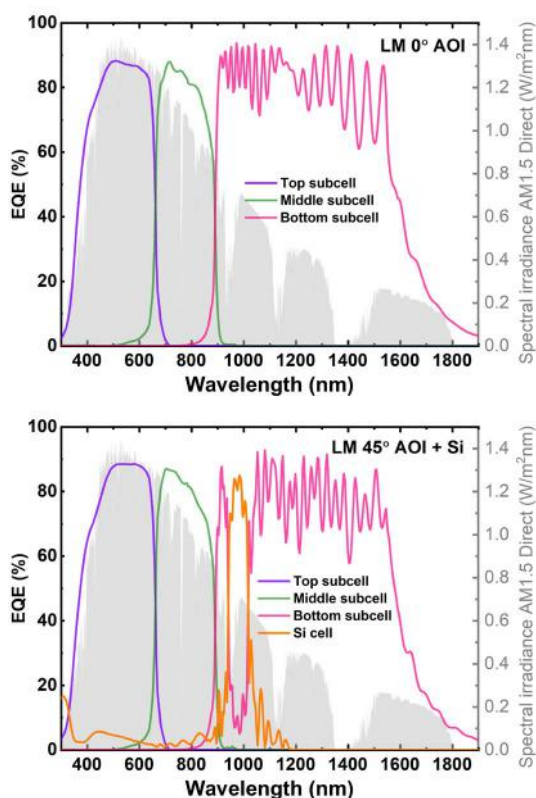


Figure 6.43.7: Modelled EQE of (a) the original TJSC @ 0° AOI; and (b) the four-junction spectrum splitting receiver consisting of a TJSC @ 45° AOI with spectrum splitting DBR + a Si cell.

There is a broad distribution of AOIs on the receiver of the CPV power tower (Figure 6.43.3), which could limit the benefits of spectrum splitting using a dielectric filter (cover glass) due to the sensitivity to AOI. The proposed DBR approach, by contrast, exhibits a greatly reduced sensitivity to AOI. Using the Perkin-Elmer spectrophotometer with a universal reflectance accessory, we measured the specular reflectance of the TJSC with spectrum splitting DBR for incident angles ranging from 8 to 60° and determined the cut-on and cut-off wavelengths (defined as 50% of the reflectance maximum) of the reflectance band. For comparison with the AOI dependence of the Bragg filter, we include AOI data for a representative high performance dielectric band-pass filter. For AOI increasing from 0 to 80°, the cut-on and cut-off wavelength of the dielectric filter blue-shifted by a massive 160 nm and 211 nm respectively, whereas the DBR filter exhibits shifts of only 30 nm and 32 nm from 0 to 60° AOI (Figure 6.43.8). The DBR filter therefore has a significant advantage over the dielectric filter when the incident light has a broad distribution of AOIs, which is the case for high concentration PV applications.

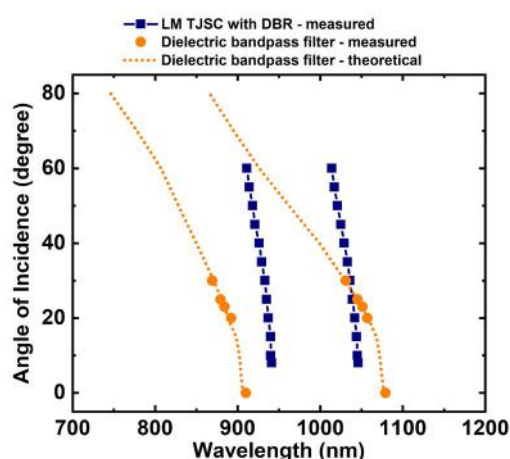


Figure 6.43.8: AOI dependence of the cut-on and cut-off wavelengths for two different approaches to spectrum splitting: intermediate DBR in a TJSC versus a dielectric filter.

Highlights

- Distributed Bragg reflector (DBR)-assisted spectrum splitting between a triple-junction solar cell (TJSC) and Si cell was demonstrated with high efficiency.
- The DBR approach to spectrum splitting shows significantly reduced angular dependence compared to dielectric filters.

Future Work

- Broaden the spectrum splitting reflection band, to achieve closer to current matching conditions between three sub-cells in the GaInP/GaInAs/Ge TJSC.
- Outdoor LIV measurements of the TJ(Bragg)/Si spectrum splitting CPV receiver, targeting over 40% efficiency.

References

ALONSO-ÁLVAREZ, D., WILSON, T., PEARCE, P., FÜHRER, M., FARRELL, D. & EKINS-DAUKES, N. 2018. Solcore: a multi-scale, Python-based library for modelling solar cells and semiconductor materials. *Journal of Computational Electronics*, 17, 1099-1123.

JIANG, Y., KEEVERS, M. J., PEARCE, P., EKINS-DAUKES, N. & GREEN, M. A. 2019. Design of an intermediate Bragg reflector within triple-junction solar cells for spectrum splitting applications. *Solar Energy Materials and Solar Cells*, 193, 259-269.

MEUSEL, M., ADELHELM, R., DIMROTH, F., BETT, A. W. & WARTA, W. 2002. Spectral mismatch correction and spectrometric characterization of monolithic III-V multi-junction solar cells. *Progress in Photovoltaics: Research and Applications*, 10, 243-255.

NELSON, J. 2003. *The Physics of Solar Cells*, Imperial College Press.

6.44 LANDMARK 50% EFFICIENT PV RECEIVER

Lead Partner

UNSW

UNSW Team

Dr Mark Keevers, Dr Yajie Jiang, Dr Anastasia Soeriyadi, A/Prof. Ned Ekins-Daukes, Prof. Martin Green

Industry Partners

Tianjin Institute of Power Sources and 18th Research Institute of China Electronics Technology Group (CETC-18), Tianjin, China: Prof. Qiang Sun, He Wang
RayGen Resources Pty Ltd: Dr John Lasich
IQE (informal collaboration): Andrew Johnson

Funding Support

ACAP

Aim

Based on the UNSW spectrum splitting approach that was the first to achieve sunlight-to-electricity conversion efficiency above 40%, a more sophisticated concentrator photovoltaic (CPV) module capable of efficiency above 50% has been designed. This project provides seed funding to enable progress along the development path towards demonstrating this landmark efficiency, including establishing suitable collaborations, planning development paths, and applying for the required larger project funding.

Progress

Increasing efficiency is a key driver for PV cost reduction. In 2014, UNSW gained international attention by demonstrating the first PV receiver to achieve a sunlight-to-electricity conversion efficiency above 40% (independently confirmed by NREL). The prototype submodule uses a dielectric band-pass filter to divert otherwise wasted (900–1050 nm) photons away from a GaInP/GaInAs/Ge triple-junction (3J) solar cell to a Si cell to form a 4J receiver (Green et al. 2015) (Figure 6.44.1). In 2016, UNSW further improved this efficiency to 40.6%

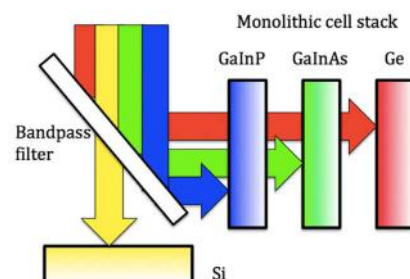


Figure 6.44.1: Schematic of the 3J + 1J spectrum splitting approach used to achieve 40% efficiency (Green et al. 2015).

A potential commercial application of this spectrum splitting approach is to upgrade the central receiver in Australian company RayGen's CPV power tower system, where sunlight is reflected from a field of sun-tracking heliostats to a dense-packed PV array receiver mounted on a central tower (Figure 6.44.2, also see section 6.1). In such systems, improved efficiency of the central receiver not only reduces costs by increasing energy output for a given investment in heliostats and towers but also reduces unwanted heat generation at the central tower. RayGen's technology is future-proofed due to the relative ease of swapping out the central PV receiver with higher efficiency receivers as these become available.



Figure 6.44.2: (left) RayGen's 750 kW_p PV power plant in Newbridge, Victoria. Each 250 kW_p unit uses a field of heliostats to concentrate sunlight onto a 1 m² high-efficiency PV receiver. (right) Close-up of a receiver.

A more sophisticated PV receiver capable of increasing efficiency towards the historically significant value of 50% has been designed (Green 2017), which involves extending the spectrum splitting approach to a combination of two 3J solar cells for even better utilisation of the solar spectrum (Figure 6.44.3). The optimal design identified is predicted to have a practical efficiency of 51% at 300 suns concentration and 51.7% at 500 suns. The higher energy ($1.4 < E_{ph} < 2.3$ eV) photons are converted using a 3J solar cell (based on lattice-matched solid solutions of GaAs, GaP, InP, AlP and AlAs) on a GaAs (or, equivalently, an inert Ge) wafer, while the lower energy ($0.73 < E_{ph} < 1.4$ eV) photons are converted using a 3J cell (based on lattice-matched solid solutions of GaAs, InAs, InP, AlAs and GaSb) on an InP wafer. A long-pass filter performs the required spectrum splitting.

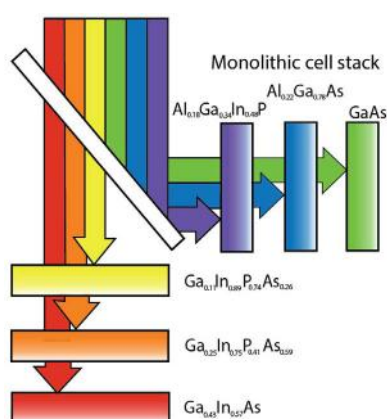


Figure 6.44.3: Conceptual design of a 3J + 3J spectrum splitting receiver using a long-pass filter and two 3J cells on GaAs and InP substrates, capable of achieving 50% efficiency (Green 2017).

The seed funding provided by this small ACAP grant is enabling us to develop various pathways to the ideal 3J + 3J = 6J receiver, in close consultation with official project partners CETC-18 and RayGen, as well as potential new partners IQE (III-V epitaxy experts), including enabling the team to apply for the larger funding required to achieve the 50% efficiency result.

Highlights

- Conceptual design of 50% efficient receiver.
- Omega Optical design of a suitable dielectric long-pass filter.
- Global Innovation Linkage grant application (submitted November 2018, unsuccessful April 2019).
- Meeting with CETC-18 and IQE in Xi'an, China, in November 2019 leading to ARENA R&D grant application (submitted February 2020).
- Development of UNSW capabilities for III-V solar cell fabrication and packaging.

Future Work

Progress along the development path towards a landmark 50% efficient PV receiver, including initial work on a 3J-on-GaAs (or inert Ge) + 1J-on-InP spectrum splitting receiver.

References

- GREEN, M.A. 2017. Landmark 50% efficient solar module design. Information Sheet MAG/ACAP1705, 15 November 2017 (confidential).
- GREEN, M. A., KEEVERS, M. J., THOMAS, I., LASICH, J. B., EMERY, K. & KING, R. R. 2015. 40% efficient sunlight to electricity conversion. Progress in Photovoltaics: Research and Applications, 23, 685–691

6.45 THIN SILVER NANOWIRE-BASED PROMISING TRANSPARENT CONDUCTIVE LAYER FOR SOLAR CELLS

Lead Partner

UNSW

UNSW Team

Dr Arastoo Teymouri, Dr Supriya Pillai, A/Prof. Xiaojing Hao, A/Prof. Ashraf Uddin, Mushfika Upama, Prof. Martin A. Green

Academic Partners

Macquarie University (Sydney): Dr Supriya Pillai, Dr Noushin Nasiri
National Institute for Material Science (Japan): Dr Esmaeil Adabifiroozjaei

Funding Support

ACAP

Aim

The aim of this work is to find a suitable replacement for indium tin oxide (ITO) transparent conducting layer (TCL) for potential application as the top electrode in tandem solar cells. This study has utilised silver nanowires (AgNWs) as a potential transparent conducting layer with focus on low temperature processing so as to be compatible with emerging cell technologies suitable in a top cell configuration as previously reported. A novel concept for deposition and post treatment of thin and long silver nanowires at 60°C is proposed in order to achieve sheet resistance $<30 \Omega \square^{-1}$, which is comparable to traditionally used ITO and transmission above 97%. We extended the study to analyse the AgNW joints so as to get a better understanding of the evolution for the excellent conductive properties at such low temperatures.

Progress

Previously we had reported the effect of annealing on sheet resistance. The effect of AgNW aspect ratio and surface coverage on sheet resistance was also studied. We also used the percolation theory to predict the optimum surface coverage for the different aspect ratio NWs. The study proposed not only a simple and cost-effective process for deposition, but also a new concept of post heat treatment for AgNWs. Further to our previous report, we thoroughly studied the nanowire junctions using high magnification rotary scanning transmission electron microscopy (STEM). The nature of the joints realised is further investigated by tomographic reconstruction images and further analysed using molecular dynamic (MD) simulations. Our observations facilitate a better understanding of fused joints in a silver nanowire network obtained by low temperature processes.

Traditionally, AgNWs have had to be heated to 200°C for a good conductive network. In order to study the reasoning behind the low sheet resistance of AgNWs heat treated at 60°C, in this study we investigated the microstructural features of the junctions (including the welded joints) using a field emission transmission electron microscopy (FE-TEM) Philips

CM20 and STEM JEOL JEM-F200, both operated at 200 kV. The angular imaging in STEM was used to construct three-dimensional tomographic images of the joints.

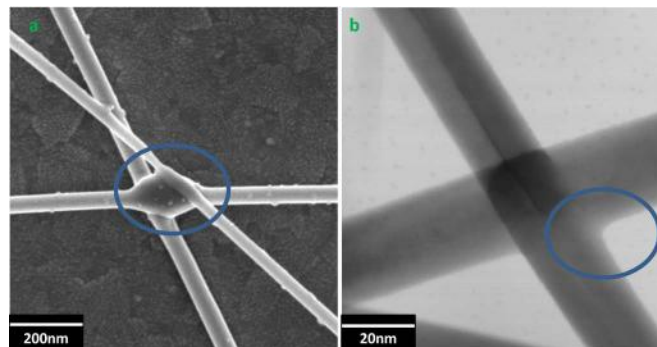


Figure 6.45.1: (a) AgNWs joint at 200°C (Annealing treatment). (b) 60°C (in situ treatment). The circled part shows the joints which are either welded as in (a) and in its early stages of broadening (b).

Figure 6.45.1(a) shows AgNWs are well-joint (welded) at the intersection at 200°C with annealing treatment evident from the bulged intersections as proof of welding. On the other hand Figure 6.45.1(b) (in situ treatment at 60°C) pictured with STEM at a 45° angle does not provide any evidence of welding, however clearly shows that nanowires are at the early stage of broadening.

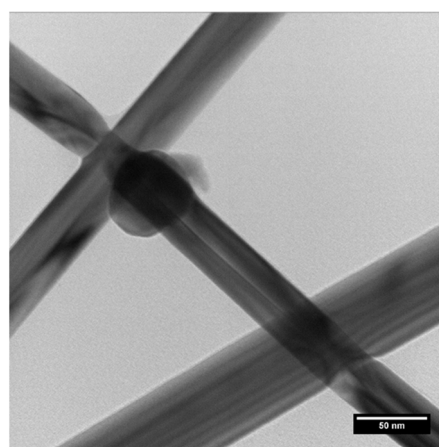


Figure 6.45.2: STEM image showing the presence of nanoparticles at the AgNWs intersection heat treated at 60°C.

Another interesting observation was the presence of small nanoparticles (~30 nm) next to the junctions of AgNWs heat treated at 60°C (Figure 6.45.2). Top view TEM images cannot give clear information about joints, but it seems that these nanoparticles are created through the flow or mass transfer of the materials from the junctions, which confirms deformation and a possibility of fused joints at such low temperatures. The presence of NP closer to the joints in all the images validates this claim.

To demonstrate a better understanding of fused joints, tomography reconstruction images were employed. The reconstruction images can speculate the position of wire at the junction. The STEM takes a series of images around the limited angles from the joint and then creates a three-dimensional view of the wires.

The tomography image showed that AgNWs at 60°C deforms at the joint, which we refer to as thinning in this study (Figure 6.45.3(a)). These images are then aligned using cross-correlation and then an intensity-dependent selection of expression ratios (ISER) algorithm is applied to reconstruct a three-dimensional model of the sample.

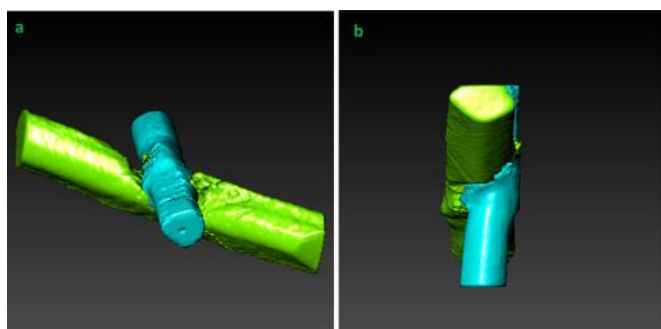


Figure 6.45.3: Tomographic reconstruction images of the AgNWs intersection heat treated at 60°C.

Figures 6.45.3(a) and (b) show reconstruction at two different angles. This shows that rather than pure bending over the wire there is some deformity caused at the junction (removal of Ag) as corroborated earlier by the presence of small metal nanoparticles in the vicinity of the junctions. As the thinning is evident in the network of 30 nm AgNWs heat treated at 60°C, we believe that thin AgNWs in order to bind with each other, dip into the bottom wire. This deformation is due to simultaneous top pressure and heating. It is noteworthy that it has not been observed in high temperature processes as the heating energy is too much for such a thin nanostructure. It only appears at very low temperatures such as 60°C

as used in this study, and can be more sensitive to the diameter of the NWs as well, but it proves that the wires are fusing in to provide the conductive network even at such low temperatures.

While the static nanoscale features of the process were studied with imaging techniques, we utilised MD simulation to study the dynamic atomic-scale features of the early stage of joining in the NWs. MD simulation of joining of AgNWs at different temperatures (25°C, 60°C, and 200°C) and under pressure load were undertaken. Figure 6.45.4 shows the simulated figure for 60°C under pressure load from the top wire. We used a Virtual Nanolab (VNL) (Schneider et al. 2017) to prepare Ag nanowires (thickness: 17 nm, length: 353 nm, number of atoms: 10^6). The direction of the nanowires is {101}, and is similar to those used for the experiments.

After annealing, the top nanowire gets thinner at all temperatures (only 60°C shown in Figure 6.45.4), although the thinning is more significant at a higher temperature (200°C). The data are in good agreement with our experimental data that indicate thinning is the first step of nanowires joining. The main difference is that we have not observed the thinning phenomenon in our experiment for nanowires heated at 200°C. This is due to the superfast kinetics (<1 ns) of the thinning process at 200°C, which only can be observed from MD simulation data. Nonetheless, here we can infer that thinning is a phenomenon that occurs at a low temperature (60°C) as well. This is validated by the extra layer of atoms aligned on the pre-existing atoms from

the surface of the bottom nanowire (circled atoms in Figure 6.45.4). These aligned atoms seem to be from the thinned area and brought to these necking points to fill the gap between the two nanowires. This phenomenon is also observed at the joint heat treated at 200°C with a much greater number of migrated atoms.

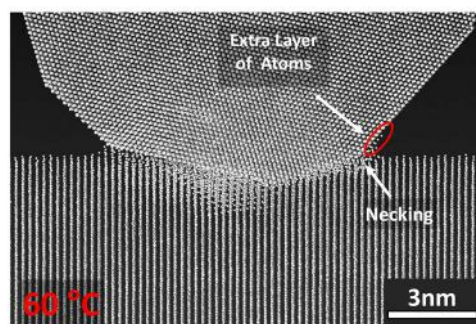


Figure 6.45.4: Simulated images from molecular dynamic simulation of the AgNWs intersection heat treated at 60°C.

Following our proof-of-concept demonstration on CZTS solar cells (Teymouri et al. 2017), we repeated the process on an organic solar cell (OSC). A continuous ZnO layer coupled with AgNWs was tested on OSCs replacing ITO in a bottom-up structure. The standard cell structure has a ZnO hole transport layer (HTL) on top of ITO as TCL. A mix of ZnO-AgNWs was deposited on glass as a replacement of ITO followed by 40 nm thickness ZnO as HTL. This structure of an OPV solar cell is compared with the reference cell using ITO. In this case the ITO was replaced with high aspect ratio AgNWs and the subsequent cell results are shown in Figure 6.45.5. For the OSCs (0.045 cm²), the cell with AgNWs as the TCL outperformed that of the ITO as TCL although the results were not as good for larger area devices.

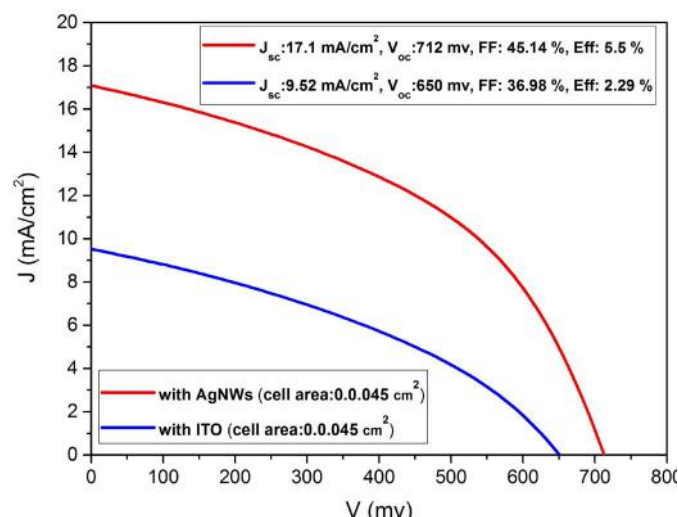


Figure 6.45.5: Performance improvement of the AgNW network

While the result is promising to pursue the replacement of ITO with hybrid ZnO-AgNWs, further optimisation is required for larger area OSCs.

Highlights

- Demonstration of AgNWs as a potential low temperature transparent conducting layer for emerging and current heat sensitive solar or other opto-electronic devices.
- This study proves to establish that silver nanowires do not require the conventional high temperature post-treatment process at 200°C to form fused contacts at the intersections.
- Evidence of low temperature joint formation established through various imaging techniques.
- Demonstration of proof of concept in organic solar cells in addition to CZTS cells reported previously.
- Molecular dynamic simulation to further understand the superior performance of AgNWs and confirmation of experimental findings.

Publications

TEYMOURI, A., ADABIFIROOZJAEI, E., WEBSTER, R. F., HAGH, S. M., HAO, X., GREEN, M. A. & PILLAI, S. Evidence of Low Temperature Joints in Silver Nanowire Based Transparent Conducting Layers for Solar cells, submitted to ACS Applied Nano Materials and is currently under second review.

TEYMOURI, A., ADABIFIROOZJAEI, E., WEBSTER, R. F., MA, H., HAO, X., GREEN, M. A. & PILLAI, S. AgNWs heat-treatment at low temperature (60°C): a combined scanning transmission electron microscopy and molecular dynamic investigation, Oral presentation at the XVI International Conference on Intergranular and Interphase Boundaries in Materials (IIB-2019), 1–5 July 2019, Paris.

TEYMOURI, A., GREEN, M. A. & PILLAI, S. Low temperature silver nanowires as transparent conducting layer for solar cells, Oral presentation at 29-PVSEC, 4–8 Nov 2019, Xian, China.

Future work

Future work will involve optimising the AgNWs to be integrated into the cell architecture

References

SCHNEIDER, J., HAMAEEKERS, J., CHILL, S. T., SMIDSTRUP, S., BULIN, J., THESEN, R., BLOM, A. & STOKBRO, K. 2017. ATK-ForceField: a new generation molecular dynamics software package. *Modelling and Simulation in Materials Science and Engineering*, 25, 085007.

TEYMOURI, A., PILLAI, S., OUYANG, Z., HAO, X., LIU, F., YAN, C. & GREEN, M. A. 2017. Low-Temperature Solution Processed Random Silver Nanowire as a Promising Replacement for Indium Tin Oxide. *ACS Applied Materials & Interfaces*, 9, 34093-34100.

6.46 MANIPULATING THE PROPERTIES OF OXYGEN-RELATED DEFECTS FOR RECORD EFFICIENCY CELLS

Lead Partner

UNSW

UNSW Team

Dr Fiacre Rougieux

Academic Partners

Fraunhofer Institute for Solar Energy Systems ISE:

Prof. Martin Schubert

University of Freiburg: Dr Wolfram Kwapil

Australian National University: Prof. Daniel Macdonald,

Manjula Siriwardhana

Funding Support

ACAP

Aim

This project aims to understand and control the properties of defects limiting high efficiency silicon solar cells, focusing on oxygen-related defects. This class of defect is still poorly understood and current defect-engineering techniques are particularly inadequate at annihilating such defects.

Progress

This project spans the period April 2018 to April 2020. As part of this project, Dr Fiacre Rougieux from UNSW spent a month at Fraunhofer ISE in September 2018. Manjula Siriwardhana from ANU spent a month at Fraunhofer ISE in September 2019 and a month at UNSW in October 2019.

In this project, we invented a new technique to image defects in solar wafers and solar cells (Rougieux 2019). We developed new techniques to measure the electronic properties of oxygen-related defects (Siriwardhana et al. 2018; and manuscripts in preparation). We also developed new defect-engineering techniques to increase the open-circuit voltage of commercial silicon solar cells by manipulating the properties of defects (Tan et al. 2018) (as presented at the EUPVSEC and APSRC with manuscripts under review).

Highlights

- Invention of a new technique to image the concentration of slow traps in silicon wafers.
- Development of a new technique to determine the electronic capture properties of oxygen-related defects.
- Development of new thermal processes to increase the open-circuit voltage of solar cells limited by defects.

Future Work

- Unravel the impact of thermal donor species on recombination parameters.
- New insights into activation and deactivation of oxygen-related defects.

References

ROUGIEUX, F. E., KWAPIL, W., HEINZ, F., SIRIWARDHANA, M. & SCHUBERT, M. C. 2019. Contactless transient carrier spectroscopy and imaging technique using lock-in free carrier emission and absorption. *Scientific Reports*, 9.

SIRIWARDHANA, M., MACDONALD, D., HEINZ, F. D. & ROUGIEUX, F. E. 2018. Slow minority carrier trapping and de-trapping in Czochralski silicon: Influence of thermal donors and the doping density. 2018 IEEE 7th World Conference on Photovoltaic Energy Conversion (WCPEC), 2018, pp. 3312–3314, doi: 10.1109/PVSC.2018.8547946.

TAN, X., CHEN, R., LEE CHIN, R., CHEN, D. & ROUGIEUX, F. E. 2018. Defect Engineering of n-type bifacial silicon solar cells using dark annealing. 2018 IEEE 7th World Conference on Photovoltaic Energy Conversion (WCPEC), 2018.

6.48 ITO-FREE PVS PRINTED DIRECTLY ONTO FLEXIBLE BARRIER FILMS

Lead Partner

CSIRO

CSIRO Team

Dr Doojin Vak, Mrs Fiona Glenn

Academic Partners

Chonbuk National University (CBNU): A/Prof. Seok-In Na

KoreaTech: A/Prof. Yoon Chae Nah

Industry Partner

Norwood Industries: Mr Graham Dancey

Funding Support

ACAP

Aim

Printed PV produced by roll-to-roll (R2R) printing is flexible, lightweight and semitransparent (in some cases), creating access to new PV markets, especially for portable applications. However, some materials and process steps are costly and make the technology heavier and less flexible. This project aims to produce PV printed directly onto barrier films, resulting in lighter weights, improved flexibility and lower potential manufacturing costs.

Challenge

Finding printable low-cost transparent conductive electrodes (TCEs) to replace commonly used indium tin oxide (ITO) has long been of great interest to the research community and wider flexible and printed electronics (FPEs) industry, which includes flexible solar cells. Producing practically high conductivities (that is low sheet resistance) economically while managing surface roughness and transparency has been a challenge.

Progress

The project uses a composite of metal and conductive polymers (CPs) and only industry-compatible methods are used to assist in the commercialisation of the development.

Hot roll-pressed silver nanowires (AgNWs): A layer of AgNWs combined with a CP composite formulation is one of the most promising candidates for a TCE in a printed PV device. The CSIRO team have demonstrated the fabrication of a TCE using a commercial formulation using an industry-compatible method. In this case, a low sheet resistance could be obtained, however, there was an increased potential for “shorting” in the resultant PV device.

The R2R-produced TCE films can be planarised by a hot press and the conductivity can be further improved due to a “welding” effect at the junctions. Such an effect has been reported by flat pressing at both ambient and elevated temperatures. The challenge is performing this process in a scalable way, particularly with a method that is compatible with R2R printing processes for printed PV. Therefore, hot roll pressing was proposed for this project. In this case, the process can be performed on an R2R production line for solar cells.

A hot roll press was purchased for the project and used to planarise the composite film. The composite TCE films with various thicknesses were prepared to find the optimum conductivity/transparency for the printed PVs. The films were hot-pressed under various temperatures, pressures and pressing speeds. Despite expending enormous effort with this approach, we found no meaningful improvement in the conductivity or surface roughness using a processing condition that does not damage the plastic substrates. We concluded that this approach is not effective enough to manage the shorting issue. Instead, device configurations that can tolerate the roughness of an as-printed TCE will be explored next year

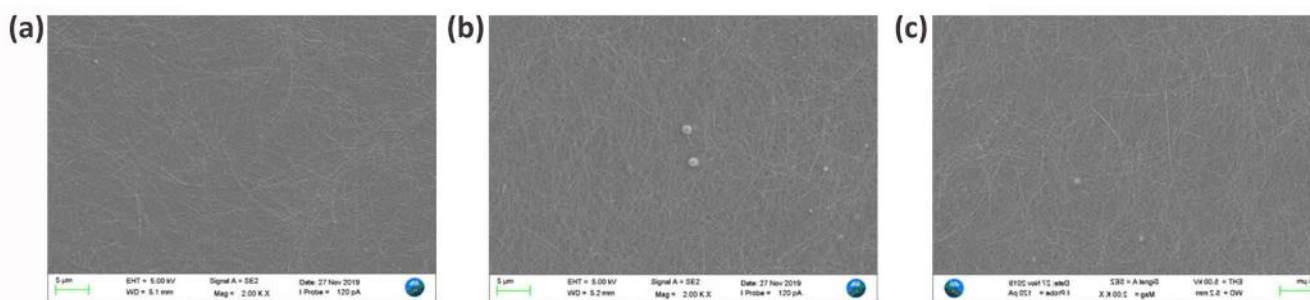


Figure 6.48.1: SEM images of the AgNW distribution on the PET substrate after (a) one coating ($\sim 22 \Omega/\square$); (b) two coatings ($11 \Omega/\square$); and (c) three coatings ($7 \Omega/\square$).

Conductive polymer layer: Thin layers of CPs can be used as TCEs depending on the conductivity requirement of the application. Poly(3,4-ethylenedioxythiophene)-poly(styrenesulfonate) (PEDOT:PSS) has been the most popular CP for TCE in PV, however, the material has been used only with small cells due to its limited conductivity or used as a composite with metals for large-area applications. Therefore, there have been intensive research efforts to increase the conductivity of the CP and the bulk conductivity of the CP has now increased to that of ITO. However, most methods are not practical for use in industrial production methods. Therefore, a practical method, namely dripping a mild chemical solution onto the thin film of the CP, was chosen and used with an industrial R2R printer located in CSIRO. The deposition parameters of the PEDOT:PSS and the chemical treatments were optimised via R2R experiments. In the first project year, the deposition of methanol onto a hot PEDOT:PSS film improved the conductivity significantly. To further improve conductivity, various formulations used in the literature were tested. We found some formulations including organic salts can produce slightly better conductivities, however, such an approach reduces the transparency and makes the film less attractive as a TCE. Therefore, we concluded that a methanol treatment at 120°C is the best when considering its merit factor as a TCE and also the practicality of implementing it into the R2R production of TCEs in the future.

The treatment condition was used to prepare TCEs via an R2R process. The deposition parameter for PEDOT:PSS was also optimised to achieve uniformity across the coating direction. A hot deposition (90°C) was found to be an effective solution to achieve a uniform

PEDOT:PSS layer. A preliminary result for the device fabricated on PEDOT:PSS TCE is shown in Figure 6.48.2. CSIRO's standard recipe of perovskite PV was used to test the TCE. The device result was not as good as that of devices on commercial TCEs. Further optimisation of formulation and device configuration will be carried out next year. Both perovskite and organic PVs will be explored.

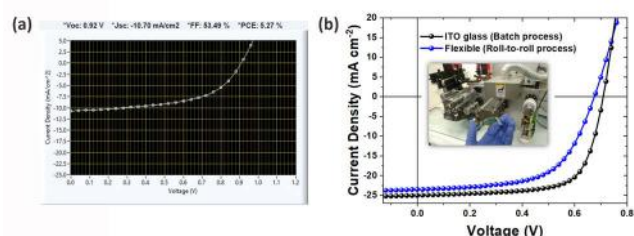


Figure 6.48.2: (a) J-V curve of perovskite PV on R2R produced TCE. (b) J-V curves of organic PV with printed-TCE-friendly solar ink fabricated by slot die coating. The device showed the highest PCE from R2R processed organic PV in literature.

Printed-TCE-friendly solar inks:

Printed TCEs are typically rougher than commercial vacuum-deposited TCEs and require robust solutions to produce solution-processed PV. Recent reports show such solutions can be made by a ternary approach, in contrast to the conventional binary blend of a donor and an acceptor. Therefore, a formulation was developed for R2R processing via a collaboration with Professor Na, the project partner. Following the achievement of the highest PCE (8.25%) from R2R processed organic PV last year, the efficiency was further improved to 9.6%. This formulation will be used with printed TCEs next year.

Cost benefit:

It was expected that printed TCEs would be cheaper than conventional commercial TCEs, however, the amount of expected savings was not calculated before. Therefore, a simple calculation was carried out based on the material usage of optimised fabrication conditions and cost of materials (based on actual cost for research quantity orders). The table below clearly shows the cost benefit of printed TCEs based on PEDOT:PSS and a AgNW-PEDOT:PSS composite. Projected manufacturing costs based on printed TCEs will be carried out through collaboration with UNSW next year.

Film coatings	R (Ω/\square)	Transmittance @550 nm	Cost per square metre (research cost)
Commercial ITO-coated PET – OC50	50	85%	\$170
Commercial IZO-coated PET – LRS15	15		\$393
Commercial OMO-coated PET – OPV8	8		\$225
AgNW – PEDOT:PSS x 1 coating	23	81%	\$66.5
PEDOT:PSS Clevios PH 1000 R2R PET	50	80–85%	\$14

Highlights

- The realisation of R2R produced perovskite devices on R2R produced TCEs.
- Development of a printed-TCE-friendly formulation for the photo-active layer of organic PV, showing the highest PCE from R2R produced flexible OPVs in literature. The result was published in a top-tier journal in the field.

Future Work

- Further trials of device fabrication on printed TCEs on barrier films.
- Calculation of projected manufacturing costs based on the research outcome of the project.

References

LEE, J., SEO, Y. H., KWON, S. N., KIM, D. H., JANG, S., JUNG, H., LEE, Y., WEERASINGHE, H., KIM, T., KIM, J. Y., VAK, D. & NA, S. I. 2019. Slot-Die and Roll-to-Roll Processed Single Junction Organic Photovoltaic Cells with the Highest Efficiency. *Advanced Energy Materials*, 9, 1901805

6.50 DEVELOPMENT AND IMPLEMENTATION OF INORGANIC TRANSPORT LAYERS IN THE PEROVSKITE CELLS OF PEROVSKITE/SILICON TANDEM STRUCTURES

Lead Partner

ANU

ANU Team

A/Prof. Klaus Weber, Mr Yiliang Wu, Ms Nandi Wu

Academic Partner

Peking University (PKU): A/Prof. Huanping Zhou
Beijing Institute of Technology

Funding Support

ACAP, ANU, PKU

Aim

The aim of the project is to develop hole transport layers (HTLs) that enable perovskite/silicon tandem devices with high efficiency and stability.

Specifically, in the project the partners will further develop the processes for synthesis and application of inorganic HTPs; carry out detailed optical characterisation to determine the complex refractive index dispersion, and dependence on processing conditions; implement optical and electronic modelling as a guide to cell optimisation and fabricate tandem cells incorporating all inorganic transport layers. The project will contribute to the goal of ultimately pushing tandem efficiencies to 30% and beyond.

Progress

In collaboration with PKU, NiO_x films deposited by sputtering were developed and optimised, using previous studies on film properties as a basis for the work. These NiO_x films function as HTLs in the perovskite cells. Excellent cell results were achieved at ANU on the basis of these NiO_x films. However, a significant issue was encountered due to contamination in the sputter deposition system, which is also used for the deposition of many other materials.

Nevertheless, the work led to impressive device results. The highlight was the demonstration of a 4cm^2 , 21.2% efficient perovskite/silicon tandem cell. Importantly, this cell was based on a conventional silicon solar cell fabricated on p-type Cz silicon rather than exotic, high quality material as is used for most tandem efficiency results that are reported in the literature. Furthermore, the silicon cell used only mass production techniques and the top cell surface was not polished. As a result, the architecture is more commercially relevant and demonstrates what can be achieved industrially. The cell efficiency was certified by CSIRO (Figure 6.50.1).

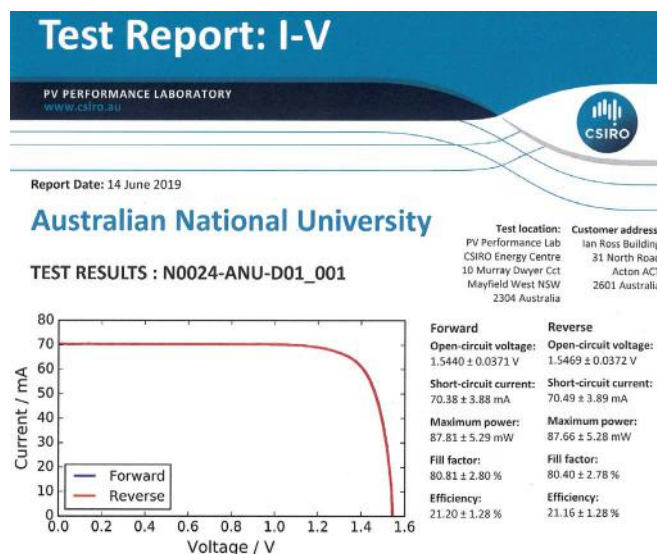


Figure 6.50.1: I-V curves of the 4cm^2 perovskite/Si tandem cell.

Highlights

- Development of high quality, sputtered NiO_x films.
- Demonstration of high efficiency tandem cells featuring the improved NiO_x films and commercial c-Si cells.

Future Work

The project has been successful at building collaboration between ANU and PKU. ANU hosted two researchers from PKU, Mr Yihua Chen and Dr Zhiwen Qiu for two weeks in July 2019. Currently (December 2019 to January 2020) Dr Yiliang Wu from ANU is being hosted at PKU, where he is carrying out further experiments on NiO_x using the equipment at PKU, as well as having discussions with researchers.

ANU and partners at PKU and Beijing Institute of Technology have submitted several joint project proposals, led by both sides, including an ARC Discovery project and a successful application to the Beijing Natural Science Foundation on two-terminal tandem solar cells. We have also co-authored one joint publication to date (Chen et al. 2019).

References

CHEN, Y. H., TAN, S. Q., ZHOU, N., YANG, N., ZHOU, W. T., WU, Y. L., WEBER, L., CHEN, Q. & ZHOU, H. P. 2019. 30% Enhancement of Efficiency in Layered 2D Perovskites Absorbers by Employing Homo-Tandem Structures. *Solar RRL*, 3.

6.51 HIGH EFFICIENCY SEMI-PLANAR PEROVSKITE CELLS COMBINING NANOTEXTURED ELECTRON TRANSPORT LAYERS AND INORGANIC HOLE TRANSPORT MATERIALS

Lead Partner

ANU

ANU Team

A/Prof. Thomas White, Dr Jun Peng

Academic Partner

Sun Yat-sen University (SYSU), Guangzhou, China

Funding Support

ACAP

Aim

The objective of this project is to develop highly efficient and stable semi-planar perovskite solar cells using nanostructured TiO₂ electron transport layers (ETLs) and NiO_x nanoparticle hole transport layers (HTLs). By optimising the novel nanostructured TiO₂ ETL, we hope to improve electron collection, extraction and transportation, while minimising the surface recombination losses at or near the perovskite/ETL interface. In parallel we will develop novel doping approaches to tune the HTL work function and conductivity to achieve optimal interface band alignment and carrier transport properties required for high performance perovskite cells and perovskite/silicon tandems.

Progress

We have developed a semi-planar perovskite cell using nanostructured TiO₂ ETLs, where the detailed device structure is ITO/compact-In-TiO₂/TiO₂ nano-pattern/PMMA:PCBM/CsFAMA triple cation perovskite / PMMA/HTL/Metal electrode (Peng et al. 2017; Peng et al. 2018). This nanostructured TiO₂ ETL can facilitate efficient collection, extraction and transportation of electrons compared to conventional mesoporous TiO₂ ETLs or fully planar devices. In addition, we have developed a dopant-free P3HT:CuPC blend HTL that significantly improves the stability of the PSCs compared to commonly used HTL Spiro-OMeTAD, where the P3HT and CuPC respectively represent poly(3-hexylthiophene-2,5-diyl) and copper phthalocyanine.

The cell fabrication was a joint undertaking of ANU and SYSU. The fabrication of nano-patterned TiO₂ layers was performed at SYSU; the rest of the device fabrication, including the deposition of the compact In-TiO₂ layer, perovskite active layer, P3HT:CuPC HTL and gold electrode was conducted at ANU. J-V characterisation was then performed at ANU. ANU researcher Jun Peng also visited SYSU to perform X-ray and UV photoelectron spectroscopy (XPS-UPS) measurements and analysis to optimise the TiO₂ nano-patterned layer.

As seen in Figure 6.51.1, a PCE of 21.956% (measured by reverse scan (V_{oc} to J_{sc}) at a scan rate of 20 mVs⁻¹) with V_{oc} = 1.205 V, J_{sc} = 21.804 mAcm⁻² and FF = 0.836 was obtained for the champion

cell (effective area ~1.02 cm²), where the corresponding forward scan efficiency is 22.030%. External quantum efficiency (EQE) measurement was then conducted to further verify the current of the champion cell. A certified efficiency of 21.6% was obtained for our 1 cm² semi-planar perovskite cell (see Figure 6.51.2).

To evaluate the light-soaking and thermal stability of these cells, we performed a steady-state power output (SPO) measurement (tested at a maximum power point voltage (V_{mpp}) under continuous one-sun illumination) and a damp heat test (85°C/85% RH, under dark) (see Figure 6.51.1). The results show that the non-encapsulated perovskite cell based on P3HT:CuPC HTL retained ~95% of its initial efficiency after 260 hours of the V_{mpp} tracking test; while the control cell based on Spiro-OMeTAD HTL maintained only ~76.1% of its initial efficiency after 250 hours of testing. Under damp-heat conditions, as can be seen in Figure 6.51.1, the control cell (with Spiro-MeTAD) exhibited stark degradation within 240 hours due to severe deterioration at the interface between the perovskite and Spiro-OMeTAD HTL, which is most likely caused by diffusion of lithium ions (used as a dopant for the Spiro-OMeTAD). On the contrary, the P3HT:CuPC-based cell retained >91% of its initial efficiency after 1009 hours of exposure. Thus it is evident that the hydrophobic and thermally stable nature of P3HT:CuPC HTLs can effectively preserve the longevity of the perovskite cells.

Although we have achieved a very high efficiency for the TiO₂ nanopattern-based perovskite cells, further work is underway to develop NiO_x nanomaterials to substitute the organic HTLs in these cells.

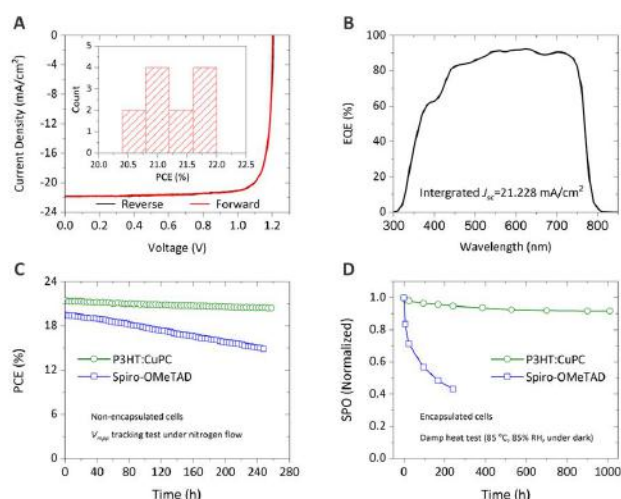


Figure 6.51.1: J-V performance of the best semi-planar perovskite solar cell and the corresponding stability measurement in this project.

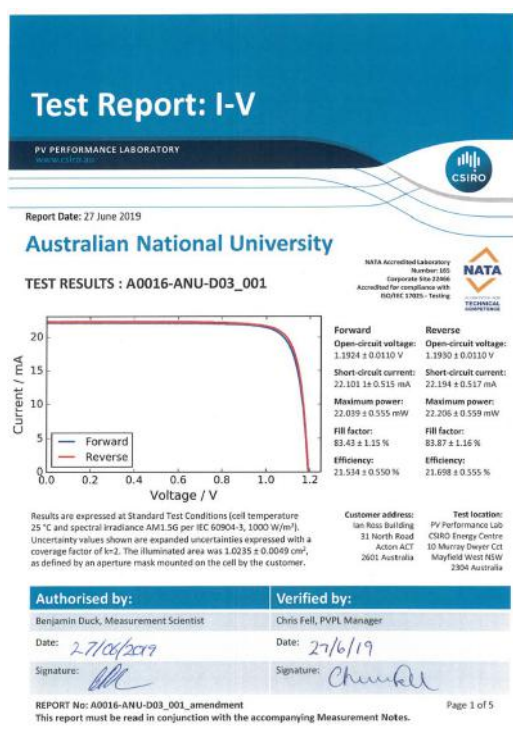


Figure 6.51.2: J-V curve of the certified semi-planar perovskite solar cell in this project.

Highlights

- Optimised nanostructured TiO₂ electron transport layers.
- Achieved a world record efficiency of 21.6% (certified) for 1 cm² perovskite cell.
- The cell retained over 95% of its initial efficiency after 260 hours of V_{mpp} tracking test.
- The cell retained over 91% of its initial efficiency after 1,000 hours of damp heat (85°C and 85% RH) test.

Future Work

- Synthesise/optimize NiO_x nanomaterials with various dopants.
- Fabricate/optimize the performance of perovskite cells using nanostructured TiO₂ (ETLs) and NiO_x nanoparticles (HTLs).
- Test the perovskite cell's stability.

References

- PENG, J., DUONG, T., ZHOU, X. Z., SHEN, H. P., WU, Y. L., MULMUDI, H. K., WAN, Y. M., ZHONG, D. Y., LI, J. T., TSUZUKI, T., WEBER, K. J., CATCHPOLE, K. R. & WHITE, T. P. 2017. Efficient Indium-Doped TiO_x Electron Transport Layers for High-Performance Perovskite Solar Cells and Perovskite-Silicon Tandems. *Advanced Energy Materials*, 7, 1601768.
- PENG, J., KHAN, J. I., LIU, W. Z., UGUR, E., DUONG, T., WU, Y. L., SHEN, H. P., WANG, K., DANG, H., AYDIN, E., YANG, X. B., WAN, Y.M., WEBER, K. J., CATCHPOLE, K. R., LAQUAI, F., DE WOLF, S. & WHITE, T. P. 2018. A Universal Double-Side Passivation for High Open-Circuit Voltage in Perovskite Solar Cells: Role of Carbonyl Groups in Poly(methyl methacrylate). *Advanced Energy Materials*, 8, 1801208.
- PENG, J., WU, Y., YE, W., JACOBS, D. A., SHEN, H. P., FU, X., WAN, Y., DUONG, T., WU, N., BARUGKIN, C., NGUYEN, H. T., ZHONG, D., LI, J. T., LU, T., LIU, Y., LOCKREY, M. N., WEBER, K. J., CATCHPOLE, K. R. & WHITE, T. P. 2017. Interface passivation using ultrathin polymer-fullerene films for high-efficiency perovskite solar cells with negligible hysteresis. *Energy & Environmental Science*, 10, 1792-1800.

6.52 MICROSTRUCTURE CHARACTERISATION OF THERMALLY EVAPORATED PEROVSKITE SOLAR CELLS FOR THE APPLICATION OF MONOLITHIC PEROVSKITE/SILICON TANDEM SOLAR CELLS

Lead Partner

Monash University

Monash Team

Prof. Udo Bach

Academic Partner

Wuhan University of Technology (WHUT), China: Dr Wei Li,
Prof. Yi-Bing Cheng

Funding Support

ARENA, Monash, WHUT

Aim

This project aims to combine complementary expertise at Monash and WHUT in the field of microstructure characterisation of materials for solar cells. In particular, the ultra-low dose transmission electron microscope techniques developed at Monash will be applied to some outstanding thermally evaporated perovskite solar cells, especially in relation to understanding microstructure in perovskite solar cells.

Progress

This two-year project was commenced in January 2019. Dr Wei Li from WHUT made a two-month visit to Monash from January to March 2019, during which time he defined following collaborative research topics in detail and utilised advanced electron microscope facilities to carry out these activities at Monash.

(1) Intra-grain microstructure focuses on the internal structure of the grain itself: its chemical composition, morphology, crystallinity, crystallographic orientation, intra-grain defects, to mention a few properties, which are intrinsic factors controlling the performance of polycrystalline perovskite solar cells.

(2) Grain boundaries in a crystalline semiconductor material interrupt the long-range periodicity of the crystal leading to electronic states at energies that would otherwise be forbidden in a bulk single crystal. Since thermally evaporated perovskites are polycrystalline materials, imperfections on differently oriented grain surface facets and at grain boundaries may also introduce localised states, which can capture photo generated carriers and therefore induce a field across the material that would eventually counteract the photo generated potential.

(3) The heterojunction interfaces of perovskite solar cells are responsible for their promising performance. A typical perovskite solar cell is made up of a series of heterojunctions, layers of materials with vastly different properties, and the perovskite light absorber

is sandwiched between two carrier selective layers. Therefore, the interfaces between perovskite and the carrier selective layers determine the charge extraction efficiency and are thus critical for the overall solar cell efficiency.

Highlights

- Two-month visit to Monash University by Dr Wei Li (January to March 2019) and follow-up.
- The power conversion efficiency of thermally co-evaporated inorganic perovskite solar cell has reached 10% at Wuhan University of Technology.
- The power conversion efficiency of a thermally evaporated organic-inorganic hybrid perovskite solar cell has reached 20% at Wuhan University of Technology.
- Electron beam induced current (EBIC) has been set up in Monash Centre for Electron Microscopy for characterisation of carrier collection at a nanoscale at Monash University.
- Cathodoluminescence identified a nanoscale halides segregation which is effectively mitigated by optimisation of Ostwald ripening through controlling the chemical composition in the CsPbIBr₂ precursor solution.
- The critical role of planar defects in the performance of MA_{1-x}FA_xPbI₃ perovskite solar cells" has been submitted to Nature Energy for peer review.
- One oral presentation by Dr Wei Li, 2nd International Conference on Clean Energy Materials and Technology, held from 29 November to 1 December 2019 in Suzhou China.

Future Work

We will continue to improve the efficiency and stability of thermally evaporated perovskite solar cells. Intra-grain defects, such as dislocations, twins and stacking faults in the perovskite films will be firstly identified by using transmission electron microscopy (TEM). The role of these intra-grain defects on the solar cells performance will be further studied by other characterisation techniques such as electron beam induced current, Kelvin probe, conductive AFM and other methods. Ageing experiments will be performed by keeping the perovskite films in varied temperatures, electric bias, humidity and light intensity to understand the role of intra-grain defects on the perovskite films' and solar cells' stability.

References

- BACH, U. et al. The critical role of planar defects in the performance of MA_{1-x}FA_xPbI₃ perovskite solar cells. (submitted to Nature Energy).
- BACH, U. et al. Enhanced Ostwald ripening and defect annihilation for efficient CsPbIBr₂ inorganic perovskite solar cells. (in preparation for journal publication).

6.53 MAGNETIC FIELD IMAGING FOR PHOTOVOLTAIC CELLS AND MODULES

Lead Partner

UNSW

UNSW Team

Dr Oliver Kunz, Prof. Thorsten Trupke, Dr Appu Paduthol

Industry Partner

DENKweit GmbH, Halle (Saale) Germany

Funding Support

ACAP

Aim

UNSW photoluminescence (PL) imaging has revolutionised photovoltaic research and manufacturing by making it possible to visualise electronic material quality and local voltage differences, while similarly, lock-in thermography has made it possible to identify power losses through the visualisation of the resulting heat patterns. Magnetic field imaging (MFI) represents the missing link that allows visualising 3-dimensional current flows in solar cells, modules and solar materials. The proposed project aims at pioneering the field of MF imaging at UNSW.

Progress

(A) Deliverable: Setting up of a prototype system for magnetic field imaging at SPREE

As the basis of this work a measurement system needed to be established at our UNSW labs to perform magnetic field imaging (MFI) and to be able to develop this technology and to compare it to our in-house photoluminescence (PL) and electroluminescence (EL) capabilities. This deliverable has been achieved.

Figure 6.53.1(a) depicts the imaging system, a 3D robotic measuring system with a linear magnetic sensor array attached to it. We are using this tool now to routinely perform MFI measurements. The system can reliably measure magnetic fields down to $1 \mu\text{T}$ magnetic resolution and any spatial resolution required. In Figure 6.53.1(b) we see an EL image of a multicrystalline silicon solar cell with three busbars under 5A current injection. The same solar cell was imaged using our in-house MFI tool as seen in Figure 6.53.1(c). During the imaging the scanning direction was chosen to be perpendicular to the busbar direction in order to get a very high spatial resolution in the direction perpendicular to busbars where the biggest magnetic field gradient is expected. The magnetic field component displayed is the component in x-direction, B_x , that is, the component perpendicular to the busbars. The system, however, measures simultaneously the magnetic fields in all three spatial directions.

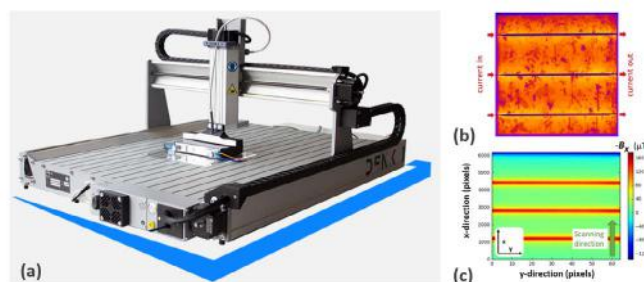


Figure 6.53.1: (a) Magnetic field imaging (MFI) measurement system at UNSW with a DENKweit linear magnetic sensor array attached. (b) EL image taken at our labs of a multicrystalline silicon solar cell with three busbars. (c) Equivalent magnetic field image of the same solar cell when scanned from bottom to top.

(B) Deliverable: Setting up MF measurement capabilities for field measurements

Magnetic field imaging is particularly interesting to detect faults in operating solar power plants. Faults like bypass diodes in short circuit or missing/faulty solder connections can conveniently be detected using this technique without the need for disrupting the operation of the solar power plant. This deliverable has been achieved.

The hand-held sensor array that can be used for such purposes is depicted in Figure 6.53.2(a). It is similar in design and has the same magnetic measurement capabilities as the sensor array that is mounted on the MFI robotic system in Figure 6.53.1(a). However, it can be used on large-area photovoltaic modules in the lab or to measure current flows on solar power plants during normal operation.

Further enhancement of our measurement capabilities has been achieved using a high performance magnetic field sensor (Memsic – MMC5883MA) that has an approximate 50 times improved magnetic measurement sensitivity compared to our linear sensor arrays. This point sensor can be used where, for example, very small currents in solar grid lines need to be detected or for precise imaging of regions of interest that were previously identified with our standard line sensor array.

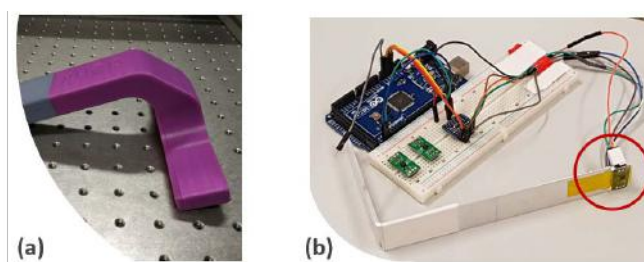


Figure 6.53.2: (a) Hand-held MFI line sensor array for inspection of large solar modules or field work. (b) Point sensor (red circle) with 50 x higher magnetic field sensing capability and the corresponding peripheral readout electronics.

(C) Deliverable: Presenting at two or more major PV conferences on MFI

At the 2019 IEEE 46th Photovoltaic Specialist Conference (PVSC) we had one oral (Paduthol et al. 2019) and one poster presentation (Kunz et al. 2019) on the topic of magnetic field imaging. The results obtained were also presented at the 2019 Asia Pacific Solar Research Conference in Canberra as an oral presentation (“Investigating metal-semiconductor contacts in solar cells using magnetic field imaging”). In the latter work we measure and model current flows in solar cells when current is injected and extracted using contacts from one solar cell polarity only. Figure 6.53.3 (a, left) shows the results of our measurements for different current flow patterns ((A)–(C)). These images were then modelled using circuit simulation software LT SPICE. The modelling results are displayed to the right of the measurements.

(D) Deliverable: Publishing of at least three research publications in the course of this project

We published our work in the proceedings of the 46th PVSC IEEE specialist conference in Chicago in 2019. Two much more detailed journal publications on this topic are now in preparation and expected to be submitted to journals by the end of April and the end of June 2020, respectively. Two-thirds of this deliverable has been achieved.

Highlights

- We have successfully established magnetic field imaging capabilities for lab and field measurements. Additionally, we have installed a high performance point sensor on our system in order to significantly enhance the sensitivity for measurements of small currents and smaller regions of particular interest (“MFI zoom images”).

- We have presented on this work at the IEEE specialist conference in Chicago 2019 via an oral and a poster presentation. We also have orally presented this work at the annual APV APSRC conference in Canberra in December 2019.
- We have to date published two conference papers on this work (Paduthol et al. 2019; Kunz et al. 2019).

Future Work

- Two journal publications are currently in preparation and expected to be submitted by the end of April and June 2020, respectively. One deals with the fundamentals of magnetic field imaging for photovoltaic applications and a second one with determination of metal semiconductor interface properties using MFI in conjunction with equivalent circuit modelling.
- We are pursuing further work on contact measurements via a collaboration with Jinko Solar at the moment and hope that this will lead to a further journal or conference publication.

References

KUNZ, O., PADUTHOL, A., SLADE, A., EDWARDS, M., KAUFMANN, K., PATZOLD, M., LAUSCH, D. & TRUPKE, T. Investigating metal-semiconductor contacts in solar cells using magnetic field measurements. 2019 IEEE 46th Photovoltaic Specialists Conference (PVSC), 16-21 June 2019. 2764-2768.

PADUTHOL, A., KUNZ, O., KAUFMANN, K., PATZOLD, M., LAUSCH, D. & TRUPKE, T. Magnetic Field Imaging: Strengths and limitations in characterising solar cells. 2019 IEEE 46th Photovoltaic Specialists Conference (PVSC), 16-21 June 2019. 0822-0824.

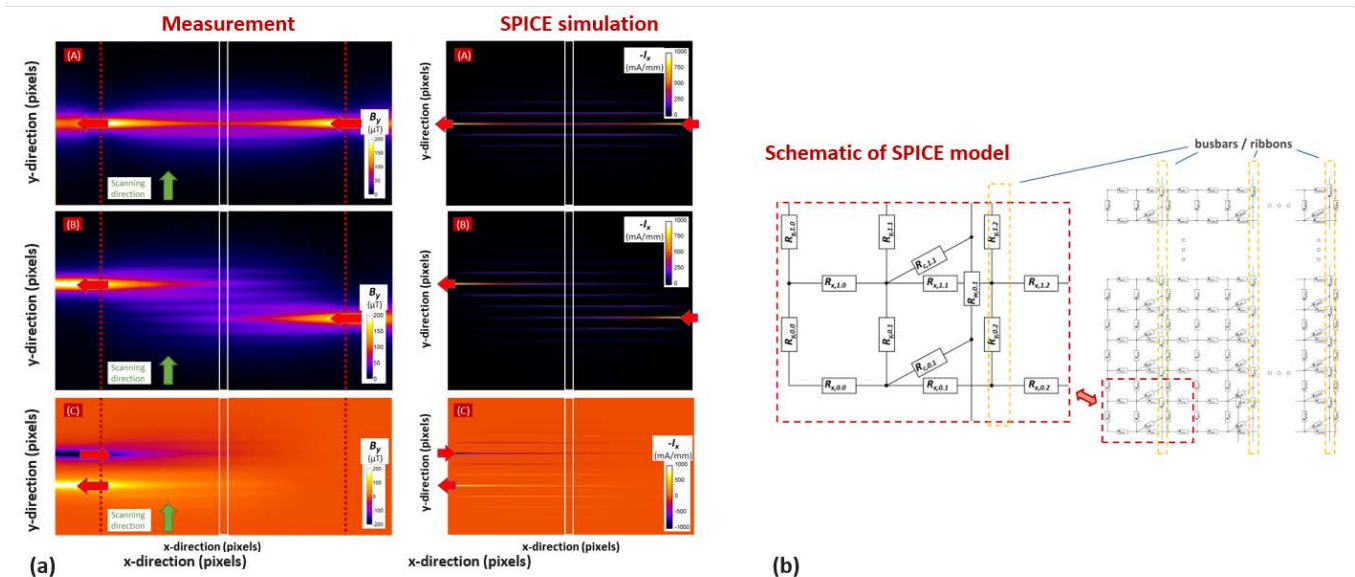


Figure 6.53.3: (a) left: Magnetic field images (B_y) of a multi-wire contacted silicon solar cell for different current injection patterns; (a) right: SPICE electronic network simulations of the measured current flows. (b) Schematic display of the equivalent circuit SPICE model used to obtain the simulation results.

6.54 INVESTIGATION OF PERFORMANCE DEGRADATION PATHWAYS IN SILICON PHOTOVOLTAIC MODULES ARISING FROM COPPER-PLATED METALLISATION

Lead Partner

UNSW

UNSW Team

Prof. Alison Lennon

Academic Partner

Arizona State University (ASU), USA: Dr André Filipe Rodrigues Augusto, Prof. Stuart Bowden

Funding Support

ARENA, UNSW

Aim

The aim of this project is to investigate possible degradation pathways in copper-plated silicon photovoltaic modules arising from copper-plated contacts on cells. The project uses cross-sectional imaging and material analysis of fabricated modules to identify the physics and chemistry associated with degradation pathways in both copper-plated p-type PERC and ASU's copper-plated silicon heterojunction (SHJ) cells. The project involves the fabrication and environmental testing of one and/or two cell modules from copper-plated silicon solar cells. Electrically degraded regions of the modules are then identified using electroluminescence and photoluminescence imaging, cross-sections prepared from these regions and then analysed using plasma-focused ion beam (PFIB) imaging and electron dispersive x-ray spectroscopy (EDS). Potential degradation pathways that are of particular interest to this study include:

- Cu diffusion through barrier layers, transparent conducting oxides (TCOs) (for example of SHJ cells) and capping layers
- void formation due to metal interdiffusion
- weak adhesion of cell metallisation.

Progress

This two-year project commenced in January 2019. Cross-sectional analyses have been performed on one cell mini-modules, fabricated at ASU with copper-plated p-type back-surface field solar cells, and exposed to 2000 hours of damp heat treatment (Karas et al. 2017). Electroluminescence (EL) imaging was used to detect regions that had been degraded by the exposure to damp heat and compared to regions where no degradation was observed (Figure 6.54.1). We have demonstrated that copper can out-diffuse through tin capping layers and be in direct contact with the ethylene vinyl acetate (EVA) encapsulant. This out-diffusion is frequently associated with voids in the encapsulant as shown in Figure 6.54.2. Copper out-diffusion through the tin capping has also been detected in regions where no

electrical degradation is observed suggesting that, although use of a tin capping layer can reduce cost, tin does not provide a sufficient barrier for copper diffusion.

Copper in-diffusion has also been detected in UNSW fabricated modules comprising copper-plated ps laser-ablated p-type PERC cells (Phua et al. 2019). For these modules, the very narrow contact opening widths (<15 μm) make it challenging to achieve strong adhesion and it is hypothesised that weak interfacial adhesion between the copper-plated fingers and the silicon can result in a pathway for copper diffusion into the silicon, and subsequent electrical degradation.

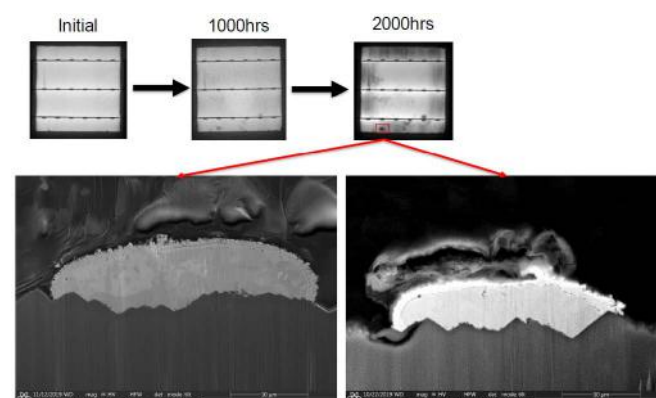


Figure 6.54.1: Electroluminescence images of an ASU-fabricated mini-module comprising a p-type back surface field (BSF) cell showing electrical degradation with damp heat testing and the regions selected for cross-sectional analysis.

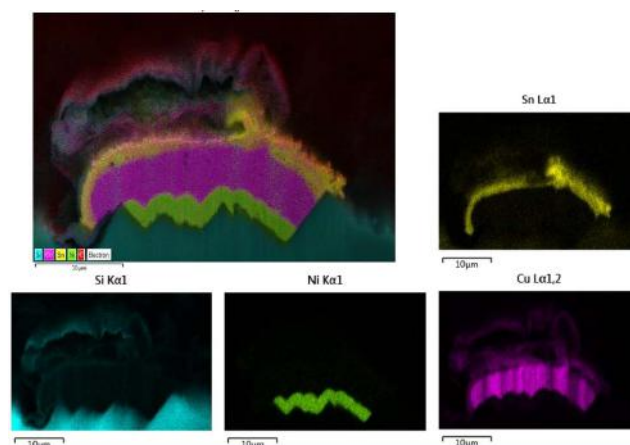


Figure 6.54.2: Cross-sectional energy-dispersive X-ray spectroscopy (EDS) maps of a copper-plated finger in the indicated region in Figure 6.54.1 showing copper out-diffusion through a tin capping layer and the formation of a void in the EVA encapsulant.

Highlights

- Demonstrated the ability to perform cross-sectional images of modules (even with tempered glass) using plasma focused ion beam (FIB) imaging and EDS.
- Copper out-diffusion through tin capping layers has been demonstrated and has been shown to occur at electrically degraded regions of copper-plated p-type BSF modules.

- Copper in-diffusion has been identified in modules comprising ps laser-ablated cells.
- Results of this project were presented at the Asia-Pacific Solar Research Conference in December 2019.

Future Work

The project has been very successful in building a collaboration between the ASU and UNSW researchers in the area of durability of silicon PV modules comprising copper-plated cells. To date, most analysis has focused on modules with p-type BSF or PERC cells, however, in the second year of the project, we will also compare degradation mechanisms with ASU's silicon HJT cells. Additionally, now that technical challenges with regard to the cross-sectional imaging of modules have been addressed, a greater focus will be placed on understanding the physical and chemical reasons for observed degradation.

References

KARAS, J., MICHAELSON, L., CASTILLO, M. L., MUNOZ, K., BAILLY, M., JAIN, H., AKEY, A., RAND, J., TYSON, T., BUONASSISI, T. & BOWDEN, S. Addressing adhesion and reliability concerns of copper-plated c-Si solar cells and modules. 2017 IEEE 44th Photovoltaic Specialist Conference, PVSC 2017, 2017. 1-5.

PHUA, B., SHEN, X., MO, A., HSIAO, P.-C., KARAS, J., AUGUSTO, A. F. R., BOWDEN, S. & LENNON, A. 2019. Performance degradation pathways in silicon photovoltaic modules arising from copper-plated metallisation Australian Pacific Solar Research Conference. Canberra, ACT.

6.55 COMPUTATIONAL MATERIALS DISCOVERY: AB INITIO MODELLING OF NEW, HIGH PERFORMANCE SEMICONDUCTORS FOR TOP CELLS IN MULTI-JUNCTION TANDEMS ON SILICON SOLAR CELLS

Lead Partner

UNSW

UNSW Team

Dr Rob Patterson, Dr Judy Hart, A/Prof. Xiaojing Hao, Prof. Martin Green

Academic Partners

University of Bristol, United Kingdom: Neil Allen
Beijing Computational Science Research Center: Su-huai Wei

Funding Support

ARENA, ACAP

Aim

The search for stable and scalable alternatives to high efficiency III-V and Pb-halide perovskite solar cells for silicon tandems has shown significant progress in its first year. Over 70 materials were screened in 2019 for their crystal structure and bandgap. Corrections to bandgap predictions to improve accuracy were made using the well-known DFT+U (Hubbard U augmented density functional theory) approach (Kulik 2006), essentially introducing a free empirical parameter. Also the purely ab initio GLLB-SC (Gritsenko, van Leeuwen, van Lenthe, Baerends – Solid Correlation) functional that accounts for excitonic effects to first order is very computationally efficient (Castelli 2014; Reining 2018). When assessing materials that have never been fabricated previously, the GLLB-SC has been preferred.

Progress

This task emphasises the computational materials discovery aspect of the work. Over 50 novel adamantine materials not previously synthesised have been screened for their crystal structures and bandgaps in 2019. Of particular interest were compounds involving Ni in the zero oxidation state, Ni⁰. However the search quickly spread to a number of transition and d-block metals, including Fe, Mn, Co and Ti. High throughput techniques that provided rapid materials screening and assessment were developed in 2019. These were tested on 16 ternary (2 cation) compounds, for example CoMnS₂. These will be applied to the large number of candidate compounds that still exist, given the number of interesting combinations that remain from the periodic table.

Still, the most promising Ni0 compound that has emerged from this search has been NiZnAl₂S₄. The GLLB-SC functional was applied and predicted a bandgap of 1.7 eV, highly suitable for top cells in silicon tandems.

An additional material system investigated were sulfiodides, looking for the stability of a sulfide and the solution processability of an iodide. The particular compound series was $\text{Cu}_x\text{Zn}_y\text{S}_y\text{I}_{x'}$, in which there were three feasible compounds Cu_3ZnSI_3 , CuZnSI and $\text{CuZn}_3\text{S}_3\text{I}$. The bandgaps and stability of these compounds were assessed using the GLLB-SC technique and a Gibbs free energy calculation. This showed bandgaps above 2.0 eV and stability similar to the Pb-halide perovskites. Further work is required to find a mixed ion compound that shows increased stability. The band structure and relative stability of CuZnSI is shown in Figure 6.55.1.

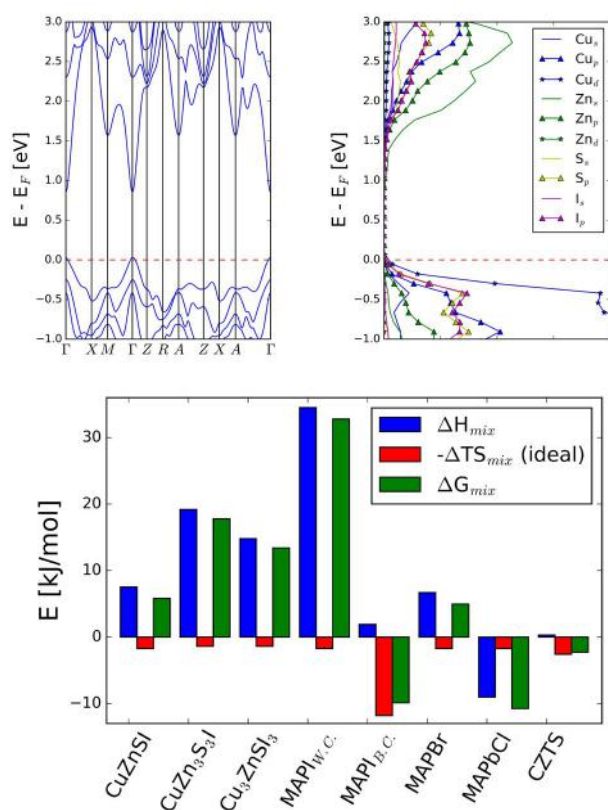


Figure 6.55.1: Band structure (PBE-GGA), pDOS and relative stability of the sulfiodide compound CuZnSI .

Stable perovskite compounds

Surprisingly, simulations and bandgap assessments of oxide perovskites of the type of initial interest (for example $\text{BaMn}_{0.5}\text{Mo}_{0.5}\text{O}_3$) have in our work shown themselves to be semi-metals ($E_g \leq 0$), in contrast to previous reports (Jain 2013). Additional work on the oxide perovskites BiFeO_3 and LaFeO_3 is slated for 2020. As stable perovskites are still of interest, investigations into new stable sulfide perovskites have been performed, to supplement oxide perovskite work. These sulfide perovskites are little explored and under-developed despite being known to possess bandgaps of 1.8 eV (Niu 2017), nearly ideal for silicon tandem applications. Additionally, sulfides have historically performed better than oxides as absorber materials in photovoltaic applications, making sulfide perovskites attractive. The band structure of an Sn-doped BaZrS_3 perovskite is shown in Figure 6.55.2.

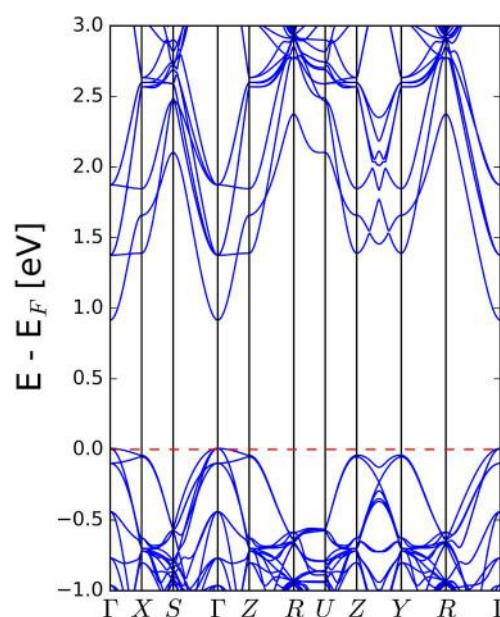


Figure 6.55.2: Band structure of a $\text{Ba}(\text{Zr}_{0.875}\text{Sn}_{0.125})\text{S}_3$ perovskite, with the bandgap enlarged to the GLLB-SC value. Despite the application of this correction, bandgap predictions remain small, with the GLLB-SC prediction of ~ 0.87 eV in the 50% Sn compound only enlarged to approximately ~ 0.96 eV in the material having 12.5% substitution of Zr by Sn. This is still very far away from the bulk bandgap of BaZrS_3 , known to be approximately 1.8 eV.

CuInS_2 and CIGS variations

Limited work on CuInS_2 and CIGS variations was done in 2019. The more novel systems, materials discovery of adamantine compounds and sulfide perovskites, have taken priority as these are less explored. However, AgBiS_2 and a number of niobium compounds, Nb^{3+} , were simulated. The work with Nb showed significant changes in the predicted crystal structure on incorporation, implying in all cases that unfortunately Nb is not a suitable substituting element for rare and expensive In^{3+} in these compounds. Screening of these novel candidate materials theoretically gives an indication of their potential much more quickly than experiment.

Highlights

- Over 70 materials screened.
- More accurate and computationally efficient bandgap prediction algorithms implemented.
- Identified two interesting material systems, adamantine $\text{NiZnAl}_2\text{S}_4$ and BaZrS_3 perovskite.

Future Work

Sustained efforts to find highly novel, stable adamantine compounds is a focus in the second year of the project. To this end, implementation of Gibbs free energy calculations as a function of atom chemical potential are essential. Work on sulfide perovskites

will be expanded in early 2020. Oxide and CIGS material variations will also be investigated in the first half of 2020, in parallel on the new NCI supercomputer Gadi, located at ANU in Canberra.

References

CASTELLI, I. E., GARCIA-LASTRA, J. M., THYGESEN, K. S. & JACOBSEN, K. W. 2014. Bandgap calculations and trends of organometal halide perovskites. *APL Materials*, 2. doi: 10.1063/1.4893495.

JAIN, A., ONG, S. P., HAUTIER, G., CHEN, W., RICHARDS, W. D., DACEK, S., CHOLIA, S., GUNTER, D., SKINNER, D., CEDER, G. & PERSSON, K. A. 2013. Commentary: The Materials Project: A materials genome approach to accelerating materials innovation. *APL Materials*, 1. doi: 10.1063/1.4812323.

KULIK, H. J., COCOCCIONI, M., SCHERLIS, D. A. & MARZARI, N. 2006. Density functional theory in transition-metal chemistry: A self-consistent Hubbard U approach. *Physical Review Letters*, 97. doi: 10.1103/PhysRevLett.97.103001.

NIU, S. Y., HUYAN, H. X., LIU, Y., YEUNG, M., YE, K., BLANKEMEIER, L., ORVIS, T., SARKAR, D., SINGH, D. J., KAPADIA, R. & RAVICHANDRAN, J. 2017. Bandgap Control via Structural and Chemical Tuning of Transition Metal Perovskite Chalcogenides. *Advanced Materials*, 29.

REINING, L. 2018. The GW approximation: content, successes and limitations. *Wiley Interdisciplinary Reviews-Computational Molecular Science*, 8. doi: 10.1002/wcms.1344.

6.56 TOWARDS A MULTIPLE EXCITON-GENERATING SILICON SOLAR CELL

Lead Partner

UNSW

UNSW Team

Dr Murad Tayebjee, Prof. Dane McCamey

Academic Partners

Harvard University, USA: Dr Daniel Congreve

Columbia University, USA: A/Prof. Luis Campos

Funding Support

ARENA, UNSW

Aim

This project creates new ACAP partnerships with Columbia University and Harvard University to develop an organic layer which will augment the current of existing silicon solar cell technologies. The potential energy conversion efficiency of these devices exceeds 35% (Tayebjee et al. 2014). The project brings together world leaders in singlet fission synthesis (Campos Group, Columbia University); fabrication of multiple exciton-generating devices (Congreve Group, Harvard University); and optical and magnetic resonance spectroscopies (Tayebjee and McCamey Groups, UNSW).

A key outcome of this project is the use of magnetic resonance and THz spectroscopy to identify and characterise singlet fission in working devices. This will provide benchmarks and screening for potential singlet fission silicon tandem candidate materials.

Progress

This two-year project was commenced in January 2019. Thus far we have liaised on the device constraints for the spectroscopic methods to be used (electrically detected magnetic resonance and optically detected magnetic resonance), and preliminary devices have been fabricated (compare Figure 6.56.1). THz measurements of several device layers have been made and the spectroscopic system has been adapted to house different device configurations.

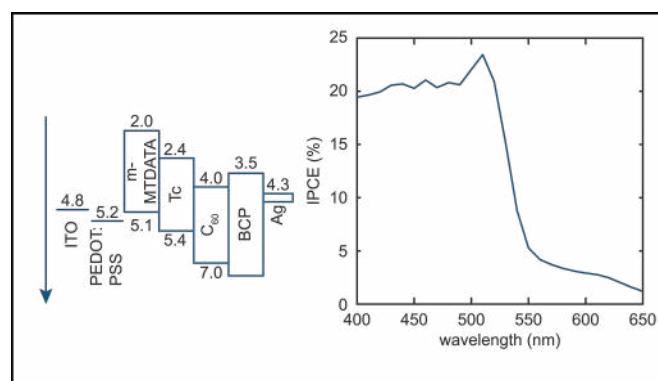


Figure 6.56.1: (left) The device structure used in these experiments. (right) Internal photocurrent efficiency plot showing the contribution of tetracene to the photocurrent of the device.

Tayebjee travelled to the Rowland Institute at Harvard University in July 2019 to discuss the development of the project. Further communication channels are regularly used to assess the progress of the work.

Highlights

- Tayebjee trip to Harvard.
- Fabrication of singlet-fission-capable organic device.
- Publication of preceding collaborative work demonstrating the efficacy of magnetic resonance in studying singlet fission (Pun et al. 2019).
- Presentation of work at OSA conference (Tayebjee, invited Talk).

Future Work

- Initial magnetic resonance experiments are being carried out in January 2020 and results are expected in the first quarter of 2020.
- The spectroscopy from this work is being used as part of a larger DP21 application.
- A "Singlet Fission Summit" is being planned in Sydney in 2020 where USA collaborators will attend to discuss the direction of this project into the future.

References

- PUN, A. B., ASADPOORDARVISH, A., KUMARASAMY, E., TAYEBJEE, M. J. Y., NIESNER, D., MCCAMEY, D. R., SANDERS, S. N., CAMPOS, L. M. & SFEIR, M. Y. 2019. Ultra-fast intramolecular singlet fission to persistent multiexcitons by molecular design. *Nature Chemistry*, 11, 821-828. doi: 10.1038/s41557-019-0297-7.
- TAYEBJEE, M. J. Y., SOUFIANI, A. M. & CONIBEER, G. J. 2014. Semi-Empirical Limiting Efficiency of Singlet-Fission-Capable Polyacene/Inorganic Hybrid Solar Cells. *Journal of Physical Chemistry C*, 118, 2298-2305. doi: 10.1021/jp4101637.

6.57 PV EDUCATION EXPANSION: LEARN HOW TO OPTIMISE PV MODULE PERFORMANCE

Lead Partner

UNSW

UNSW Team

Prof. Bram Hoex

UNSW Student

Zubair Abdullah-Vetter

Industry Partner

PV Lighthouse: Ben Sudbury, Malcolm Abbott, Keith McIntosh

QESST Team

Prof. Stuart Bowden, Dr Andre Augusto

Funding Support

ACAP, UNSW

Aims

UNSW has a strong track record in the development of (online) educational resources in the field of PV manufacturing. In 2014, PV Factory, a cloud-based simulation platform (UNSW and PV Lighthouse 2015), was developed through an ACAP-supported collaboration involving PV Lighthouse, UNSW and Arizona State University (ASU) as a teaching application that engages PV and Solar Energy Engineering students as they learned about how solar cells are made. PV Factory was released to the public in January 2015 and can be accessed at <https://factory.pvlighthouse.com.au>. It has attracted more than 9,000 unique users since its inception and is currently used by at least five universities in their teaching programs (including UNSW and ASU). More recently, the PV-Manufacturing.org platform was released in January 2018 (Hoex 2018). This platform was developed in an ACAP-funded project in a collaboration between UNSW and ASU and combines text with videos and tailored animations to teach students and engineers about solar cell manufacturing. The site has received over 10,000 unique visitors to date from all over the world and is complemented by a playlist on YouTube (Hoex 2017).

The manufacturing process of solar cells is very well covered by the combination of the practical PV Factory and PV-Manufacturing platform. On the other hand, the PV module part of the value chain is not extensively covered on existing platforms such as PVEducation and PV-Manufacturing.org, nor is there an equivalent of PV Factory available for modules. We felt that it was time to significantly enhance the educational resources in the area of PV module manufacturing and optimisation, incorporating current industry trends such as black silicon, heterojunction solar cells, multi-busbars, and bifacial solar cells so that they can be fully appreciated at the PV module level. We felt that the SunSolve platform from PV Lighthouse was the ideal vehicle to address these important trends. The usage of an existing and highly successful platform such as SunSolve has additional benefits as it significantly reduces the cost of the project while also training the students and engineers in software that is actively used in the PV industry.

Progress

The following work packages were completed during the reporting period.

WP1: Development of a dedicated SunSolve version that can be used for educational purposes (Lead: PVL)

SunSolve is actively used by the PV industry and research institutes to optimise their PV modules. SunSolve is a high performance ray tracer that is coupled with electrical solar cell and circuit solver allowing the simulation of the full optical and electrical performance of PV modules. The standard version is “out of the box” and not suitable for use in tertiary education or for the training of engineers. We implemented significant changes in terms of administrative management, user management, cloud capacity allocation, undergraduate-level self-run tutorials on how to use the software and expanded the availability of features. The updated version of SunSolve went live in April 2019 (PV Lighthouse 2019).

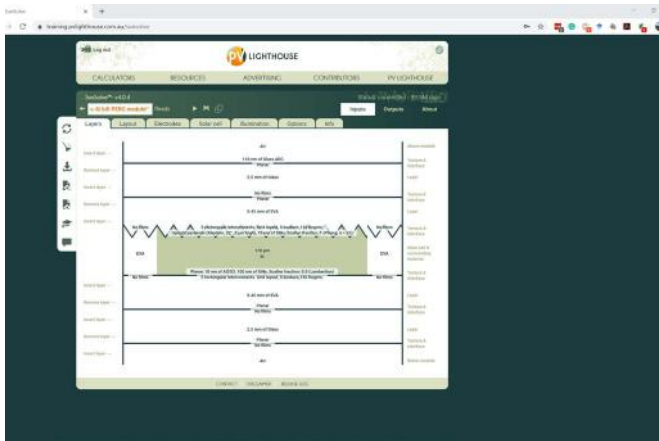


Figure 6.57.1: Screenshot of the dedicated SunSolve server for teaching education. The screenshot shows the template for a bifacial PERC module which was developed as part of this project.

WP2: Development of the online educational modules (Lead: UNSW)

We developed online education modules targeting key manufacturing steps and trends in PV manufacturing. Each module consists of a tailored exercise in the SunSolve server developed in WP1 complemented with a section on PV-Manufacturing.org which contains the training material. The topics which were released in 2019 on PV-Manufacturing.org are (Abdullah-Vetter & Hoex 2019b):

1. Optimisation of anti-reflection coatings.
2. Optimisation of surface texturing.
3. Optimisation of front and rear surface metallisation from an electrical and optical point of view.
4. Optimisation of bill of materials (for example backsheets, encapsulants) for PV module manufacturing.
5. Bifacial vs monofacial solar cells.

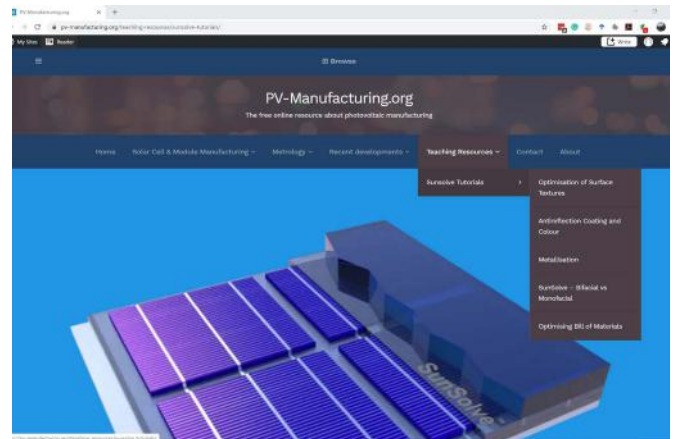


Figure 6.57.2: Screenshot of the training resource section of PV-Manufacturing.org. It currently contains five SunSolve tutorials and more tutorials will be released in the near future.

WP3: Beta-testing of the online educational resources

The tutorials developed in WP2 have already been used during the SOLA3020 course at UNSW in 2019 – the students were really happy using them and it definitely improved their learning. The students also stress-tested the SunSolve server and provided valuable feedback on the tutorials which are already implemented in the online versions.

WP4: Expansion of the PV module section of PV-Manufacturing.org

Due to the very significant reduction in the costs of solar cells many innovations in terms of PV module design were enabled such as paving, shingling and half cells. These innovations are now described in quite some detail in the new “Recent advances in PV Modules” section of PV-Manufacturing.org (Abdullah-Vetter & Hoex 2019a).

Highlights

- A new version of SunSolve was developed, tailored for education and was released in 2019.
- Five tutorials were developed to teach students and engineers various aspects of PV module optimisation. The tutorials are available free of charge on PV-Manufacturing.org.
- The PV module section of PV-Manufacturing.org was significantly expanded.

Future Work

We will continue to work on developing more tutorials using SunSolve as well as articles about recent development and publishing them on PV-Manufacturing.org.

References

ABDULLAH-VETTER, Z. & HOEX, B. 2019a. *Recent advances in PV modules* [Online]. Available: <https://pv-manufacturing.org/solar-cell-manufacturing/recent-advances-in-pv-modules/> [Accessed 20 January 2020].

ABDULLAH-VETTER, Z. & HOEX, B. 2019b. *Sunsolve Tutorials* [Online]. Available: <https://pv-manufacturing.org/teaching-resources/sunsolve-tutorials/> [Accessed 20 January 2020].

HOEX, B. 2017. *UNSW E-Learning playlist on PV Manufacturing*. [Online]. Available: <https://www.youtube.com/playlist?list=PLHSIfioizVW0zKzDhCwU3MhwCqKz0ORk> [Accessed 20 January 2020].

HOEX, B. 2018. *PV-Manufacturing.org* [Online]. Available: <https://pv-manufacturing.org/> [Accessed 20 January 2020].

PV LIGHTHOUSE. *SunSolve* [Online]. Available: <https://www.pvlighthouse.com.au/sunsolve> [Accessed 20 January 2020].

PV LIGHTHOUSE. 2019. *Sunsolve Teaching Server* [Online]. Available: <https://training.pvlighthouse.com.au/sunsolve> [Accessed 20 January 2020].

UNSW & PV LIGHTHOUSE. 2015. *PV Factory* [Online]. Available: <https://factory.pvlighthouse.com.au/> [Accessed 20 January 2020].

6.58 MICROWAVE PROCESSING: FOR SILICON SOLAR CELLS AND BEYOND

Lead Partner

UNSW

UNSW Team

A/Prof. B. Hallam, A/Prof. S. Huang

UNSW Student

Yuchao Zhang

Academic Partner

Macquarie University: Dr B. Puthen Veetil, Dr D. Payne

Funding Support

ARENA, ACAP

Aim

This project aims to investigate the potential of microwave processing techniques for advanced hydrogenation of silicon solar cells and further this study to investigate the potential role of microwave processing for solution-processed solar cell materials. Through this project, we aim to establish microwave processing as an efficient alternative to conventional processing steps.

Progress

A custom-built microwave oven has been installed and tested at Macquarie University. The operating frequency of this equipment is at 2.45 GHz, the same as a kitchen microwave. This equipment can process materials at temperatures up to 1800°C. The temperature inside the microwave cavity is monitored using an IR detector and is used to control the heating rate according to specific temperature profiles generated using a computer. The microwave setup is shown in Figure 6.58.1. Not all materials respond to microwave radiation. To process materials that are transparent to microwave, sample boxes with SiC susceptor layers were used.



Figure 6.58.1: Computer-controlled high temperature microwave oven. The inset in red shows sample holder boxes, with silicon carbide susceptor (right) and without any susceptor (left).

Numerous different silicon solar cell samples were prepared at UNSW for microwave processing. These included as-deposited and fired test structures fabricated on boron-doped p-type Cz substrates. B-O defects were introduced into the material by light soaking for one subset of samples prior to microwave processing. A subset of samples was light soaked again after microwave processing. The main objective here was to look at any temporary and permanent impacts of microwave processing on B-O defects based on excess minority carrier lifetime measurements. The characterisation was mainly conducted using PL-imaging and Sinton lifetime measurements. We have observed some promising results that need to be explored further through continued experimentation and analysis. Although microwave processing was performed for 5, 20 and 40 seconds, the processed samples showed a significant improvement in carrier lifetime, related to either B-O dissociation or passivation. The PL images of the non-fired, light soaked silicon solar cell samples showed the greatest improvement in our preliminary experiments. Increased processing time resulted in better improvements in bulk lifetime. PL images from the second light soaked samples showed that the improvement in bulk lifetime due to microwave processing did not completely reverse under light soaking, hence indicating a successful partial passivation of the B-O defects with microwave processing.

Microwave processing itself presented several challenges that limited the microwave processing time. The rectangular shape of the samples caused arcing at the corners; in some cases, samples broke during the cooling time, indicating a thermal gradient while processing. Circular samples and a mode-stirrer inside the microwave cavity can be used to overcome these challenges. The mode-stirrer has already been installed, and processing times up to 3 minutes have been tested.

Understanding the effects of microwave on novel materials requires rigorous study, both theoretical and experimental. Two research assistants are employed at UNSW to develop the theoretical model of microwave field interaction with molecules. The models are being developed using AVOGADRO and GAMESS software packages. The results are expected to give us insights into the impact of microwave processing on solution processed materials, including quantum dot arrays and perovskites.

Highlights

- Installed and tested a microwave processing oven with computer-controlled heating profiles that goes up to 1800°C.
- The first batch of experimentation completed with very promising results.
- Up to 40 seconds of microwave processing showed to improve dissociation from B-O defects caused by light soaking.
- The improvements in bulk-lifetime seem to outlast the defects introduced by subsequent light soaking.

Future Work

Ongoing work with creating optimised conditions for microwave processing is underway. This includes optimising the temperature profile for the microwave processing step and is expected to produce uniform heating and repeatable results while minimising sample breaking. Further work to look into the optimised processing conditions for non-toxic quantum dot materials will be developed following the same procedures. Development of the molecular dynamics models for studying the interaction between the microwave field and materials is underway to include novel materials.

6.59 COLLATING AND SHARING INFORMATION ON DEFECTS IN SILICON

Lead Partner

UNSW

UNSW Team

Dr Mattias Juhl, Dr Fiacre Rougieux

Academic Partners

Australian National University: Professor Daniel MacDonald

ECN Solar Energy: Dr Stuart Bowden

Fraunhofer ISE: Dr Martin Schubert

Industry Partner

PV Lighthouse: Keith Macintosh

Funding Support

ACAP Fellowship

Aims

This project aims to collate the electronic parameters of defects in silicon and store them online in an editable open access repository. The name of this repository is the global defect repository (GDR). The repository will be linked to be able to be explored on PV Lighthouse, and used in its online calculators. The data within the GDR will also be analysed for trends to aid in the study of defects.

Progress

The GDR is already online, with numerous people adding data on defects. The GDR can be found at <https://github.com/MK8J/semiconductorDefects>. Work has started on the PV Lighthouse defect explorer, and calculator integration.

Highlights

- The repository has over 190 unique defects in it.
- Defects entered for 59 elements.
- Several conference papers highlighting the repository have been made.
- Visit to Fraunhofer ISE by Dr Juhl.
- Visit to ECN
- Two presentations at international conferences.

References

JUHL, M.K., HEINZ, F.D., COLETTI, G., MACDONALD, D., ROUGIEUX, F.E., SCHINDLE, F., NIEWELT, T. & SCHUBERT, M.C. 2018. An Open Source Based Repository for Defects in Silicon, Presented at the 7th World Conference on Photovoltaic Energy Conversion (WCPEC), Hawaii, USA, pp. 0328–0332.

JUHL, M.K., HEINZ, F.D., COLETTI, G., ROUGIEUX, F.E., SUN, C., NIEWELT, T., KRICH, J.J., MACDONALD, D., SCHUBERT, M.C. 2019. Insights on the electronic parameterisation of defects in silicon obtained from the formation of the defect repository. Presented at the 36th European Photovoltaic Solar Energy Conference and Exhibition, Marseille, France, p. 4.

6.60 SILICON SOLAR CELLS WITH SILICON CARBIDE PASSIVATED CONTACTS

Lead Partner

UNSW

UNSW Team

Dr Ning Song, Dr Udo Römer, Prof. Alison Lennon

Industry Partners

Trina Solar Co., Ltd. China.

Funding Support

ACAP

Aim

This project aims to conduct fundamental research into the passivation properties of doped Silicon Carbide (SiC_x) passivated contacts for silicon solar cells

Progress

The use of doped polysilicon (poly-Si) for electrical contacts is attracting significant interest in both PV research institutes and silicon PV manufacturing companies due to the record high efficiency (26.1%) achieved with this contacting technology (Green et al. 2019; Haase et al. 2018). Meanwhile, SiC_x as an alternative to poly-Si also draws more attention due to its greater resilience to blistering when deposited on SiO_x, low thermal budget for dopants activation, high chemical and thermal stability and high transparency and conductivity (Nogay et al. 2017; Xu et al., 2020; Pomaska et al., 2020). This project investigates a new silicon rich SiC_x material for contacting of both polarities of silicon instead of/ or in combination with poly-Si. However, progress in this project has been delayed by the maintenance of TETB labs in UNSW. Because our work is heavily relying on the equipment in rooms that were off-access from December 2018 to December 2019, limited progress has been made. The lab is now opened, and the sputtering machine is expected to be back online soon. The project is ready to move ahead with the targets which will be used for SiC_x film deposition have been prepared and are ready for use and a research assistant (0.4 FTE) has been employed to work through the year 2020.

Highlights

- Lab maintenance caused no access to the equipment and limited project progress
- Targets are ready and a research assistant is employed.

Future Work

- Develop a highly-doped SiC_x deposition process using UNSW's existing sputtering techniques by varying the carbon concentration, doping density, thermal annealing temperature and duration.
- Study the composition, optical, structural and electrical properties of the SiC_x.
- Fabricate silicon solar cells with doped SiC_x passivated contacts.

References

GREEN, M. A., DUNLOP, E. D., LEVI, D. H., HOHL-EBINGER, J., YOSHITA, M. & HO-BAILLIE, A. W. Y. 2020. Solar cell efficiency tables (Version 55). *Progress in Photovoltaics*, 28, 3-15.

HAASE, F., HOLLEMANN, C., SCHAFFER, S., MERKLE, A., RIENACKER, M., KRUGENER, J., BRENDEL, R. & PEIBST, R. 2018. Laser contact openings for local poly-Si-metal contacts enabling 26.1%-efficient POLO-IBC solar cells. *Solar Energy Materials and Solar Cells*, 186, 184-193.

NOGAY, G., STUCKELBERGER, J., WYSS, P., RUCAVADO, E., ALLEBE, C., KOIDA, T., MORALES-MASIS, M., DESPEISSE, M., HAUG, F. J., LOPER, P. & BALLIF, C. 2017. Interplay of annealing temperature and doping in hole selective rear contacts based on silicon-rich silicon-carbide thin films. *Solar Energy Materials and Solar Cells*, 173, 18-24.

POMASKA, M., KÖHLER, M., PROCEL MOYA, P., ZAMCHYI, A., SINGH, A., KIM, D. Y., ISABELLA, O., ZEMAN, M., LI, S., QIU, K., EBERST, A., SMIRNOV, V., FINGER, F., RAU, U. & DING, K. 2020. Transparent silicon carbide/tunnel SiO₂ passivation for c-Si solar cell front side: Enabling J_{sc} > 42 mA/cm² and iVoc of 742 mV. *Progress in Photovoltaics: Research and Applications*, 1– 7. <https://doi.org/10.1002/pip.3244>.

XU, Z., TAO, K., JIANG, S., JIA, R., LI, W., ZHOU, Y., JIN, Z. & LIU, X. 2020. Application of polycrystalline silicon carbide thin films as the passivating contacts for silicon solar cells. *Solar Energy Materials and Solar Cells*, 206, 110329

6.61 ALL-SCREEN-PRINTED NANOPARTICLE CONTACTS

Lead Partner

UNSW

UNSW Team

Dr Malcolm Abbott

Industry Partner

Bert Thin Films, USA: Dr Thad Druffel, Dr Ruvini Dharmadasa

Funding Support

ARENA, UNSW, BTF

Aim

This project aims to develop next generation crystalline silicon contacting technology to enable higher efficiency and lower cost solar cells. Specifically, the program aims to develop novel screen-printable pastes containing nanoparticles that will be combined with laser processing to form layers of doped silicon-carbide contacted via a thick film copper conductor. The project aims to develop these processes and integrate them with working solar cells in collaboration with a US company Bert Thin Films (BTF).

Progress

The first year of the project has seen the successful fabrication of solar cells with copper-printed contacts to traditional laser-doped regions. Processing was done at a combination of the facilities at UNSW and BTF. The processing equipment at the BTF site was upgraded to facilitate the aligned screen print. This resulted in good, repeatable alignment between the laser doping from UNSW and the screen-printing process at BTF. Variations in laser-doping settings, belt firing and copper paste chemistry were all investigated to optimise the contact formation. Initial versions of copper paste chemistry were rejected as they resulted in either too much line spreading or poor contact formation at all conditions. An optimal frit chemistry was identified and will be used as the basis for subsequent experiments. For that paste, the hold time during rapid firing was identified as a critical parameter (more so than the laser-doping conditions). Too little firing resulted in poor contact formation, however overfiring caused increased recombination within both the contact region and the pre-formed aluminium back surface field. BTF's firing process also resulted in the contacts having a porous structure. The company secured the use of an industrial IR belt furnace at an external academic facility in the US to continue improving this process. The changes to the firing resulted in densification of the contacts. BTF is in the process of modifying its in-house firing setup to mimic this process and apply the same settings to the next round of laser-doped cells. Future rounds of cell fabrication will use the heaviest laser doping settings, as well as focus on further optimisation of the firing process in tandem with more minor changes to copper paste chemistry.

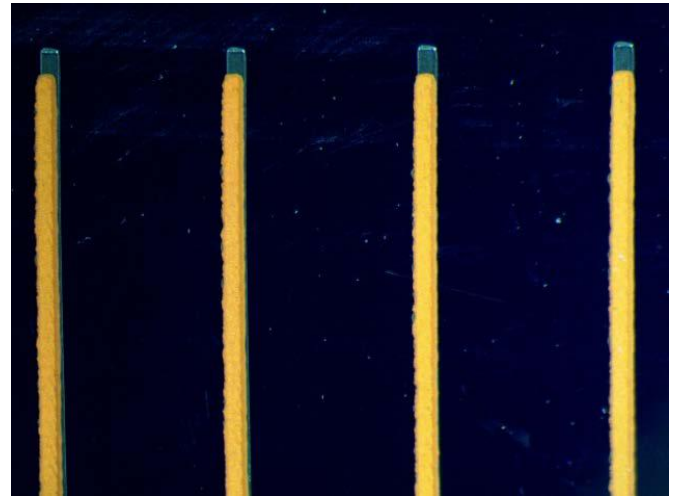


Figure 6.61.1: Optical microscope image of copper-printed lines aligned to locally laser-doped regions.

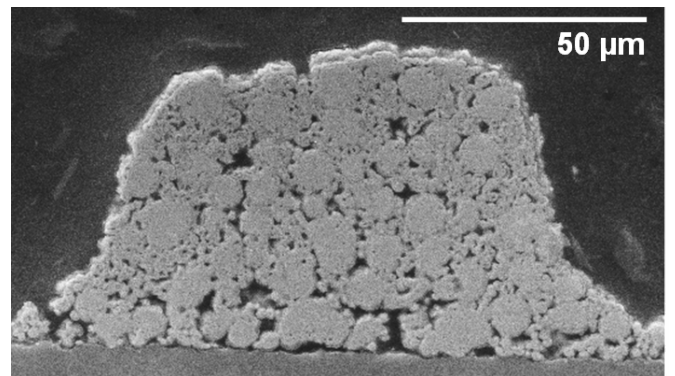


Figure 6.61.2: SEM image of the copper contact fired in BTF's original furnace setup.

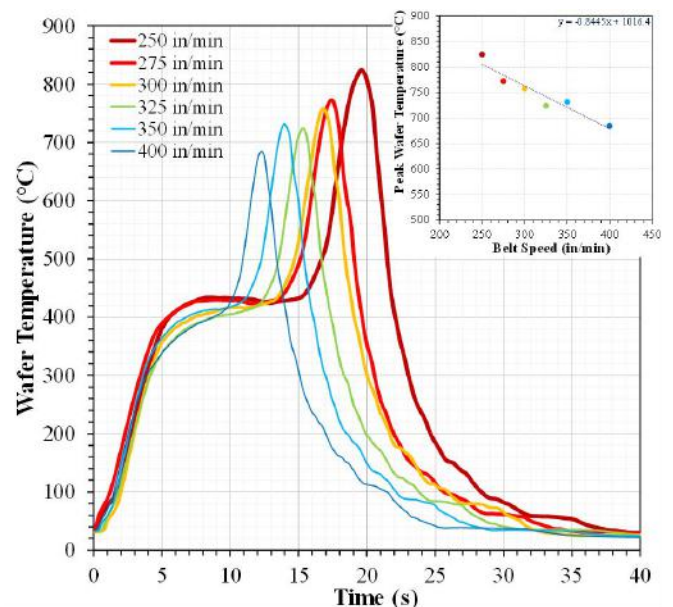


Figure 6.61.3: Examples of the firing profiles used to optimise the firing of the copper contacts in the industrial IR belt furnace.

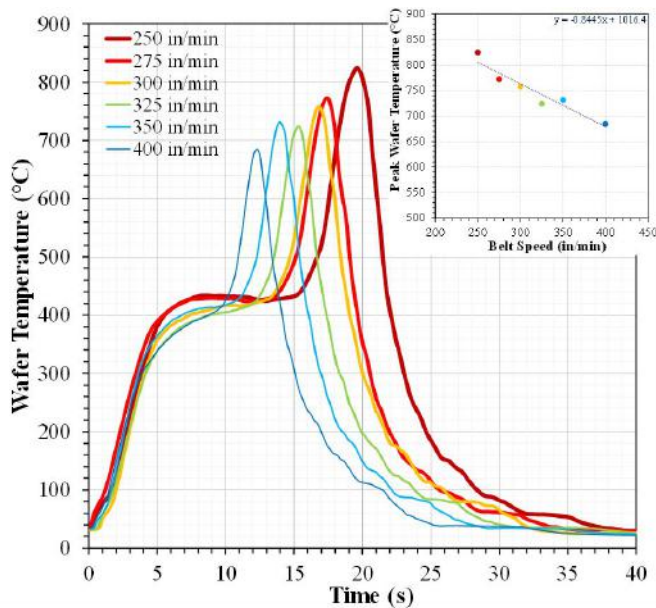


Figure 6.61.4: SEM image of the copper contact fired using the industrial IR belt furnace with a belt speed of 300 in/min.

Highlights

- Visit by Dr Abbott to the Bert Thin Films Louisville, Kentucky site in June 2019.
- Alignment of screen printing to laser-doped regions successfully achieved.
- First working solar cells combining laser doping and copper screen-printed electrodes achieved.

Future Work

The first year of the project has been very successful in building a collaboration between UNSW and BTF. The logistics of fabricating solar cells jointly between the two facilities have been established. Future work will now build on this good start with the aim of improving the quality of contact formation and final efficiency of the solar cells. The second year of the project will see the commencement of the integration of silicon-carbide into the laser-doping process. This will involve an initial screening of new nanoparticle dispersions followed by optimisation of the laser-doping process.

6.62 DEVELOPMENT OF QUANTUM DOTS SOLAR INKS FOR ECONOMICAL MASSIVE-SCALE PRODUCTION OF THIN-FILM PHOTOVOLTAIC CELLS

Lead Partner

UNSW

UNSW Team

Dr Shujuan Huang, Prof. Gavin Conibeer, Dr Robert Patterson

UNSW Students

Mr Zhi Li Teh, Mr Yijun Gao

Academic Partner

AMOLF

AMOLF Team

Prof. Albert Polman, Mr Stefan Tabernig

Aims

This project aims to develop an economical high-throughput quantum dot "solar ink" technology for high efficiency thin film solar cells. This technology will be enabled by two innovations – liquid-phase surface chemistry modification to improve quantum dot deposition and advanced optical optimisation to further improve efficiencies through light trapping at strategically chosen wavelengths.

Progress

The first innovation is liquid-phase surface chemistry modification to improve quantum dot deposition. For a long time, the layer-by-layer "solid-phase" ligand exchange method has been used in fabrication of the quantum dot solar cells. However, defects concentration can be increased as this method introduced multiple interfaces between layers. Also, the incomplete ligand exchange is another problem hindering further development of layer-by-layer method. The liquid-phase ligand exchange method completely solved the multi-interface problem and can provide a higher level passivation to quantum dot surface defects (Liu et al. 2017; Xu et al. 2018). This work proposes to provide surface chemistry modification to improve quantum dot liquid-phase, that is, quantum dot "ink" deposition. Currently a champion cell with an efficiency of 11.9% (Figure 6.62.1) has been achieved based on this proposed technique, ~30% higher than that of devices fabricated by "solid-phase" method.

The quantum dot "ink" was prepared using the liquid-phase ligand exchange method. First, the as-synthesised quantum dots with original long-chain ligands (oleic acid) were mixed with short-chain ligands (iodine) in solution, in which the long-chain ligands on quantum dots' surfaces would be exchanged by short-chain ligands. Then, the ligand-exchanged quantum dots were purified by hexane. After precipitating by centrifugation, the purified ligand-exchanged quantum dots were finally dissolved in a mixed solution (butylamine, amylamine and hexylamine) to form quantum dot "ink".

The quantum dot solar cells were fabricated by spin-coating quantum dot "ink" in "one-step". In contrast, the traditional solid-state method needs the film to be deposited layer by layer, which leads to a long processing time. Averagely, the time spent on the solid-phase method per device is 30 minutes, while the liquid-phase quantum dot "ink" method can reduce the processing time to 7 minutes.

On the light management part, optical simulations as well as the first fabrication steps were completed. To begin with, optical simulations were conducted in order to find the ideal structure to tailor light interaction on the nanoscale, within the cell, such that the absorption per unit volume in the absorber material was maximised. The optimisation was done using the Lumerical software package, which is a program that solves Maxwell's equations numerically. The result was that the ideal interface between the electron transport layer ZnO and quantum dot layer should be patterned such that a periodic array of holes, printed into the ZnO layer, would be filled up with quantum dots as shown Figures 6.62.2(a) and 6.62.2(b) (Tabernig et al. 2019). In addition to the optical simulations, we looked into simulating the electronic properties of this geometry as well. For that, Lumerical's DEVICE, which solves the drift-diffusion equations numerically, was used. The simulations suggest that the structure that we obtained from the optimisation of the optical performance, would also benefit from enhanced voltages, as the charge carrier generation happens more closely to the contacts as shown in Figure 6.62.2(c).

In order to be able to fabricate such a structure, substrate conformal imprint lithography (SCIL) was used. This technique allows for nano-patterning of solgel-SiO₂, with a feature resolution of down to 6 nm. For that, a Si-master was fabricated using e-beam lithography. That master contained the pattern which was designed by simulations. In order to translate this pattern from the Si-master into the ZnO layer, a PDMS-rubber stamp was obtained from the master, containing the negative pattern. The pattern is then etched into the ZnO layer, by utilising the full capabilities of SCIL as well as reactive ion etching, in order to translate the pattern from the patterned SiO₂ layer downwards into the ZnO. First patterned ZnO samples have been obtained already, but the process still requires some optimisation.

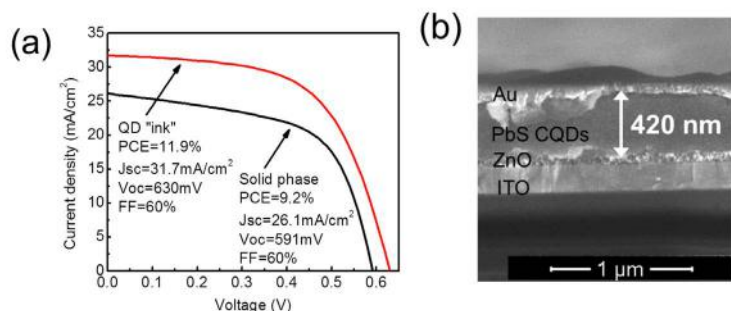


Figure 6.62.1.: (a) J-V curves of PbS quantum dot solar cell fabricated by liquid-phase "ink" method and solid-phase method. (b) Cross-sectional SEM image of quantum dot solar cell with liquid-phase "ink" method. The thickness of quantum dot layer is 420 nm.

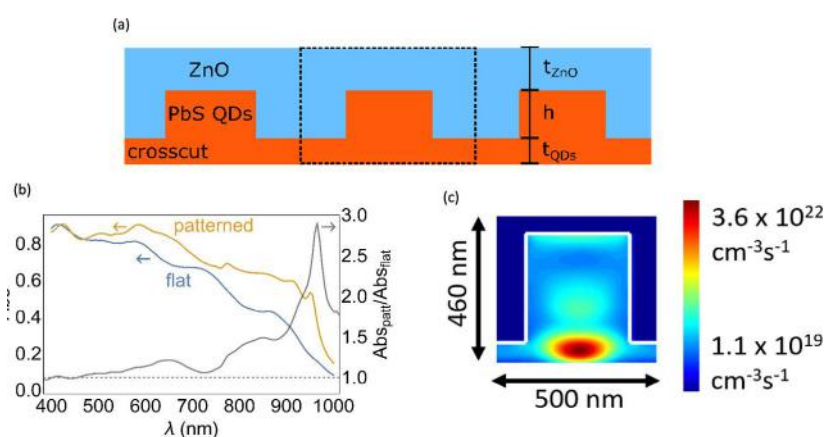


Figure 6.62.2.:(a) Illustration of the re-shaped interface. (b) Absorption enhancement per unit volume in the quantum dot layer, due to utilization of nanophotonic effects. The absorption enhancement increases towards the infrared regime. Due to positioning of sharp resonances around the bandgap, the absorption onset is now much sharper. (c) Charge carrier generation closer to interfaces. Light is coming from the top. Instead of generating the bulk of the carriers right when they enter the absorber, the structure causes most of the generation to happen in the back, where both charge species only have short paths to travel in order to be extracted. This reduces VOC losses.

Highlights

- Based on the proposed liquid-phase quantum dot "ink" deposition, an average efficiency of 11.4% has been achieved (with 8 parallel cells). The champion cell reached an efficiency of 11.9% with small hysteresis (Figure 6.62.1).
- A novel structure for the interface of the p-n junction in the quantum dot solar cell has been designed by employing optical as well as electronic simulation methods. The structure (Figure 6.62.2a) is predicted to boost optical (Figure 6.62.2(b)) and electronic (Figure 6.62.2(c)) performance.

Future Work

- Based on currently used PbI_2 ligand, the ligand exchange chemistry reaction condition will be studied and developed for further increasing solar cells' performance. A paper will be yielded based on this research and submitted to a high quality journal.
- New types of ligand source suitable for liquid-phase deposition will be explored and studied for more complete surface passivation to quantum dots to further improve device performance.
- Optimise the fabrication of the patterned ZnO layer.
- Fabricate a complete quantum dot solar cell with patterned ZnO layer using the developed quantum dot ink method.

References

- LIU, M. X., VOZNY, O., SABATINI, R., DE ARQUER, F. P. G., MUNIR, R., BALAWI, A. H., LAN, X. Z., FAN, F. J., WALTERS, G., KIRMANI, A. R., HOOGLAND, S., LAQUAI, F., AMASSIAN, A. & SARGENT, E. H. 2017. Hybrid organic-inorganic inks flatten the energy landscape in colloidal quantum dot solids. *Nature Materials*, 16, 258-263.
- TABERNIG, S., TEH Z.-L., CORDARA, A., PATERSON, R., CONIBEEER, G., HUANG, S. & POLMAN, A. Light management for absorption enhancement in PbS quantum dot solar cells. Asia-Pacific Solar Research Conference 2019, Publisher: Australian PV Institute, Dec 2019, ISBN: 978-0-6480414-3-6.
- XU, J. X., VOZNY, O., LIU, M. X., KIRMANI, A. R., WALTERS, G., MUNIR, R., ABDELSAMIE, M., PROPPE, A. H., SARKAR, A., DE ARQUER, F. P. G., WEI, M. Y., SUN, B., LIU, M., OUELLETTE, O., QUINTERO-BERMEDEZ, R., LI, J., FAN, J., QUAN, L. N., TODOROVIC, P., TAN, H. R., HOOGLAND, S., KELLEY, S. O., STEFIK, M., AMASSIAN, A. & SARGENT, E. H. 2018. 2D matrix engineering for homogeneous quantum dot coupling in photovoltaic solids. *Nature Nanotechnology*, 13, 456

6.63 ENGINEERING INTERFACES FOR HIGH PERFORMANCE SILICON TANDEM CELL STRUCTURES

Lead Partner

CSIRO, Energy, Newcastle

CSIRO Team

Dr Gregory Wilson, Dr Timothy Jones, Dr Jacob Wang, Dr Terry Yang, Dr Chris Fell, Dr Benjamin Duck

Academic Partner

UNSW: A/Prof. Anita Ho-Baillie

Funding Support

ACAP

Aim

This project will undertake an initial scoping study in assessment of the family of N-chelation compounds based on aromatic pyridyl structures in charge-selective layers of perovskite/silicon tandem cells.

Progress

As part of the ARENA project, we have made the purchase of a SENTECH atomic layer deposition (ALD) system, which will aid in the essential fabrication capability for the perovskite/silicon tandem solar cell. The carefully chosen vacuum-based ALD system allows for the deposition of oxides, nitrides and metals by thermal as well as plasma enhanced processing with a future system upgrade. The ALD system is designed for direct manual loading of industry-sized solar wafers (156.75 mm x 156.75 mm) and of carriers for smaller wafers and pieces. This will allow for the eventual fabrication of industrial-sized perovskite/silicon tandem solar cells. The versatile ALD system will allow the deposition of a range of different materials required in the design of the perovskite/silicon tandem solar cell. These include the dual electron transport layer and buffer layer, for example SnO_2 , transparent conductive contacts, for example IZO, AZO, passivation layers for the Si solar cell, for example Al_2O_3 , and inorganic hole transport layers, for example NiO_x for the perovskite solar cell.

A custom low temperature atmospheric chemical vapour deposition chamber has been planned and commissioned to exploit CSIRO's patent ("Process of forming a photoactive layer of an optoelectronic device"; US Patent 10,157,710) for the fabrication of organometal halide perovskite layers. The concept exploits sequential formation processes of perovskites. Simple solid/vapour acid bases and redox chemistry processes are exploited to form uniform perovskites via a readily scalable process. Given all deposition techniques are "line of sight", in contrast to printing and spin-coating, we anticipate the process to be compatible with existing and future silicon front-surface texturing, required for monolithic two-terminal silicon/perovskite tandem devices. Furthermore, the method will have application to post-passivation with volatile reagents.

Our current commissioning efforts have extended previous internal experiments for perovskite formation, which relied on manual valve operation, while preparing our reactors to a larger scale, up to 100 cm².

Previous attempts demonstrated promising early results (initial ~10% PCE from a highly novel fabrication procedure). However, advances were hampered by insufficient control of environmental conditions, line contamination and operator variability. The current iteration of the atmospheric chemical vapour deposition (CVD) has been designed and engineered to overcome these limitations. We have more precise control of reagent temperature control and better inline monitoring during deposition. Valve and manifold operation have been automated with control software, as have chemical reagent dispensing and line washing / purging.

A first trial run gave successful formation of a MAPbI_3 film, with high surface roughness. We are presently calibrating the inline monitoring system, analysing and improving internal fluid dynamics, and troubleshooting control software, before commencing a routine empirical optimisation of our perovskite layers on fluorine-doped tin oxide (FTO) and textured Si substrates.

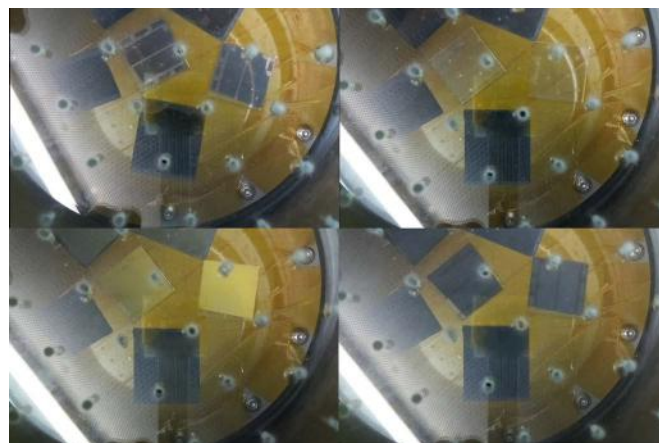


Figure 6.63.1: Automated CVD conversion – Top left: lead on silicon wafer and FTO glass. Top right: Conversion of lead to lead acetate. Bottom left: Conversion of lead acetate to lead iodide. Bottom right: Final conversion from lead iodide to perovskite film.

Highlights

- New atomic layer deposition (ALD) capability allowing deposition of the transport, buffer, contact and passivation layers.
- Demonstration of perovskite formation using a novel CVD process on textured silicon and FTO substrates.

Future Work

- Leverage ALD capability to deposit novel charge-selective layer compositions.
- Optimisation of CVD process for device performance.
- Assess effectiveness of interface layers in single junction and four-terminal stack configurations.
- Determine compatibility between novel charge-selective layers and device manufacturing steps using CVD process.
- Fabrication of proof of concept two-terminal perovskite on Si devices using optimised charge transport layers.

6.65 ADVANCED LUMINESCENCE CHARACTERISATION FOR DOPED-POLY AND PASSIVATION FILMS IN SILICON PHOTOVOLTAICS

Lead Partner

ANU

ANU Team

Dr Hieu Nguyen (lead), Thien Truong, Mike Tebyetekerwa, Prof. Daniel Macdonald

Academic Partner

Fraunhofer ISE (Fh-ISE), Germany: Dr Martin Schubert

Funding Support

ARENA, ACAP, ANU, Fh-ISE

Aim

This project aims to combine complementary leading expertise at the Australian National University (ANU) and the Fraunhofer Institute for Solar Energy Systems (Fh-ISE), Germany, in the development of novel luminescence-based techniques for characterising silicon (Si) materials and solar cells. This will primarily be achieved through the investigation and application of luminescence of doped poly-silicon films and other passivation layers. The scientific findings will improve our understanding of the impacts and performances of various solar cell components, whereas the technique inventions will provide tools to characterise and optimise Si solar cells.

Progress

This two-year project was commenced in November 2018. The ANU team, led by Dr Hieu Nguyen, has discovered that at low temperatures the doped poly-Si films, employed in passivating contact solar cells, emit a characteristic broad photoluminescence (PL) peak at energies lower than the crystalline Si (c-Si) bandgap. Based on such phenomenon, they have demonstrated several applications to understand the behaviour of poly-Si/SiO_x passivating contacts in terms of carrier recombination and transport: (i) the films contain radiative defects whose energy levels continuously stretch from the band edges to deep levels inside the poly-Si bandgap; (ii) even though UV light generates carriers inside the poly-Si films, these carriers cannot contribute usefully to the solar cell current, since they are blocked by the ultra-thin oxide layer; (iii) it is possible to detect hydrogen introduced in the passivating contact stacks by analysing the PL emission from its partial amorphous phase.

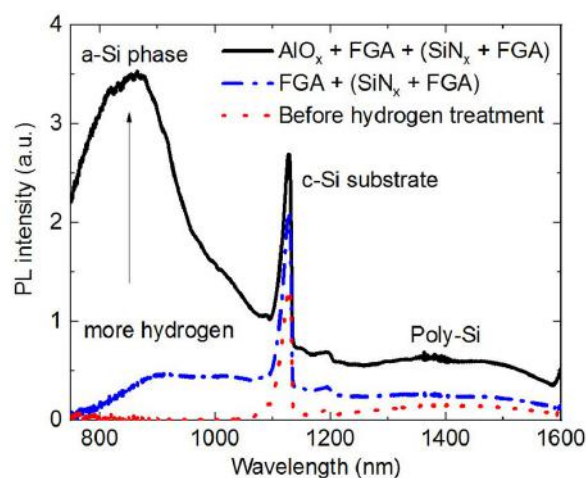


Figure 6.65.1: Various components inside poly-Si films emit different luminescence peaks at 80K. The luminescence peak from the a-Si phase in poly-Si films indicates the effectiveness of various hydrogen treatments.

Particularly, the team has developed a luminescence-based method to quickly track hydrogen content inside the poly-Si films. The technique relies on various photoluminescence (PL) features from doped poly-Si films and their mixed-phase nature (amorphous and crystalline). After high temperature diffusion processes to form the doped poly-Si films, most of the hydrogen content has effused out of the films, leaving the film un-hydrogenated. Un-hydrogenated amorphous Si (a-Si) contains a very high density of non-radiative defects, yielding no PL signal. Once hydrogenated, the a-Si:H phase will emit a strong PL peak in which the intensity is proportional to the hydrogen content inside the films. Tracking the a-Si:H PL emission, the team can study the effectiveness and mechanisms of various hydrogenation techniques on different poly-Si films. The method and its various applications have been reported in a series of four journal papers (Nguyen 2018; Truong et al. 2019a, b and c).

Highlights

- Poly-Si films contain both amorphous and crystalline phases, each of which yields distinct luminescence peaks at low temperatures.
- The luminescence signatures can be used to understand the behaviour of poly-Si/SiO_x passivating contacts in terms of carrier recombination and transport.
- Luminescence from the amorphous Si phase in poly-Si films can be used to track the hydrogen content inside the films.
- Four journal papers (Nguyen 2018; Truong et al. 2019 a, b and c) and four conference oral presentations (Nguyen 2019a, b and c; Truong 2019).
- Fh-ISE support (AUS\$60K in-kind plus equipment access) for Dr Nguyen's ACAP Fellowship Round 3.

Future Work

- The team will refine their techniques and apply their findings to support high efficiency silicon solar cell teams at ANU and UNSW. In addition, the team will continue exploring luminescence properties of different poly-Si film technologies and their evolution after different hydrogen treatments.

References

NGUYEN, H. T. 2019a. Luminescence from poly-Si films and its applications in Si PV. 46th IEEE Photovoltaic Specialists Conference, Chicago, June 2019.

NGUYEN, H. T. 2019b. Luminescence from poly-Si films and its applications in Si PV. 29th International Photovoltaic Science and Engineering Conference, Xi'an, November 2019.

NGUYEN, H. T. 2019c. Luminescence from poly-Si films and its applications in Si PV. 6th Asia-Pacific Solar Research Conference, Canberra, December 2019.

NGUYEN, H. T., LIU, A. Y., YAN, D., GUTHREY, H., TRUONG, T. N., TEBYETEKERWA, M., LI, Z. Y., LI, Z. F., AL-JASSIM, M. M., CUEVAS, A. & MACDONALD, D. 2018. Sub-Bandgap Luminescence from Doped Polycrystalline and Amorphous Silicon Films and Its Application to Understanding Passivating-Contact Solar Cells. *Acs Applied Energy Materials*, 1, 6619-6625.

TRUONG, T. N. 2019. Effects of hydrogenation on poly-Si/SiO_x passivating contacts for silicon solar cells. 6th Asia-Pacific Solar Research Conference, Canberra, 3–5 December 2019.

TRUONG, T. N., YAN, D., CHEN, W. H., TEBYETEKERWA, M., YOUNG, M., AL-JASSIM, M., CUEVAS, A., MACDONALD, D. & NGUYEN, H. T. 2019b. Hydrogenation Mechanisms of Poly-Si/SiO_x Passivating Contacts by Different Capping Layers. *Solar RRL*. DOI: 10.1002/solr.201900476

TRUONG, T. N., YAN, D., SAMUNDSETT, C., BASNET, R., TEBYETEKERWA, M., LI, L., KRERNER, F., CUEVAS, A., MACDONALD, D. & NGUYEN, H. T. 2019a. Hydrogenation of Phosphorus-Doped Polycrystalline Silicon Films for Passivating Contact Solar Cells. *ACS Applied Materials & Interfaces*, 11, 5554-5560.

TRUONG, T. N., YAN, D., SAMUNDSETT, C., LIU, A. Y., HARVEY, S. P., YOUNG, M., DING, Z. T., TEBYETEKERWA, M., KREMER, F., AL-JASSIM, M., CUEVAS, A., MACDONALD, D. & NGUYEN, H. T. 2019c. Hydrogen-Assisted Defect-Engineering of Doped Poly-Si Films for Passivating Contact Solar Cells. *ACS Applied Energy Materials*, 2, 8783-8791.

6.66 SILICON DEVICES FOR III-V TANDEM

Lead Partner

ANU

ANU Team

Matthew Stocks, Teng Kho

Academic Partner

SERIS: Armin Aberle

Funding Support

ARENA

Aims

- Evaluate if excellent in situ SiO_x- low pressure chemical vapor deposition (LPCVD) polysilicon passivation demonstrated at ANU can be replicated on textured surfaces.
- Examine opportunity for tunnel junctions formed from polysilicon.
- Manufacture polysilicon-based silicon devices as bottom cells for tandems, particularly four-terminal GaAs devices.

Progress

The choice of a silicon bottom cell for tandem applications has often been a device originally designed to deliver high efficiency under the full AM1.5G spectrum, as was the case for ANU's 26% and 27% perovskite/silicon tandem. Optimal cell design is a compromise between recombination, resistive and optical losses. A broad range of cell bandgaps work well with silicon (Stocks 2016). The bandgap for GaAs is 1.4 eV and, consequently, the silicon bottom cell only receives infrared light. A high contribution to tandem efficiency therefore relies primarily on high voltage and effective infrared absorption. This project is exploring the potential of polysilicon to enable an IR responsive Si bottom cell.

Progress on this project has been significantly impacted by equipment and facilities failures. A fire in the silane line of the polysilicon LPCVD tube at ANU led to the tube being down for the first half of 2019. Significant time was then required to replicate previous passivation results due to contamination which prevented effective analysis of passivation quality due to very low lifetime for several months. While not strictly in the reporting period, it should be noted that a storm in January has damaged the supporting facilities and it is unclear how long it will take to replace the damaged scrubber, given restrictions on China imports.

Some promising progress was made on polysilicon development, however. The in situ oxide that was used in early ANU studies (Fong 2018) was replaced with a chemically grown oxide. This comprised immersing the wafer in nitric acid at 90–100°C. Figure 6.66.1 shows the passivation quality as a function of chemical oxide growth duration. Oxide process times of 30 and 35 minutes demonstrated comparable J_{OS} (4fA) and effective lifetime (>10 ms) as the in situ grown oxide.

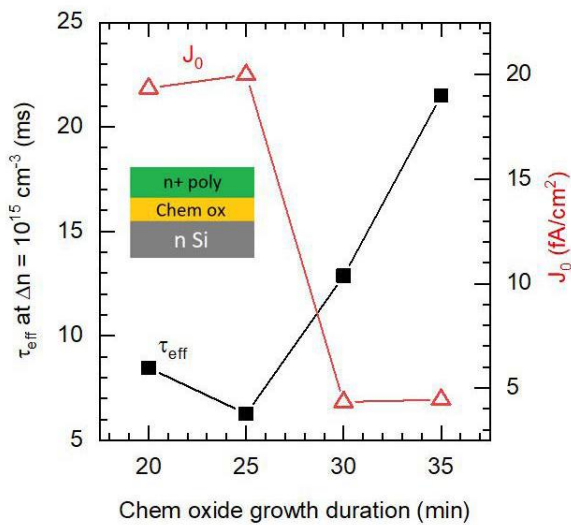


Figure 6.66.1: Measurement of effective lifetime and J_0 for different chemical oxide thicknesses on 100 Ω .cm n-type wafer.

Explorations then progressed to looking at polysilicon tunnel junctions for the front surface of devices. A preliminary result of an n+p+ polysilicon recombination junction achieved contact resistivity of 61 m Ω .cm². This measurement was determined from the Cox and Strack method as shown in Figure 6.66.2. This would result in only 1 mV resistive drop in a bottom cell configuration. Passivation quality was much poorer (93fA) than the n+ polysilicon result shown earlier. The stack will be explored further to see if lower results can be achieved.

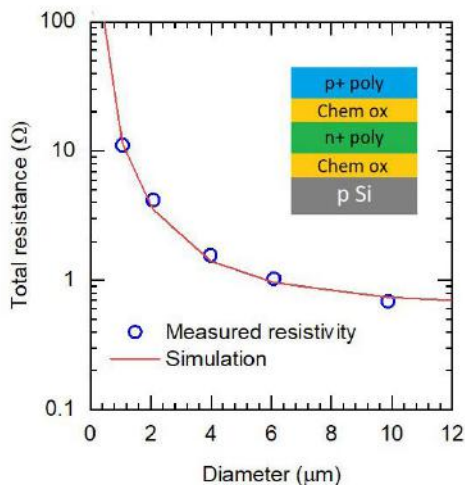


Figure 6.66.2: Preliminary results of an n+p+ polysilicon recombination junction that achieved contact resistivity.

During the remainder of the project we aim to further explore the chemical passivation of polysilicon on textured surfaces and implement the findings in a tandem bottom cell for integration with SERIS GaAs cells.

Highlights

- Very low surface recombination rates of polysilicon with chemical oxides.
- Demonstration that a p+/n+ polysilicon tunnel junction could be formed with acceptable contact resistance.

References

FONG, K. C., KHO, T. C., LIANG, W., CHONG, T. K., ERNST, M., WATER, D., STOCKS, M., FRANKLIN, E., MCINTOSH, K. & BLAKERS, A. 2018. Phosphorus diffused LPCVD polysilicon passivated contacts with in-situ low pressure oxidation. *Solar Energy Materials and Solar Cells*, 186, 236-242. DOI:10.1016/j.solmat.2018.06.039.

STOCKS, M., LOO, Y. & LAL, N. 2016. Free the Bandgap! Series-Parallel Connection of Tandem Cells. 32nd European Photovoltaic Solar Energy Conference, Munich, 20–24 June 2016, 223-227. DOI:10.4229/EUPVSEC20162016-1BV.6.12.

6.67 SINGLET FISSION ENHANCED SOLAR CELLS

Lead Partner

UoM

UoM Team

Dr David Jones, Dr Jegadesan Subbiah

Academic Partner

KIT (Germany): Dr Alexander Colsmann, Mr Lorenz Graf von Reventlow

Funding Support

AUSIAPV, UoM, KIT

Aims

- Scale up synthesis of high performance FHBC(TDPP)₂ singlet fission (SF) material.
- Demonstrate EQE enhancement in solar cell devices (QD).
- Identify SF material energy matched to silicon.
- One patent or publication.

Progress

Multiple exciton generation (MEG) in organic semiconductors through singlet fission (SF) is a process that produces multiple charge-carrier pairs from a single excitation. MEG is a viable route to overcome the Shockley-Queisser limit in single-junction solar cells, and hence to enhance their performance to generate third generation solar cells. Therefore, any proof of principle of this concept has the potential to substantially change the field of solar energy harvesting. Yet, as of today, it remains challenging to harvest charge carrier pairs generated by MEG in working photovoltaic devices. Initial yields of additional carrier pairs may be reduced due to ultrafast intra-band relaxation processes that compete with MEG at early times. We have recently developed a new class of SF materials based on an acceptor-donor-acceptor (A-D-A) design to promote intra-molecular SF. We designed these materials to remove local order constraints normally required for molecular SF materials, like acenes, and have designed materials that are solution processible, promote SF in the solid state, and surprisingly show little order in spin-cast thin films. The key aim of this project is to understand this new material and its behaviour in devices, especially routes to charge extraction.

A research assistant was employed to complete a large-scale synthesis of the FHBC(TDPP)₂, our published singlet fission material, Figure 6.67.1. The synthesis of FHBC(TDPP)₂ was completed on a 2 gram scale to provide sufficient material for all the required device optimisation and later translation to larger scale optimisation of devices. This material has now been distributed to our collaboration partners at KIT. In addition, significant quantities of key synthetic intermediates have been synthesised to allow access to new materials better matched with silicon for future studies.

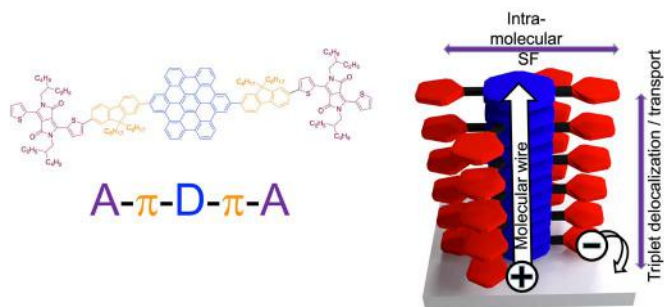
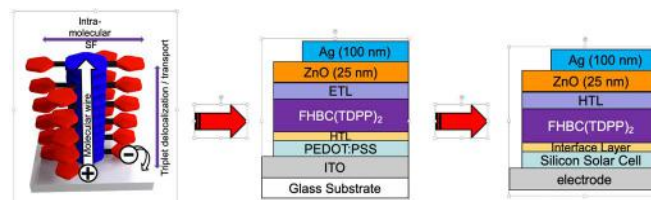


Figure 6.67.1: Self-assembly of intra-molecular A-D-A singlet-fission (SF) FHBC(TDPP)₂ allows control of SF in one direction, triplet delocalisation and transport in a second, and after charge separation at an interface generation of molecular wires.

Definitive proof for enhanced efficiency due to SF is to record EQEs above 100%, which has rarely been achieved in the literature. It is possible to incorporate SF materials into devices either through direct electrical connection or through energy transfer. Direct electrical connection is predicted to give higher overall efficiencies. We have chosen to investigate homojunction solar cells, where we use only the SF material, in the first instance in anticipation of inclusion through direct electrical contact with silicon to gain a better understanding of the SF material properties, and a direct measurement of the EQE from the SF material. The device architecture used is shown in Figure 6.67.2. The challenge in direct electrical connection is to promote charge separation from the triplet energy level, rather than the singlet energy level. Surprisingly our initial devices were functional, however at only low PCE. We are currently examining electron transfer layers (ETL) and their impact on charge generation and collection, and V_{oc} .



(a) SF Self-Assembly (b) Homojunction (c) SF enhanced silicon

Figure 6.67.2: The self-assembly and preferred orientation of FHBC(TDPP)₂ (a) leads to simplified device design with basic materials and spectroscopic properties studied in a homojunction (b) before translation to an SF enhanced solar cell architecture (c).

Highlights

- The key organic SF material FHBC(TDPP)₂ has been synthesised at scale (2 grams) for the device screening program.
- Fundamental studies on FHBC(TDPP)₂ have been initiated in conjunction with KIT.
- Results from homojunction solar cells indicate working devices, however as expected no evidence of significant extraction of charges from the triplet energy level.
- Dr Alexander Colsmann (KIT) spent two weeks in Australia for discussions and was a keynote speaker at the ACAP conference in December 2019.

Future Work

- Complete full analysis of FHBC(TDPP)₂ material properties, so that the next generation of material can be designed.
- Fundamental studies on FHBC(TDPP)₂ directed material design for silicon compatible materials.
- Optimise homojunction solar cells to demonstrate EQEs of greater than 100%.
- Assemble SF enhanced solar cell devices.

References

MASOOMI-GODARZI, S., LIU, M., TACHIBANA, Y., MITCHELL, V. D., GOERIGK, L., GHIGGINO, K. P., SMITH, T. A. & JONES, D. J. 2019. Liquid Crystallinity as a Self-Assembly Motif for High-Efficiency, Solution-Processed, Solid-State Singlet Fission Materials. *Advanced Energy Materials*, 9(31), 1901069.

6.68 ORGANIC ELECTRON TRANSPORT LAYER TOWARDS UPSCALING OF HIGH EFFICIENCY PEROVSKITE SOLAR CELLS

Lead Partner

CSIRO

CSIRO Team

Dr Dechan Angmo, Dr Doojin Vak, Dr Andrew Scully

Academic Partner

Chinese Academy of Sciences (CAS), Beijing: Prof. Jinhui Hou
University of Cambridge, UK: Dr Samuel Stranks

Funding Support

ARENA, CSIRO, University of Cambridge, Chinese Academy of Science.

Aims

1. To investigate indacenodithiophene (IDT) -based molecules to find optimum electronic properties suitable for printed stable perovskites.
2. To investigate IDT-based molecules targeted as a printable electron transport layer (ETL) for PSCs.
3. To conduct comprehensive fundamental characterisation of films and interfaces fabricated by scalable and roll-to-roll (R2R)/sheet-to-sheet compatible printing/coating techniques under ambient conditions using cutting-edge spectroscopic methods

Progress

The project commenced on 1 July 1 2019. A Research Internship position was advertised in Australia through various networks and abroad through CSIRO's Internship program. After failing to recruit Australian students, we received over ten overseas applications through CSIRO's internship programs in France and Switzerland. A student from École Centrale de Marseille, France, was selected. He will join the project at the beginning of March 2020.

Meanwhile, we worked on the fabrication of control devices in the ambient environment and finding a more robust scalable method for the deposition of mixed cation perovskite. Progress includes:

Benchmarking lab-cells

We optimised formulation and processing conditions for the fabrication of a stable mixed cation perovskite formulation under an ambient environment with a spin-coating method. Most laboratory cells are fabricated in a glovebox with oxygen and humidity levels of less than one part per million. However, maintaining such a glovebox-like environment in continuous R2R processing is not only costly but also technically impractical. Thus, a true benchmark for R2R devices is an ambient-processed laboratory cell. However, processing of cells under an ambient environment requires re-optimisation and often complete reconfiguration of materials and their processing than widely reported in the literature.

We fabricated laboratory cells with spin-coating under an ambient environment using the “anti-solvent” method of enabling uniform perovskite film (Xiao et al. 2014; Jeon et al. 2014). We found the commonly reported anti-solvents, such as toluene and chlorobenzene, generate porous perovskite films under an ambient fabrication environment as moisture interferes in the crystallisation process (Angmo et al. 2019). After optimisation, we found ethyl acetate is best at generating uniform films in an ambient environment.

We fabricated devices in the p-i-n structure (Glass/ITO/PEDOT:PSS/MA_{0.61}FA_{0.37}Cs_{0.02}PbI_{2.88}Br_{0.025}/PCBM/PEIE/Au). We chose this structure because it enables superior stability even when all functional layers, except the electrodes, are solution-processed and annealed at or below 140°C. Thus, the process is compatible with R2R fabrication on low-cost polyethylene substrates that can only withstand up to 150°C. Additionally, we adopted the one-step process as this approach allows precise control of the complex perovskite compositions. The best performing device gave a power conversion efficiency (PCE) of >15% (Figure 6.68.1(c)). This efficiency sets the laboratory benchmark performance against devices with IDT-based ETL materials, and printed perovskite solar cells can be assessed.

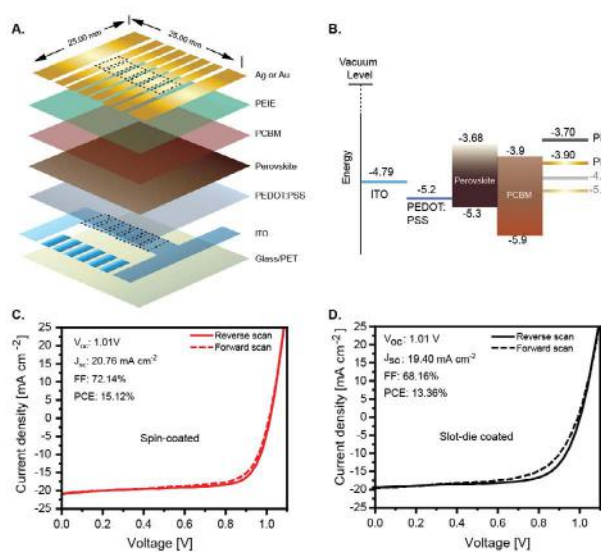


Figure 6.68.1: (a,b) Schematic illustrations of the device structure and the corresponding energy level alignment. (c,d) J-V curves of the spin-coated and slot-die coated solar cells measured under standard one-sun condition (100 mW cm⁻², AM 1.5G).

R2R compatible scalable fabrication method for perovskite films

Slot-die coating, a scalable R2R compatible deposition method, was employed to deposit perovskite films on glass substrates using a benchtop coater. If successful, this method can be directly transferred to large-scale R2R processing. The common laboratory methods of inducing uniform pinhole-free perovskite films by dropping anti-solvent or blowing nitrogen-gas immediately after the deposition of perovskite solution are highly challenging to produce consistent film quality in continuous R2R manufacturing especially with mixed cation perovskite formulations fabricated in a one-step deposition. Thus, we evaluated a simplified method whereby we slot-die coated perovskite solution on a heated substrate above 100°C. Perovskite solar cells fabricated with

this approach led to a maximum PCE of over 13.5% (Figure 6.68.1(d)) – which is within 10% of the spin-coated lab cells.

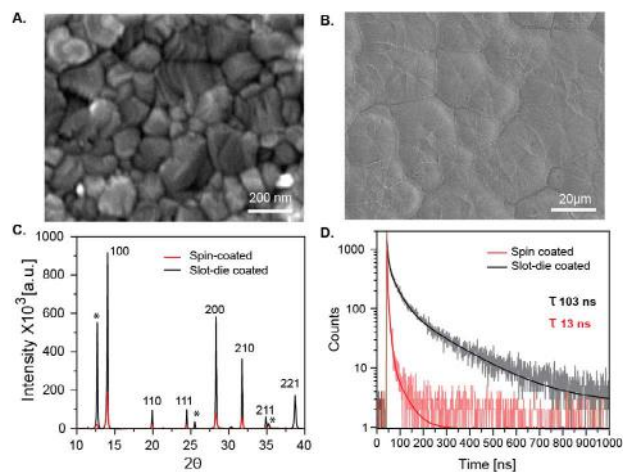


Figure 6.68.2: (a,b) SEM image of spin-coated and slot-die coated perovskite films, respectively. (c,d) J-V curves of the spin-coated and slot-die coated solar cells measured under standard one-sun conditions (100 mW cm⁻², AM 1.5G), respectively.

Characterisation

We carried out characterisation of the perovskite films and cells to understand the loss in performance of the slot-die coated perovskite and to strategise future approaches for improving device performance. Scanning electron microscopy (SEM) images revealed contrasting morphology of the spin-coated and the slot-die coated perovskite films (Figure 6.68.2(a,b)). Spin-coating with the anti-solvent method leads to nucleation-driven films, as evident in the presence of dense nano-sized grains. On the other hand, slot-die coating of a perovskite solution on heated substrates led to crystal growth-driven perovskite film formation, evidenced by the presence of micron-sized clusters of >20 μm diameter. Despite the stark morphological difference, X-ray diffraction (XRD) revealed both types of films possessed the same cubic phase perovskite structure. An XRD pattern also showed the overall crystallinity of slot-die coated films was significantly higher than the spin-coated film, further attesting to the growth-driven film formation with slot-die coating on heated substrate. The long-range crystallinity of the slot-die coated film leads to an improved charge-carrier lifetime, which is an order of magnitude higher compared to spin-coated perovskite films (Figure 6.68.2(c)). The bandgaps extracted from photoluminescence (PL) spectra showed both spin-coated and slot-die coated films had similar values of 1.61 eV and 1.62 eV, respectively. Photoelectron spectroscopy in air (PESA) measurements also revealed similar ionisation potential of 5.30 and 5.28 eV, for spin-coated and slot-die coated films, respectively. Therefore, the mechanism for producing the perovskite films did not influence the electronic properties of the perovskite films. On the contrary, the carrier lifetime measurement suggests the slot-die coated films should be significantly better than the spin-coated films (Figure 6.68.2(d)).

Thus, the loss in PCE of slot-die coated films, albeit less than 10%, could arise from recombination losses due to bulk and surface defects, as evident in slightly lower fill factor (FF) and generally lower current density (J_{sc}) than spin-coated films. SEM images revealed pin-holes at the surface of the slot-die coated films (Figure 6.68.3). These defects could arise due to film fabrication in an ambient environment, as moisture can selectively withdraw organic cations and solvent molecules during film formation. We confirmed that the location of the pin-holes was only on the surface and not through the bulk by conducting dark J-V measurement and measuring shunt resistance (R_{sh}) and series resistance (R_s). No leakage current was detected, while both R_{sh} and R_s values were very identical for both spin-coated and slot-die coated cells. We found a spherulitic feature embedded in each micro-cluster in the slot-die coated films (Figure 6.68.3(b)). Numerous imaging methods (electroluminescence imaging, dark field optical imaging, PL imaging, fluorescence microscopy, etc) showed these features trap charges and do not contribute to current production (Figure 6.68.3(c)). This observation explains why slot-die coated cells generally have a lower current than the spin-coated cells.

Furthermore, these spherulitic features have a lower bandgap than the bulk of the cluster, indicating phase-separation into iodide rich regions. Thus, the performance of slot-die coated films could be improved if the phase-separated region could be retarded or eliminated. We are currently preparing a manuscript to communicate the results thus far.

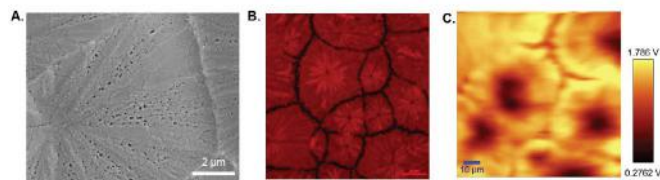


Figure 6.68.3: (a) SEM image of slot-die coated perovskite films shows surface defects. (b) Fluorescence imaging shows spherulitic islands embedded in the micro-sized clusters in the slot-die perovskite films. (c) Current mapping of the slot-die coated film shows the spherulitic islands do not produce current.

Highlights

- Reference lab cells with mixed cation composition were successfully fabricated in an ambient environment with spin-coating, and a PCE of 15.12% was achieved.
- Slot-die coating of mixed cation perovskite in an ambient environment was optimised and a PCE of 13.30% was achieved.
- Microstructural and optoelectronic characterisation were carried out to understand device performance and to strategise the future approach for increasing device performance.
- Part of the research results was presented at the Asia-Pacific Solar Research Conference (APSRC), held in Canberra on 3–5 December 2019.

Future work

- With benchmark spin-coated devices and slot-die coated devices completed, we will now explore IDT-based molecules as ETL.
- We will test a range of buffer layers with the best IDT-based molecules and study defect passivation methods for slot-die coated films and cells.
- The University of Cambridge will characterise printed films and devices.
- Manuscript preparation.
- Conference attendance.

References

- ANGMO, D., PENG, X., SEEBER, A., ZUO, C., GAO, M., HOU, Q., YUAN, J., ZHANG, Q., CHENG, Y.B. & VAK, D., 2019. Controlling Homogenous Spherulitic Crystallization for High-Efficiency Planar Perovskite Solar Cells Fabricated under Ambient High-Humidity Conditions. *Small*, 15, 1904422.
- JEON, N.J., NOH, J.H., KIM, Y.C., YANG, W.S., RYU, S. & SEOK, S.I., 2014. Solvent engineering for high-performance inorganic-organic hybrid perovskite solar cells. *Nature materials*, 13, 897-903.
- NIE, W., TSAI, H., ASADPOUR, R., BLANCON, J.C., NEUKIRCH, A.J., GUPTA, G., CROCHET, J.J., CHHOWALLA, M., TRETIAK, S., ALAM, M.A. & WANG, H.L., 2015. High-efficiency solution-processed perovskite solar cells with millimeter-scale grains. *Science*, 347, 522-525.
- XIAO, M., HUANG, F., HUANG, W., DKHISSI, Y., ZHU, Y. ETHERIDGE, J., BACH, U., CHENG, Y.B., & SPICCIA, L. 2014. A Fast Deposition-Crystallization Procedure for Highly Efficient Lead Iodide Perovskite Thin-Film Solar Cells. *Angew. Chem.*, 126, 10056-10061.

FELLOWSHIPS

ACAP's competitively selected Fellowships, are reported online at <http://www.acap.net.au/annual-reports>.

F1 TECHNO-ECONOMIC ANALYSIS OF PHOTOVOLTAIC CELL AND MODULE FABRICATION TECHNOLOGIES

Lead Partner

UNSW

UNSW Team

Dr Nathan L. Chang, Prof. Renate Egan

Funding Support

ACAP Fellowship

Aims

This Fellowship has two broad aims. The first is to focus on individual technologies that are being developed, and to apply techno-economic analysis with the expectation that insightful understanding will be obtained of the technology's particular strengths and weaknesses.

The second is to develop and improve the innovative cost analysis methodology so that it is able to analyse each successive technology with greater effectiveness.

This Fellowship has its primary focus on contributing to ACAP's PP4 Manufacturing Issues, and this report should be read in conjunction with the PP4 report.

Progress

A. The ACAP cost analysis method and its role in technology development

At the 2019 Asia-Pacific Solar Research Conference, Canberra, an invited oral presentation was given to the ACAP stream, entitled "Techno-economic analysis – WHAT is it, WHY is it important, and HOW to do it?". This presentation aimed to clarify and emphasise the importance of techno-economic analysis (TEA) among ACAP and other PV researchers. Some of the key ideas from this presentation are outlined here.

Motivation for techno-economic analysis

Techno-economic analysis (TEA) considers the financial costs and financial benefits of a technology as a way to assess its commercial viability. Costs typically are those required for manufacturing (equipment investment costs, materials, labour, electricity, etc), and benefits typically include those that impact market price (performance/efficiency, market value, competition, market size, etc). Some non-financial concerns (for example environmental costs or social impacts) can be included in the financial analysis using methods such as carbon pricing. Such an assessment may be conducted on the current state of the technology, and/or the projected future state of the technology once certain technical changes are implemented. The outcomes of these assessments can help in the following ways.

i) Motivating further investment: A favourable assessment of the "current" state of the technology can motivate industry investment in commercial trials, since the technology already has a positive commercial value; while a favourable assessment of the "future" state of the technology motivates further research and development of the technology, since the technology has potential once the technical changes are achieved.

ii) Informing researchers of the key drivers of both cost and value so that they can focus their resources to improve the technology with maximum leverage – for example focusing on reducing or replacing a dominant cost component.

These two objectives can be seen by researchers as being in conflict with each other. To motivate further investment, it is ideal to paint a technology in the best possible light. This means assuming the best performance and estimating the cost of the cheapest process – even if the best performance can only be achieved with the higher cost process. However, to identify the key cost issues impacting commercial viability, it is best to analyse the "real" state of the technology as it has been demonstrated in the lab – since the results reflect the real issues that must be solved in order for the technology to become commercially viable. In this Fellowship, the aim is to keep both objectives in mind, although the focus may lean more towards one or the other depending on the circumstances.

Difficulty of conducting techno-economic analysis

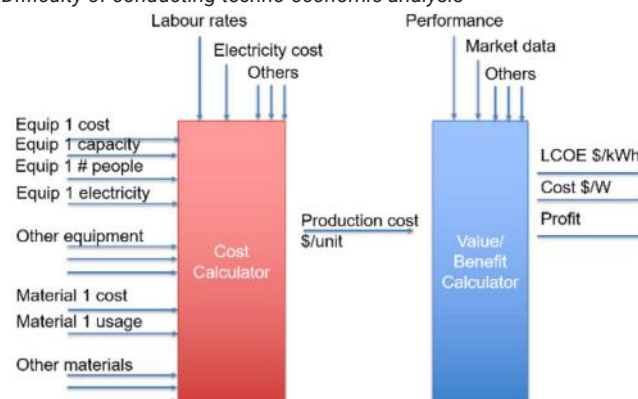


Figure F1.1: A representation of a techno-economic analysis methodology.

A commonly used cost analysis method is used to define a process sequence and estimate its cost using a bottom-up calculator with the best available input data, as shown in Figure F1.1. Typically, analysis as represented by the red cost calculator can be done to calculate the cost of producing each unit (such as \$/cell, \$/module or \$/m²), and then further analysis as represented by the blue value/benefit calculator (which includes performance and market data) can be used to analyse other metrics such as the cost in \$/W or the levelised cost of electricity (LCOE).

Such an approach is most appropriate when a technology is at a high technology readiness level (TRL), and the input data is relatively easy to obtain with high accuracy. However, if some or all of the inputs are difficult to obtain at high accuracy (for example the cost of materials when being purchased in large batch sizes for high volume

production), it becomes very hard to define each input number. This inaccuracy is almost always present for lower TRL technologies. As a result, those who do not believe the accuracy of the inputs may reject the conclusions of such analyses.

Methods used in this Fellowship

The cost analysis methodology used in this research has been developed (Chang 2017; Chang 2018) in particular to address a key problem facing early-stage technology development – how to conduct a commercial assessment of these technologies when there are so many uncertainties about the process, production equipment, materials and market value.

The underlying cost calculator is similar to that shown in Figure F1.1. The difference is that instead of a single number for each input, an uncertainty range is used. For every cost parameter, a “Nominal”, “High” an “Low” value is determined from the available data, and from this an uncertainty distribution is generated, as illustrated by example in Figure F1.2.

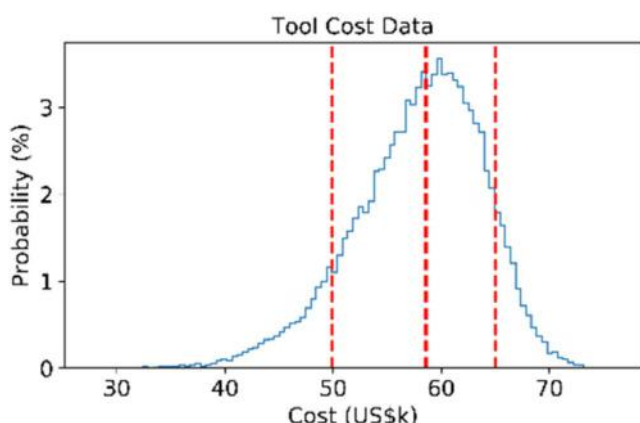


Figure F1.2: An example of input uncertainty distribution.

The cost calculator combines the uncertainties of all the inputs using a Monte Carlo methodology, where typically 50,000 iterations are calculated. The output of this is a histogram of costs rather than a single cost number, for example as shown in Figure F1.3

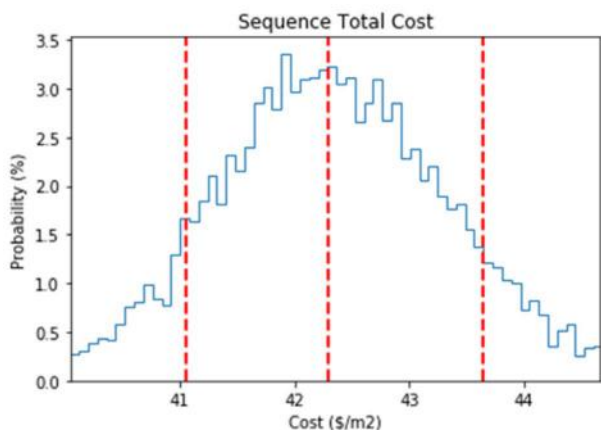


Figure F1.3: An example of cost output distribution.

Because of the large number of iterations used in the Monte Carlo analysis, data analysis methods can be used to explore the complex relationship between the various input parameters and the cost/ value of each technology. Many examples of insights from such analyses are described in the PP4 report, where results from analyses completed in 2019 are shown.

This costing methodology can be used periodically as processes and knowledge develop. With each use, the key factors requiring research effort can be identified to focus development resources. As research progress is made, new issues become dominant and the research focus can shift. A healthy partnership between researchers and those conducting economic assessment should lead to a faster and more cost-effective commercialisation of technologies.

B. Specific technologies analysed

In 2019, the method was applied to a number of different PV cell and module technologies. Further detail on these analyses is provided in the accompanying PP4.1 report.

Most of the analyses focused on low TRL technologies, including (i) an updated analysis of perovskite/silicon tandem cells, (ii) colloidal quantum dot solar cells and (iii) III-V/silicon tandem cells. These analyses were conducted primarily on the \$/m² metric, and are described in PP4.1, sections B, C and D.

As part of the tandem cell analysis, some exploration of the interaction between increased efficiency and cost were explored in the context of the LCOE, with limits of efficiency and cost that must be combined to improve the cost of electricity to the end user. This is shown in Figure F1.4. This figure helps technologists to understand the trade-off between cost and efficiency for a technology to compete in the market.

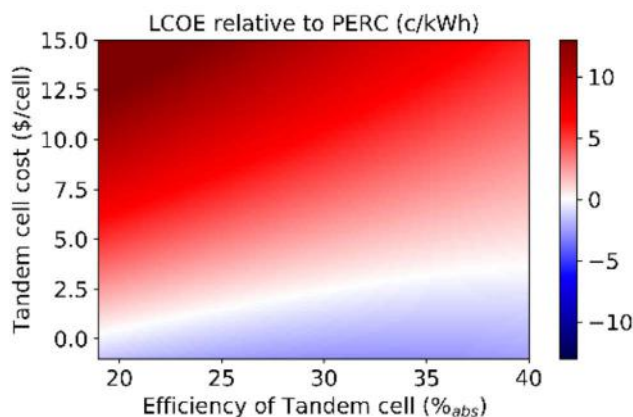


Figure F1.4: Output from an LCOE model comparing improved efficiency of a tandem cell with total tandem cell cost and the impact on LCOE. Blue represents areas where the tandem cell has an improved LCOE compared to a standard PERC cell.

The manufacturing cost of established technologies does not require the uncertainty methods used in this Fellowship, since the manufacturing cost data is known to manufacturers to a high level of accuracy. However, projections of future cost are subject to uncertainty and can benefit from the use of this uncertainty

model. Such an analysis is described in PP4.1 section E, where in a collaboration with TNO, Netherlands, the 5-year future projection of c-Si module costs is estimated using a bottom-up cost model and defining uncertainty ranges for all cost inputs based on historical data and reasonable future projections.

Finally, the uncertainty model has been expanded further to consider the application of PV technology within a larger system – that of a green hydrogen generation using PV-driven electrolysis. In collaboration with the School of Chemical Engineering at UNSW, a model was built that includes real-world PV generation from weather files, uncertain costs of the PV system, the electrolysis system, and uncertainty in other financial parameters. The levelised cost of hydrogen (LCOH) was generated from this, as described in more detail in PP4.1 section F.

Highlights

- Wide dissemination in the PV research community of techno-economic analysis methods and their benefits.
- Techno-economic analysis of a wide variety of PV technologies at different TRLs.
- Expansion of the methods to consider future uncertainty.
- Application of the methods to a related application of the generation of green hydrogen using PV-driven electrolysis.
- Collaboration with a variety of institutions in Australia and internationally.

Future Work

- Analysis of additional PV technologies and processes.
- Development of the methodology as required for new analyses.
- Continuing dissemination of the methods via collaboration and the creating of tools to enable effective collaboration.

References

CHANG, N. L., HO-BAILLIE, A. W. Y., BASORE, P. A., YOUNG, T. L., EVANS, R. & EGAN, R. J. 2017. A manufacturing cost estimation method with uncertainty analysis and its application to perovskite on glass photovoltaic modules. *Progress in Photovoltaics*, 25, 390-405.

CHANG, N. L., HO-BAILLIE, A., WENHAM, S., WOODHOUSE, M., EVANS, R., TJAHJONO, B., QI, F., CHONG, C. M. & EGAN, R. J. 2018. A techno-economic analysis method for guiding research and investment directions for c-Si photovoltaics and its application to Al-BSF, PERC, LDSE and advanced hydrogenation. *Sustainable Energy & Fuels*, 2, 1007-1019.

F2 DEVELOPMENT OF PRACTICAL HIGH EFFICIENCY PEROVSKITE-SILICON TANDEM MODULES

Lead Partner

ANU

ANU Team

Dr The Duong

Academic Partners

Peking University: A/Prof. Huanping Zhou

UNSW: A/Prof. Anita Wing Yi Ho-Baillie

Funding Support

ACAP

Aim

This project aims to develop complete and practical perovskite-silicon tandem modules in the mechanically stacked configuration with an efficiency of $\geq 25\%$ for a size $\geq 5 \text{ cm}^2$ and stability passing the damp heat test as described in the IEC-61646 standard.

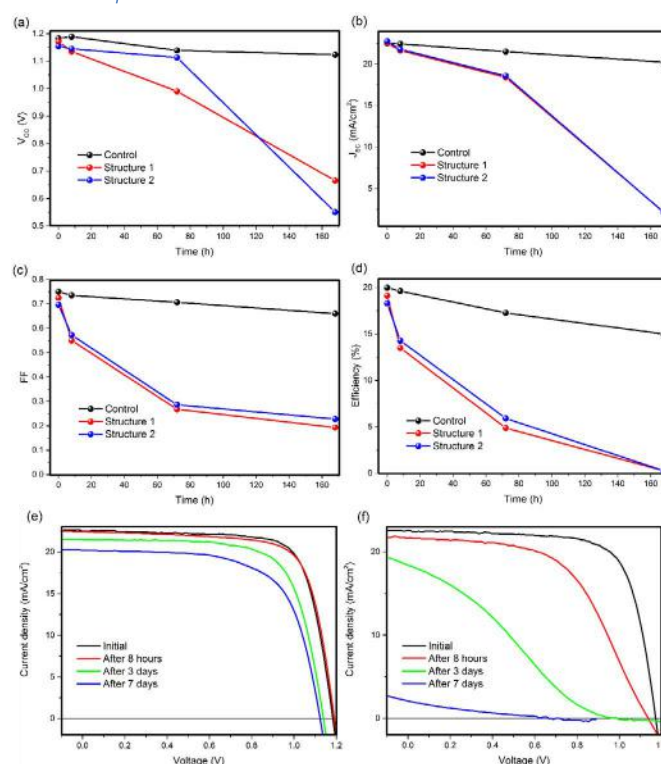
Progress

1. Investigating the impact of using MoO_3 interlayers on the ambient stability of semi-transparent perovskite solar cells

For perovskite top cells in tandem configurations, their contacts need to be semitransparent to allow infrared light to reach silicon bottom cells. Transparent conducting oxides (TCOs) such as indium-doped tin oxide (ITO), indium-doped zinc oxide (IZO) and aluminium-doped zinc oxide (AZO) are normally utilised in the semitransparent contacts due to their high transparency and good conductivity. However, those TCOs are typically deposited by magnetron sputtering with high energy ion bombardment which can damage the underlying charge transport layer and the active layer in perovskite solar cells (PSCs). As a result, an interlayer (or sputtering buffer layer) is required to prevent the sputter damage. The interlayer needs to have a high optical bandgap with low absorption, and most importantly, well-aligned energy levels with the charge transport layer for efficient carrier extraction. For inverted (p-i-n) PSCs, tin oxide (SnO_2) is normally used as the interlayer for semitransparent contacts to extract electrons, while MoO_3 is most commonly used as the interlayer at the hole extraction side of n-i-p structured PSCs. Environmental exposure to oxygen and moisture can have a significant impact on the electronic structure and surface properties of metal oxides. This is especially the case with MoO_3 as demonstrated by numerous reports, potentially leading to ambient stability issues in semitransparent PSCs. However, so far very few reports have investigated the stability of PSCs employing an MoO_3 interlayer in the presence of oxygen or moisture. Sanehira et al. reported that the ambient stability of PSCs is improved when an MoO_3/Al electrode is used instead of an Ag or Au electrode. However, the devices with MoO_3/Al electrodes still degraded severely under high relative humidity (RH $> 50\%$) which was ascribed to the degradation of the perovskite active layer (Sanehira 2016). In the present study, we investigated the impact of the MoO_3 interlayer on the stability of PSCs

in the presence of moisture and oxygen. As shown in Figure F2.1, we found that PSCs with MoO_3/Au or MoO_3/IZO electrodes degrade much more severely than devices with only an Au electrode under ambient exposure, while the degradation under oxygen exposure was comparably low.

Figure F2.1: (a–d) Monitoring of photovoltaic parameters of PSCs in three different structures in ambient environment. (e) Evolution of J-V curves of the control device during the ambient exposure. (f) Evolution of J-V curves of the device in Structure 1 during the ambient exposure.



Using photoelectron spectroscopy, we detect a substantial change in the electronic structure of MoO_3 upon ambient exposure, which creates a large carrier extraction barrier inside the device. The experimental results are supported by simulation using a Solar Cell Capacitance Simulator (SCAPS). The study emphasises the need for more robust interlayers for the fabrication of stable PSCs, especially for tandem application.

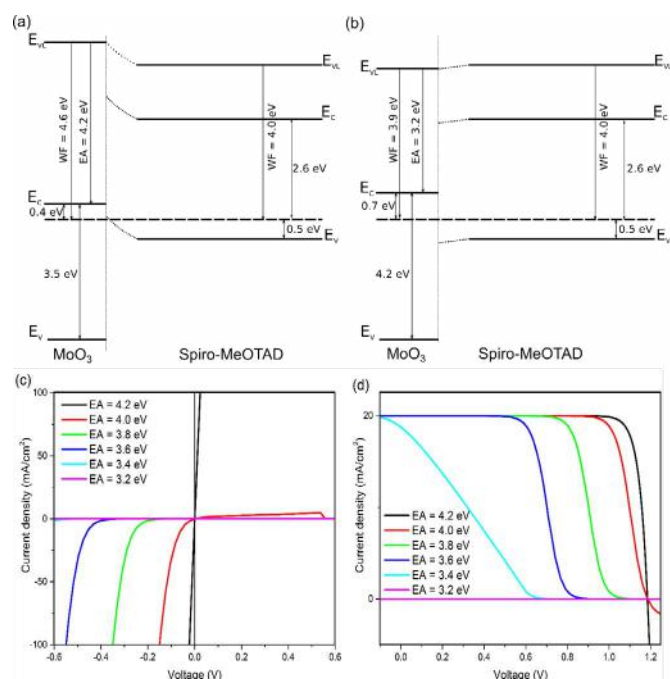


Figure F2.2: (a) Energy alignment at the fresh $\text{MoO}_3/\text{Spiro-MeOTAD}$ interface. (b) Energy alignment at the ambient exposed $\text{MoO}_3/\text{Spiro-MeOTAD}$ interface. (c) Simulated J-V curves of $\text{MoO}_3/\text{Spiro-MeOTAD}$ contact with different values of electron affinity (EA) of MoO_3 . (d) Simulated J-V curves of PSCs with Structure 1 with varied EA of the MoO_3 .

2. High efficiency four-terminal perovskite-silicon tandem

In order to further improve the efficiency of the four-terminal mechanically stacked perovskite-silicon tandem, we need to improve the efficiency of each sub-cell and/or improve the optical management of the design. We found that by coating the surface of quadruple-cation mixed halide perovskite with different aliphatic alkylammonium bulky cations, the 2D Ruddlesden-Popper perovskite phase with $n=2$ was formed which passivated the surface defects, changed the electronic structure at the surface of the 3D perovskite and resulted in better carrier lifetime and higher efficiency. In contrast, incorporating the aliphatic alkylammonium bulky cations into the bulk of the 3D perovskite negatively affected the crystallinity, induced the formation of the pure 2D perovskite with $n=1$, greatly changed the electronic structure of the 3D perovskite and finally led to lower device performance. As shown in Figure F2.1 and Table F2.1, using the surface coating strategy with *n*-butylammonium bromide cation, we fabricated semitransparent perovskite cells with an efficiency up to 17.1% and average transparency over 80% in the long wavelength region. When combined with IBC silicon cells, we achieved an efficiency of 27.7% in a four-terminal perovskite-silicon tandem. In addition, a tandem efficiency of 26.2% was attained when combining a 1 cm^2 semitransparent perovskite cell with a 1 cm^2 PERL silicon cell. The work paves the way for the development of high efficiency four-terminal perovskite-silicon tandems.

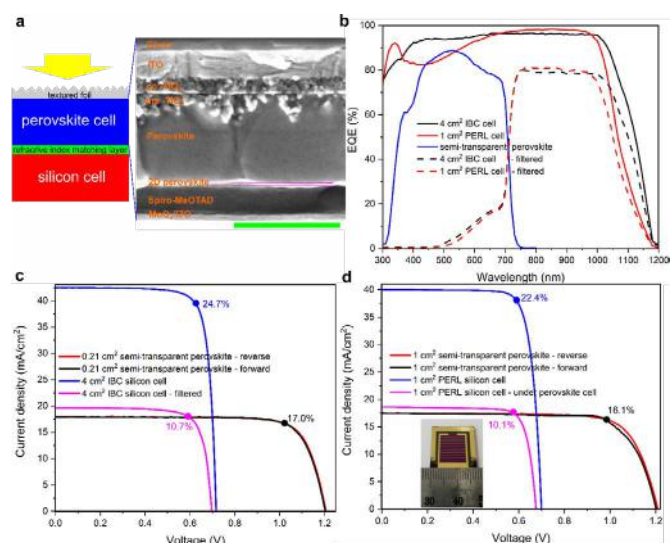


Figure F2.3: (a) Schematic showing the four-terminal perovskite-silicon tandem in the four-terminal tandem configuration and the cross-section SEM image of a semitransparent perovskite solar cell. The scale bar is 500 nm. (b) EQE of perovskite cell and silicon cells performing as stand-alone devices or under the perovskite cell. (c) J-V curves of perovskite-IBC silicon tandem. (d) J-V curves of perovskite-PERL silicon tandem.

Table F2.1: Summary of the efficiency of perovskite-silicon tandems.

Devices	Aperture [cm ²]	V _{oc} [V]	J _{sc} [mAcm ⁻²]	FF	Efficiency [%]
Semitransparent perovskite cell (reverse scan)	0.21	1.205	18.0	0.789	17.1
Semitransparent perovskite cell (forward scan)	0.21	1.202	18.0	0.785	17.0
Semitransparent perovskite cell (steady state)	0.21				17.0
IBC silicon cell	4	0.717	42.5	0.81	24.7
IBC silicon cell (filtered)	4	0.697	19.6	0.78	10.7
Calculated four-terminal perovskite-IBC silicon tandem					27.7
Semitransparent perovskite cell (reverse scan)	1	1.205	17.5	0.763	16.1
Semitransparent perovskite cell (forward scan)	1	1.2	17.5	0.763	16.1
Semitransparent perovskite cell (steady state)	1				16.1
PERL silicon cell	1	0.699	40.1	0.801	22.4
PERL silicon cell (under perovskite cell)	1	0.675	18.6	0.804	10.1
Four-terminal perovskite-PERL silicon tandem	1				26.2

We carried out a light stability test of an encapsulated four-terminal perovskite-silicon tandem solar cell for 5 day/night cycles (12 hours under light and 12 hours in the dark for each cycle). The perovskite cell and silicon cell were held at fixed voltages close to their maximum power points and J-V curves were recorded every hour. We found that in each cycle, after 12 hours operating under light, the efficiency of the semitransparent perovskite top cell retained around 95% of the initial efficiency recorded at the start of the cycle. The efficiency then recovered to about 98–99% of the efficiency recorded at the start of the previous cycle after the cell stayed in the dark for 12 hours. After 5 day/night cycles, the efficiency of the semitransparent perovskite top cell retained 96% of the original efficiency. For the silicon bottom cell, the photocurrent was stable under light which indicated a negligible change in the absorption/transmission of the perovskite top cell. The overall four-terminal perovskite silicon tandem efficiency retained over 97% of the original efficiency after 5 day/night cycles (Figure F2.4). The result indicates that the four-terminal perovskite-silicon tandem solar cell is relatively stable under operating conditions, however more stability improvement is needed to achieve a fully robust device.

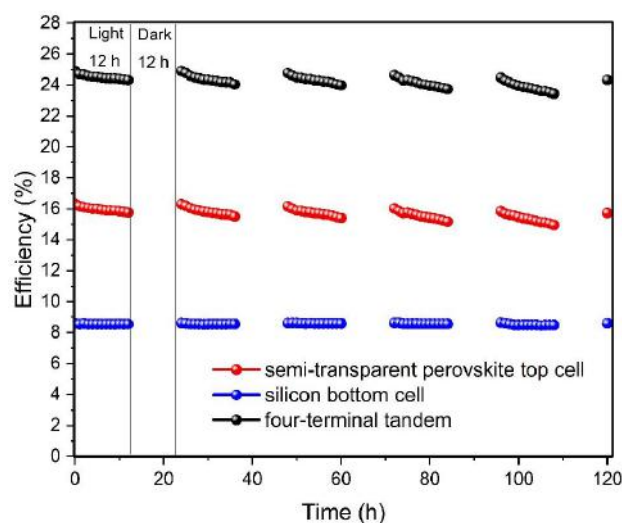


Figure F2.4: Stability of four-terminal perovskite-silicon tandem solar cell after 5 day/night cycles.

Highlights

- Discovered the negative impact of using MoO_x interlayer on the ambient stability of semitransparent perovskite solar cells. A manuscript on this topic is under revision at Solar Energy Materials and Solar Cells.
- Achieved an efficiency of 27.7% for four-terminal mechanically stacked perovskite-silicon tandem using surface passivation method with alkylammonium bulky cations (n-butylammonium bromide), which is the highest value reported to date. A manuscript reporting this result has been accepted by Advanced Energy Materials.

- Achieved an open circuit voltage of 1.27 V for perovskite solar cells with a 1.72 eV active material bandgap.

Future Work

- Optimise the perovskite cell using a 1.72 eV active material bandgap and 2D passivation to improve the V_{oc} to over 1.3 V.
- Scale up the device active area to the scale of 5 cm² by using metal grids in both front and rear sides.
- Integrate the perovskite top cell and silicon bottom cell in the tandem configuration.

References

DUONG, T., et al. 2019a. Instability of Molybdenum Oxide Interlayer under Ambient Conditions and Implications for Perovskite Solar Cells. *Solar Energy Materials and Solar Cells*, under revision (SOLMAT-D-19-01159).

DUONG, T., et al. 2019b. High Efficiency Perovskite-Silicon Tandem Solar Cells: Effect of Surface Coating versus Bulk Incorporation of 2D Perovskite. *Advanced Energy Materials*, accepted (aenm.201903553R1).

SANEHIRA, E. M., et al. 2016. Influence of Electrode Interfaces on the Stability of Perovskite Solar Cells: Reduced Degradation Using MoO_x/Al for Hole Collection. *ACS Energy Letters*, 1, 38-45.

F3 TRANSPARENT DOPED LPCVD POLYSILICON

ACAP Fellow

Dr Kean Chern Fong

Supervisor

Prof. Andrew Blakers

Funding Support

ACAP

Aim

LPCVD polysilicon-oxide (poly-ox) passivated contact is among the most promising solutions towards high efficiency Si solar cells due to its excellent electrical performance and compatibility with standard industrial fabrication processes. Most prominently, the potential of this technology has been demonstrated when applied on the rear surfaces of both IBC and front contact single junction Si cells reaching above 25% efficiencies.

This technology is typically applied on non-light-facing surfaces due to its high parasitic optical absorption combined with poor contact resistivity. Parasitic absorption is undesirably for obvious reasons, while having a high contact resistance makes it incompatible with metal fingers which typically cover only 2–5% of the surface.

This project has the ambitious aim to develop an optically optimised poly-ox contact for application on a light-facing surface, by having a combination of: (1) high optical transparency; (2) anti-reflection properties; (3) compatibility with transparent conductive oxides; (4) ultra-low contact resistivity; and (5) retains the promising electrical qualities of poly-ox contacts.

The rewards for successfully developing an optically optimised poly-ox technology is tremendous as it would provide passivation, contact and anti-reflection in an extremely elegant process sequence. Such a technology is particularly relevant within the near future for application in bifacial solar cells, and as a carrier transport layer between Si and a top cell in Si-tandem devices.

Progress

The processes developed within this project currently exhibit among the best combinations of surface passivation as measured via saturation current density (J_0) and contact resistivity (ρ_c).

As plotted in Figure F3.1, very low ρ_c values of less than $1 \text{ m}\Omega\text{cm}^2$ were measured for a wide range of processing conditions owing to the excellent control of the in situ low pressure oxidation deposited between 700 and 800°C in a pure oxygen ambient under low pressures of 600 mTorr. TEM imaging of this stack shows a well intact Si-oxide layer with a thickness of approximately 1–1.2 nm.

Although the developed poly-ox contact passivation provides excellent J_0 and ρ_c consistent with very high efficiency silicon solar cells, with potential for over 25% efficiency, the objective of this project is to investigate its application on a light-facing surface, either the front for Si and Si-tandem cells or the rear light-facing surface in the case of a bifacial solar cell.

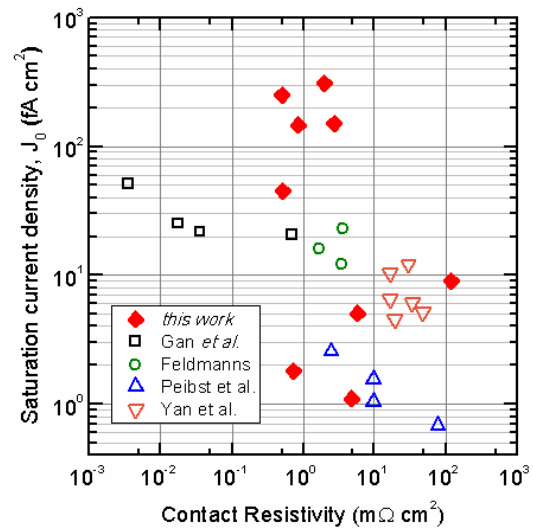


Figure F3.1: Comparison of J_0 and ρ_c to other recent work on poly-ox contacts in literature.

A. Optical characteristics of thin doped-polysilicon

The most elegant approach in cell fabrication is to avoid all masking steps via application of a very thin doped polysilicon over the entire surface, followed by a hydrogenating capping layer and screen-printed metal fingers, thereby providing a semitransparent front passivating and contacting layer. Obviously the key drawback is the high parasitic absorption within the polysilicon layer, which must therefore be very thin in order to avoid unpractical levels of losses.

However, in order to provide an accurate assessment of the optical performance, the optical characteristics of doped polysilicon must first be well characterised. In this work, polysilicon films were deposited on quartz wafers with various doping and process conditions, which were measured using a JA Woollam spectroscopic ellipsometer. The measurements were taken at three angles, while the thickness of the film was measured via TEM measurements, where the combination of accurate film thickness and ellipsometry measurements were then fitted to optical models for extraction of the refractive index, n , and extinction coefficient, k , values.

The resulting measurements are as presented in Figure F3.2 for five samples, starting with as-deposited PECVD polysilicon, phosphorus diffusion, phosphorus diffusion with 25 minutes 900°C drive-in, boron diffusion, and boron diffusion with 25 minutes 940°C drive-in, with final conditions representing optimised film deposition conditions for low J_0 and contact resistivity.

The key observation is the large difference between as-deposited polySi to the diffused samples, particularly the extinction coefficient, k value, noting the significantly lower absorption for samples after subsequent temperature processing post-deposition.

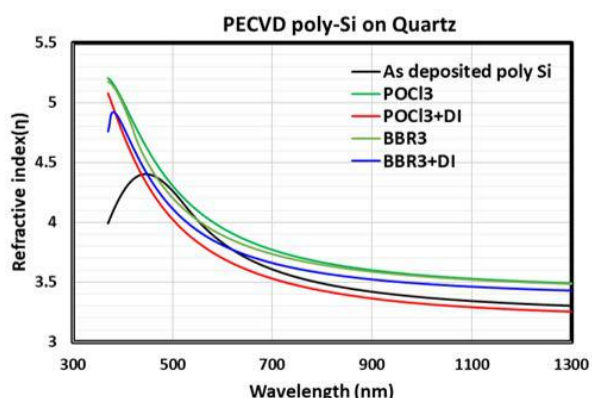


Figure F3.2: *n-k* values of doped polysilicon deposited on quartz wafer extracted via spectroscopic ellipsometry.

As demonstration of the validation process for the *n-k* value extraction, the *n-k* values are used as input parameters in ray tracing software as provided by PV Lighthouse to generate reflection and transmission of the film, which is then compared against measurements using a Perkin-Elmer integrating sphere spectrophotometer. The results of this validation are presented in Figure F3.3 for a 48 nm thick n^+ PolySi layer on the 1.5 mm quartz wafer.

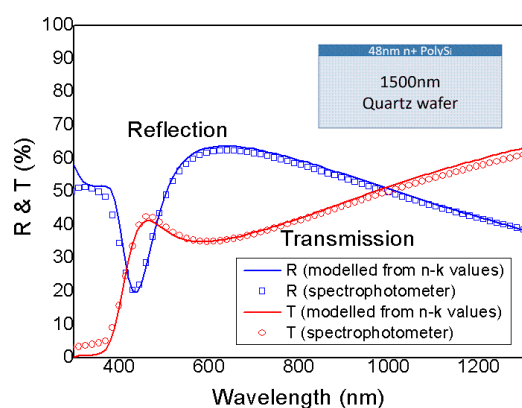


Figure F3.3: Validation of *n-k* values for 48 nm thick phosphorus doped polysilicon with drive-in.

The key advantage of this approach is the enhanced predictive capabilities for a wider range of thickness and surface morphology, especially once the *n-k* values are established for a particular film doping level density and annealing temperature, both of which affect the film crystallinity.

In a preliminary comparison between PECVD and LPCVD polysilicon (not presented here), significant differences in the optical characteristics were observed even for films after annealing. Subsequent efforts in detailed characterisation and comparison will ensue in the coming months.

B. Patterning of doped polysilicon

A more conventional approach towards the application of doped polysilicon films on light-facing surfaces is patterning to form selective area coverage. The key challenge in such a process is the difficulty in the masking and etching of polysilicon, which once annealed has similar chemical resistance to crystalline silicon. Although silicon-

dioxide typically exhibits higher etch resistance to KOH and TMAH etching used for removal of polysilicon, SiO_2 layers with thicknesses below 1.5 nm as is typically used for the tunnel oxide layers are too thin to form an effective barrier to allow termination of alkaline etching solution prior to the c-Si base wafer.

A plausible process sequence which is likely industrially relevant is to perform a mask removal step on the top SiN_x hydrogenating capping layer via laser or screen-printed paste, followed by a texturing process, which would selectively remove the doped polysilicon, etch through the tunnel oxide and subsequently complete the random-pyramid structure as it would on a conventional c-Si wafer surface.

The mechanical feasibility of such a process was experimentally tested, replicated in the ANU laboratory using photolithography for the masking process. Naturally, the photolithography process can be replaced with other masking processes upon demonstration of mechanical feasibility of etching and texturing through SiN /poly-ox film layers.

Figure F3.4 shows the successful implementation of the direct texture-through process, showing retention of doped polysilicon areas (blue), an overhanging mask layer (peach colour) and fully formed textured regions (out of focus in the image).

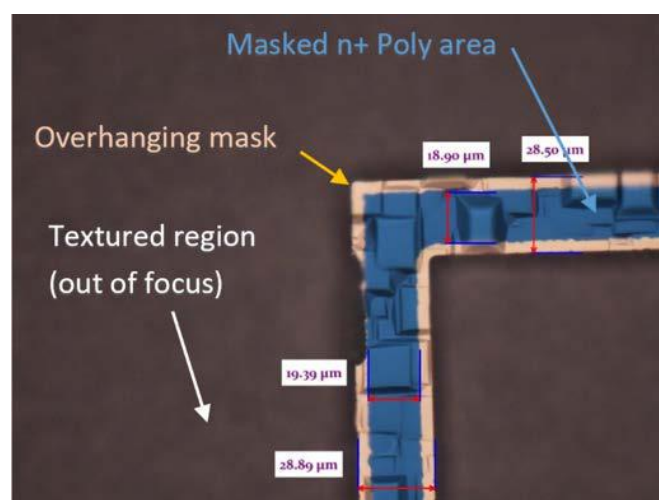


Figure F3.4: Texture-through process for formation of selective doped polysilicon contact structure formation.

Highlights

- Excellent J_0 and contact resistivity $<1 \text{ fAcm}^2$ and $<1 \text{ m}\Omega\text{cm}^2$ was achieved.
- Successful characterisation of *n-k* values of as-deposited and doped polysilicon.
- Development of texture-through process for formation of local doped polysilicon regions.

Future Work

- Expanding library of n-k values for a wider range of PECVD and LPCVD doped polysilicon.
- Demonstration of texture-through process on an operational solar cell.

References

FONG, K. C., KHO, T. C., LIANG, W. S., CHONG, T. K., ERNST, M., WALTER, D., STOCKS, M., FRANKLIN, E., MCINTOSH, K. & BLAKERS, A. 2018a. Phosphorus diffused LPCVD polysilicon passivated contacts with in-situ low pressure oxidation. *Solar Energy Materials and Solar Cells*, 186, 236-242.

FONG, K. C., KHO, T. C., LIANG, W. S., CHONG, T. K., ERNST, M., WALTER, D., STOCKS, M., FRANKLIN, E., MCINTOSH, K. & BLAKERS, A. 2018b. Optimization and Characterization of Phosphorus Diffused LPCVD Polysilicon Passivated Contacts with Low Pressure Tunnel Oxide, 2018 IEEE 7th World Conference on Photovoltaic Energy Conversion (WCPEC), 2002-2005.

F4 HYDROGEN DRIFT AND DIFFUSION IN SILICON SOLAR ARCHITECTURES AT INTERMEDIATE TEMPERATURES

Lead Partner

UNSW

UNSW Team

Dr Phillip Hamer, Dr Catherine Chan, Chandany Sen, Daniel Chen, Dr Michael Pollard, Prof. Renate Egan

Academic Partner

The University of Oxford, Department of Materials: Dr Sebastian Bonilla, Prof. Peter Wilshaw

Aim

This project aims to create a model for the transport of hydrogen within silicon solar cell structures. This involves both the creation of a software program to perform the simulations and experiments to obtain more accurate values for some of the physical parameters involved. The understanding gained from the model can then be used to develop improved processes for controlling the behaviour of hydrogen in solar cells.

Progress

Initial modelling has predicted that during post-firing anneals hydrogen will often redistribute from the bulk of a silicon solar cell towards the surfaces. This is largely driven by the electric fields in the vicinity of emitters or surface charges. This has two potential impacts for solar cell performance after these processes. The first is an increase in front contact resistance due to the interaction of hydrogen with the screen-printed metal contacts, and the second is the formation of hydrogen-related defects in the near surface region.

The increase in contact resistance is particularly concerning for attempts to mitigate light and elevated temperature induced degradation (LeTID) using post-firing anneals. Processes have been demonstrated to eliminate LeTID, but with fill factor losses of more than 5% on finished cells. In this project we have combined these post-firing anneals with an applied bias to prevent hydrogen reaching the contacts, as well as improved control of both the applied bias and thermal profile during cooling. As seen in Figure F4.1 this process not only prevents any measurable loss of efficiency due to LeTID but provides a slight boost in performance when compared with cells before treatment. We are now working to demonstrate this as a commercial process, using a modified "coin-stacker", which is a widely used industrial tool.

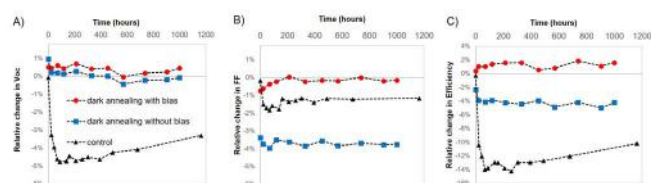


Figure F4.1: Change in parameters during light soaking at 70°C under 1 sun illumination for p-type PERC cells with no post-firing anneal (control), a standard dark anneal (dark annealing without bias) and an anneal using bias control (dark annealing with bias). (a) Relative change in open circuit voltage. (b) Relative change in fill-factor. (c) Relative change in efficiency.

Surface Related Degradation (SRD) is another effect with the potential to decrease the performance of cells in the field. The timescale is even longer than LeTID (typically into the thousands of hours at 80°C) and so it is of limited concern for current PERC solar cells but is likely to have a greater impact on future cell architectures, particularly those with more lightly doped emitters. Hydrogen has already been speculated to play a role in this effect, and we have conducted investigations that support the role of hydrogen redistribution. Not only does the rate at which SRD occur depend upon the bulk doping but by replacing dielectric layers after firing we were able to show that the degradation is not related to the surface passivation layer itself. It was also seen that severe SRD could occur even on a diffused surface, something previously reported to suppress SRD (Sperber et al. 2018), provided the peak doping was low enough. We then examined SRD in cells with a light emitter and found that the degradation could not be explained by a simple increase in the effective surface dark saturation current (J_0), as would be expected of an increase in defect density at the interface itself. Instead lifetime fitting found a band of possible defect distributions, all of which extended over 150 nm from the surface. Figure F4.2 presents three of these possible configurations (I, II and III) as well as defect evolutions and lifetime fits for defect profile II.

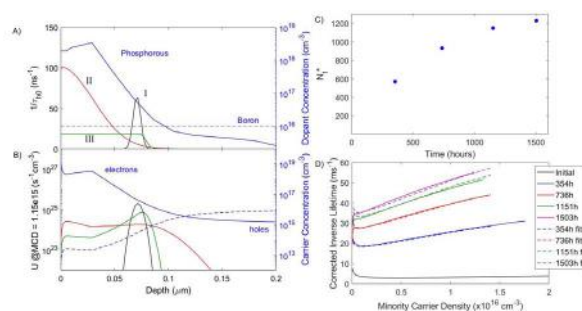


Figure F4.2: (a) Three viable defect distributions (I, II and III) in the near surface region along with local dopant concentrations. (b) The spatially resolved recombination rates for all three profiles at a minority carrier density of $1.15 \times 10^{15} \text{ cm}^{-3}$ along with the local carrier concentrations. (c) Peak defect concentration for defect profile II required to accurately fit lifetime data during degradation. (d) Fits to lifetime data obtained using defect profile II.

We have also investigated how these defect profiles compare to the expected behaviour of hydrogen. The formation of hydrogen-related defects in silicon was first observed in 1987 and has been extensively

reported since (Johnson et al. 1987; Nickel et al. 2000). Of particular interest is the observation that they form much more readily in n-type silicon, potentially due to the formation of a specific form of hydrogen dimer. We have simulated the distribution of hydrogen charge states and dimer precursor products in our structure in Figure F4.3. It may be seen that there is good agreement between the dimer precursor products and the defect profiles found by lifetime fitting although further data is needed to establish greater confidence in which set of precursors is the critical one.

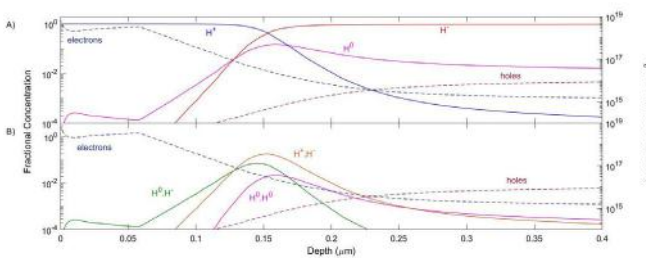


Figure F4.3: (a) Fraction of interstitial hydrogen in each charge state as a function of depth at a minority carrier density of $1.15 \times 10^{15} \text{ cm}^{-3}$ along with local carrier concentrations. (b) Spatial distribution of the $\text{H}^+.\text{H}^+$, $\text{H}^+.\text{H}^0$ and $\text{H}^0.\text{H}^0$ fractional concentration products that may be critical for defect formation.

Hold-ups with equipment have meant that the planned further refinements to the simulation model have been pushed to 2020.

Highlights

- Industrially viable process demonstrated to mitigate LeTID without increasing contact resistance.
- Important evidence obtained for the role hydrogen plays in SRD.
- SRD in structures with light emitters modelled and in good agreement with hydrogen behaviour.

Future Work

- More work needs to be done on the simulation model and parameters for hydrogen motion in n-type, based on SIMS profiles of deuterium.
- The LeTID mitigation process needs to first be demonstrated, and then optimized, in an industrial tool
- Further work on SRD and the role of hydrogen will be carried out in collaboration with others in the school.

References

- JOHNSON, N. M., PONCE, F. A., STREET, R. A. & NEMANICH, R. J. 1987. Defects in single-crystal silicon induced by hydrogenation. *Physical Review B*, 35, 4166-4169.
- NICKEL, N. H., ANDERSON, G. B., JOHNSON, N. M. & WALKER, J. 2000. Nucleation of hydrogen-induced platelets in silicon. *Physical Review B*, 62, 8012-8015.
- SPERBER, D., SCHWARZ, A., HERGUTH, A. & HAHN, G. 2018. Enhanced stability of passivation quality on diffused silicon surfaces under light-induced degradation conditions. *Solar Energy Materials and Solar Cells*, 188, 112-118.

F5 CHARACTERISATION OF MICROSTRUCTURE FORMATION IN SOLUTION-PROCESSED PHOTOVOLTAIC PEROVSKITE THIN FILMS WITH SYNCHROTRON-BASED X-RAY SCATTERING TECHNIQUES

Lead Partner

Monash University

Monash Team

Dr Wenchao Huang, Prof. Christopher R. McNeill, Prof. Udo Bach

Academic Partners

Wuhan University of Technology: Prof. Fuzhi Huang, Prof. Yi-Bing Cheng

Funding Support

ACAP

Aim

The objective of this project is to investigate microstructure formation mechanism of solution-processed perovskite by using synchrotron-based X-ray scattering techniques and then to establish a relationship between film microstructure and device performance. Based on the fundamental understanding gained from film formation mechanism from solution state to solid state, new perovskite materials and processing techniques will be developed to simultaneously improve the efficiency and stability of solution-processed perovskite solar cells.

Progress

The interface plays an important role in determining the power conversion efficiency (PCE) and stability of perovskite solar cells. Surface defects will induce non-radiative charge recombination and also initiate the decomposition of perovskite structure at the elevated temperature or high moisture atmosphere. Recently, selective growth of an additional stacking layer with hydrophobic bulky organic cations on the original 3D perovskite film offered a promising route to passivate these surface defects and also act as a barrier layer to prevent oxygen and moisture ingress. (Cho et al. 2018; Liu et al. 2019; Wang et al. 2017). This is achieved by using a sequential two-step deposition method that the 3D perovskite layer is firstly prepared on the substrate, followed by post-treating with a solution containing large organic cations. The additional capping layer is spontaneously formed via cation exchange. However, the precise control of thickness and microstructure of the additional layer is very challenging, because the cation exchange is sensitive to organic cations and processing conditions used in post-treatment. As charge transport across large organic cations is not highly efficient, the formation of a too thick additional layer will inevitably impede charge injection from the perovskite layer to electron transport layer (ETL) or hole transport layer (HTL). Here, we demonstrate a novel post-treatment using tert-butylammonium iodide (t-BAI)/isopropanol (IPA) solution to passivate the surface of CsFAMA perovskite without forming the thick

2D perovskite layer (Bu et al. 2019). The post-treated device shows an improved PCE of 20.1% with significantly suppressed hysteresis phenomenon and enhanced stability under ambient atmosphere.

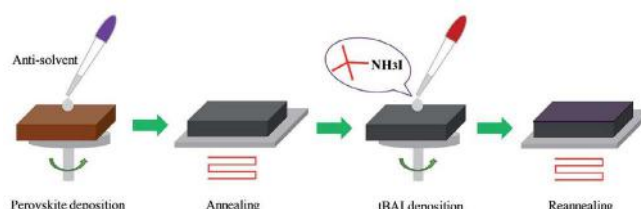


Figure F5.1: The schematic of the post-treatment of t-BAI/IPA solution on the surface of 3D perovskite films.

In this project, after the deposition of $\text{Cs}_{0.05}(\text{FA}_{0.85}\text{MA}_{0.15})_{0.95}\text{Pb}(\text{I}_{0.85}\text{Br}_{0.15})_3$ (CsFAMA) perovskite films, the post-treatment solution was then spun onto the perovskite surface, followed by a re-annealing process (Figure F5.1). A self-assembling layer is spontaneously formed on the top of CsFAMA perovskite. The perovskite films are post-treated by two different types of organic cations: BAI and its isomeride t-BAI. The synchrotron-based grazing incident wide angle X-ray scattering (GIWAXS) is applied to investigate the microstructure of self-assembling layers after post-treatment, as shown in Figure F5.2. In the previously published literature, BA is a popular organic cation widely used for the fabrication of 2D perovskite. From GIWAXS pattern, a 2D structured perovskite film has also been observed in the film post-treated with BAI solution (Figure F5.2(a)), even when the concentration of BAI/IPA solution is low. On the other hand, perovskite films treated with the t-BAI shows the similar morphology compared to the 3D perovskite and there is no 2D perovskite formed. Due to the smaller size, the small amount of t-BA may be fully incorporated into the surface of the perovskite 3D structure. This study opens up a pathway to manipulate the interfacial morphology via tuning the size of organic cation.

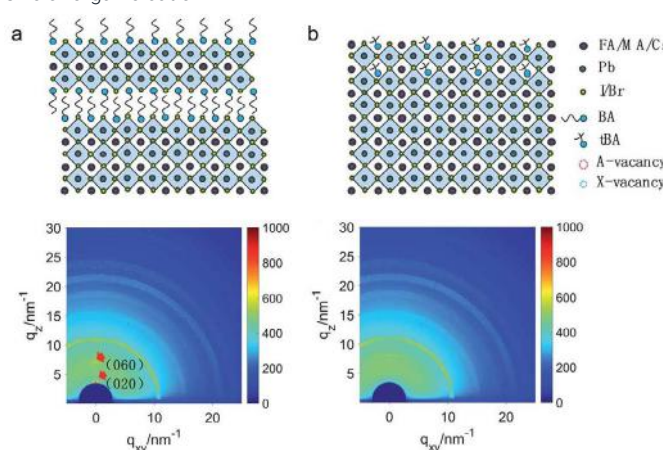


Figure F5.2: Grazing incident wide angle X-ray scattering of perovskite post-treated with (a) BAI solution and (b) t-BAI solution.

Perovskite solar cells are fabricated with a structure of $\text{FTO}/\text{SnO}_2/\text{PCBM}/\text{Perovskite}/\text{Spiro-MeOTAD}/\text{Au}$. The device post-treated with 3 mg/mL t-BAI/IPA solution exhibits the best device performance with an efficiency of 20.1%, a J_{sc} of 22.8 mAcm^{-2} and a V_{oc} of 1.13 V under reverse scan (RS), while the device without post-treatment yields an

efficiency of 19.3% with a J_{sc} of 22.7 mAcm⁻² and a V_{oc} of 1.10 V under RS (Figure F5.3(a)). It is also worth noting that the hysteresis is almost eliminated after post-treatment. The increased V_{oc} and suppressed hysteresis are mainly contributed to the surface passivation. The incorporation of large cations into the perovskite results in reducing surface defects and thus minimising the charge recombination. Furthermore, the long-term stability of a t-BAI-treated device is also significantly enhanced compared to that of the pristine devices (Figure F5.3(b)). After 1000 hours aging, the device still exhibits more than 90% of its initial efficiency. As the concentration of solution used for post-treatment increases above 3 mg/mL, the device performance starts to decrease, because t-BAI cannot fully react with perovskite and the residual t-BAI hinders the charge transport from perovskite to HTL.

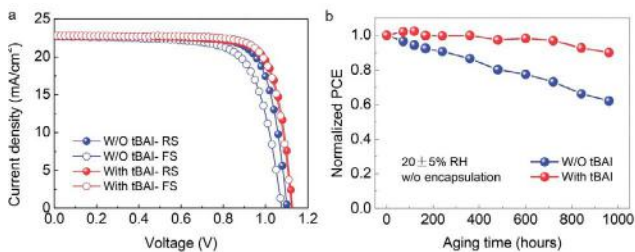


Figure F5.3: (a) J-V curves of the champion devices and (b) stability of efficiency, with and without 3 mg/mL.

Highlights

- A novel post-treatment on the 3D CsFAMA perovskite surface is developed for surface passivation.
- The microstructure of perovskite is optimised by precisely controlling the cation exchange.
- Perovskite solar cells after the post-treatment shows an improved efficiency of over 20% with enhanced long-term stability and suppressed hysteresis.

Future Work

- The thermodynamic and kinetic behaviors behind the transformation through the cation exchange will be systematically investigated.
- The relationship between the interfacial morphology and charge transport and recombination will also be established.
- New bulky organic cations and methods to control the microstructure of perovskite will be developed for further improving the efficiency and stability of perovskite solar cells.

References

- BU, T. L., LI, J., HUANG, W. C., MAO, W. X., ZHENG, F., BI, P. Q., HAO, X. T., ZHONG, J., CHENG, Y. B. & HUANG, F. Z. 2019. Surface modification via self-assembling large cations for improved performance and modulated hysteresis of perovskite solar cells. *Journal of Materials Chemistry A*, 7, 6793-6800.
- CHO, K. T., GRANCINI, G., LEE, Y., OVEISI, E., RYU, J., ALMORA, O., TSCHUMI, M., SCHOUWINK, P. A., SEO, G., HEO, S., PARK, J., JANG, J., PAEK, S., GARCIA-BELMONTE, G. & NAZEERUDDIN, M. K. 2018. Selective growth of layered perovskites for stable and efficient photovoltaics. *Energy & Environmental Science*, 11, 952-959.
- LIU, Y. H., AKIN, S., PAN, L. F., UCHIDA, R., ARORA, N., MILIC, J. V., HINDERHOFER, A., SCHREIBER, F., UHL, A. R., ZAKEERUDDIN, S. M., HAGFELDT, A., DAR, M. I. & GRATZEL, M. 2019. Ultrahydrophobic 3D/2D fluoroarene bilayer-based water-resistant perovskite solar cells with efficiencies exceeding 22%. *Science Advances*, 5, 2543
- WANG, Z. P., LIN, Q. Q., CHMIEL, F. P., SAKAI, N., HERZ, L. M. & SNAITH, H. J. 2017. Efficient ambient-air-stable solar cells with 2D-3D heterostructured butylammonium-caesium-formamidinium lead halide perovskites. *Nature Energy*, 2, 17135

F6 HIGH DIELECTRIC CONSTANT SEMICONDUCTORS FOR HOMOJUNCTION ORGANIC SOLAR CELLS

Lead Partner

UQ

UQ Team

Dr Hui Jin, Mr Mohammad Babazadeh, Prof. Paul Burn

Funding Support

ACAP, ARC Laureate Fellowship (PB), National Computing Infrastructure

Aim

The objective of this project is to develop organic semiconductors that possess high dielectric constant at both low and high frequencies to minimise the energy losses in free charge carrier generation in single chromophore homojunction organic photovoltaic devices.

Progress

High dielectric constant organic semiconductors can in principle have a dramatically lower exciton binding energy and reduced geminate and non-geminate recombination, leading to minimisation of energy losses and improvement in the performance of homojunction photovoltaic devices (Koster et al. 2012). Such an approach could enable homojunction organic solar cells to have an efficiency comparable to inorganic and hybrid solar cells. One of the strategies developed for high dielectric constant organic semiconductors is replacing the alkyl solubilising groups with ethylene glycol groups to enhance the dipole polarisability (Donaghey et al. 2016). The flexibility of the glycol side chains can lead to less steric hindrance (Meng et al. 2015), resulting in closer π - π stacking and thus a higher film density (Armin et al. 2017). A high film density is an important characteristic for increasing the optical frequency dielectric constant, and also sometimes leads to a redshift in the absorption. This requires materials that can adopt a planar geometry with extended π -conjugation and long-range π -electron delocalisation. In the annual report of 2018, a series of glycolated linear materials containing different numbers of fluorenes was reported, which will be included in a manuscript that is currently under preparation. Further to the experimental results, density functional theory (DFT) calculations have now been carried out on the fluorenyl dimer structure. Figure F6.1(a) and (b) show how the simulated geometry of the fluorenyl dimer adopts a twisted conformation at its lowest energy configuration, compared to the dithienocyclopentadiene (DTCPD) dimer, which adopts a near co-planar geometry. The DTCPD dimer possesses an inherently higher film density, a redshifted absorption spectrum, and a higher optical-frequency dielectric constant than the fluorenyl dimer (Figure F6.1(c)). To effectively increase optical dielectric constant, which is important for lowering the exciton binding energy and enhancing charge generation, effort has been invested into developing co-planar molecules. It has also been found that less conformational

diversity contributes to more ordered alignment of molecules and stronger edge-on orientation (McDowell, Narayanaswamy et al. 2018). A flow chart shown in Figure F6.2 discloses the correlation between the material design and increase of both low-frequency and optical-frequency dielectric constants. To this end, a novel series of materials have been designed and synthesised during the past year (Figure F6.3). Thienothiophene was employed in a ring-fused core to increase the chromophore co-planarity and reduce conformational diversity. Crown ethers of different numbers of carbons, a form of glycol solubilising groups, were introduced to the structure to enhance the dipole polarisability in the molecule. It is anticipated that the crown ethers can complex lithium ions to simultaneously increase the dielectric constant and hole mobility of the materials (Liu, Jeong et al. 2013).

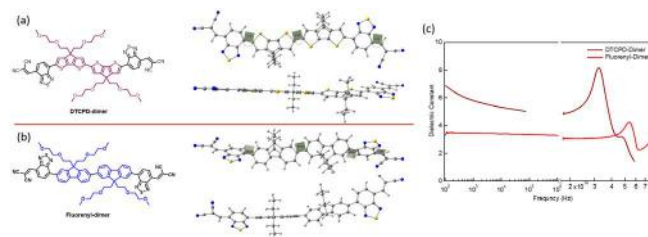


Figure F6.1: (a) Molecular structures of the glycolated DTCPD-dimer and the simulated molecular ground-state geometry (top and side view) at the ground state. (b) Molecular structures of the glycolated fluorenyl-dimer and simulated molecular ground-state geometry (top and side views). (c) comparison of the low- and optical-frequency dielectric constant of both dimers.

The synthesis of crown ether-included materials has proven to be more difficult than expected due to: (1) the crown ether is a strained version of its glycolated linear equivalent. Thus, during the synthesis there is a competing side reaction in which a less strained dimer is formed; (2) alkali metal salts have to be avoided during the reaction and work-up otherwise metal-crown ether complexes are formed before final materials are developed; and (3) Lewis acids used in some of the later reactions can cleave the crown ether, even at very low temperatures (for example -80°C), but, are very hard to be replaced in the oxidative cyclisation that is used to form the fused core ring system. The material substituted with 12-crown-4 has therefore been redesigned several times to enable an optimised version to be prepared (Scheme F6.1). To further increase solubility of the material for solution processing, two strategies have been proposed, namely to replace 12-crown-4 with a larger crown ether, 14-crown-4, and to add linear glycol solubilising groups to the ends of the materials (Figure F6.4). 14-Crown-4 has been reported to have the highest stability coefficient when forming a complex with a lithium ion (Kitazawa, Kimura et al. 1984). The new series of materials are currently being synthesised. An additional aspect of the structural optimisation is to create a controllable long-range order over two dimensions by non-covalent bonding, such as hydrogen bonding or strong intermolecular interactions enabled by the choice of functional groups. A 2D network will help increase the film density and molecular alignment in the desired orientation, and is likely to lead to a redshift and enhancement in the solid-state absorption.

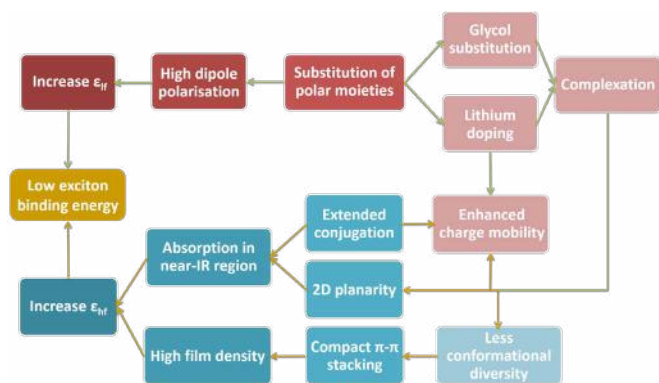


Figure F6.2: A flow chart that illustrates the correlation between material design and dielectric constant.

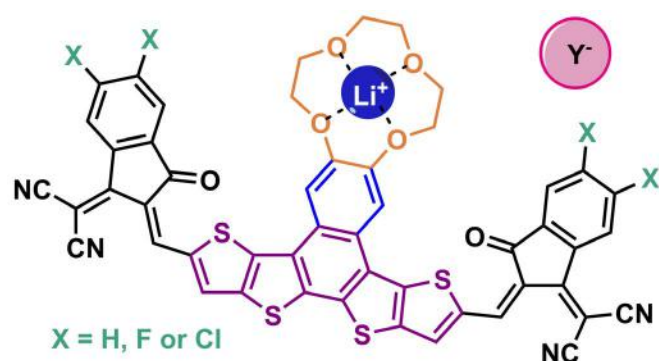
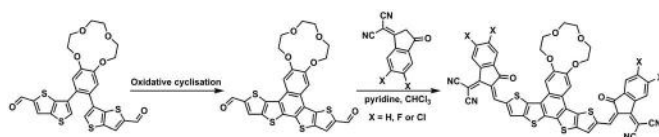


Figure F6.3: A new series of lithium incorporated materials that have been designed for the increase of both low- and optical-frequency dielectric constant.



Scheme F6.1: The synthesis of the new series of materials before the lithium ion is incorporated.

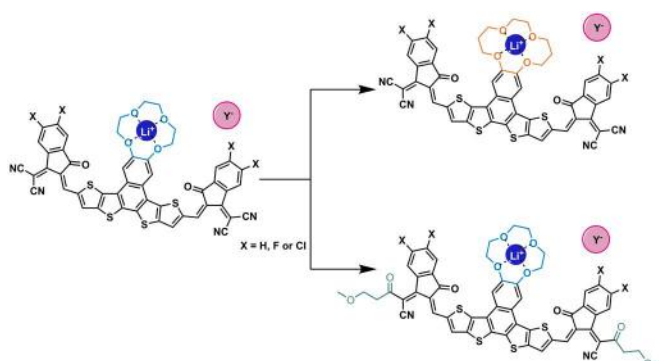


Figure F6.4: Strategies to increase the solubility of the materials for solution processing, and the stability coefficient of lithium-crown ether complexes.

Highlights

- The correlation between the molecular geometry and dielectric constant of organic semiconductors has been studied for the series of developed glycolated oligo-fluorenyl materials in the comparison with a DTCPD-containing series.
- A manuscript is being prepared on the outcomes of the work.
- The work has been presented at conferences in 2019 including the 10th International Conference on Materials for Advanced Technologies (ICMAT) in Singapore, the 2nd International Conference on Flexible Electronics (ICFE) in Hangzhou, China, Wuhan University Workshop in Wuhan, China, Australasian Community for Advanced Organic Semiconductors Symposium (AUCASOS) in Katoomba, Australia, and the 7th Annual Australian Centre for Advanced Photovoltaics (ACAP) Conference in Canberra, Australia.
- With the deeper understanding gained from the preliminary series, a new range of lithium-incorporated materials with a co-planar molecular geometry has been designed and synthesised.

Future Work

- The main focus is still to increase the optical-frequency dielectric constant by developing novel organic/hybrid materials.
- Molecular alignment in solid state is being optimised by reduction of the conformation diversity of the molecules, with further optimisation aiming to realise long-range order through creating non-covalent interactions between molecules in the solid state.
- Improve homojunction device performance by increasing charge generation through simultaneously increasing the low- and optical-frequency dielectric constant, charge separation through balanced charge mobility, and optimising the film morphology.

References

ARMIN, A., STOLTZFUS, D. M., DONAGHEY, J. E., CLULOW, A. J., NAGIRI, R. C. R., BURN, P. L., GENTLE, I. R. & MEREDITH, P. 2017. Engineering dielectric constants in organic semiconductors. *Journal of Materials Chemistry C*, 5, 3736-3747.

DONAGHEY, J. E., ARMIN, A., STOLTZFUS, D. M., BURN, P. L. & MEREDITH, P. 2016. Correction: Dielectric constant enhancement of non-fullerene acceptors via side-chain modification. *Chemical Communications*, 52, 13714-13715.

KITAZAWA, S., KIMURA, K., YANO, H. & SHONO, T. 1984. Lipophilic crown-4 derivatives as lithium ionophores. *Journal of American Chemical Society*, 106, 6878-6983.

KOSTER, L. J. A., SHAHEEN, S. E. & HUMMELEN, J. C. 2012. Pathways to a new efficiency regime for organic solar cells. *Advanced Energy Materials*, 2, 1246-1253.

LIU, X., JEONG, K. S., WILLIAMS, B. P., VAKHSHOURI, K., GUO, C., HAN, K., GOMEZ, E. D., WANG, Q. & ASBURY, J. B. 2013. Tuning the dielectric properties of organic semiconductors via salt doping. *The Journal of Physical Chemistry B*, 117, 15866-15874.

MCDOWELL, C., NARAYANASWAMY, K., YADAGIRI, B., GAYATHRI, T., SEIFRID, M., DATT, R., RYNO, S. M., HEIFNER, M. C., GUPTA, V., RSKO, C., SINGH, S. P. & BAZAN, G. C. 2018. Impact of rotamer diversity on the self-assembly of nearly isostructural molecular semiconductors. *Journal of Materials Chemistry A*, 6, 383-394.

MENG, B., SONG, H., CHEN, X., XIE, Z., LIU, J. & WANG, L. 2015. Replacing alkyl with oligo(ethylene glycol) as side chains of conjugated polymers for close π - π stacking. *Macromolecules*, 48, 4357-4363.

F7 PRACTICAL 50% EFFICIENT SPECTRUM SPLITTING CPV RECEIVERS USING INTERMEDIATE BRAGG REFLECTORS

Lead Partner

UNSW

UNSW Team

Dr Yajie Jiang, Dr Mark Keevers, Scientia Prof. Martin Green

Industry Partners

AZUR SPACE Solar Power
RayGen Resources Pty Ltd

Funding Support

ACAP

Aim

The aim of this project is to demonstrate the advantages of the distributed Bragg reflector (DBR) assisted spectrum splitting concept compared with discrete dielectric filters. We are also working towards world record system efficiency exceeding 50% using spectrum splitting between two triple-junction solar cells (TJSCs) under standard concentrator photovoltaic (CPV) test conditions, including all optical losses.

Progress

We investigate the use of DBRs within TJSCs for spectrum splitting photovoltaics. Metamorphic (MM) TJSCs have a more ideal sub-cell bandgap combination and higher efficiency than lattice-matched (LM) TJSCs (Dimroth et al. 2009; Guter et al. 2009). A multilayer buffer structure is an essential part of MM TJSCs to overcome the high lattice mismatch between the Ge substrate and the two upper sub-cells. The buffer typically consists of several step-graded layers with increasing lattice constant, thereby relaxing lattice strains and confining dislocations to buffer layer interfaces. For example, the buffer in a 41% efficient MM TJSC $\text{Ga}_{0.35}\text{In}_{0.65}\text{P}/\text{Ga}_{0.83}\text{In}_{0.17}\text{As}/\text{Ge}$ has a total thickness of 1.6 μm , consisting of 8 200-nm thick GaInAs layers with stepwise increasing indium content from 1% to (an overshooting) 20% (Dimroth et al. 2009; Guter et al. 2009).

The MM TJSC considered in this project is a $\text{Ga}_{0.44}\text{In}_{0.56}\text{P}/\text{Ga}_{0.92}\text{In}_{0.08}\text{As}/\text{Ge}$ cell for CPV applications (Guter et al. 2009) and we assume a buffer consisting of 8 GaInAs layers with stepwise increasing indium content from 1% to 8% (Figure F7.1(a)). We developed a baseline optical model of the MM TJSC without DBR using refractive index data shown in Figure F7.1(b), resulting in the simulated reflectance shown in Figure F7.1(c).

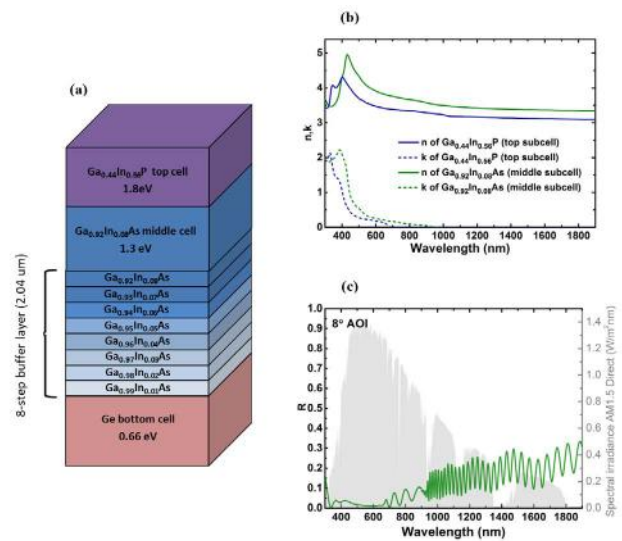


Figure F7.1: (a) Key layers of the modelled MM TJSC (other layers not shown are similar to the LM structure, including DLAR and metal contacts). (b) Complex refractive index of the top and middle sub-cells in the modelled MM TJSC. (c) Modelled specular reflectance of an MM TJSC.

We propose that the 8-step buffer could additionally function as a (spectrum splitting) DBR, by for example converting each GaInAs buffer layer into a GaInAs/GaInP bilayer (Figure F7.2(a)), or into trilayers of GaInAs and GaInP (Figure F7.2(b)), with the same lattice constant but different refractive indices. These two new designs preserve the original stepwise lattice matching, while introducing the advantage of an intermediate DBR allowing improved efficiency and radiation tolerance (relevant to space cells) and the potential for spectrum splitting. However, the reflectance of these two simple DBR/buffer designs is only moderately effective for spectrum splitting purposes (Figure F7.2(c)), with the 8-trilayer case being the most promising of the two.

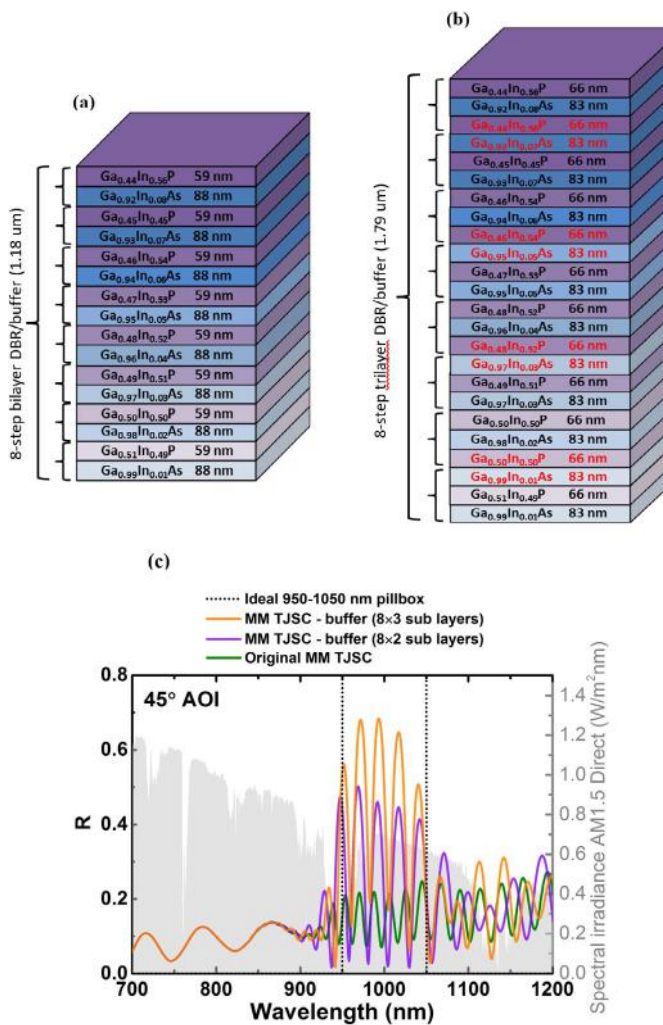


Figure F7.2: Proposed DBR/buffer structure composed of 8 (a) bilayers or (b) trilayers (additional layers have red text) for an MM TJSC, and (c) the corresponding calculated specular reflectance (45° AOI) compared to an idealised 950–1050 nm pillbox band-reflect filter (note the cut-on wavelength is shifted to 950 nm compared to 900 nm used for the lattice-matched case).

Given that the insertion of ‘reverse-step’ buffer layers with tensile strain in the common compressive step-graded buffer structure has proven to significantly reduce threading dislocation density (Li et al. 2015), we also considered the corresponding tensile/compressive DBR/buffer structures. The reflectance of these tensile/compressive structures is quite similar to that of the conventional step-graded buffer structures, therefore only the conventional step-graded structures are presented in the following.

To further increase the reflectance for spectrum splitting, the 8-trilayer DBR/buffer structure of Figure F7.2(b) is combined with a 16-bilayer DBR, and the bilayer and trilayer thicknesses reoptimised (Figure F7.3(a)). The reflectance in the spectrum splitting band is improved with the additional DBR (Figure F7.3(c)). The spectral reflectance of the DBR on a GaAs substrate is also presented to show the “bare” DBR reflectance (without overlying layers). To further enhance spectrum splitting reflectance, a 2 × 16 bilayer + 8-trilayer DBR/buffer structure is also modelled (Figure F7.3 (b) and (d), and Table F7.1).

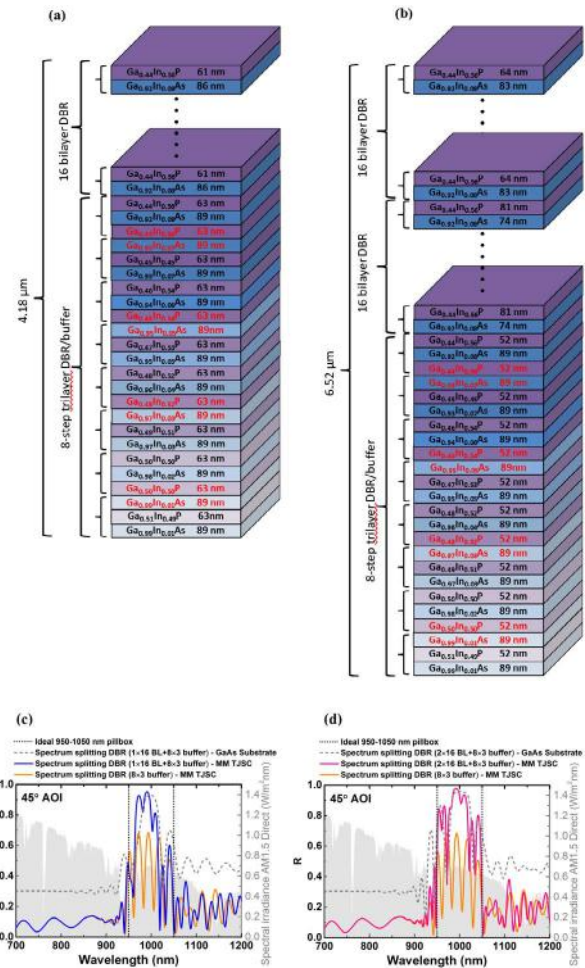


Figure F7.3: Improved spectrum splitting designs for an MM TJSC: (a) 8-step trilayer DBR/buffer with additional 16-bilayer DBR; (b) 8-step trilayer DBR/buffer with additional 2 × 16-bilayer DBR; (c) and (d) are the calculated specular reflectance for structure (a) and (b), respectively. The best case of Figure 7.3(c) (i.e. without the extra DBR) is included for comparison. The spectral reflectances of the various DBR designs on a 1- μm thick GaAs substrate are included to show the “bare” reflectance range (without overlying layers). An idealised pillbox band-reflect filter is also shown for comparison.

Note that the thickness of each trilayer (193–241 nm in Figure F7.2(b) and F7.3(a) and (b) in these proposed 8-step trilayer DBR/buffer structures, optimised for spectrum splitting to a Si cell, happens to be close to the optimum buffer step size (~250 nm) found experimentally for lattice-mismatched single-junction GaInAs/GaN buffer/GaAs solar cells (Levander & Geisz 2007), suggesting a compatibility of the optical DBR and physical buffer functions.

The photocurrent densities of the top, middle and bottom sub-cells of the MM TJSC with intermediate DBR/buffer and the efficiencies of all cells are calculated (Table F7.1). The AR coating is reoptimised for 45° AOI. For 45° AOI, the photocurrent density of the Ge bottom sub-cell is progressively reduced as expected due to reflecting/diverting the excess photocurrent with the additional DBR structures, while the top and middle sub-cells are not affected. The 2 × 16 bilayer + 8-trilayer DBR/buffer structure provides the desired spectrum splitting between the MM TJSC and a Si solar cell and yields the highest overall

efficiency. Figure F7.4(a) shows the modelled external quantum efficiency (EQE) of the original MM TJSC, and the modelled EQE of MM TJSC with optimised spectrum splitting DBR/buffer with the effective EQE of an additional Si cell shown in Figure F7.4(b). efficiency. Figure F7.4(a) shows the modelled external quantum efficiency (EQE) of the original MM TJSC, and the modelled EQE of MM TJSC with optimised spectrum splitting DBR/buffer with the effective EQE of an additional Si cell shown in Figure F7.4(b).

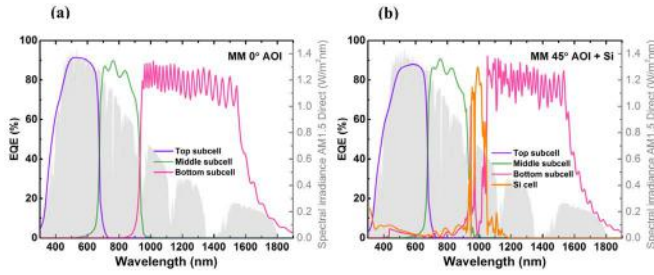


Figure F7.4: Modelled EQE of (a) the original MM TJSC @ 0° AOI and (b) the 4-junction spectrum splitting receiver consisting of the modified MM TJSC @ 45° AOI with optimised spectrum splitting DBR (2 x 16-bilayer DBR + 8-trilayer DBR/buffer) plus the Si cell.

For comparison with the AOI dependence of the Bragg filter, we include AOI data for a representative high performance dielectric band-pass filter, the exact filter we used to achieve the 40% efficiency world record (Figure F7.5). For AOI increasing from 0 to 80°, the cut-on and cut-off wavelengths of the dielectric filter blue-shifted by a massive 160 nm and 211 nm respectively, whereas the DBR filter exhibits shifts of only 37 nm and 41 nm for MM TJSC. The DBR filter therefore has a significant advantage over the dielectric filter when the incident light has a broad distribution of AOIs, which is the case for high concentration PV applications including RayGen's PV power tower system.

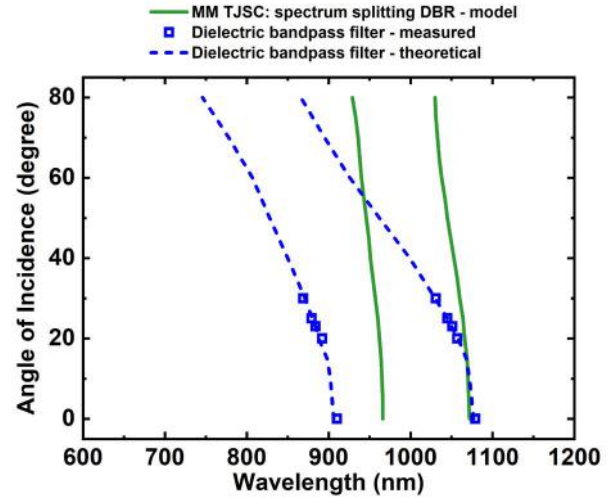


Figure F7.5: Simulated AOI dependence of the cut-on and cut-off wavelengths for two different approaches to spectrum splitting: intermediate DBR in a TJSC versus a dielectric filter.

Highlights

- A novel approach is proposed to enhance the performance of MM TJSC by integrating a DBR into the conventional buffer layer structure.
- For better practicality and cost-effectiveness, we demonstrated that the buffer layers in MM TJSCs could additionally function as a DBR for spectrum splitting applications.
- The intermediate DBR approach to spectrum splitting has the advantage of a greatly reduced angle-of-incidence dependence compared to a discrete dielectric filter.

Table F7.1: Calculated sub-cell photocurrent densities and MM TJSC + Si cell efficiencies for various DBR/buffer designs.

Device structure	J _{sc} top sub-cell (mA/cm ²)	J _{sc} middle sub-cell (mA/cm ²)	J _{sc} bottom sub-cell (mA/cm ²)	Efficiency MM TJSC (%)	Efficiency Si cell (%)	Efficiency total (%)
Original TJSC (DLAR, no DBR) @ 0° AOI	13.6	12.9	16.4	41.0	N/A	41.0
Original TJSC (DLAR, no DBR) @ 45° AOI	13.1	12.9	17.2	40.4	1.3	41.7
TJSC with 8-trilayer DBR/buffer @ 45° AOI	13.1	12.9	15.6	40.2	2.4	42.6
TJSC with spectrum splitting DBR (1 x 16-bilayer DBR + 8-trilayer DBR/buffer) @ 45° AOI	13.1	12.9	14.7	40.1	2.9	43.0
TJSC with spectrum splitting DBR (2 x 16-bilayer DBR + 8-trilayer DBR/buffer) @ 45° AOI	13.1	13.0	13.9	40.0	3.4	43.4

Note: The AR coating for 45° AOI is reoptimised. The concentration on the TJSC at 45° is 800/√2 = 566', the contribution from the Si cell is conservative because reflection from the metal on the TJSC is assumed lost and not captured by Si cell.

Future Work

- Fabricate and characterise TJSCs with spectrum splitting DBR.
- Practical design for 50% efficient spectrum splitting CPV receivers.

References

DIMROTH, F., GUTER, W., SCHÖNE, J., WELSER, E., STEINER, M., OLIVA, E., WEKKELI, A., SIEFER, G., PHILIPPS, S. P. & BETT, A. W. 2009. Metamorphic GaInP/GaInAs/Ge triple-junction solar cells with 41 % efficiency. 34th IEEE Photovoltaic Specialists Conference (PVSC), 7-12 June 2009. 001038-001042.

GUTER, W., SCHÖNE, J., PHILIPPS, S. P., STEINER, M., SIEFER, G., WEKKELI, A., WELSER, E., OLIVA, E., BETT, A. W. & DIMROTH, F. 2009. Current-matched triple-junction solar cell reaching 41.1% conversion efficiency under concentrated sunlight. *Applied Physics Letters*, 94, 223504.

LEVANDER, A. & GEISZ, J. 2007. Examination of Dislocations in Lattice-Mismatched GaInAs/Buffer Layer/GaAs for III-V Photovoltaics. *Journal of Undergraduate Research*, VII, 55-62.

LI, K. L., SUN, Y. R., DONG, J. R., HE, Y., ZENG, X. L., ZHAO, Y. M., YU, S. Z. & ZHAO, C. Y. 2015. Control of threading dislocations by strain engineering in GaInP buffers grown on GaAs substrates. *Thin Solid Films*, 593, 193-197.

F8 DETERMINATION OF DEFECT ENERGY LEVELS FROM INJECTION-DEPENDENT TRAPPING

Lead Partner

UNSW

Supervisor

Dr Mattias K. Juhl, Prof. Thorsten Trupke

Academic Partners

Australian National University: Prof. Daniel MacDonald

Arizona State University: Prof. Stuart Bowden

Fraunhofer ISE: Dr Martin Schubert

Funding Support

ACAP Fellowship

Aims

This fellowship investigates the use of transient photoconductance for the identification of defects via measuring “trapping” effects present in transient photoconductance data. Previous work by Haynes and Hornbeck (1955) and Hornbeck and Haynes (1955) demonstrated an elegant approach to analyse trapping, accounting for minority carrier capture, emission, recombination by the defect, and the total bulk recombination rate, with a complex solution:

$$\frac{1}{\tau_{pc}} = \frac{1}{c_{mj}N_{dop}} + \frac{1}{\frac{1}{e_{mn}} + \frac{\tau \times c_{mn} \times N_d(1-y)}{e_{mn}}} \quad (\text{Eq. F8.1})$$

Where τ_{pc} is the time constant measured by photoconductance, c_{mj} is the majority capture coefficient, e_{mn} is the minority carrier emission coefficient, c_{mn} is the minority carrier capture coefficient, τ is the effective lifetime of the sample, N_{dop} is the doping density, N_d is the defect density, and y is the fraction of unfilled defects. The present work takes a different approach, through preventing minority carrier recapture, the system of governing equations simplifies to a linear differential equation, which is easy to solve. It is postulated that carrier recapture can be prevented by increase minority carrier recombination, such as increasing the number of defects or surface recombination. When a two-state defect does not recapture minority carriers, the time constant measured by photoconductance is given by

$$\frac{1}{\tau_{pc}} = e_{mj} + e_{mn} + c_{mj}N_{dop} \quad (\text{Eq. F8.2})$$

Where e_{mj} is the emission rate of majority carriers. This result is promising, as this photoconductance time constant is independent of concentration of the defect (N_d), while dependent on the sample properties that can be measured, for example the doping density (N_{dop}). The time constant depends on all three of the Shockley-Read-Hall (SRH) defect parameters, with their impact modified by the

sample’s doping density. However, as the doping is typically on the order of $1 \times 10^{16} \text{ cm}^{-3}$, it typically dominates the photoconductance rate. The capture rate will dominate this time constant at room temperature unless the defect is closer than 180 meV from the closest band edge, a significant restriction. Thus, this approach is expected to allow study of the defect values, through variation of sample doping, with the rate expected to be primarily dominated by the majority carrier capture rate. However, to see these trapping rates the effective lifetime must be lower than τ_{pc} , something that does not occur for most silicon samples. Moreover, for highly recombination active defects, i.e. capture cross section $\approx 10^{-14} \text{ cm}^2$, the time constant will be in the range of nanoseconds for $1 \Omega \cdot \text{cm}$ p-type material. This can be a real barrier to such measurements, however these time constants are possible to be made if the effective lifetime of the sample is low enough.

Reduction of effective lifetime

A method to reduce the effective lifetime of a sample to access fast trapping time constants is critical to this method. The method must also not create extra trapping sites. The approach investigated here was to increase the surface recombination rate, via removal of surface passivation. Several wafers of different thicknesses were obtained. The samples were first passivated with SiN_x , to emulate how standard material is received, then had the SiN_x chemically stripped and surfaces cleaned. Their effective lifetime was then measured with a microwave-based conductivity tool (MDP-spot, Freiburg instruments), at the partner institute Fraunhofer ISE. The results are listed in Table F8.1 and highlight that wafer thinning enables sub-microsecond time constants to be accessed. It is clear, and well known, that the effective lifetime trends as the square of a surface limited sample lifetime. Thus, for fast time constant thinner samples can be used, with $<7 \mu\text{m}$ thickness required for ns time constants. More detailed analysis of the results provided that the average surface recombination velocity for these samples is $5 \times 10^3 \text{ cm s}^{-1}$ in agreement with previous studies (Mäckel & Cuevas 2003). This is significantly lower than the commonly assumed surface recombination velocity of $1 \times 10^7 \text{ cm s}^{-1}$ for an unpassivated surface, with a value of $5 \times 10^3 \text{ cm s}^{-1}$ limiting unpassivated wafers of standard thickness (200 μm) to only 4 μs . Boiling the wafers in deionised water has been shown to increase the surface recombination velocity for unpassivated wafers to $5 \times 10^5 \text{ cm s}^{-1}$ (Lim et al. 2013), resulting in lifetimes for 200 μm of 1.5 μs . Thus, removing surface passivation can be used to access trapping time in the microsecond range for wafers of standard thickness. This is similar to the fastest time constants that can be measured by deep-level transient spectroscopy (DLTS).

Table F8.1: Lifetimes of wafers with surface passivation on one or both sides.

Thickness (μm)	Passivaion	Lifetime (μs)	Seff (cm/s)
200	Single sided	10	6×10^3
45	None	0.7	4×10^3
30	Single sided	0.7	5×10^3

To demonstrate this approach and the above theory, the interstitial iron defect in silicon was investigated. The samples were 200 μm thick, $125 \pm 10 \Omega \cdot \text{cm}$, p-type silicon that was intentionally contaminated with iron. The sample had no surface passivation and was boiled in water for several minutes to increase its surface recombination velocity and reduce its effective lifetime. The effective lifetime reduced to 1.1 μs range expected from the above results for an infinite surface recombination. Using equation F8.2 interstitial iron is expected to provide a trapping time constant in such a sample of 7.5 μs ($\sigma_b = 7 \times 10^{-17} \text{ cm}^{-2}$, $N_d = 1 \times 10^{14} \text{ cm}^{-3}$, $V_{th} = 1.7 \times 10^7 \text{ cm}^2$) (Istratov et al. 1999). The transient photoconductance of the samples was measured with an MDP-spot. As iron can exist in two different states in p-type silicon, in either an iron–boron pair or as interstitial iron, measurements were made with it in both configurations. In the first measurement iron was bound as iron–boron, and no trapping is observed, as expected. The iron was then converted from the iron–boron defect into interstitial iron, by subjecting the sample to high-intensity light from a flash lamp. A second photoconductance measurement was then performed. The measurements showed an extra decay with a time constant of $6.5 \pm 0.5 \mu\text{s}$, as shown in Figure F8.1. The similarity with the predicted value (7.5 μs) supports the outlined theory, that defects can be observed as “traps”, and their relaxation time is a result of the recombination process, for example majority carrier capture, rather than the more commonly assumed emission process. This analysis was then applied to thermal donors in silicon, assuming they were single level, to extract their defect parameters (Zhu et al. 2019).

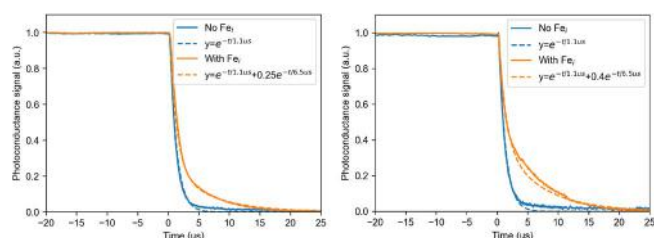


Figure F8.1: Measurement of interstitial iron as a trap in photoconductance data for two samples. The blue curve is for when the iron exists as bounded with an iron–boron complex, while the orange curve is when the iron is on interstitial sites.

Highlights

- To view defects as traps a sample's effective carrier lifetime must be reduced. Two methods were tested to reduce carrier lifetime which do not introduce defects into the material
- It was demonstrated that on standard material similar time constants are measurable as compared to DLTS, being several microseconds.
- It is suggested that most trapping in photoconductance is the result of majority carrier capture and not minority carrier emission. This was demonstrated using the well-studied defect on interstitial iron in silicon, which had its effective carrier lifetime reduced using the developed methods.

References

- HAYNES, J. R. & HORNBECK, J. A. 1955. TRAPPING OF MINORITY CARRIERS IN SILICON .2. N-TYPE SILICON. *Physical Review*, 100, 606-615.
- HORNBECK, J. A. & HAYNES, J. R. 1955. TRAPPING OF MINORITY CARRIERS IN SILICON .1. P-TYPE SILICON. *Physical Review*, 97, 311-321.
- ISTRATOV, A. A., HIESLMAIR, H. & WEBER, E. R. 1999. Iron and its complexes in silicon. *Applied Physics A*, 69, 13-44.
- LIM, S. Y., FORSTER, M., ZHANG, X., HOLTkamp, J., SCHUBERT, M. C., CUEVAS, A. & MACDONALD, D. 2013. Applications of Photoluminescence Imaging to Dopant and Carrier Concentration Measurements of Silicon Wafers. *IEEE Journal of Photovoltaics*, 3, 649-655.
- MÄCKEL, H. & CUEVAS, A. 2003. Determination of the surface recombination velocity of unpassivated silicon from spectral photoconductance measurements. Presented at the 3rd World Conference on Photovoltaic Energy Conversion, IEEE, 71-74.
- ZHU, Y., JUHL, M. K., COLETTI, G. & HAMEIRI, Z. 2019. Reassessments of Minority Carrier Traps in Silicon with Photoconductance Decay Measurements. *IEEE Journal of Photovoltaics*, 9, 652-659.

F10 TOWARDS A 50% EFFICIENT MULTIJUNCTION PV SYSTEM

Lead Partner

UNSW

UNSW Team

Dr Dongchen Lan

Funding Support

ACAP

Aim

The objective of this project is to find industrially viable methods capable to take photovoltaic (PV) energy conversion efficiencies to levels beyond present worldwide expectations. The project planned to assess existing limitations in state-of-the-art solar cell technologies (for example the world record spectrum splitting modules) and suggest improvements. This will include two main aspects, namely, designing new cell architectures and investigating novel photovoltaic materials, etc. In particular, perovskite solar cells as potential building blocks for next generation multi-junction PV systems will be investigated.

Progress

A. Next generation spectrum splitting approach

UNSW holds the current efficiency record for spectrum splitting photovoltaics (Green et al. 2016). In order to find feasible methods capable of enhancing the efficiency further, we first analysed the primary power losses in the existing system, where an external filter directed a portion of the sunlight normally wasted by commercial InGaP/InGaAs/Ge triple-junction cells to a silicon cell. We identified two primary efficiency loss mechanisms which are expanded as follows.

First, we realised that emissions from high- to low-bandgap cells are detrimental to the emitting cell's voltage. This is due to the cell's rear emissions increasing its dark saturation current (Lan & Green 2014). Our analysis shows that, if such rear emissions are reflected back for reabsorption, in the radiative limit where only radiative recombination occurs, the top two cells will have an increase of 0.067 V in its voltage with a total increase of 0.134 V for the tandem device (Lan & Green 2018c; Lan & Green 2018a; Lan & Green 2018b). This would give an absolute increase of $\sim 1.8\%$ in the tandem efficiency. For good real cells with radiative efficiencies $\sim 30\%$, the tandem voltage will have an increase of ~ 0.08 V, corresponding to an absolute increase of $\sim 1.1\%$ in the tandem efficiency part. Noticeably, the above data are for cells using concentrated sunlight and the relative improvements will be larger for one-sun modules since each cell operates at a lower voltage but with the same absolute improvement.

Second, we noticed that the current band-pass filter directs out light from 880 to 1030 nm (1.41 to 1.206 eV) only (Figure F10.1), suggesting that the Ge cell is still generating more photocurrent than

the top two cells hence still dissipating some power. The wavelength range for the directed light can be extended further to ~ 1190 nm (1.04 eV) where the Ge cell can generate just-matched photocurrent, unless it has significant defects resulting in too much bend in its I-V curve before reaching its maximum power point voltage. Noting that silicon has a bandgap of 1.11 eV, corresponding to 1120 nm, light of wavelengths above 1120 cannot be harnessed by a silicon cell. Hence, replacing the silicon cell by another high quality cell with a 1.04 eV or slightly lower bandgap, such as an InPAs cell, may improve the efficiency further. Compared with the old scheme where only light from 880 to 1030 nm is directed to the silicon cell, the current will be increased by $\sim 85.7\%$ and the voltage will be decreased by $\sim 6.3\%$. This can boost the detached single cell efficiency by $\sim 74\%$, corresponding to an absolute increase of $\sim 3.3\%$ in the detached cell efficiency part.

Hence, addressing the two power losses identified above can increase the overall photovoltaic energy conversion efficiency to 45% (40.6% + 1.1% + 3.3%).

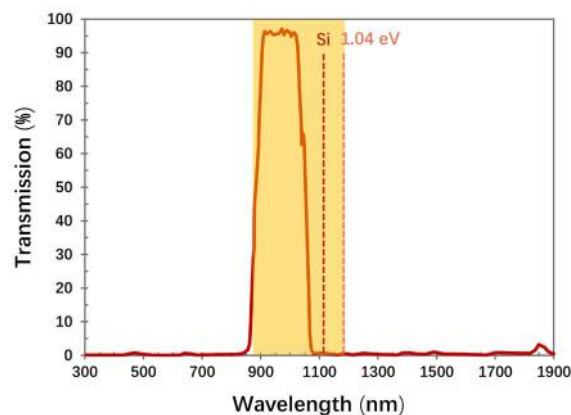


Figure F10.1: The actual (solid line) and ideal (shaded) transmission spectra of the band-pass filter in the state-of-the-art spectrum splitting photovoltaic module (Green et al. 2016). Note that the transmitted light here is light diverted to the Si cell (Lan & Green 2018).

Interestingly, filters with suitable optical windows built into the rear of the cells themselves can address the above two power loss mechanisms simultaneously. For instance, as shown in Figure F10.2, a filter capable of reflecting light of 750–1190 nm built into the rear of the 1.41 eV GaInAs cell can both reflect its rear emissions (750–900 nm) back for reabsorption and direct the extra light (900–1190 nm) to another cell for additional photovoltaic power production. Such built-in filters may be realised through Bragg-type structures that are essentially stacked thin-film layers of alternating high and low refractive indices. They use light interference to reflect certain wavelengths but transmit others. Key requirements of these thin-film optical layers include transparency to the wavelengths of interest and good conductivity of electricity.

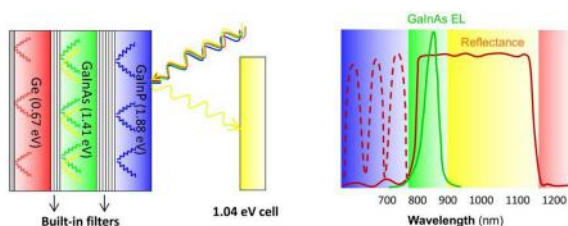


Figure F10.2. Schematics of (a) a proposed new spectrum splitting system with built-in filters and the silicon cell replaced by a slightly lower gap (1.04 eV) cell; and (b) the GaInAs electroluminescence and an effective rear filter's reflectance. Colours are indicative only (Lan & Green 2018).

The above concept may be further generalised by having two monolithic tandem cells with built-in filters, where a second tandem absorbs light directed out from the first tandem (Figure F10.3). This can improve the overall efficiency on two accounts. First, sunlight may be better harnessed with an increased number of cells of appropriate bandgaps. Second, splitting a long cell stack into two short stacks can reduce a range of mismatch issues that limit the performance of series-connected cells. Note that these include more than photocurrent mismatching. For instance, the lowest-bandgap cell normally has the largest dark saturation current which can move the operating points of the other series-connected cells away from their maximum power points. This can have a most severe impact on the performance of the highest-bandgap cell that normally has the smallest dark saturation current. Having two electrically separate tandems ensures that the lowest-bandgap cell can only lightly impact its series-connected medium-bandgap cells instead of all other cells with higher bandgaps.

Figure F10.3 shows an optimal design using the dual tandem concept where two monolithic cell stacks are lattice matched to the GaAs and InP wafer substrates. As one of our interests is to predict its practical performance, we conducted a realistic assessment for cells of $\sim 1 \text{ cm}^2$ area based on real data. With the state-of-the-art cell technologies, this design was predicted to have a practical efficiency of 51.0% at 300 suns and 51.7% at 500 suns, with an absolute further improvement of $\sim 1\%$ possible using built-in filters.

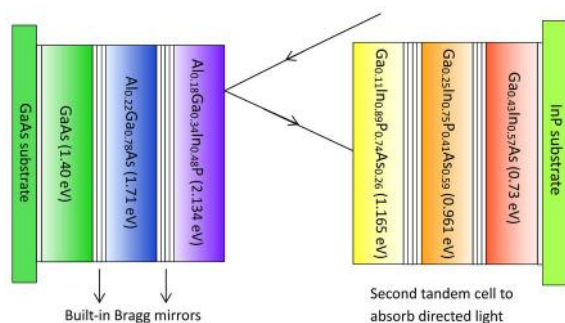


Figure F10.3: Conceptual design of a next generation spectrum splitting module consisting of two monolithic cell stacks lattice matched to GaAs and InP wafers. Each stack has built-in filters and is current matched (though not necessarily to the same value). Colours are indicative only (Lan & Green 2018).

We evaluated the feasibility of the above two developments, namely application of built-in filters and generalisation of concept, as a crucial step before eventual fabrication.

For the design of rear Bragg-type mirrors, current industrial facilities can deposit at least 32 optical layers onto the rear of a cell, which is sufficient to make an effective built-in filter. However, provided the filters can divide light appropriately, a minimal number of optical layers is desired as this would improve the electrical conductivity and lower the potential fabrication cost. This can be realised by noting two points. First, the built-in feature allows the requirements of filter properties over some wavelengths to be relaxed compared with external ones. Taking the 1.41 eV GaInAs cell in Figure F10.2 as an example, its rear filter's reflectivity for wavelengths below 800 nm would not matter because incident light of these wavelengths is largely absorbed before reaching its rear and the cell does not have appreciable self-emissions in this wavelength range. Second, instead of using repeated periods of optical layers, we may design chirped Bragg reflectors by tuning the thicknesses and refractive indices of certain optical layers for more desired reflection patterns.

For the implementation of dual tandem concept, each cell stack is designed to be current matched, though not necessarily to the same value. The first cell stack is lattice matched to a GaAs wafer substrate and the second is lattice matched to an InP wafer substrate. For the cells on the GaAs wafer, bandgaps between 1.40 and 2.30 eV are accessible using lattice matched solid solutions of GaAs, GaP, InP, AlP and AlAs (Vurgaftman et al. 2001). For the cells on the InP wafer, bandgaps between 0.73 and 1.40 eV are accessible using lattice matched solid solutions of GaAs, InAs, InP, AlAs and GaSb (Vurgaftman et al. 2001). Figure F10.3 shows a rather sophisticated 6-cell module that can take photovoltaic conversion of sunlight to efficiency levels beyond present worldwide expectations. But a much simpler 4-cell module consisting of 1.89/1.40 eV cells on the GaAs wafer and 1.041/0.73 eV cells on the InP wafer, is predicted to deliver an over 48% efficiency under 500 suns, which can already beat the current efficiency record for solar cells of any type.

Notably, the dual tandem approach will not only make better use of the solar spectrum but allow more flexibility in the filter design since the requirement on the spectral shape of the directed light can be significantly relaxed. In particular, the spectrum of the light directed out from the first tandem no longer needs to be a continuous band. It can even be two discrete parts with irregular shapes, which can still be well utilised by a second tandem cell with suitable bandgaps (Figure F10.4). A more flexible requirement on the reflectance spectrum is likely to lead to even fewer optical layers required to make an effective filter, which can result in both improved efficiencies and reduced fabrication costs.

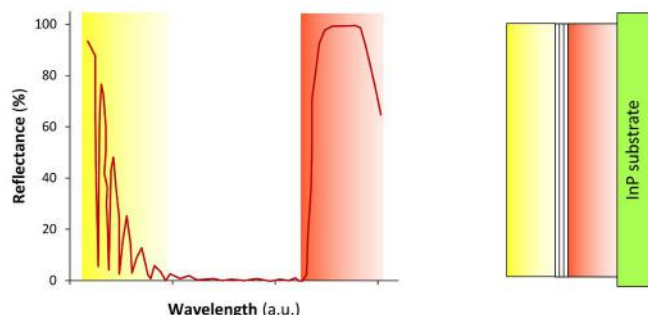


Figure F10.4: A schematic example of reflected spectrum consisting of two distinct parts (left) that can be well harnessed by a two-cell tandem stack (right). Colours are indicative only (Lan & Green 2018).

Compared with the monolithic architecture, having physically separate cells is also more compatible with future generation photovoltaics in the sense that low-cost photovoltaics often involve combining materials of vastly different properties (for example silicon and perovskites), where the traditional monolithic approach may be more restricted in some aspects.

B. Perovskite-based photovoltaic devices

Perovskite solar cells promise to reach the highest efficiencies at the lowest costs but the mobile ions create challenges in both cell measurements and performance improvement. Being able to understand the ion migration mechanism and its impacts would help to solve relevant issues and may open up opportunities for further development. Here, familiar knowledge in device physics is used to explain a range of ion-related issues in perovskite devices.

Figure F10.5(a) left shows a schematic of the electronic and ionic charge distributions under the dark equilibrium condition. Figure F10.5(b) left shows a schematic of how electrons move immediately after light turns on, when ionic charges have not moved much yet. Upon light illumination, the depletion region near contacts shrinks immediately under open circuit conditions. This suggests that the bulk region becomes wider and some ionic charges that were previously inside the depletion region are now in the bulk region. Before these bulk ionic charges move to their new equilibrium positions, electrons move rapidly to screen these ionic charges to make the bulk region remain quasi-neutral, in a direction opposing the photo generated current if the cell were connected to an external circuit. The electron screening reduces much of the ionic drift due to Coulomb force and suggests that the bulk ionic charges move to their new equilibrium positions through diffusion mainly. As the screening can reduce the Coulomb attraction between negative and positive ionic charges, it can make the ionic migration even slower. After sufficient illumination time, the mixed ionic-electronic system will reach a new equilibrium with new ionic and electronic distributions (Figure F10.1(c) left). The continuing electron redistribution with the ion migration helps to keep the bulk neutrality, in a way similar to the more familiar screening process in plasmonics but with much slower speed. This electron redistribution process has great implications for the impact on device characterisation and performance.

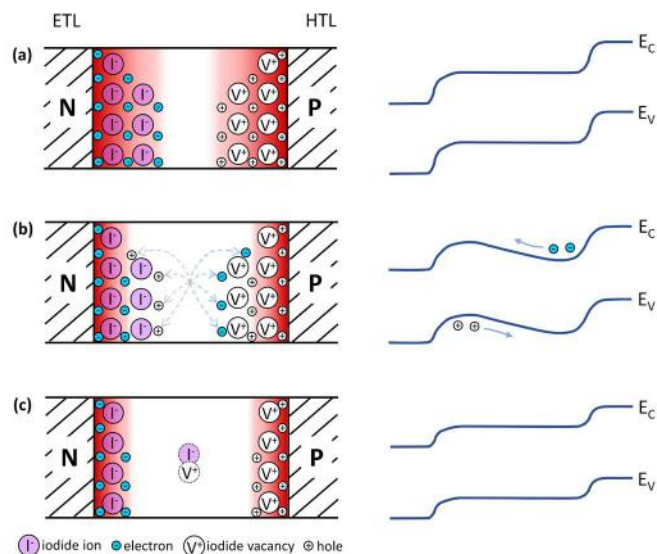


Figure F10.5: Schematics of ionic and electronic carrier distributions (left) and corresponding band diagrams (right) for three situations of interest: (a) the dark equilibrium; (b) immediately after light turns on; and (c) after prolonged illumination. The red-colour shaded region is the depletion region with the shade grading indicating the electric field strength (Lan 2019).

The hysteresis in I-V curves can be well understood following above considerations of the depletion edge moving during the scanning process and the resulting time-varying ionic and electronic distributions. Noting the depletion region width will reduce with an increasing forward bias, scanning from short-circuit to forward-bias under illumination will cause the depletion region to shrink towards the contact during the process, thereby widening the bulk region. Hence, an increasing volume of ionic charges that were in the depletion region before will become in the bulk region that expands with the scanning. Before these ionic charges move slowly to new equilibriums, electrons and holes move rapidly in response to the ionic fields. Most of the redistributed electrons and holes are actually semi-bounded due to their mobilities being significantly limited by the ionic field. This causes a bending in the perovskite band diagram (see the right of Figure F10.5(b)) and macroscopically a reduction in the overall currents, which can recover as ionic charges move to new equilibriums.

Slow time-evolution of photoluminescence (PL) exhibited by perovskite cells has attracted great attention since the rapid emergence of this area. This feature has been shown to be related to ion migration using experiments but the physics is not well understood yet. Figure F10.5 shows that ion migration causes electron redistribution. The electron redistribution will affect the Shockley-Read-Hall and Auger processes differently. Depending on which one of the two non-radiative processes changes more, it may lead to either an increase or a decrease in the overall non-radiative recombination rate, hence either PL quenching or PL enhancement over time as ionic charges move to new equilibriums.

Ion migration can also impact cell performance by affecting the electron distribution inside the perovskite layer. On the one hand, the depletion edge movement due to changes in the cell-operating condition will cause ions to move slowly to their new equilibriums.

Consistently, the electron distribution will change over time with the slow ion migration, as argued previously. This can at least partly explain why perovskite solar cells are unstable with their properties changing over time. On the other hand, whether ionic charge distribution should positively or negatively affect the cell performance depends on a range of factors such as the material quality and cell-operating conditions, consistent with how it affects the non-radiative processes discussed previously. We can confidently state that the bulk ionic charge distribution can lead to spatially varying bulk electron-hole distributions due to charge balance. This is likely to suppress non-radiative recombination when the Shockley-Read-Hall process dominates, thereby improving the cell performance; but it is likely to increase non-radiative recombination when the Auger process dominates, thereby reducing the cell performance. Since the bulk ion distribution changes with the cell-operating condition, the impact of bulk ion distribution on cell performance discussed above reveals one previously unaddressed mechanism for variations in the perovskite cell performance.

Highlights

- Built-in filters can both divide the sunlight appropriately for sub-cells and reduce voltage losses due to rear emissions, pushing the efficiency to ~45%.
- Two tandem cell stacks can make 50% system efficiency a realistic task with state-of-the-art technologies.
- Tardy ionic charges can distort the perovskite bands hence reducing the net currents before they move to new equilibriums, causing the hysteresis effect.
- Ion migration affects the Shockley-Read-Hall and Auger processes differently, hence may either reduce or increase the ratio of radiative to non-radiative recombination.
- Ion migration may lead to PL quenching, enhancement or staying the same, depending on which recombination process changes more as ions migrate.
- Ion migration may lead to device performance improvement and degradation due to the same mechanism as for the PL enhancement and quenching.

Future Work

- Investigate perovskite devices at the module level.
- Find the reciprocity relation between the PL from photovoltaic materials and the PL from devices made of those materials (valuable for predicting the performance of devices using novel materials).

References

- GREEN, M. A., KEEVERS, M. J., CONCHA-RAMON, B., JIANG, J., VERLINDEN, P. J., YANG, Y. & ZHANG, X. 2016. 37% Efficient One-Sun Minimodule and over 40% Efficient Concentrator Submodules, 32nd EU PVSEC. *Munich, June* (2016).
- LAN, D. 2019. The physics of ion migration in perovskite solar cells: Insights into hysteresis, device performance, and characterization. *Progress in Photovoltaics: Research and Applications*.
- LAN, D. & GREEN, M. A. 2014. Ideal solar cell equation in the presence of photon recycling. *Journal of Applied Physics*, 116, 174511.
- LAN, D. & GREEN, M. A. 2018a. Pathways towards a 50% efficiency spectrum-splitting photovoltaic system: Application of built-in filters and generalization of concept. *Energy Procedia*, 150, 83-86.
- LAN, D. & GREEN, M. A. 2018b. The potential and design principle for next-generation spectrum-splitting photovoltaics: Targeting 50% efficiency through built-in filters and generalization of concept. *Progress in Photovoltaics: Research and Applications*, 1-6.
- LAN, D. & GREEN, M. A. 2018c. The potential and design principle for next-generation spectrum-splitting photovoltaics: Targeting 50% efficiency through built-in filters and generalization of concept. 35th EU PVSEC. *Brussels*, September, 951-955.
- VURGAFTMAN, I., MEYER, J. & RAM-MOHAN, L. 2001. Band parameters for III-V compound semiconductors and their alloys. *Journal of Applied Physics*, 89, 5815-5875.

F11 NEW IMPURITY REMOVAL TECHNOLOGIES FOR LOW-COST, HIGH EFFICIENCY SILICON SOLAR CELLS

ACAP Fellow

Dr AnYao Liu, ANU

Academic Partners

UNSW: A/Prof. Ziv Hameiri

Aalto University (Finland): Toni Pasanen, A/Prof. Hele Savin

Funding Support

ACAP

Aim

The aim of this project is to understand and develop new gettering technologies in silicon solar cells, namely gettering by dielectric films, and gettering by poly-silicon passivating contacts.

Progress

Project resumed on 1 August 2019 after a one-year parental leave.

One part of the project is to understand the gettering effects of plasma-enhanced chemical vapour deposited (PECVD) silicon nitride (SiN_x) films. For this, we investigated the correlations between gettering rates and bulk film properties, which are the refractive indices, Si-N, N-H, Si-H bond densities, and hydrogen fraction. No clear correlations were observed, but the results indicated that most PECVD SiN_x films have such gettering effects. This work was published in IEEE Journal of Photovoltaics (Liu et al. 2018). This publication is listed here as the publication details were not documented in the 2018 report.

To understand the gettering effects of PECVD SiN_x films for other metals, gettering of Cu, Ni, Cr and Fe in p-type high-performance multicrystalline silicon (HP mc-Si) wafers was studied. The concentration and distribution of these metals in SiN_x film were examined by secondary ion mass spectrometry (SIMS). The gettering effect of SiN_x films for metals other than Fe was confirmed by this study. SiN_x films were also shown to be as effective as conventional phosphorus diffusion gettering, if an appropriate temperature-time profile was chosen. This work was published in Journal of Applied Physics (Liu et al. 2019). A similar work was carried out to examine SiN_x gettering for cast-monocrystalline silicon materials, and the results further confirmed the gettering effects of SiN_x for metallic impurities such as Cu, Ni, Cr and Fe (Sun et al. 2019).

The distribution of impurity at the SiN_x/Si near-surface region was studied by SIMS, as shown in Figure F11.1. Results show that, despite the different gettered Fe concentrations, gettering occurs at the SiN_x/Si interface, rather than within the bulk of the SiN_x film, as previously observed in (Liu et al. 2016). This finding counters the suspicion (Liu et al. 2019) that distribution could relate to the impurity concentration. The exact reason for the different Fe profiles in (Liu et al. 2019) and (Liu et al. 2016) remains unknown and will be further investigated.

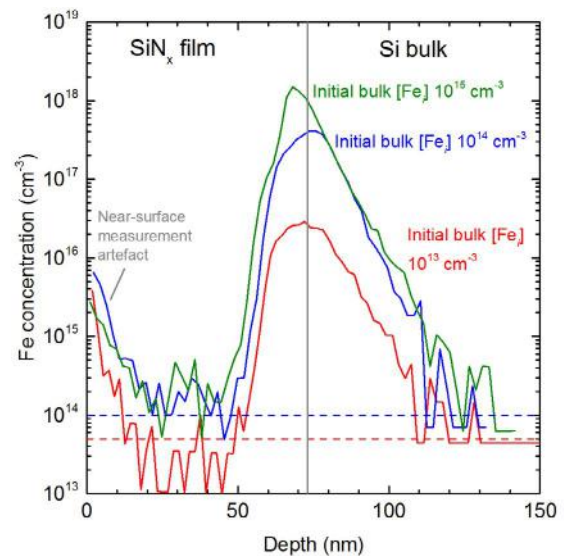


Figure F11.1: Fe distribution at the near-surface region of SiN_x/Si for samples with different gettered Fe concentrations.

To fully unravel the mechanisms underlying the gettering effects of PECVD SiN_x films, further work is currently underway. One aspect is to examine the impact of film interface properties on the gettering effectiveness, as the SiN_x/Si interface is shown to be the dominant gettering site in Figure F11.1. Capacitance-voltage (C-V) measurements, both from contact-MOS and non-contact approaches, are currently being tested for extracting information about the interface defect density and charge density. This has been challenging due to the leaky nature of the films. Another aspect is investigation of the correlation between film deposition temperature and gettering effectiveness (Liu et al. 2018). This may relate to the film density, and/or crystallinity. Fe-contaminated samples with SiN_x films of different deposition temperatures, from both ANU and UNSW PV laboratories, are currently being prepared for this experiment.

The second part of the project aims to further understand gettering by aluminium oxide (AlO_x) films from atomic layer deposition (ALD). As gettering takes place by accumulating metals at the dielectric/Si interface, how gettering affects the passivation quality of the films is of a primary concern. To address this question, samples with and without intentional Fe contamination and AlO_x gettering were prepared, and surface passivation was assessed and compared. Surface passivation quality was quantified by carrier lifetimes and C-V measurements of the interface properties. Some of the preliminary results are shown in Figure F11.2. As shown in Figure F11.2, samples with and without Fe gettered to the surface AlO_x/Si regions demonstrate similar interface properties in terms of the interface defect density and total charge density. This suggests that gettering, in other words the accumulation of impurities at the AlO_x/Si near-surface regions, may not have a significant impact on the passivation quality of the films. However, further tests are required to confirm our early findings.

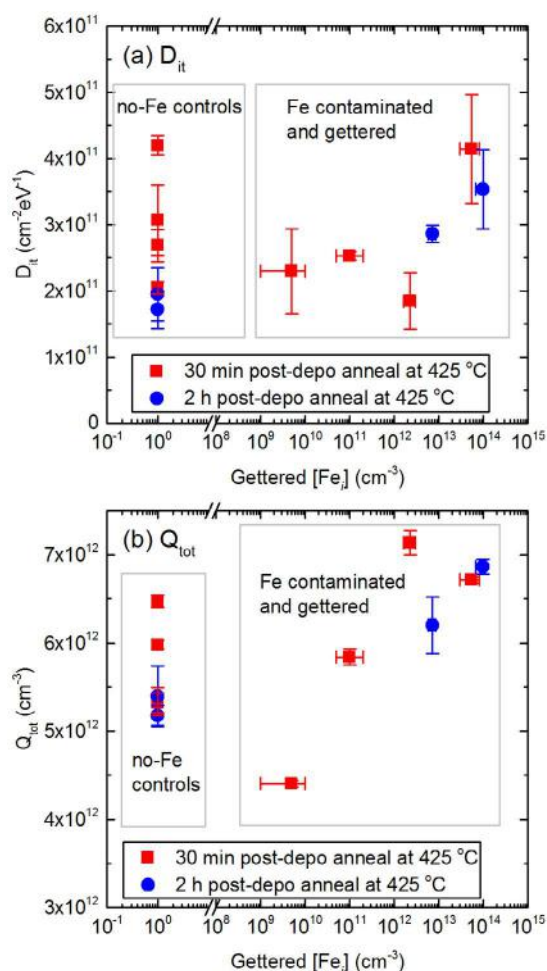


Figure F11.2: Comparison of the interface defect density (a) and total charge density (b) of samples with and without Fe contamination and gettering to the surface AlO_x regions. Non-contact C-V was used to measure the film interface properties.

The third part of the project is about studying the gettering effects associated with poly-silicon passivating contact formation processes. Our previous work indicated that in diffusion-doped p+ passivating contacts, boron-rich layers act as the main gettering layers in the poly-Si structure (Liu et al. 2018b). Therefore, questions remain as to whether or not gettering occurs in other p+ contact formation techniques, such as in-situ doping from PECVD and ion implantation into low pressure chemical vapor deposition (LPCVD) poly layers, where boron-rich layers may or may not be present. Experiments are currently being planned, in collaboration with other institutes where poly-Si contacts are fabricated by these other techniques.

Highlights

- SiN_x gettering of metallic impurities in addition to Fe is demonstrated for the first time.
- Impurity distribution at the near-surface region of SiN_x/Si is investigated.
- Preliminary results on the effect of gettering on passivation quality of ALD AlO_x films are obtained.
- Publication of two journal papers (Liu et al. 2018 – included here as it was not previously reported; Liu et al. 2019).
- Two oral presentations at international conferences, with one being an invited speaker (Liu et al. 2019a – invited speaker, 2019b).

Future Work

- Identify and investigate properties of PECVD SiN_x films that affect their gettering effectiveness, as well as the impurity distribution.
- Confirm and understand the effect of gettering on passivation quality of ALD AlO_x films.
- Examine the gettering effects of PECVD in situ doped, and LPCVD + ion implantation doped, p+ poly-silicon passivating contacts.

References

- LIU, A.Y. 2019. An overview of gettering by deposited thin films in silicon solar cells. 6th Asia-Pacific Solar Research Conference, Canberra, December 2019.
- LIU, A. Y., HAMEIRI, Z., WAN, Y. M., SUN, C. & MACDONALD, D. 2019. Gettering Effects of Silicon Nitride Films From Various Plasma-Enhanced Chemical Vapor Deposition Conditions. *IEEE Journal of Photovoltaics*, 9, 78-81.
- LIU, A.Y. & MACDONALD, D. 2019. Impurity gettering to deposited thin films in silicon photovoltaic materials. 18th Conference on Gettering and Defect Engineering in Semiconductor Technology, Zeuthen, August 2019.
- LIU, A. Y., SUN, C., MARKEVICH, V. P., PEAKER, A. R., MURPHY, J. D. & MACDONALD, D. 2016. Gettering of interstitial iron in silicon by plasma-enhanced chemical vapour deposited silicon nitride films. *Journal of Applied Physics*, 120.
- LIU, A. Y., SUN, C., SIO, H. C., ZHANG, X. Y., JIN, H. & MACDONALD, D. 2019. Gettering of transition metals in high-performance multicrystalline silicon by silicon nitride films and phosphorus diffusion. *Journal of Applied Physics*, 125.
- LIU, A. Y., YAN, D., WONG-LEUNG, J., LI, L., PHANG, S. P., CUEVAS, A. & MACDONALD, D. 2018. Direct Observation of the Impurity Gettering Layers in Polysilicon-Based Passivating Contacts for Silicon Solar Cells. *ACS Applied Energy Materials*, 1, 2275-2282.
- SUN, C., LIU, A. Y., SAMADI, A., CHAN, C., CIESLA, A. & MACDONALD, D. 2019. Transition Metals in a Cast-Monocrystalline Silicon Ingot Studied by Silicon Nitride Gettering. *Physica Status Solidi-Rapid Research Letters*, 1900456.

F12 BLOCK COPOLYMERS FOR HIGH PERFORMANCE, THERMALLY ROBUST ORGANIC PHOTOVOLTAIC DEVICES VIA AN INDUSTRIALLY RELEVANT PRINTING PROCESS

Lead Partner

UoM

UoM Team

Dr Valerie Mitchell, Dr David Jones, Gagandeep Ahluwalia

Academic Partners

Melbourne Energy Institute: Prof. Mukundan Thelakkat (University of Bayreuth), A/Prof. Chris McNeill (Monash University), Dr Mei Gao (CSIRO Manufacturing Flagship, Victoria)

Funding Support

ACAP, MEI

Aim

The objective of this project is to increase the industrial viability of organic photovoltaics through the design, synthesis and application of amphiphilic donor-acceptor block copolymers. This will be accomplished by the development of new synthetic routes which are capable of incorporating high performance polymers into diblock copolymers in a controlled and reproducible manner. Upon their successful synthesis, these new materials will then be optimised in a large-scale printing process of high-efficiency organic photovoltaic devices with enhanced thermal stability and reproducibility.

Progress

The success of this project relies on the development of synthetic routes capable of producing asymmetric aromatic cores which can be polymerised to form an asymmetric polymer with a single reactive terminus. This design will allow controlled coupling of the donor and acceptor polymers to produce a well-defined block copolymer product. This is in contrast to the traditional synthetic polymerisation routes which rely on random cross-couplings of symmetric monomers and produces polymer products with a distribution of reactive end-groups. As a second material design parameter, a series of donor monomers with side-chains of varying hydrophilicity have been synthesised and will be employed to generate a series of amphiphilic block copolymers with enhanced self-assembly properties, a strategy we have developed previously (Mitchell et al. 2017).

During this period, significant progress has been made in the synthesis of the asymmetric monomers and related homopolymers. The library of target materials was expanded to include a second acceptor material, and now includes a single donor core with three side-chain variants and two acceptor materials. This will allow the synthesis of a series of donor-acceptor block copolymers in order to identify the highest performing combination. In addition to the asymmetric monomer synthesis, polymerisation techniques capable of producing a desired molecular weight have been investigated. This has involved the

evaluation of potential catalyst systems for the individual monomers and is essential for the production of consistent block copolymer molecular weights capable of achieving well-defined morphologies as shown in Figure F12.1. The precise control of polymerisation via reaction conditions and catalyst choice will also enable the tailoring of donor and acceptor domain size for optimum photocurrent generation.

A key benefit of the block copolymer design is the morphological control it affords. In order to probe this morphological behaviour, X-ray scattering techniques using synchrotron radiation are often required. It is key for the success of this project that expertise in synchrotron techniques is developed. This year the University of Melbourne team submitted three successful beamtimes on the SAXS/WAXS beamline of the Australian Synchrotron. During these experiments a large body of valuable data was collected, and inexperienced students were trained on the use and interpretation of this valuable technique, which is expected to contribute significantly to this program in the future.

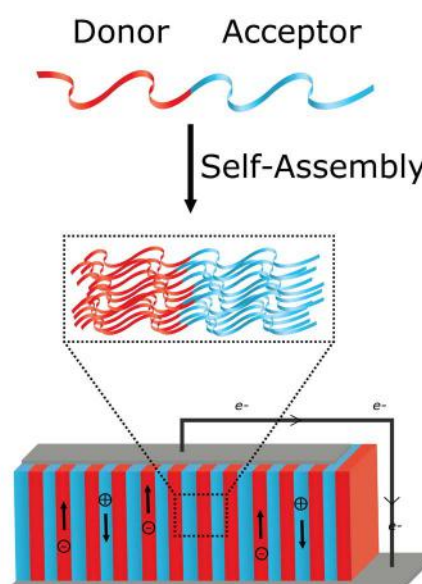


Figure F12.1: Illustration of donor-acceptor block copolymer self-assembly to form an ideal morphology for organic photovoltaic devices.



Figure F12.2: Dr Mitchell adjusting the sample stage at the SAXS/WAXS beamline of the Australian synchrotron.

- Expansion of the asymmetric donor and acceptor monomer and homopolymer library.
- Three successful applications for beamtime at the SAXS/WAXS beamline of the Australian Synchrotron.

Future Work

- Optimise polymerisation conditions to achieve molecular weight control.
- Incorporate the donor and acceptor materials into block copolymers.
- Characterise and optimise the block copolymer film morphology.
- Scale-up of block copolymer synthesis and device fabrication.

References

MITCHELL, V. D., E. GANN, S. HUETTNER, C. R. SINGH, J. SUBBIAH, L. THOMSEN, C. R. MCNEILL, M. THELAKKAT AND D. J. JONES (2017). "Morphological and Device Evaluation of an Amphiphilic Block Copolymer for Organic Photovoltaic Applications." *Macromolecules* 50(13): 4942-4951.

Highlights

- Contribution to the following peer reviewed publications:

LEE, C., MITCHELL, V. D., WHITE, J., JIAO, X., MCNEILL, C. R., SUBBIAH, J. & JONES, D. J. 2019. Solubilizing core modifications on high-performing benzodithiophene-based molecular semiconductors and their influences on film nanostructure and photovoltaic performance. *J. Mater. Chem. A*, 7, 6312-6326.

LEE, C. J., JRADI, F. M., MITCHELL, V. D., WHITE, J., MCNEILL, C. R., SUBBIAH, J., MARDER, S. & JONES, D. J. 2020. A structural study of p-type A-D-A oligothiophenes: effects of regioregular alkyl sidechains on annealing processes and photovoltaic performances. *Journal of Materials Chemistry C*, 8, 567-580.

MASOOMI-GODARZI, S., LIU, M., TACHIBANA, Y., MITCHELL, V. D., GOERIGK, L., GHIGGINO, K. P., SMITH, T. A. & JONES, D. J. 2019. Liquid Crystallinity as a Self-Assembly Motif for High-Efficiency, Solution-Processed, Solid-State Singlet Fission Materials. *Advanced Energy Materials*, 9(31), 1901069.

SAJJAD, M. T., ZHANG, Y., GERAGHTY, P. B., MITCHELL, V. D., RUSECKAS, A., BLASZCZYK, O., JONES, D. J. & SAMUEL, I. D. W. 2019. Tailoring exciton diffusion and domain size in photovoltaic small molecules by annealing. *J. Mater. Chem. C*, 7, 7922-7928.

F13 MULTISCALE AND DEPTH-RESOLVED SPECTRAL PHOTOLUMINESCENCE FOR CHARACTERISING SOLAR CELLS

Lead Partner

ANU

ANU Team

Dr Hieu Nguyen

Academic Partners

National Renewable Energy Laboratory (NREL), UNSW

Funding Support

ACAP

Aim

The objective of this project is to develop a class of novel spectral photoluminescence (PL) mapping and imaging techniques to identify and characterise important properties of various materials and structures employed in photovoltaics (PV) with ultra-high spatial resolution.

Progress

The first topic is to develop a contactless, non-destructive approach to study degradation across perovskite and perovskite/silicon tandem solar cells. The technique employs spectrally and spatially resolved absorptivity at sub-bandgap wavelengths of perovskite materials, extracted from their PL spectra, as shown in Figure F13.1. Parasitic absorption in other layers, carrier diffusion, and photon smearing phenomena are all demonstrated to have negligible effects on the extracted absorptivity. The absorptivity is demonstrated to reflect real degradation in the perovskite film and is much more robust and sensitive than its PL spectral peak position, representing its optical bandgap, and intensity. The technique is applied to study various common factors which induce and accelerate degradation in perovskite solar cells (PSCs) including air and heat exposures and light soaking. Also, it is employed to extract the individual absorptivity component from the perovskite layer in a monolithic perovskite/silicon tandem structure. The results demonstrate the value of this approach for monitoring degradation mechanisms in perovskite and perovskite/silicon tandem cells at early stages of degradation and various fabrication stages. This research has been published in *Advanced Energy Materials* (Nguyen et al. 2019a) and selected as an issue's inside back cover.

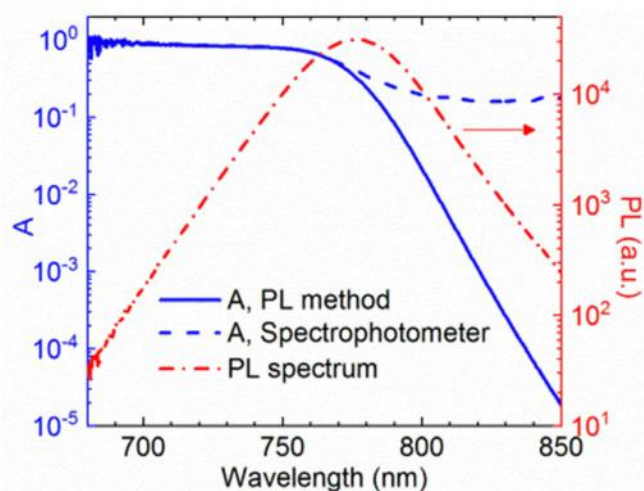


Figure F13.1: Comparison of spectrophotometer-based and PL-based absorptivity spectra. The spectrophotometer-based curve was captured at the centre of a PSC with a spot size of ~ 2 mm in diameter. The PL-based curve was averaged from the centre of a PL map (2 mm \times 2 mm).

As an example, Figure F13.2 shows evolutions of PL intensities, spectral peak locations (i.e. approximate optical bandgaps), and absorptivity at various wavelengths from a PSC left at a room condition ($\sim 25^\circ\text{C}$, $35\% \pm 15\%$ relative humidity). The sub-bandgap absorptivity map (row 4) clearly shows that the air slowly invades the solar cell through the edge of the gold contact when the cell is exposed in the atmosphere. Various localised degraded regions can also be observed, as indicated by the white circles (row 4, absorptivity at 800 nm). Both the edges and localised regions display similar evolutions with time. Therefore, the localised spots must be affected by the air exposure over time due to pinholes on the gold contact as this is the only way the air can penetrate the locations without passing across the edge.

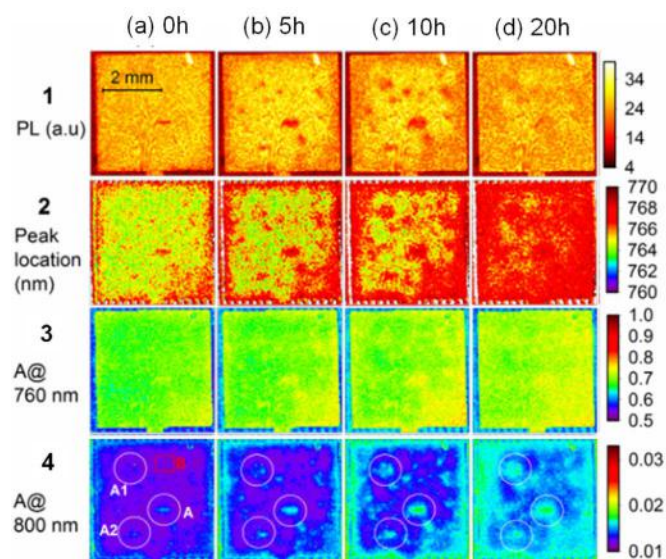


Figure F13.2: PL intensity, spectral peak location and extracted absorptivity maps of a perovskite solar cell versus exposure time in a room atmospheric environment.

Beside a stronger sensitivity than the spectrophotometer-based method, another advantage of the PL-based method is to separate absorptivity values of perovskite and silicon cells in monolithic perovskite/silicon tandem solar cells (Figure F13.3). From the absorptivity spectrum of the perovskite layer (extracted from its PL spectrum) and the total absorptivity spectrum of the tandem structure (measured by a spectrophotometer), one can extract the remaining absorptivity spectrum of other layers (including the bottom silicon solar cell, interlayers, and top layers of the perovskite solar cell). Around the optical bandgap of the perovskite material (790 nm), the absorptivity of the perovskite layer is ~40–50% and thus there is still a significant fraction of light absorbed in other layers. Combining the PL-based and spectrophotometer-based methods, we can separate the absorption inside the perovskite film from the entire tandem structure around the perovskite optical bandgap, which is otherwise impossible with the conventional spectrophotometer method alone. Although these results are preliminary, they demonstrate the high value of the technique to study degradation in tandem cells (mainly happen in the perovskite cell) by monitoring the absorptivity at sub-bandgap wavelengths of the perovskite film.

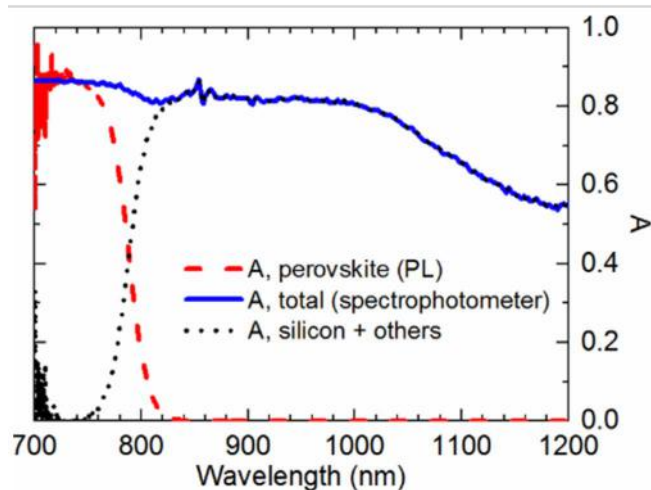


Figure F13.3: Various absorptivity components from a monolithic perovskite/silicon tandem solar cell.

The second topic is to advance the understanding of microscopic structural and optoelectronic properties of doped polycrystalline silicon (poly-Si) films employed in passivating contact solar cells, and to develop a luminescence-based method to quickly track hydrogen content inside the films. The ANU team's poly-Si films are fabricated from plasma-enhanced chemical vapour deposition (PECVD) amorphous Si films followed by thermal diffusion processes at high temperatures. However, the poly-Si films still contain both amorphous (a-) and crystalline (c-) Si phases, as shown by the transmission electron microscope (TEM) image in Figure F13.4(a). These different Si phases yield very distinct PL peaks at low temperatures (Figure 13.4(b)), compared to the c-Si substrate.

After high temperature diffusion processes to form the doped poly-Si films, most of the hydrogen content has effused out of the films, leaving them un-hydrogenated. Un-hydrogenated amorphous Si (a-Si) contains a very high density of non-radiative defects, yielding no PL

signal. Once hydrogenated, the a-Si:H phase will emit a strong PL peak in which the intensity is proportional to the hydrogen content inside the films. Tracking the a-Si:H PL emission, the team can study the effectiveness and mechanisms of various hydrogenation techniques on different poly-Si films. Their findings and the various applications of their method have been reported in a series of four journal papers (Nguyen et al. 2018; Truong et al. 2019a, b, c).

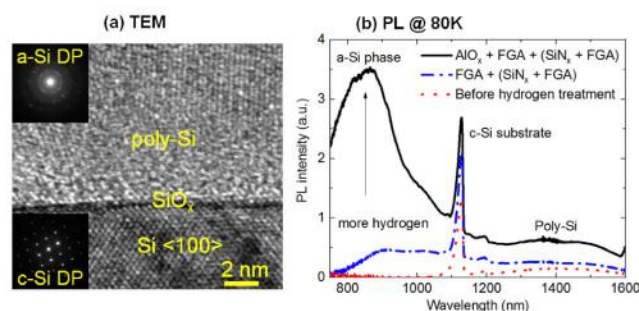


Figure F13.4: (a) Doped poly-Si films contain both amorphous (a-Si) and crystalline phases (c-Si). (b) Photoluminescence from the a-Si phase in poly-Si films indicates the effectiveness of various hydrogen treatments.

The third topic is to develop a PL-based technique to determine dopant profiles of localised boron diffused regions in c-Si wafers and solar cell precursors. It is fast, contactless and non-destructive. The measurements can be performed at room temperature with micron-scale spatial resolution. The ANU team has applied the technique to reconstruct dopant profiles of a large-area boron diffused sample and heavily doped regions (30 μm in diameter) of passivated emitter rear locally diffused (PERL) solar cell precursors. The reconstructed profiles are confirmed with the well-established electrochemical capacitance voltage (ECV) technique. The developed technique helps quickly determine boron dopant profiles in small doped features employed in c-Si solar cells.

During a thermal boron diffusion process, if the boron-rich layer is removed before the final thermal drive-in step (i.e. the dopant source is finite), the resultant dopant profile can be fitted with a Gaussian function (Figure F13.5):

$$N(z) = N_p \times \exp \left[\frac{-(z - z_p)^2}{z_l^2} \right] \quad (\text{Eq. 1}),$$

where N_p is the peak dopant concentration, z_p is the depth at which the peak locates, and z_l is a depth factor. Therefore, it is possible to reconstruct the dopant profiles using Eq. 1 given that PL spectra from boron diffused regions can be converted into the parameters $\{N_p, z_p, z_l\}$.

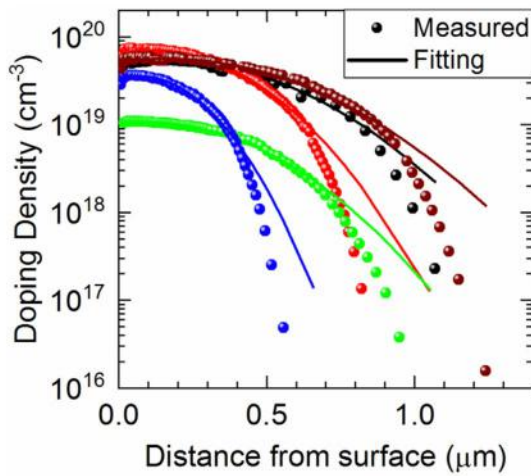


Figure F13.5: ECV dopant profiles of some boron diffused samples and their corresponding Gaussian fits using Eq. 1.

At low temperatures ~ 80 K, a diffused c-Si sample emits two distinct PL peaks associated with the substrate and the diffused layer (Figure F13.6(a)). At room temperature, although the two PL peaks are indistinguishable due to thermal broadening effects, the effect of the diffused layer is still noticeable at the long wavelength side of the normalised PL spectrum (Figure F13.6(b)). Moreover, by varying excitation wavelengths, the long wavelength side varies significantly due to the different penetration depths of the light in the sample (Figure F13.6(c)). These two characteristics, the relative intensity at the long wavelength side and its change versus excitation wavelength, are unique for a certain diffusion dopant profile. From fifteen boron diffused samples with known dopant profiles, the team establishes calibration curves to extract $\{N_p, z_p, z_b\}$ based on the two spectral characteristics.

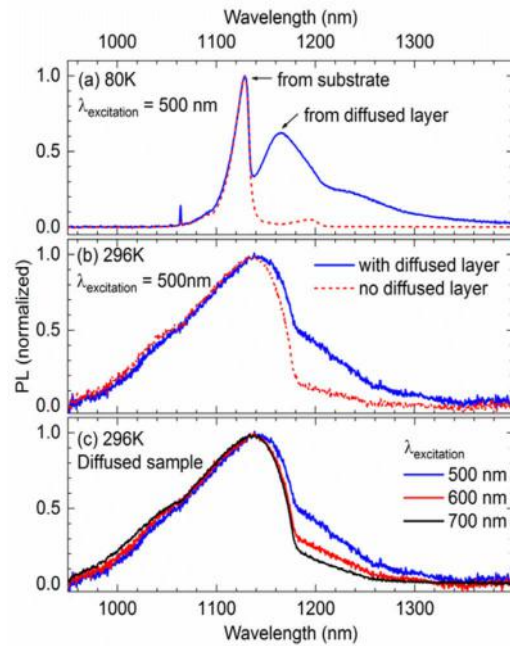


Figure F13.6: Comparison of normalised PL spectra from c-Si samples with and without a diffused layer at (a) 80 K and (b) 296 K, captured with the 500 nm excitation wavelength. (c) PL spectra from the diffused wafer with various excitation wavelengths at 296 K.

The technique is then demonstrated to re-establish dopant profiles of a localised p+ region of a PERL solar cell precursor (Figure F13.7). Micro-PL spectroscopy (micro-PLS) mapping is performed around a localised p+ region using the 500 nm and 600 nm excitation wavelengths. The map provides an entire spectrum for every pixel in the X-Y map, allowing an extraction of the PL intensity at various wavelengths with micron-scale spatial resolution. Based on the two spectral characteristics, the relative intensity at the long wavelength side and its change with 500 nm and 600 nm excitation light, of every single pixel, N_p , z_p , and z_b maps can be extracted (Figure F13.7(a) and F13.7(b)) using the calibration curves. The reconstructed dopant profile at the centre of the p+ region reasonably matches the measured dopant profile on a test location (1 cm \times 1 cm diffused region on the PERL precursor) (Figure F13.7(c)). The sheet resistances calculated from the reconstructed and measured dopant profiles are 67 and 60 Ω/\square , respectively. This work has been published in Scientific Reports (Nguyen et al. 2019b).

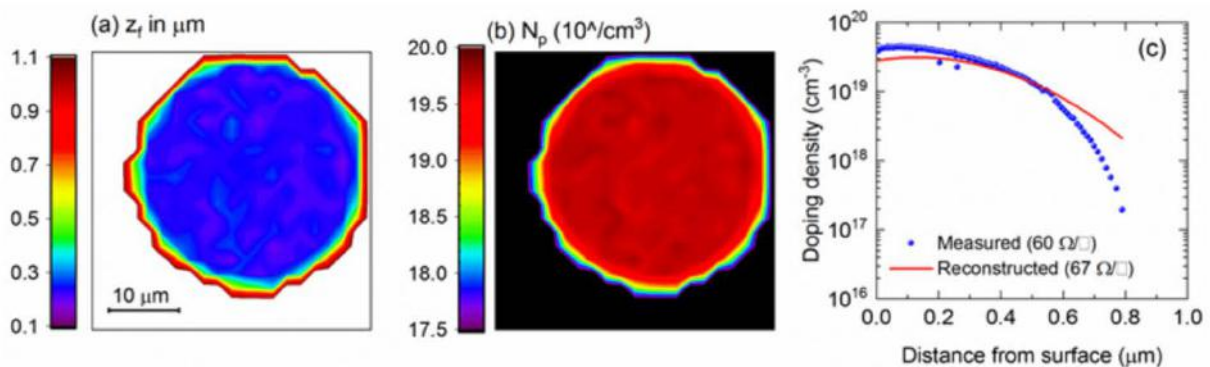


Figure F13.7: (a) z_t and (b) N_p maps of a localised p+ region in the PERL solar cell precursor, determined by the μ -PLS method at room temperature. (c) Comparison between the ECV measured and reconstructed dopant profiles. Note: z_p and z_t are inherently correlated.

The fourth topic is to calculate the potential of two-dimensional (2D) transition metal dichalcogenides (TMDs) for solar cells. 2D TMDs are currently receiving enormous attention for photovoltaic applications due to their very strong light-matter interaction, atomic thickness and naturally occurring surface passivation. Also, there has been a rapid improvement in their large-scale material processing capability and quality (Kang et al. 2015). This signals that in the next few years, large-area (millimetres to centimetres) solar cells based on TMDs could be fabricated. Therefore, it is crucial to understand and quantify the potential of these future solar cells using experimental and/or theoretical means in early days.

One of the most fundamental parameters of any photovoltaic material is its quasi-Fermi level splitting $\Delta\mu$ under illumination. This quantity represents the maximum open circuit voltage (V_{oc}) that a solar cell fabricated from that material can achieve. The relationship among $\Delta\mu$, PL and absorptivity (A) spectra is given by the generalised Planck law (Würfel 1982):

$$PL(\hbar\omega) = A(\hbar\omega) \times \vartheta_{bb}(\hbar\omega) \times \exp\left(\frac{\Delta\mu}{kT}\right) \quad (\text{Eq. 2}),$$

where $\hbar\omega$ is photon energy, k is Boltzmann's constant, T is the absolute temperature of the sample and ϑ_{bb} is the black body radiation. By quantifying light absorbed (A) and emitted (PL) from the TMDs, the ANU team extracts the quasi-Fermi splitting $\Delta\mu$ and hence predicts the possible V_{oc} that could be achieved from TMD-based solar cells, at the material stage. The team applies the technique to quantify the upper limits of V_{oc} that can possibly be achieved from monolayer WS_2 , MoS_2 , WSe_2 and $MoSe_2$ -based solar cells, and compares them with other thin-film technologies. Their results show that V_{oc} values of ~ 1.4 , ~ 1.12 , ~ 1.06 and ~ 0.93 V could be potentially achieved from solar cells fabricated from WS_2 , MoS_2 , WSe_2 and $MoSe_2$ monolayers at one-sun illumination, respectively, as shown in Figure F13.8.

If considering a complete solar cell and substituting $\Delta\mu$ and A in Eq. 2 by qV (q is the elemental charge and V is the junction voltage) and EQE_{pv} (photovoltaic external quantum efficiency, i.e. ratio of collected charge carriers to the number of photons incident on the device surface), respectively, one can obtain the reciprocity relation between its EQE_{pv} and electroluminescent (EL) emission (Rau 2007):

$$EL(\hbar\omega) = EQE_{pv}(\hbar\omega) \times \vartheta_{bb}(\hbar\omega) \times \exp\left(\frac{qV}{kT}\right) \quad (\text{Eq. 3}).$$

In PL, the absorptivity A only reflects the optical properties of the absorber. Meanwhile, in EL, the quantity EQE_{pv} contains both the absorptivity A and the charge carrier collection efficiency within the cell. This collection efficiency (often < 1) reflects how perfect the cell fabrication process is. Therefore, the value of $\Delta\mu$ implies the final cell maximum voltage at the material stage, assuming a lossless device fabrication process.

Another implication of the results in Figure F13.8 is that, even in ideal absorbers, V_{oc} is always lower than their bandgaps due to the thermodynamic detailed balance which requires equilibrium cells to

re-emit photons into the environment (Shockley and Queisser 1961). This is known as "Shockley-Queisser limit" of V_{oc} ($V_{oc,S-Q}$). However, as recently pointed out by Blank et al. (Blank et al. 2017), $V_{oc,S-Q}$ is just another ideal quantity after accounting for the bandgap and the real incident light. It still ignores the absorbers' optical and electronic properties. When considering the optical (refractive index, absorption coefficient, thickness, etc) and electronic (recombination rate, defect density, doping, etc) properties of the materials, the achievable V_{oc} , assuming a perfect device fabrication process, should be lower than $V_{oc,S-Q}$. In this work, as the ANU team captures the absorbed and emitted light, the predicted V_{oc} has already incorporated the materials' optoelectronic properties. In other words, the predicted V_{oc} should reflect the material potential better than $V_{oc,S-Q}$. The gap between $V_{oc,S-Q}$ and the predicted V_{oc} indicates an available room for material improvements.

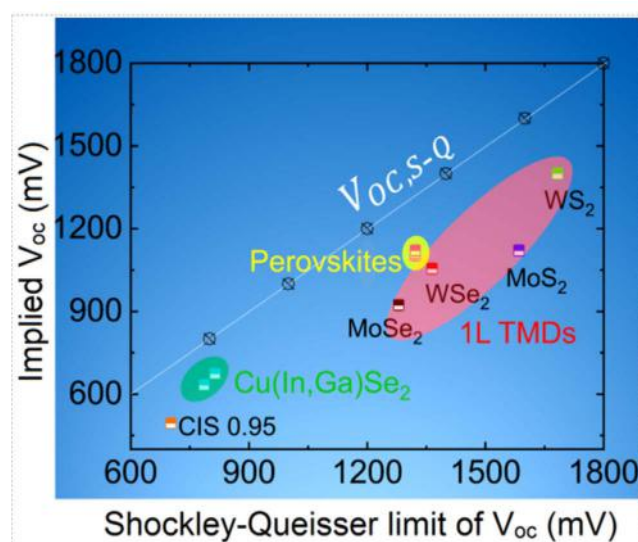


Figure F13.8: 2D TMD-based solar cells could potentially yield high voltages, very competitive to other thin-film technologies.

The team also observes that the predicted V_{oc} values are inhomogeneous across different regions of these monolayers. Therefore, they attempt to engineer the observed V_{oc} heterogeneity by electrically gating the TMD monolayers in a metal-oxide-semiconductor (MOS) structure which effectively changes the doping level of the monolayers electrostatically and improves their V_{oc} heterogeneity (Figure 13.9). These preliminary results demonstrate that indeed both the predicted V_{oc} and its homogeneity can be manipulated by the doping levels inside monolayer TMDs. The results suggest that the requirements of high-voltage, flexibility, ultralight, transparency and stability for future solar cells are possible with 2D TMDs. More significantly, the established limits could be a reference for numerous future works on fabricating TMD-based photovoltaic devices. This work has been published in *Advanced Materials* (Tebyetekerwa et al. 2019) and selected as an issue's frontispiece.

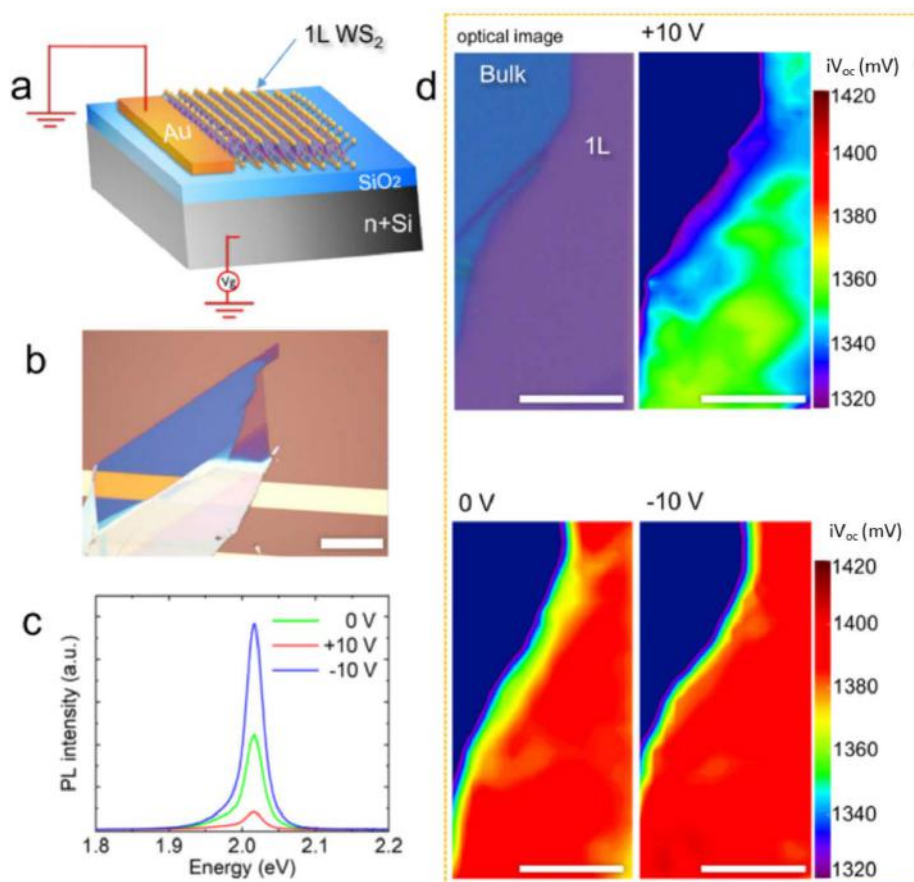


Figure F13.9: Effects of electrical gating on predicted V_{oc} of the monolayer WS_2 . (a) Schematic assembly of the monolayer-based MOS structure with electrical connections. (b) Optical microscope image of the analysed monolayer on the MOS setup (scale bar $50 \mu m$). (c) Photoluminescence spectra obtained from the monolayer WS_2 with back gate voltages of -10, 0 and +10 V. (d) The corresponding mapping of predicted V_{oc} across the monolayer WS_2 (scale bar $10 \mu m$).

Highlights

- Development of a spectrally and spatially resolved absorptivity method to study degradation in perovskite and perovskite/silicon tandem solar cells.
- Poly-Si films contain both amorphous and crystalline phases, each of which yields distinct luminescence peaks at low temperatures. Luminescence from the amorphous Si phase in poly-Si films can be used to track the hydrogen content inside the films.
- Development of a fast, contactless, non-destructive luminescence-based method to extract doping profiles of localised heavily-doped regions in silicon solar cells at room temperature.
- 2D TMDs could yield very high implied open circuit voltages of more than 1V, and can be engineered by doping to improve their uniformity and implied open circuit voltages.
- Publication of seven high-quality journal papers (three as first author and four as last author).
- Two publications were featured by prestigious journals (Advanced Materials' frontispieces and Advanced Energy Materials' inside back cover).
- Five oral presentations at international conferences by Dr Hieu Nguyen (2019a-e).

Future Work

- Comparisons of structural and optoelectronic properties of poly-Si films among various deposition technologies.
- Comparisons of hydrogen treatments among the various poly-Si film technologies.
- Exploration of techniques to improve implied open circuit voltages of the 2D TMD materials.

References

- BLANK, B., KIRCHARTZ, T., LANY, S. & RAU, U. 2017. Selection Metric for Photovoltaic Materials Screening Based on Detailed-Balance Analysis. *Physical Review Applied*, 8, 024032.
- KANG, K., XIE, S. E., HUANG, L. J., HAN, Y. M., HUANG, P. Y., MAK, K. F., KIM, C. J., MULLER, D. & PARK, J. 2015. High-mobility three-atom-thick semiconducting films with wafer-scale homogeneity. *Nature*, 520, 656-660.
- NGUYEN, H. T. 2019a. Luminescence from poly-Si films and its applications in Si PV. 46th IEEE Photovoltaic Specialists Conference, Chicago, June 2019.
- NGUYEN, H. T. 2019b. Imaging spatial variations of optical bandgaps in perovskite solar cells. 46th IEEE Photovoltaic Specialists Conference, Chicago, June 2019.

- NGUYEN, H. T. 2019c. Luminescence from poly-Si films and its applications in Si PV. 29th International Photovoltaic Science and Engineering Conference, Xi'an, November 2019.
- NGUYEN, H. T. 2019d. Imaging spatial variations of optical bandgaps in perovskite solar cells. 29th International Photovoltaic Science and Engineering Conference, Xi'an, November 2019.
- NGUYEN, H. T. 2019e. Luminescence from poly-Si films and its applications in Si PV. 6th Asia-Pacific Solar Research Conference, Canberra, December 2019.
- NGUYEN, H. T., GERRITSEN, S., MAHMUD, M. A., WU, Y. L., CAI, Z. Y., TRUONG, T., TEBYETEKERWA, M., DUONG, T., PENG, J., WEBER, K., WHITE, T. P., CATCHPOLE, K. & MACDONALD, D. 2020. Spatially and Spectrally Resolved Absorptivity: New Approach for Degradation Studies in Perovskite and Perovskite/Silicon Tandem Solar Cells. *Advanced Energy Materials*, 10. DOI: 10.1002/aenm.201902901.
- NGUYEN, H. T., LI, Z. F., HAN, Y. J., BASNET, R., TEBYETEKERWA, M., TRUONG, T. N., WU, H. T., YAN, D. & MACDONALD, D. 2019. Contactless, nondestructive determination of dopant profiles of localized boron-diffused regions in silicon wafers at room temperature. *Scientific Reports*, 9, 1-8.
- NGUYEN, H. T., LIU, A. Y., YAN, D., GUTHREY, H., TRUONG, T. N., TEBYETEKERWA, M., LI, Z. Y., LI, Z. F., AL-JASSIM, M. M., CUEVAS, A. & MACDONALD, D. 2018. Sub-Bandgap Luminescence from Doped Polycrystalline and Amorphous Silicon Films and Its Application to Understanding Passivating-Contact Solar Cells. *ACS Applied Energy Materials*, 1, 6619-6625.
- RAU, U. 2007. Reciprocity relation between photovoltaic quantum efficiency and electroluminescent emission of solar cells. *Physical Review B*, 76, 085303.
- SHOCKLEY, W. & QUEISSER, H. J. 1961. Detailed balance limit of efficiency of p-n junction solar cells. *Journal of Applied Physics*, 32, 510-519.
- TEBYETEKERWA, M., ZHANG, J., LIANG, K., DUONG, T., NEUPANE, G. P., ZHANG, L. L., LIU, B. Q., TRUONG, T. N., BASNET, R., QIAO, X. J., YIN, Z. Y., LU, Y. R., MACDONALD, D. & NGUYEN, H. T. 2019. Quantifying Quasi-Fermi Level Splitting and Mapping its Heterogeneity in Atomically Thin Transition Metal Dichalcogenides. *Advanced Materials*, 31.
- TRUONG, T. N., YAN, D., CHEN, W. H., TEBYETEKERWA, M., YOUNG, M., AL-JASSIM, M., CUEVAS, A., MACDONALD, D. & NGUYEN, H. T. Hydrogenation Mechanisms of Poly-Si/SiO_x Passivating Contacts by Different Capping Layers. *Solar RRL*. DOI: 10.1002/solr.201900476.
- TRUONG, T. N., YAN, D., SAMUNDSETT, C., BASNET, R., TEBYETEKERWA, M., LI, L., KRERNER, F., CUEVAS, A., MACDONALD, D. & NGUYEN, H. T. 2019. Hydrogenation of Phosphorus-Doped Polycrystalline Silicon Films for Passivating Contact Solar Cells. *ACS Applied Materials & Interfaces*, 11, 5554-5560.
- TRUONG, T. N., YAN, D., SAMUNDSETT, C., LIU, A. Y., HARVEY, S. P., YOUNG, M., DING, Z. T., TEBYETEKERWA, M., KREMER, F., AL-JASSIM, M., CUEVAS, A., MACDONALD, D. & NGUYEN, H. T. 2019. Hydrogen-Assisted Defect-Engineering of Doped Poly-Si Films for Passivating Contact Solar Cells. *ACS Applied Energy Materials*, 2, 8783-8791.. DOI: 10.1021/acsaem.9b01771.
- WURFEL, P. 1982. The chemical potential of radiation. *Journal of Physics C-Solid State Physics*, 15, 3967-3985.

F14 OVERCOMING THE MATERIAL LIMITATIONS OF CAST-GROWN MULTICRYSTALLINE AND MONO-LIKE SILICON FOR HIGH EFFICIENCY SOLAR CELLS

ACAP Fellow

Dr Hang Cheong Sio

Supervisor

Prof. Daniel Macdonald

Funding Support

ACAP Fellowship

Academic and Industrial Partners

Jinko Solar

Fraunhofer Institute for Solar Energy Systems

AF Simulations

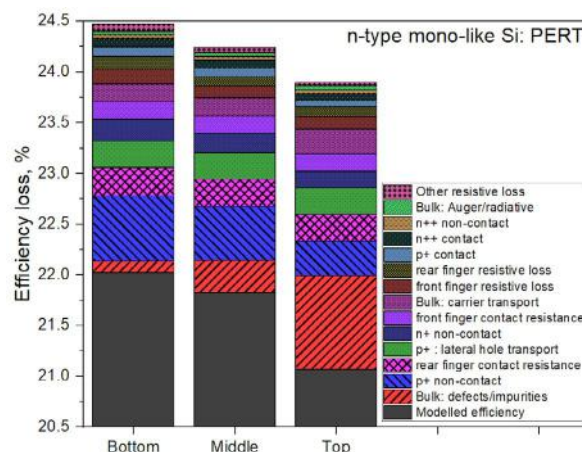
Aims

The objective of this project is to provide a holistic assessment of the material quality, cell potential, and stability of different types of cast-grown silicon materials, including both p-type and n-type high performance multicrystalline silicon (HP mc-Si) and mono-like Si, and correspondingly develop solutions to improve the efficiency and reliability of solar cells from a material perspective.

Progress

A. Device fabrication and analysis

A direct comparison of the electrical properties of p-type and n-type industrially grown HP mc-Si and mono-like Si was performed and discussed in the last report. Among the studied materials, it was found that n-type mono-like Si shows superior material properties. Through collaboration with Jinko Solar, n-type mono-like Si bifacial passivated emitter rear totally diffused (PERT) solar cells with efficiency above 22% were fabricated. An in-depth free energy loss analysis (FELA) was performed using Quokka3 to determine the associated energy loss in the n-type mono-like Si PERT cells from different ingot positions, and identify the key performance limiting factors. The FELA result is shown in Figure F14.1.



	Bottom	Middle	Top
Other resistive loss	0.07	0.05	0.03
Bulk: Auger/radiative	0.03	0.04	0.05
n++ non-contact	0.04	0.04	0.03
n++ contact	0.08	0.08	0.07
p+ contact	0.09	0.09	0.06
rear finger resistive loss	0.13	0.09	0.10
front finger resistive loss	0.14	0.12	0.13
Bulk: carrier transport	0.17	0.18	0.24
front finger contact resistance	0.18	0.17	0.17
n+ non-contact	0.21	0.19	0.16
p+ : lateral hole transport	0.26	0.26	0.26
rear finger contact resistance	0.27	0.27	0.27
p+ non-contact	0.65	0.53	0.34
Bulk: defects/impurities	0.11	0.32	0.92
Modelled efficiency	22.02	21.82	21.07

Figure F14.1: Modelled cell efficiency and detailed breakdown of all major efficiency losses for n-type mono-like Si PERT solar cells.

It is estimated that bulk recombination (dislocation clusters and intra-grain regions) contributes to around 0.1% absolute efficiency loss for the bottom wafers, 0.3% absolute efficiency loss for middle wafers and 0.9% absolute efficiency loss for the top wafers. For wafers towards the bottom of the ingot, bulk recombination loss is almost negligible when compared to other recombination losses in the simulated devices. This implies that the lifetime of the n-type mono-like Si wafers from the ingot bottom is not the main efficiency limiting factor, suggesting that the corresponding material quality is good enough for the current cell design, and the material also has the potential to be used for high efficiency solar cell structures »22%. On the other hand, bulk recombination becomes the dominant source of efficiency loss in the top wafers, due to the large number of dislocation clusters present.

The free energy loss analysis also identifies other efficiency loss mechanisms in the n-PERT devices. Apart from bulk recombination, main losses in the devices are (in descending order):

- p+ non-contact (front boron diffusion: surface passivation)
- rear finger contact resistance (rear finger contact)
- p+ lateral hole transport (front boron diffusion: lateral carrier transport)
- n+ non-contact (rear phosphorus diffusion: surface passivation)
- front finger contact resistance (front finger contact).

The results suggest that optimising the boron diffusion is the most promising way to improve the cell efficiency. This could be achieved either by optimising the boron diffusion profile, or through implementing selective boron emitter.

B. Light and elevated temperature induced degradation

Another focus of the project is light and elevated temperature induced degradation (LeTID) behaviour in cast-grown Si materials. This section summarises our findings of LeTID on different types of cast-grown Si (HP mc-Si and mono-like Si), Cz-Si materials and FZ-Si materials. Figure F14.2 shows effective lifetimes of the various studied samples as a function of illumination time at two different temperatures. All studied samples, including p-type Cz-Si, p- and n-type HP mc-Si, mono-like Si and FZ-Si materials, exhibit lifetime degradation phenomena under illumination at elevated temperature. Comparing the LeTID behaviours in p- and n-type Si materials, the degradation is considerably slower and less severe in both n-type HP mc-Si, mono-like Si and FZ-Si samples. This, nevertheless, shows that LeTID is not necessarily limited to p-type materials. In comparison with the mono-like Si samples, FZ-Si materials experience a lower extent of lifetime degradation, suggesting that defects and impurities in cast-grown Si materials might also play a role in LeTID.

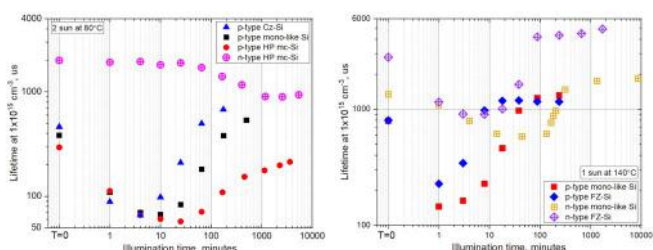


Figure F14.2: Effective carrier lifetimes of various lifetime testing samples as a function of time under (a) two-sun illumination at 80°C; and (b) one-sun illumination at 140°C.

LeTID exhibits complex characteristics. In this project, we study the detailed degradation kinetics in p-type boron-doped cast-grown mono-like Si upon light soaking (LS) and dark annealing (DA) at different temperatures, and explore the in-depth relationship between dark annealing and light soaking through cycling at various conditions. Our key experimental findings are summarised below.

- Both dark annealing and light soaking can induce a lifetime degradation and regeneration.
- A certain amount of defects already presented in the samples after firing.

- The involvement of more than one defect responsible for the degradation during dark annealing and light soaking.
- Dark annealing can alter the defect precursor that is responsible for LeTID.
- Hydrogen is a precursor/catalyst for LeTID.

Moreover, we have developed and tested various LeTID mitigation solutions. It is reported that the application of dark annealing could change LeTID kinetic (Chan et al. 2017). Figure F14.3 shows the evolution of normalised defect density (NDD) of sister mono-like Si samples during a LeTID test performed under one-sun illumination at 100°C, after being subjected to an initial dark annealing (DA) at 300°C and 500°C for different durations. It is observed that a short duration (1 min) of DA at 300°C increases the maximum extent of degradation upon the subsequent LS, when compared to the control sample without any DA pre-treatment. Increasing the DA duration, however, introduces an opposite effect. Samples subjected to a 10-minute DA treatment at 300°C show a reduced extent of LeTID, whereas samples subjected to 1200 minutes (20 hours) DA treatment show substantially less LeTID. Similar observations have been reported in multiple studies by (Yli-Koski et al. 2019; Liu et al. 2018). It was suggested that DA can alter the defect precursor that is responsible for LeTID, and the subsequent LeTID behaviours depend heavily on the stage of the DA degradation and regeneration cycle reached during the DA process, which is affected by both the annealing time and temperature (Chan et al. 2017; Yli-Koski et al. 2019). Raising the DA temperature to 500°C significantly reduces the pre-treatment time required to mitigate LeTID. As shown in Figure F14.3(b), 1 minute of DA at 500°C is sufficient to largely eliminate LeTID.

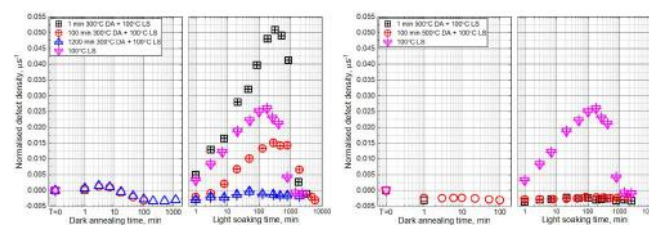


Figure F14.3: Normalised defect density (NDD) of sister mono-like Si samples during light soaking under one-sun illumination at 100°C, after subjecting to an initial dark annealing at (a) 300°C and (b) 500°C for different durations. NDD is calculated as $NDD = 1/\tau_{eff}(t) - 1/\tau_{eff}(t=0)$.

LeTID activities relate strongly to the firing temperature and the cooling rate applied during the firing process (Eberle et al. 2016). It is found that LeTID can be reduced by reducing the cooling rates of the firing process. We have tested this LeTID mitigation solution on p-type Cz-Si solar cells through collaboration with Jinko Solar, and the result is shown in Figure F14.4. It is observed that LeTID degradation can be reduced from around 1.7% to 0.9% relative by either reducing the peak firing temperature or reducing the cooling rate applied. Reducing the peak firing temperature has a big impact to the overall efficiency of the devices, due to metallisation requirement.

On the other hand, changing the cooling rates applied appears to be promising in reducing LeTID, without significantly affecting the device efficiency. Full implementation of this solution, however, would require new equipment or modification of the existing firing furnace to accommodate longer cooling times

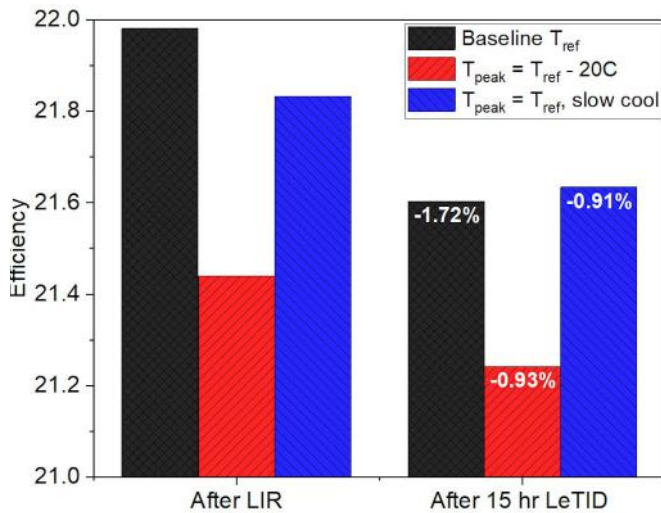


Figure F14.4: LeTID degradation test performed at Jinko Solar on p-type Cz-Si samples fired with different peak firing temperatures and cooling rates.

Highlights

- Fabrication of n-type mono-like Si PERT solar cells with efficiency above 22%.
- Performed an in-depth free energy loss analysis (FELA) to determine the energy loss in the n-type mono-like Si PERT cells from different ingot positions.
- Studied LeTID behaviours in p- and n-type FZ-Si, Cz-Si, HP mc-Si and mono-like Si materials.
- Developed and tested various LeTID mitigation solutions in an industrial production line, including the application of dark annealing and optimisation of the firing profile.

Future Work

- Develop industrially applicable LeTID mitigation solutions.
- Develop a model to describe LeTID behaviours and identify the underlying root causes for LeTID.

References

HAN, C., FUNG, T. H., ABBOTT, M., PAYNE, D., WENHAM, A., HALLAM, B., CHEN, R. & WENHAM, S. 2017. Modulation of Carrier-Induced Defect Kinetics in Multi-Crystalline Silicon PERC Cells Through Dark Annealing. *Solar RRL*, 1, 1600028.

EBERLE, R., KWAPIL, W., SCHINDLER, F., SCHUBERT, M. C. & GLUNZ, S. W. 2016. Impact of the firing temperature profile on light induced degradation of multicrystalline silicon. *Physica Status Solidi-Rapid Research Letters*, 10, 861-865.

LIU, S., PAYNE, D., CASTRILLON, C. V., CHEN, D., KIM, M., SEN, C., VARSHNEY, U., HAMEIRI, Z., CHAN, C., ABBOTT, M. & WENHAM, S. 2018. Impact of Dark Annealing on the Kinetics of Light- and Elevated-Temperature-Induced Degradation. *IEEE Journal of Photovoltaics*, 8, 1494-1502.

YLI-KOSKI, M., SERUÉ, M., MODANESE, C., VAHLMAN, H. & SAVIN, H. 2019. Low-temperature dark anneal as pre-treatment for LeTID in multicrystalline silicon. *Solar Energy Materials and Solar Cells*, 192, 134-139.

F15 DEVICE ARCHITECTURE DESIGN FOR COMMERCIAL KESTERITE SINGLE-JUNCTION AND MULTI-JUNCTION SOLAR CELLS

Lead Partner

UNSW

UNSW Team

Dr Kaiwen Sun, Prof. Martin Green, A/Prof. Xiaojing Hao, Dr Jialiang Huang, Dr Chang Yan, Xin Cui, Heng Sun, Ao Wang

Academic Partner

Nanyang Technological University (NTU): A/Prof. Lydia Helena Wong

Funding Support

ACAP

Aim

The objective of this project is to develop the specific device architecture for $\text{Cu}_2\text{ZnSnS}_4$ (CZTS) solar cells to enhance the device performance. The project planned to optimise the optical design of the window/buffer layer, conduct interface engineering of the heterojunction and explore Cd-free buffer alternatives.

Progress

Buffer layer doping

In CZTS devices, CZTS/CdS interface recombination is one of the most proposed factors that contribute to the performance limit, especially V_{oc} -deficit. In order to suppress the interface recombination, a CdS buffer layer with intentional doping by IIIA group elements was explored. Heavily n-doping the buffer can (i) decrease the buffer's resistivity (Schmid et al. 1990; Menner et al. 1988), (ii) widen the depletion width in the absorber region and enhance the collection from more deeply penetrating photons, and (iii) decrease its work function, causing more band bending of CZTS and increasing fraction of "built-in" electric field falling across the CZTS for higher V_{oc} (Mingebach et al. 2011). The conventional CdS buffer layer was deposited by chemical bath deposition (CBD) method using CdSO_4 as Cd source, thiourea as sulphur source and ammonia as the complexing agent. In order to increase the donor concentration, Ga^{3+} ions were introduced into the solution as a doping source. Different concentrations of Ga^{3+} were applied to control the doping level. The J-V curve and efficiency distribution is presented in Figure F15.1 and the device electrical parameters are summarised in Table F15.1. As evidently shown, the doped CdS buffer substantially boosts the V_{oc} compared to the undoped device. When looking into details of the parameters or different doping levels, the most efficient device is from the CdS layer doped with only a single dose of Ga^{3+} , which demonstrates all parameters' improvement. When increasing the doping dose, the fill factor drops dramatically.

Table F15.1: Device characteristics of the CZTS solar cells applying CdS buffer with different doping levels.

samples	V_{oc} (mV)	\approx	FF (%)	Eff (%)
CdS reference	554.10	16.98	59.57	5.60
CdS +1 In	663.68	18.85	67.56	8.45
CdS + 5 In	621.65	17.47	58.83	6.39
CdS + 10 In	642.52	16.31	59.50	6.23

From the parameters, it is apparent that a device with one dose of Ga^{3+} doping shows overall improvement, with the efficiency boosted from 5.6% to 8.45%. The most significant improvement comes from the V_{oc} and FF. It is reported that the CdS donor density increase will result in the n-type quasi-Fermi level near the p-n junction interface shifting towards the conduction band and, accordingly, the p-type quasi-Fermi level moving away from the valence band. As a consequence, the band bending for the valence band is enhanced, which will help suppress the interface recombination. This could explain the obvious improvement of the V_{oc} and FF.

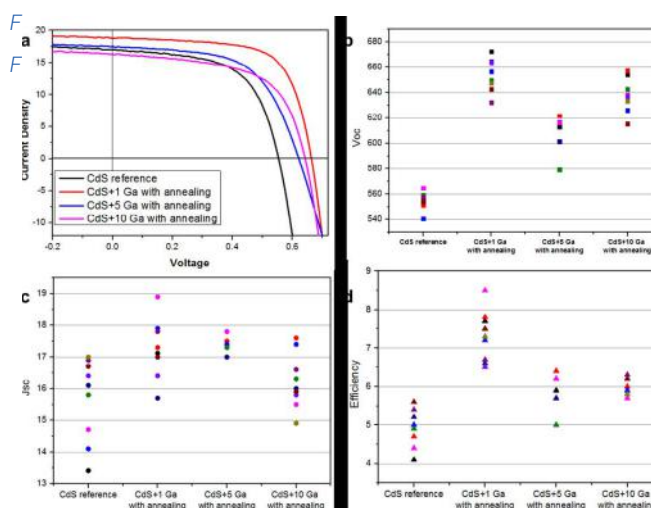


Figure F15.1: (a) Current density-voltage (J-V). (b)-(d) Statistical device parameters of devices applying CdS buffer with different doping levels.

Figure F15.2 shows the external quantum efficiency (EQE) curve and C-V profile of the devices applying CdS buffer with different doping levels. The device with 1 and 5 dose Ga^{3+} doping demonstrates improved quantum efficiency from over 500 nm, indicating their better collection efficiency. This can be explained by the spreading of the depletion region at the p-type semiconductor. Combining the EQE and C-V results, we can confirm that the EQE improvement is due to the enlarged depletion within the CZTS part. And the depletion width varies with the doping level of the CdS buffer, while the 1 dose of Ga^{3+} shows the longest depletion region among the samples. More work is being done to reveal the mechanism of the device performance and the doping level of the CdS buffer.

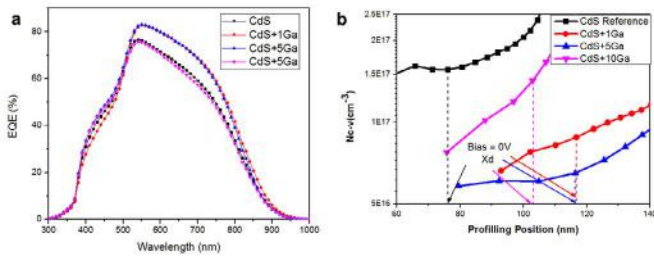


Figure F15.2: (a) EQE curve > (b) C-V profile of devices applying CdS buffer with different doping levels.

Optimisation of the ZnCdS buffer layer deposition

The performance of the device was effectively improved when we applied ZnCdS buffer thanks to the better band alignment and lattice match between ZnCdS and CZTS (summarised in ACAP Annual Report 2018). However, new problems like oxide/hydroxide impurities and metastabilities related to the Zn-based buffer emerged. Therefore, careful modification of the deposition process is crucial to the interface structure and associated device efficiency.

In the successive ionic layer adsorption and reaction (SILAR) process for ZnCdS deposition, the cation and anion solutions were separated to overcome the competing reaction of Cd²⁺ and Zn²⁺ ions, where ammonia is barely used. The rinse procedure between each soaking step and the low temperature deposition condition make it highly possible to form oxide and hydroxide impurities during the process because of the Zn-related compound reaction mechanism. Despite high temperature treatment having been reported to be effective to assist the dehydration of Zn(OH)₂, it is impossible to remove the hydroxide completely via heat treatment and the hydroxyl ion (OH)⁻ is known to form a bridge structure, which will be detrimental to the interface quality of the device. In addition, the presence of ZnO in the buffer layer may induce band fluctuation, thereby leading to severe interface recombination. As a result, Zn(OH)₂ and ZnO are undesirable for a robust p-n junction. So we explored the implementation of different concentrations of ammonia in the successive ionic layer adsorption and reaction (SILAR) process in order to modify the heterojunction interface. The ammonia in the solution is controlled in low (0.25 M) and high (1.5 M) concentrations to examine their effectiveness.

As shown in XPS results in Figure F15.3(a), the fitted peaks present in a ZnCdS film deposited with low ammonia are assigned as Zn(OH)₂ (532.7 eV), Zn(O,S) (531.7 eV), and ZnO (530.4 eV), respectively. (Li et al. 2017; Steirer et al. 2015). This indicates the formation of a large amount of Zn(OH)₂ and ZnO in the process. In contrast, the peak of Zn(OH)₂ cannot be detected in the sample deposited with high ammonia, the ZnO peak also attenuates dramatically. Zn(O,S) in the ZnCdS buffer is benign to the device performance because of its suitable bandgap. However, previous study on CIGS solar cells with a Zn-based buffer indicates that excess oxide and hydroxide impurities are found to be related to the increased amount of electronic defects in the depletion region (Bhattacharya 2008; Nakada et al. 2013) and metastabilities behaviour due to the instability of the Zn(OH)₂ (Katsumi and Osamu 2000; Buffière et al. 2015). In addition, the deterioration

of the fill factor is supposed to link to the secondary barrier for photoelectrons in the vicinity of the absorber/buffer interface, which also could be originated from the oxide and hydroxide at the interface. (Buffière et al. 2015) The ammonia in the precursor solution is evidently able to reduce these impurities formed during the SILAR process, which would be beneficial to the interface quality, thereby the device performance.

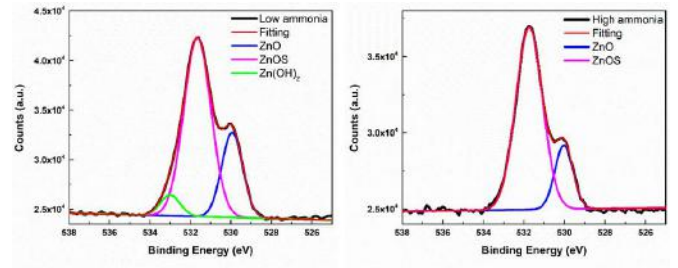


Figure F15.3: 01s spectral line shape decomposition for ZnCdS films deposited with low (a) and high (b) ammonia concentration in the cation solution.

The J-V curve and EQE spectra of the representative cell in these devices together with the CdS buffer-based reference are overlaid in Figure F15.4. The device characteristics accompanied with the electrical parameter of the representative cells are also summarised in Table F15.2. We mainly focus on the device fabricated using a ZnCdS buffer from different conditions. By applying a higher concentration of ammonia, the conversion efficiency is boosted to over 10%, overwhelming the 8.8% device from a lower concentration of ammonia. The V_{oc} is enhanced substantially, which can be attributed to the reduced heterojunction interface recombination. The dark saturation current density J₀ of the champion device is over one order lower than that of the device from low ammonia, which is related to the reduced non-radiative recombination. The ideality factor A also shows an improvement from 2.47 to 2.02, further suggesting the modified recombination in the depletion region. Therefore, the improved FF can be explained by the enhanced electron-hole pair separation in the junction region or the improved interface photo-generated electron transport. In addition, the series resistance (R_s) witnesses an obvious decrease from 1.01 to 0.53Ω·cm², contributing to the increment of FF and overall device performance. The short current density J_{sc} also demonstrates a significant increase from 21.04 to 22.19 mAcm⁻², resulting from the overall EQE improvement as indicated in Figure F15.4(b). The EQE enhancement across the whole spectrum is also strong evidence that the interface recombination is reduced in the high-ammonia condition because the p-n junction interface influences all the photo generated carriers coming from the absorber. These results are in agreement with our previous simulation work.

Table F15.2: Device characteristics of the CZTS solar cells applying a ZnCdS buffer with low and high ammonia concentrations.

Buffer	V _{oc} (mV)	JSC (mAcm ⁻²)	FF (%)	Eff (%)	R _s (Ω cm ²)	A	J ₀ (A cm ⁻²)
ZnCdS with low ammonia	659.06	21.04	63.43	8.80	1.01	2.47	6.18×10 ⁻⁴
ZnCdS with high ammonia	682.58	22.19	66.34	10.05	0.53	2.03	5.47×10 ⁻⁵

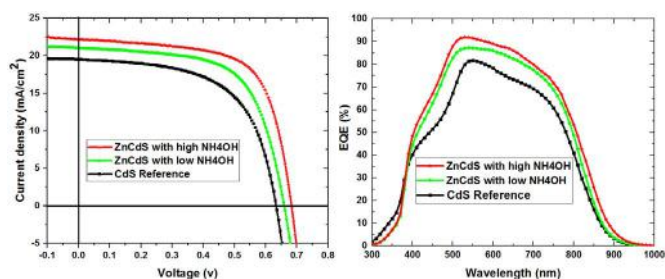


Figure F15.4: (a) J - V characteristics. (b) EQE of CZTS devices with conventional CdS buffer and ZnCdS buffer deposited with different ammonia concentrations.

Highlights

- Exploration of the doping control of CdS buffer by introducing IIIA element.
- Optimisation of the ZnCdS buffer chemistry by removing Zn-related secondary phases.

Future Work

- Optimisation of the CZTS absorber roughness to further reduce the buffer thickness.
- Investigation of additional doping in ZnCdS buffers to improve the device performance.
- Exploration of a second buffer like ZnMgO to match ZnSnO to reduce the top interface recombination.

References

- BHATTACHARYA, R. N. 2008. 19.5%-Efficient $\text{CuIn}_{1-x}\text{Ga}_x\text{Se}_2$ Photovoltaic Cells Using A Cd-Zn-S Buffer Layer, National Renewable Energy Lab. (NREL), Golden, CO (United States).
- BUFFIÈRE, M., BARREAU, N., ARZEL, L., ZABIEROWSKI, P. & KESSLER, J. 2015. Minimizing metastabilities in $\text{Cu}(\text{In,Ga})\text{Se}_2/(\text{CBD})\text{Zn}(\text{S,O,OH})/i\text{-ZnO}$ -based solar cells. *Progress in Photovoltaics: Research and Applications*, 23, 462-469.
- KATSUMI, K. & OSAMU, Y. 2000. Stabilization of PN Heterojunction between $\text{Cu}(\text{InGa})\text{Se}_2$ Thin-Film Absorber and ZnO Window with $\text{Zn}(\text{O}, \text{S}, \text{OH})_x$ Buffer. *Japanese Journal of Applied Physics*, 39, 2577.
- LI, J., LIU, X., LIU, W., WU, L., GE, B., LIN, S., GAO, S., ZHOU, Z., LIU, F., SUN, Y., AO, J., ZHU, H., MAI, Y. & ZHANG, Y. 2017. Restraining the Band Fluctuation of CBD-Zn(O,S) Layer: Modifying the Hetero-Junction Interface for High Performance $\text{Cu}_2\text{ZnSnSe}_4$ Solar Cells With Cd-Free Buffer Layer (Solar RRL 10/2017). *Solar RRL*, 1, 1770135.
- MENNER, R., DIMMLER, B., MAUCH, R. H. & SCHOCK, H. W. 1988. II-VI compound thin films for windows in heterojunction solar cells. *Journal of Crystal Growth*, 86, 906-911.
- MINGEBACH, M., DEIBEL, C. & DYAKONOV, V. 2011. Built-in potential and validity of the Mott-Schottky analysis in organic bulk heterojunction solar cells. *Physical Review B*, 84, 153201.

NAKADA, T., KOBAYASHI, T., KUMAZAWA, T. & YAMAGUCHI, H. 2013. Impacts of Post-Treatments on Cell Performance of CIGS Solar Cells With Zn-Compound Buffer Layers. *IEEE Journal of Photovoltaics*, 3, 461-466.

SCHMID, D., MAUCH, R. H., HOFMANN, M., SCHÄFFLER, R. & SCHOCK, H. W. 1990. Highly conductive Ga-doped polycrystalline (Zn,Cd)S films. *Journal of Crystal Growth*, 101, 1018-1021.

STEIRER, K. X., GARRIS, R. L., LI, J. V., DZARA, M. J., NDIONE, P. F., RAMANATHAN, K., REPINS, I., TEETER, G. & PERKINS, C. L. 2015. Co-solvent enhanced zinc oxysulfide buffer layers in Kesterite copper zinc tin selenide solar cells. *Physical Chemistry Chemical Physics*, 17, 15355-15364.

F16 COMPREHENDING CHARGE TRANSPORT IN PEROVSKITE-SILICON TANDEM SOLAR CELLS

ACAP Fellow

Daniel Walter

Supervisor

A/Prof. Klaus Weber

Funding Support

ACAP

Aim

This project aims to develop the theoretical foundation for the interpretation of optoelectronic measurements of perovskite and perovskite-tandem solar cells.

Progress

The fundamental problem facing the characterisation of perovskite materials and perovskite-based solar cells (PSCs) is how to interpret their unique, time-varying response to optical or electronic excitations. In contrast to conventional semiconductor materials (for example Si, GaAs), in which electrical current relies on mobile electrons, charge can move through perovskite semiconductors by both electrons and ions. The movement of ions through the perovskite crystal occurs on timescales ranging from microseconds to hours, many orders of magnitude slower than electron transport in conventional semiconductors. We have previously shown how the electrostatic coupling of two mobile ion species of opposite charge with non-radiative recombination reproduces many unconventional transient responses. In recent work we have explored how the interplay of the two oppositely charged ion species creates a time-varying net doping profile (to use the language of Si semiconductors), which leads to counter-intuitive responses consistent with a wide range of experimental results. These include results from transient atomic force microscopy, micro-photoluminescence and DC bias measurements. Each of these measurements typically have produced unconventional results, prompting wide-ranging speculative theorising in the literature. Our work shows that many of these theories are not required to explain the data, and we put forward a self-consistent framework based on ionic-electron drift-diffusion modelling in their place.

Foremost, perovskite solar cells exhibit unusual J-V transients, widely referred to as hysteresis. Taking a particularly unusual “bulge” in some J-V curves, which was suggested to be the result of capacitive charge trapping and release, we demonstrated how this is simply one possible expression of the movement of a positive and negative ion species influencing net doping and therefore recombination rates within the PSC (Figure F16.1). Secondly, transient atomic force microscopy provides spatially and temporally resolved measurements of the net charge density within perovskite solar cells. Electric field-induced ion generation processes have been proposed to explain transient AFM data, but we have shown that the response is consistent with

mixed ion-electron conduction and provides no evidence unique to ion generation in perovskite solar cells (Figure F16.2). It also demonstrates that the periods of excitation and relaxation are equal, telling us that widely observed asymmetric relaxation phenomena, for example sustained open circuit voltage in perovskite solar cells are not (solely) the result of ion movement.

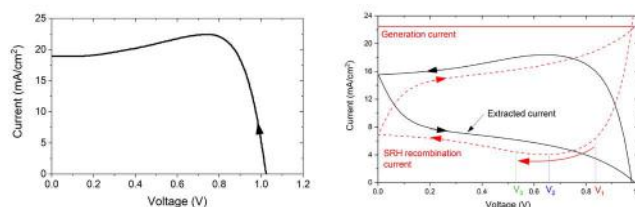


Figure F16.1: Unusual “bulge” in the J-V curve, rather than a symptom of capacitive charge storage/release, is a modification of bulk recombination via ion movement. Data on left from Ravishankar, S. et al. *J Phys Chem*, (2017).

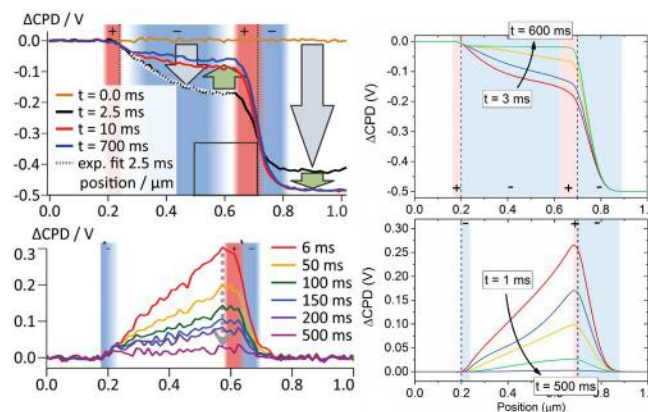


Figure F16.2: Measurement of transient evolution of spatially resolved net charge density during forward bias excitation (top left) and relaxation (bottom left) and the corresponding simulated charge density in a p-type perovskite solar cell with two mobile ions (right). Data on left from Weber et al. *En. Environ. Sci.* (2018).

In a third example, we consider so-called DC bias measurements, in which symmetrically contacted perovskite films are biased by a fixed, direct current. The measurement of the voltage over time, from which is inferred the conductivity, is used to determine the ion concentration. Our simulations of these measurement types demonstrate that an inference of ion concentration based on capacitive currents, in which ion-electron interaction in the bulk is excluded, is not reliable. As evidence, we performed DC bias experiments beyond current ranges typically reported and demonstrated that at higher currents and electric fields, non-monotonic voltage transients are observed, which is consistent with net doping variations due to two ion movement (Figure F16.3).

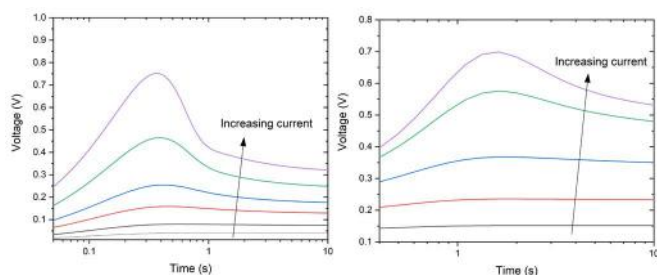


Figure F16.3: Measurement of transient voltage under direct current bias (left) and simulation of the same measurement condition (right). The non-monotonic transient response that appears at higher currents is a consequence of time-varying net ion concentrations, as per the conditions simulated in Figures F16.1 and F16.2, above.

Other examples not shown here include the evolution of micro-PL signals during the biasing of perovskite samples. Taken together we see a consistent feature of two-ion movement in perovskite semiconductors: as two independent ion species move against one another, there occurs a temporary period during which the net ion concentration (net doping) reaches a time-local maximum. This is evident in the non-monotonic changes in current in J-V measurements (Figure F16.1); in voltage in galvanostatic DC bias experiments (Figure F16.3); and the local enhancement of negative charge in the transient AFM measurements (Figure F16.2). Thus, we observe a single physical process producing disparate experimental features – and hitherto, equivalently disparate theoretical predictions – being united by a single theoretical framework, rigorously applied. It is evident from, for example, Figure F16.3 that there is information about the mobility and concentration of the ion population of the perovskite material that can be derived from simple measurement protocols. This theoretical framework is the first step in extracting this critical information.

Finally, this model has already supported interpretation of numerous perovskite-based solar cells at ANU's labs and the labs of collaborators overseas, including the passivation quality on unique nanostructured transport layers, PSCs based on mixed 2D–3D perovskite compositions and the efficiency potential of perovskite-silicon tandems.

Highlights

- A numerical drift-diffusion model of perovskite semiconductors including mobile ions has produced a theoretical framework that is consistent with multiple experimental data. This tells us that mixed ion-electron coupling is to the first order the dominant factor in unusual perovskite transience (a.k.a. hysteresis). It paves the way for more capable and precise characterisation.
- This model has allowed us to do away with numerous predictions of unique physical mechanisms in perovskites.

Future Work

- As we have shown, we can extract significant information about the ionic properties of perovskite materials from simple, straightforward opto-electronic measurements. However, the wide range of influential parameters means that it is difficult to quantify a unique solution at this stage. Future work will compare multiple measurements of single samples, e.g. galvanostatic DC bias and transient photoluminescence, to narrow down the range of possible ion properties.
- The knowledge derived above will be used to develop characterisation methods and analytical tools that other researchers can use to measure their perovskite materials.

References

- DE BASTIANI, M., AYDIN, E., ALLEN, T., WALTER, D., FELL, A., PENG, J., GASPARINI, N., TROUGHTON, J., BARAN, D., WEBER, K., WHITE, T. P. & DE WOLF, S. 2019. Interfacial Dynamics and Contact Passivation in Perovskite Solar Cells. *Advanced Electronic Materials*, 5.
- MAHMUD, M. A., DUONG, T., YIN, Y. T., PHAM, H. T., WALTER, D., PENG, J., WU, Y. L., LI, L., SHEN, H. P., WU, N. D., MOZAFFARI, N., ANDERSSON, G., CATCHPOLE, K. R., WEBER, K. J. & WHITE, T. P. Double-Sided Surface Passivation of 3D Perovskite Film for High-Efficiency Mixed-Shen, H. P., Walter, D., Wu, Y. L., Fong, K. C., Jacobs, D. A., Duong, T., Peng, J., Weber, K., White, T. P. & Catchpole, K. R. Monolithic Perovskite/Si Tandem Solar Cells: Pathways to Over 30% Efficiency. *Advanced Energy Materials*, 1902840.
- WALTER, D., FELL, A., WU, Y., DUONG, T., WU, N. & WEBER, K. 2019, Ionic-Electronic Coupling in Perovskite Semiconductors. 10th International Conference on Materials for Advanced Technologies, Singapore, 2019.
- WALTER, D., WU, Y., WU, N., JACOBS, D., WHITE, T., CATCHPOLE, K. & WEBER, K. 2019, Perovskite solar cells as ion-conducting semiconductor devices explain a wide range of hysteretic phenomena, Asia-Pacific Solar Research Conference, Canberra, Australia, 2019
- WU, N. D., WALTER, D., FELL, A., WU, Y. L. & WEBER, K. 2020. The Impact of Mobile Ions on the Steady-State Performance of Perovskite Solar Cells. *Journal of Physical Chemistry C*, 124, 219-229.

F18 TOWARDS 20% EFFICIENCY Cu₂ZnSnS₄ THIN-FILM SOLAR CELL BY DEFECT ENGINEERING AND BAND GRADING ENGINEERING

Lead Partner

UNSW

UNSW Team

Dr Chang Yan, Prof. Martin Green, A/Prof. Xiaojing Hao, A/Prof. Nicholas (Ned) Ekins-Daukes, Dr Jialiang Huang, Dr Kaiwen Sun

Academic Partner

National Renewable Laboratories (NREL): Dr Steven Johnston

Funding Support

ACAP

Aim

Kesterite Cu₂ZnSnS₄ (CZTS), a non-toxic and Earth-abundant compound, has been considered as the most promising candidate for cost-effective, environmentally benign and stable photovoltaics. Since the CZTS is very thin it has excellent prospects for flexible PV applications. Meanwhile, its high bandgap enables a better conversion of blue light, that provides potential for kesterite/silicon tandem solar cells. The aim of this project is to increase the efficiency of CZTS solar cells through reducing the non-radiative recombination and V_{oc} deficit by using a silver alloying and a bandgap grading strategy.

Progress

Among many reported V_{oc} limiting factors, the fermi-pinning at p-n interface and insufficient band bending are the dominant ones for CZTS, according to first principles calculations (Yuan et al. 2015). Ag grading at front of absorber (near p-n interface) seems to provide an effective way to reduce the Fermi-level pinning issue and increase the band bending within the space charge region. Before starting the experiment on Ag grading, we first conducted Ag alloying experiments to clarify the effect of Ag alloying on CZTS solar cells.

The methodology for Ag incorporation is through sputtering a thin layer of Ag on top of Cu/SnS/ZnS co-sputtered precursor, which is well matched with our current baseline process for record CZTS solar cells but without a MgF₂ anti-reflectance coating. By controlling the Ag sputtering time, Ag alloying content of 0%, 5% and 15% Ag/(Cu+Ag) can be readily achieved. The sulfurisation annealing and device fabrication processes are similar to descriptions in our previous reports (Yan et al. 2018). Figure F18.1 demonstrates statistical performance parameters of the CZTS devices with different Ag alloying concentrations. It clearly shows that 5% Ag alloying is able to effectively boost V_{oc} by ~20 mV on average and 15% Ag alloying shows a decreased voltage. Similarly, 5% Ag alloying demonstrates a slightly higher FF on average. Unlike the impact on V_{oc} and FF, increasing amounts of Ag alloying displays a negative relationship with the J_{sc}. Overall, 5% Ag alloying yields the highest efficiency of

8.6%, which is 0.4% absolute higher than the highest for the reference sample (8.2%). To throw further illumination on the decreased J_{sc}, external quantum efficiency measurements of devices with different Ag alloying content have been conducted, as shown in Figure F18.2(a). It seems the Ag is able to decrease the width of external quantum efficiency (EQE) absorption spectrum due to increased bandgap, which is a primary factor for decreased short current density. Meanwhile the reduced EQE within the whole spectrum is another factor responsible for decreased EQE.

Given a boosted efficiency by Ag alloying, the next step is to reveal the influence of Ag on the electrical properties for CZTS solar cells. Hence, the capacitance-voltage (CV) and drive level capacitance profiling (DLCP) characterisations have been conducted, as shown in figure F18.2(b). The carrier density from DLCP is a reflection on the real free carrier density of the absorber, whereas the CV reflects the doping density plus surface defects density. Thus, the difference between DLCP and CV reveals the influence of the surface defects density. All the relevant electrical properties are summarised in Figure F18.2(c). DLCP data demonstrates that Ag alloying can effectively decrease the free carrier density of the absorber and enlarge the depletion width. However, the surface defect densities do not show a clear trend.

After confirming the benefits and electrical properties changes due to Ag alloying, the next step is to build up an Ag alloying grading within the top part of the absorber. For this purpose, a double layer and double annealing strategy has been used. To be specific, we firstly co-sputter a Cu/SnS/ZnS precursor with a high copper content (with potential high doping density), then do a high temperature annealing. Afterward, a second precursor of co-sputtered Ag/Cu/SnS/ZnS will be directly deposited on top of the annealed first precursor. Then another high temperature sulfurisation annealing process is conducted on the stack. This design of the stack is expected to slow down the Ag diffusion rate from top to bottom so that an Ag grading (top-rich and bottom-poor) can be readily achieved.

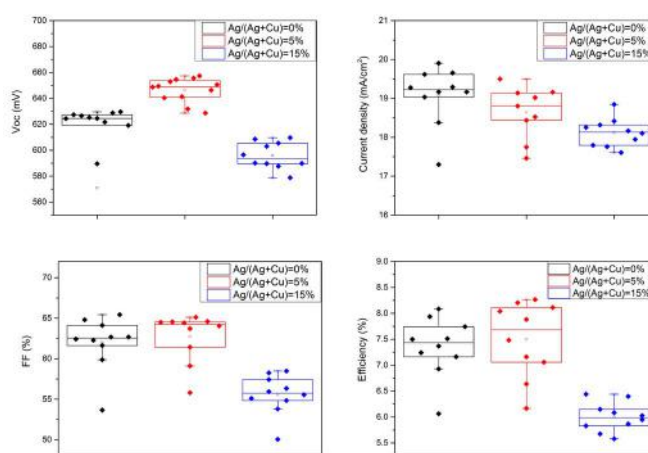


Figure F18.1: Statistical performance parameters of the CZTS devices with different Ag alloying concentrations.

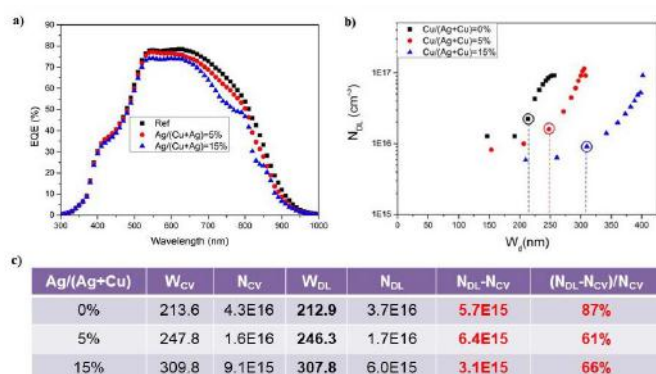


Figure F18.2: (a) External quantum efficiency curves of devices with different Ag alloying content. (b) Carrier density (obtain from drive level capacitance profiling) vs. depletion width of devices with different Ag alloying content. (c) Corresponding electrical parameters.

For the sake of reducing the Ag diffusion rate, a lower annealing temperature at the second stage is needed. In order to know the influence of a low annealing temperature on the morphologies and grains for Ag alloying CAZTS film, scanning electron microscopy (SEM) characterisations have been conducted on the CZTS and CAZTS films annealed at 460°C, 500°C and 560°C, respectively (Figure F18.3). According to these SEM images, Ag alloying can effectively enlarge the crystal grain size. In the meantime, the temperature to achieve well-grown grains of CAZTS is much lower than that of CZTS. 460°C is enough for CAZTS to produce compact grain films and this temperature is 100°C lower than normal baseline annealing temperature for CZTS.

Then we combined the low temperature annealing and double stack structure to test if this combined strategy could provide a solution to form an Ag grading. Figure F18.4 displays the XPS elemental depth profile of the double stack annealed at 460°C and 560°C, respectively. According to the estimated film thickness, this initial 0~4000 etching second is associated with the top layer and 4000~7000 corresponds to the bottom layer. According to Figure F18.4, under the annealing temperature of 560°C, the Ag is distributed homogeneously along the depth profile, indicating no grading was formed, due to the fast Ag diffusion rate at high temperature. It seems there is a slight Ag gradient at 460°C, due to the lower temperature annealing. However, this grading is not as steep as what we proposed and expected. Further processing design such as lower annealing temperature or other methodologies to enable a steeper grading are needed to be developed.

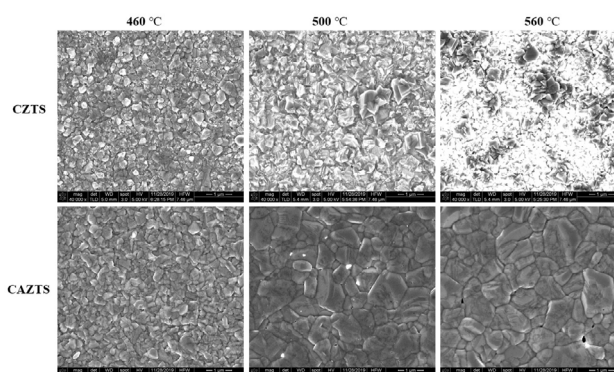


Figure F18.3: SEM images of CZTS absorber and CAZTS (Ag/Cu+Ag=25%) annealed at 460°C, 500°C, 560°C respectively.

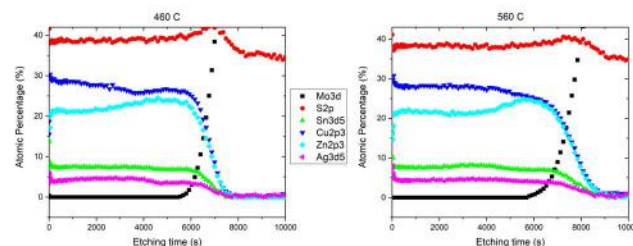


Figure F18.4: XPS elemental depth profile of the double stack annealed at 460°C and 560°C, respectively.

Highlights

- Ag alloying can reduce the sulfurisation temperature and enable larger CZTS grains.
- Incorporation of Ag decreases the doping for CZTS and enables slightly higher efficiency.
- By design of a double stack structure combined with low annealing temperature, a slight Ag gradient has been achieved.

Future Work

- Other strategies, with lower annealing temperature that enable a sharp Ag grading, need to be developed.
- The non-radiative recombination at the heterojunction interface should be further reduced via an alkali post deposit treatment.
- The processing and structure to facilitate a Ge back grading should be investigated.

References

- YAN, C., HUANG, J., SUN, K., JOHNSTON, S., ZHANG, Y., SUN, H., PU, A., HE, M., LIU, F., EDER, K., YANG, L., CAIRNEY, J. M., EKINS-DAUKES, N. J., HAMEIRI, Z., STRIDE, J. A., CHEN, S., GREEN, M. A. & HAO, X. 2018. Cu₂ZnSnS₄ solar cells with over 10% power conversion efficiency enabled by heterojunction heat treatment. *Nature Energy*, 3, 764-772.
- YUAN, Z. K., CHEN, S. Y., XIANG, H. J., GONG, X. G., WALSH, A., PARK, J. S., REPINS, I. & WEI, S. H. 2015. Engineering Solar Cell Absorbers by Exploring the Band Alignment and Defect Disparity: The Case of Cu- and Ag-Based Kesterite Compounds. *Advanced Functional Materials*, 25, 6733-6743.

F19 ADVANCED NANOSCALE CHARACTERISATION OF LOCAL STRUCTURES AND DEFECTS FOR LARGE BANDGAP MATERIALS FOR TANDEM SOLAR CELLS

Lead Partner

UNSW

UNSW Team

Dr Jae Sung Yun, Prof. Martin Green, Dr Jincheol Kim, Dr Xin Cui, A/Prof. Jeana Hao

Academic Partners

School of Materials Science and Engineering at UNSW: Prof. Jan Seidel, Dr Dohyung Kim
University of Queensland: Dr Jungho Yun

Funding Support

ACAP

Aim

We aim to study local charge separation properties of potential large bandgap semiconductors such as halide perovskites and $\text{Cu}_2\text{ZnSnS}_4$ (CZTS) using scanning probe microscopy techniques. For halide perovskites, the objective is to investigate facet-dependent electrical properties of methylammonium lead iodide (MAPbI_3) single crystals. For this purpose, we employed complementary spatial nanoscale imaging techniques and Kelvin probe force microscopy (KPFM) under illumination.

For CZTS solar cells, the project planned to unravel the role of hydrogen from atomic layer deposited (ALD) Al_2O_3 passivation layer in Cd-free CZTS solar cells. To identify morphology-dependent surface chemistry, nanoscale spatial surface potential mappings were performed. For elucidate local charge transport properties, KPFM measurement under the dark and light conditions with various wavelengths and intensities was performed.

Progress

Halide Perovskites

Figure F19.1 schematically illustrates the experimental setup for the scanning KPFM measurements of MAPbI_3 single crystals. Centimetre-scale bulk MAPbI_3 single crystals (Photo in Figure F19.1) were grown with a bottom-seeded solution growth method called inverse temperature crystallisation. Surface photovoltage is obtained from the contact potential difference (CPD) measured in dark subtracted from the CPD measured in light, that is, surface photovoltage = $\text{CPD}_{\text{light}} - \text{CPD}_{\text{dark}}$. The surface photovoltage measurements help to understand the local charge separation properties in a semiconductor.

Figure F19.2(a) and (b) show the CPD measured in dark and light on (100) and (112) facets, respectively. The initial average CPD values (dark) are approximately 35 and 96 mV on the (100) and (112) facets, respectively. On the basis of our previous reports, a higher CPD value

under the illumination implies a more positively charged surface (Yun et al. 2015). Such a difference indicates that each facet has different charge states which could arise from different types of ionic defects that are commonly reported in halide perovskites, that is, vacancy (I_v , Pb_v and MA_v), interstitial (I_i , MA_i and Pb_i), and antisite defect (I_{MA} , MA_i , Pb_i , IP_b , Pb_{MA} and $MAPb$) (Walsh et al. 2015).

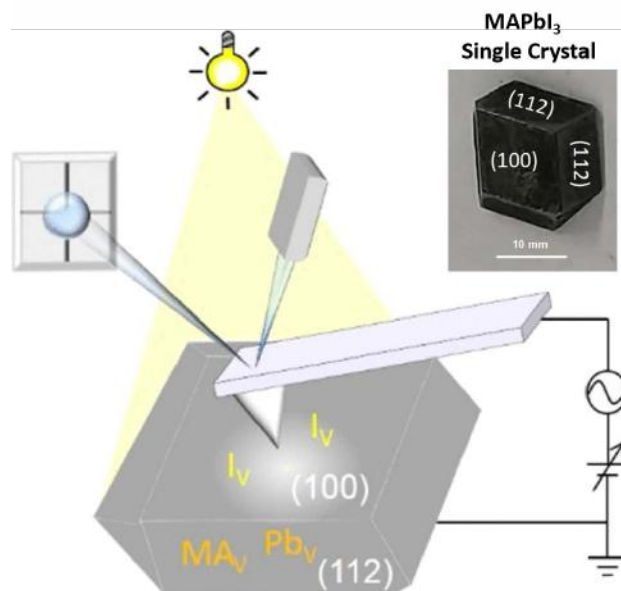


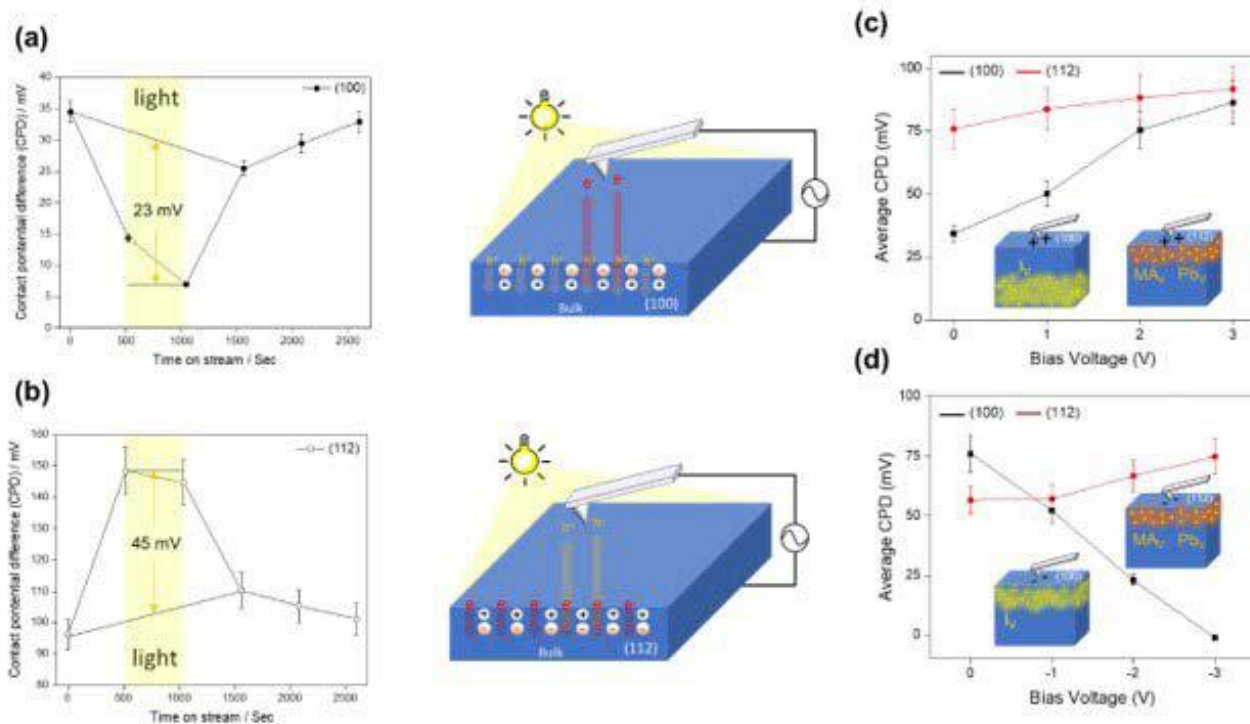
Figure F19.1: Experimental setup for the scanning probe microscope measurements of MAPbI_3 single crystals and photo of the surface polished single crystal (Kim et al. 2019).

These defects can create a trap state within the bandgap and provide n or p doping.

We have studied the migration behaviour of ionic defects on each facet using KPFM with bias voltage applied to the tip in dark. Figure F19.2(c) and (d) show variations of the average CPD extracted from KPFM images of a $2 \mu\text{m}^2$ area taken on the crystal surfaces of (100) and (112) orientation under dark conditions as a function of various positive and negative voltages. An increased trend is seen on both facets when positive biases are applied up to +3 V, indicating a relatively rapid increase on the (100) facet from around 34 to 86 mV and a moderate increase on the (112) facet from around 76 to 92 mV. This result shows that the attracted negative ions move towards the top surfaces by a positively charged tip on the (100) facet. This change is relatively higher compared with that of the (112) facet. However, the changes with negative biases reveal that one goes down on the (100) facet from approximately 76 to -1 mV, whereas the other one moves up on the (112) facet from approximately 56 up to 75 mV. On the basis of the above results, it is possible to deduce the type of specific ionic defects in each facet. In materials with the ABX_3 perovskite structure, vacancy-mediated diffusion is the most common process. Interstitial migration has not been commonly observed in inorganic perovskite oxides or halides because of the lack of interstitial space in such closely packed structures. Also, a single crystal does not comprise grain boundaries which act as ion migration channels. For the (100) facet, we suspect that iodine vacancy is the dominant defect type. An iodide vacancy creates energy states near the conduction band;

thus, the surface should be n-type, which is supported by the surface photovoltage measurements in Figure F19.2(a). The change in CPD upon biasing the tip for the (112) facet is only 19 and 16 mV for positive and negative voltages, respectively. Also, CPD increases for both cases, which implies that the surface is almost not changing and preserving its p-type characteristics regardless of the AFM tip bias polarity. Because this facet exhibited a p-type behaviour (HYPERLINK "https://pubs.acs.org/doi/full/10.1021/acs.jpcc.9b00943#fig2" Figure F19.2(b)), we suspect that the dominating defects are MA^+ and Pb^{2+} vacancies which create energy levels near the valence band.

Figure F19.2: Light-induced (on: 0.01 mW m^{-2}) average CPD as a function of time on (a) (100) and (b) (112). Corresponding illustrations show n-type behaviour of (100) facet which electrons accumulate to the tip and p-type behaviour of (112) facet which holes accumulate to the tip. Ion movement on different facets investigated by KPFM measurements. Average CPD on (100) and (112) facets as a function of (c) positive voltage biases and (d) negative voltage biases (Kim et al. 2019).



$\text{Cu}_2\text{ZnSnS}_4$ (CZTS)

Kelvin probe force microscopy (KPFM) was performed to study the effects of the Al_2O_3 treatment at the CZTS/ZnSnO heterojunction by detecting the local surface potential, providing the morphology-dependent local electronic properties of the CZTS films upon passivation treatment. The topography of the reference and Al_2O_3 samples are shown in Figure F19.3(a) and (e), no clear difference in the surface morphology and grain size due to the Al_2O_3 treatment could be seen. To compare the electrical properties of the samples, the simultaneously recorded CPD spatial maps were measured in dark for reference and the Al_2O_3 samples, as shown in Figure F19.3(b) and (f). Since there is no photo-induced charge carriers, the CPD results collected in dark conditions presents the properties of the original surface. It is visibly distinguishable that CPDs at the grain boundaries (GBs) are lower than grain interiors (GIs). This lower GB potential formed due to the built-in electrical field arising from the passivation effects through Na segregation at the GBs. Figure F19.3(i) shows the distribution of the CPD values measured in dark

where a narrower width of CPD is observed in the sample with Al_2O_3 treatment, suggesting enhanced homogeneous chemical and/or electronic characteristics. The overall CPD is shifted to a higher value for the Al_2O_3 sample which indicates higher band bending in respect to the tip and implies that the surface electronic and chemical states are different from the reference sample. To further explore the charge separation behaviour in CZTS heterojunction before and after Al_2O_3 treatment, KPFM measurements under the illumination were performed using an excitation wavelength of 400 nm and 750 nm, respectively. Note that, a laser excitation wavelength of 400 nm is expected to induce the photo generated carriers near to the surface of CZTS, whereas 750 nm excitation produces a more uniform photo-generation within the bulk of CZTS. For each excitation wavelength, the illumination intensity was increased on about every $1 \mu\text{m}$ during continuous scanning from 0 to 894 mW cm^{-2} for 400 nm and 0 to $12,000 \text{ mW cm}^{-2}$ for 750 nm (scan axis is from bottom-to-top), as shown in Figure F19.3(c), (d) and (g), (h) for reference and Al_2O_3 sample, respectively. We notice the two samples depict clearly different CPD contrasts changing with the light intensity,

as well as different responses to illumination of different excitation wavelengths. Figure F19.3(j) shows the average CPD values for the corresponding samples as a function of illumination intensity. The average CPD decreases as the light intensity increasing suggests that the photo generated free electrons are accumulated at the front surface separated by the CZTS/ZnSnO heterojunction. The CPD drops from dark to highest intensity of illumination for Al_2O_3 sample is almost 2.3-fold larger than the reference sample at a wavelength of 400 nm (750 nm) indicating the more effective charge-separation capability induced by the passivation layer.

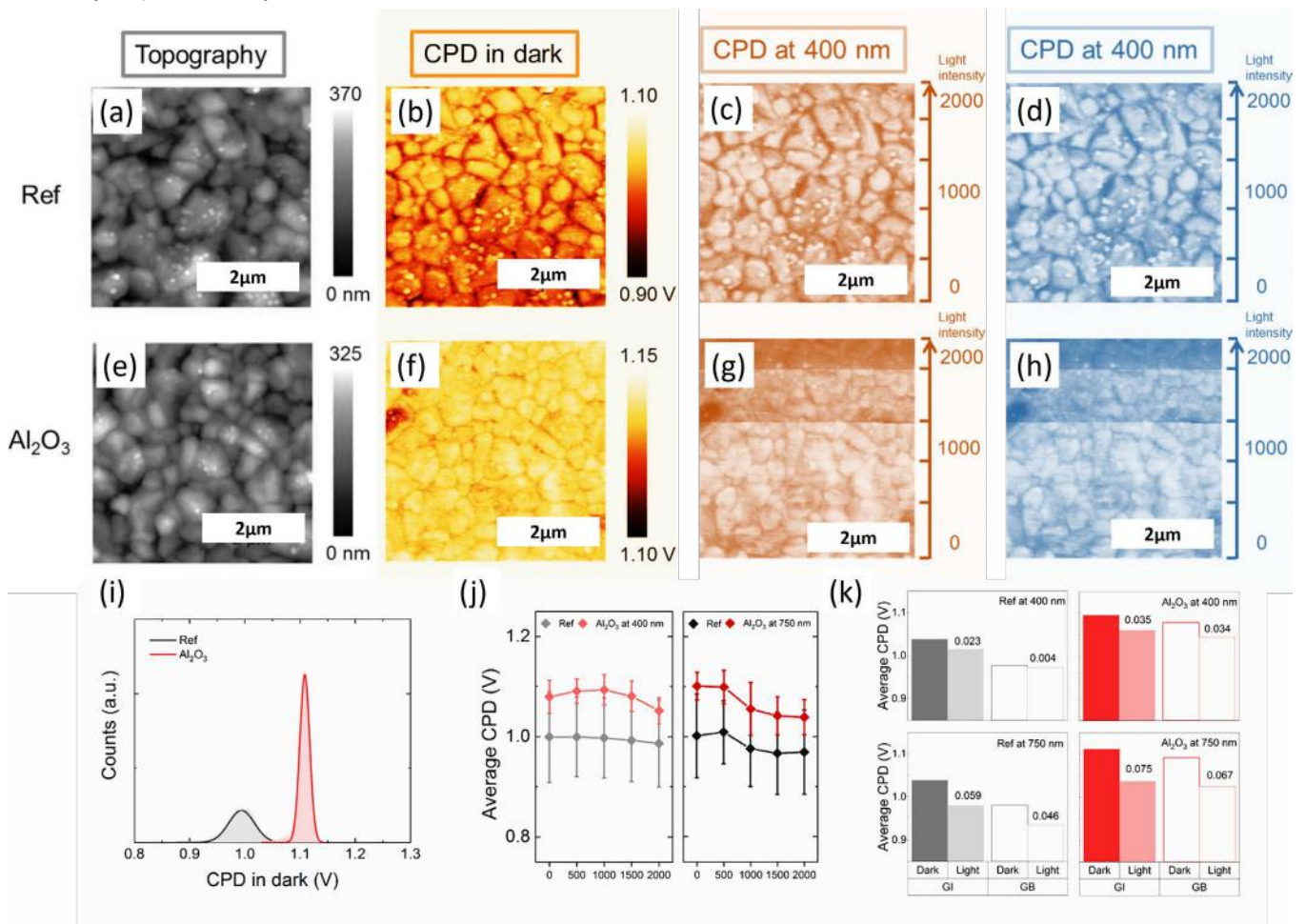


Figure F19.3: Topography and light-induced CPD images of the CZTS/ZnSnO heterojunction samples with and without Al_2O_3 treatment. KPFM measurements on the two samples showing. (a and e) Topography and (b and f) simultaneously recorded CPD spatial maps in the dark; (c and g) CPD spatial maps under various laser illumination intensities at a wavelength of 400 nm; (d and h) CPD spatial maps under different laser illumination intensities at a wavelength of 750 nm of CZTS/ZnSnO and CZTS/ Al_2O_3 /ZnSnO, respectively. (i) CPD distribution measured in dark for the reference and Al_2O_3 treated samples. (j) Average CPD values for the reference and Al_2O_3 treated samples as a function of illumination intensity at a wavelength of 400 nm and 750 nm. (k) Average CPD values and CPD values at dark and light with illumination intensities of 894 mW cm^{-2} (400 nm) and 12 W cm^{-2} (750 nm) at GBs and GIs for corresponding samples. The scanning scales were $25 \mu\text{m}^2$ (Xin et al. 2019).

At an excitation wavelength of 400 nm, the passivated sample shows an even larger CPD decrease than the reference sample, due to the higher carrier separation at the surface of CZTS. These results indicate that the Al_2O_3 sample passivates defects at the surface which promotes photo generated charges carrier collection at wavelength of 400 nm. The CPD values difference between dark and light, also known as surface photovoltage (SPV), were calculated at GBs and GIs for corresponding samples, as shown in Figure 19.3(k). For the reference sample, SPVGI was 23 mV whereas SPVGB was almost zero which indicated that there is no charge separation at the GB. On the other hand, the SPVGB becomes 34 mV when passivated and SPVGI becomes slightly higher than the reference sample, indicating that there is efficient charge separation at the GBs compare to GIs. We suspect that more Na accumulated at GBs during the negative charged interstitial O_i^- at the CZTS surface attracts the interstitial Na_i^+ from bulk to the interface.

Highlights

- Various types of ionic defects for specific (100) and (112) lattice facets in single-crystal MAPbI_3 have been investigated using KPFM. Our results indicate that the (100) facet exhibits an n-type behaviour dominated with I^- vacancies, whereas the (112) facet exhibits a p-type behavior with MA^+ or Pb^{2+} vacancies.
- Cd-free CZTS solar cells have been characterised using KPFM under dark and light with various wavelengths and intensities. When the CZTS is treated with Al_2O_3 , the charged point defects can be passivated thus resulting in reduced local potential fluctuations and improved charge separation at GBs.

Future Work

- Investigate charge separation and ion migration properties at the domains and domain walls in halide perovskite solar cells.
- Perform light wavelength and intensity-dependent KPFM on the hydrogen passivated CZTS solar cells in order to study morphological-dependent charge generation and separation properties.

References

- CUI, X., SUN, K., HUANG, J., YUN, J. S., LEE, C. Y., YAN, C., SUN, H., ZHANG, Y., XUE, C., EDER, K. & YANG, L., 2019. Cd-Free $\text{Cu}_2\text{ZnSnS}_4$ solar cell with an efficiency greater than 10% enabled by Al_2O_3 passivation layers. *Energy & Environmental Science*, 12(9), pp.2751-2764.
- WALSH, A., SCANLON, D. O., CHEN, S., GONG, X. G. & WEI, S. H., 2015. Self-regulation mechanism for charged point defects in hybrid halide perovskites. *Angewandte Chemie International Edition*, 54(6), pp.1791-1794.
- YUN, J. S., HO-BAILLIE, A., HUANG, S., WOO, S. H., HEO, Y., SEIDEL, J., HUANG, F., CHENG, Y. B. & GREEN, M. A., 2015. Benefit of grain boundaries in organic-inorganic halide planar perovskite solar cells. *Journal of Physical Chemistry Letters*, 6(5), pp.875-880.

F20 SEMITRANSSPARENT FLEXIBLE PEROVSKITE SOLAR CELLS FOR LAMINATED TANDEM CELL

Lead Partner

CSIRO

CSIRO Team

Dr Chuantian Zuo, Dr Mei Gao, Dr Doojin Vak

Academic Partners

Monash University

UoM

Funding Support

ACAP

Aim

The objective of this project is to develop semitransparent flexible perovskite solar cells for laminated perovskite/silicon tandem cells. The project focuses on how to create semitransparent flexible perovskite solar cells using scalable methods – either slot-die coating or a roll-to-roll (R2R) continuous process. Ultimately, the semitransparent cells will be integrated to form perovskite/silicon tandem cells.

Progress

In our previous work, we developed a slot-die compatible drop-casting method to prepare quasi-2D perovskite solar cells. Following the previous work, we tried to use different cations and optimise preparation conditions to improve device performance. A facile method was developed to improve the performance of drop-cast quasi-2D perovskite solar cells using alternative cations, such as phenethylammonium (PEA) and iso-butyl ammonium (iso-BA). The film morphology, phase purity, and crystal orientation of the films were improved by N_2 blowing and methylammonium chloride (MACl) additive. PCEs of 16.0% and 9.3% were achieved by drop casting and roll-to-roll process, respectively. Semitransparent cells were also tried and a PCE of 9.5% was achieved.

Figure F20.1 shows the photos for drop-cast quasi-2D perovskite films using different cations. It can be seen that only the BA cation film has uniform morphology. The other films are very rough and non-uniform. To obtain better film morphology, we found a simple N_2 blowing process. The preparation methods for the films are illustrated in Figure F20.2. The perovskite precursor solution is drop-cast onto a pre-heated substrate (Figure F20.2(a)), with the solution spreading spontaneously to form a circular wet film. Two methods are employed to dry the wet films; drying under ambient laboratory conditions, hereafter referred to as “naturally dried” (Figure F20.2 (b) and (c)), and drying under a stream of nitrogen or air to accelerate the evaporation of the solvent, hereafter referred to as “ N_2 blow-dried” or “air blow-dried”, respectively, (Figure F20.2(d) and (e)). These different drying processes lead to significantly different film qualities, as discussed in detail below.

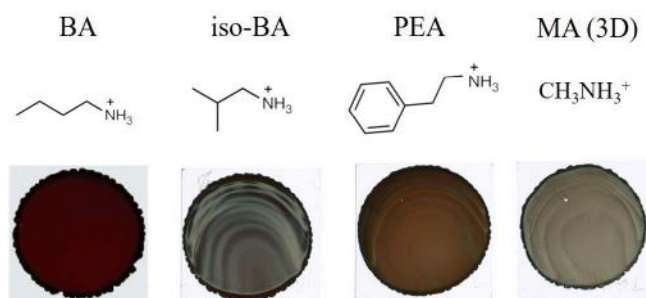


Figure F20.1: Photos for drop-cast quasi-2D perovskite films using different cations.

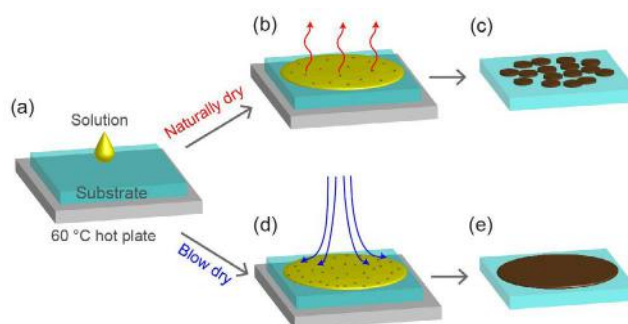


Figure F20.2: Illustration of the natural and N_2 blow-drying processes used to prepare drop-cast quasi-2D perovskite films. (a) The 2D-perovskite solution is drop-cast onto a heated substrate. (b) The solution spreads on the substrate and dries naturally; the supersaturation and number of crystal nuclei is low due to the slow drying. (c) The crystal nuclei grow into large crystal grains during drying. (d) The film spreads on the substrate and then an N_2 stream is used to dry the film rapidly; the supersaturation and number of crystal nuclei is higher owing to the fast drying. (e) The crystal nuclei grow into a compact quasi-2D-perovskite film.

Two kinds of quasi-2D perovskite with formula of $(PEA)_2(MA)_4Pb_5I_{16}$ (PEA-2D) and $(iso-BA)_2(MA)_4Pb_5I_{16}$ (iso-BA-2D) were used. Visual inspection of the drop-cast PEA-2D and iso-BA-2D films revealed significant differences in the appearance caused by the various drying techniques (Figure F20.3). The N_2 blow-dried films (Figure F20.3(c) and (d)) look smoother and more uniform than their naturally dried counterparts, which appear grey and have several fringes on the surface (Figure F20.2(a) and (b)). The morphology of the films was studied in greater detail using scanning electron microscopy (SEM) (Figure F20.3(e) and (f)), with the naturally dried PEA-2D film (Figure F20.3(e)) appearing rough and comprising some cylinder-like grains. The naturally dried iso-BA-2D film (Figure F20.3(f)) also comprises cylinder-like grains, but its surface is considerably smoother. Both of these thin films exhibited severe microstructural defects with large pinholes leading to incomplete coverage of the substrate. In contrast, the PEA-2D and iso-BA-2D films prepared using N_2 blow-drying present uniform, dense, and smooth surfaces (Figure F20.3(g) and (h)). The flow rate used during N_2 blow-drying influences film quality, with optimisation of the N_2 flow rate performed on iso-BA-2D films indicating that flow rates of at least 5 L min^{-1} are required to achieve uniform films.

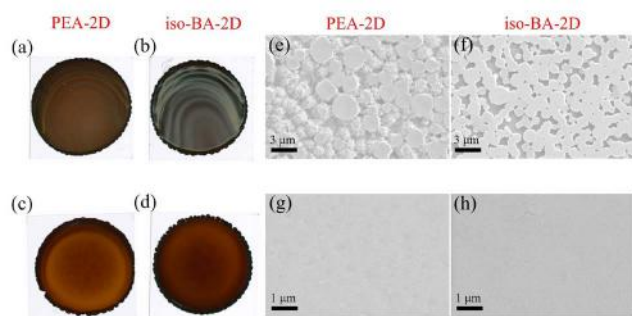


Figure F20.3: (a)–(d) Photographic images for PEA-2D and iso-BA-2D perovskite films prepared by natural drying (a) and (b), and N_2 blow-drying (c) and (d). (e)–(h) SEM images of PEA-2D and iso-BA-2D perovskite films prepared by natural drying (e) and (f), and blow-drying (g) and (h).

The difference in film morphology can be understood by considering the process of crystal growth; the slower solvent evaporation during natural drying results in lower supersaturation and a low rate of nucleation, resulting in a low crystal nuclei concentration that causes the growth of fewer, larger grains. In contrast, N_2 blow-drying causes rapid evaporation of the solvent, leading to high supersaturation and a high rate of nucleation. This ultimately causes the formation of highly uniform, compact films without defects (Figure F20.3).

The performance of drop-cast PEA-2D and iso-BA-2D perovskite layers in solar cells was investigated using devices comprising ITO/modified-PEDOT:PSS (m-PEDOT:PSS)/quasi-2D-perovskite/ $PC_{61}BM$ /PEIE/Ag (Figure F20.4(a)), which were fabricated completely under ambient laboratory conditions, with m-PEDOT:PSS being used instead of PEDOT:PSS to obtain a higher open circuit voltage (V_{oc}). The cells fabricated using naturally dried and N_2 blow-dried PEA-2D perovskite films show very low short-circuit current (J_{sc}) and PCE (Figure F20.4(b)). This may be due to the $n=1$ phase at the base of the photo-absorber film blocking hole transport to the m-PEDOT:PSS layer. A demonstrable improvement in J_{sc} and PCE was found for cells fabricated using N_2 blow-dried PEA-2D perovskite films with MACl additive, which is attributed to improved charge transport associated with the elimination of the $n=1$ phase.

Cells incorporating naturally dried iso-BA-2D perovskite films also showed very low PCE (2.2%), which is attributed to the discontinuous coverage of the perovskite layer allowing recombination between the hole transport layer (m-PEDOT:PSS) and the electron transport layer ($PC_{61}BM$). The device comprising a compact N_2 blow-dried film generated higher J_{sc} (16.3 mAcm^{-2}), FF (71.9%), and PCE (11.9%), and the addition of MACl improved the PCE to 16.0%, with a higher V_{oc} of 1.15 V, a J_{sc} of 18.1 mAcm^{-2} , and an FF of 77.2%. The PCE is much higher than the previous achieved PCE (10.6%) of iso-BA-2D PSCs prepared by spin-coating. This is ascribed to improved phase purity and crystal orientation, which facilitates charge transport in the perovskite layer. Furthermore, a low level of hysteresis is observed in the current density-voltage (J-V) curves obtained in forward and reverse scans (Figure F20.4(c)). The steady-state PCE of the “champion” cell recorded using maximum power point (MPP) tracking (Figure F20.4(d)) was 15.9%, consistent with the J-V measurement.

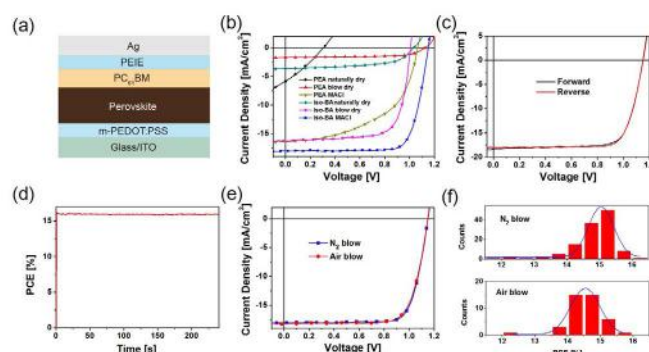


Figure F20.4: (a) Device structure of the quasi-2D perovskite solar cells. (b) J-V curves for the PEA-2D and iso-BA-2D perovskite solar cells prepared by natural drying, and N_2 blow-drying with and without MACl additive. (c) J-V curves for the “champion” cell under reverse and forward scan. (d) PCE obtained using MPP tracking. (e) J-V curves for the “champion” cells prepared by drying under N_2 or air streams. (f) Statistics of the PCE distribution for iso-BA-2D perovskite solar cells prepared by drying under N_2 or air streams.

The performance of the cells using iso-BA-2D perovskite prepared by air blow-drying was also investigated. As discussed above, the formation of high quality iso-BA-2D perovskite films does not require a high flow rate, and effective drying can be achieved with a conventional hair dryer that does not produce heat. The best cell incorporating an air-dried iso-BA-2D perovskite layer gave a V_{oc} of 1.14 V, a J_{sc} of 18.3 mAcm^{-2} , an FF of 75.5%, and a PCE of 15.8%, which is very close to the values achieved using N_2 blow-drying (Figure F20.4(e)).

The performance reproducibility of the cells using N_2 blow-drying or air blow-drying (relative humidity 35%) was also investigated (Figure F20.4(f)). Most of these cells displayed PCEs in the 14.5–15.5% and 14–15% ranges, respectively, demonstrating a high degree of reproducibility. The ease of using air-drying rather than an N_2 source not only significantly reduces the cost of the process but also addresses the operational safety concerns of using an asphyxiant, which is an important consideration in large-scale manufacturing.

A roll-to-roll (R2R) slot-die coating process was used to demonstrate the scalable production of the iso-BA-2D perovskite film (Figure F20.5(a)). Some pinholes can be observed in the SEM image, and the film was not as uniform as on a glass substrate, which is possibly due to the rougher and less hydrophilic surface of the ITO/PET substrate leading to de-wetting on the substrate. Perovskite solar cells with the same device structure as the drop-cast method were produced using an R2R slot-die process to deposit the perovskite layer; the “champion” cell displayed a V_{oc} of 1.04 V, a J_{sc} of 13.6 mAcm^{-2} , an FF of 66.0%, and a PCE of 9.3%, which is a 14% improvement from our previously reported PCE of 8%. This demonstrates the potential for these materials to be incorporated into a facile, mass-production fabrication process, with higher PCEs anticipated from the use of substrates having a more hydrophilic and smoother surface, and lower sheet resistance.

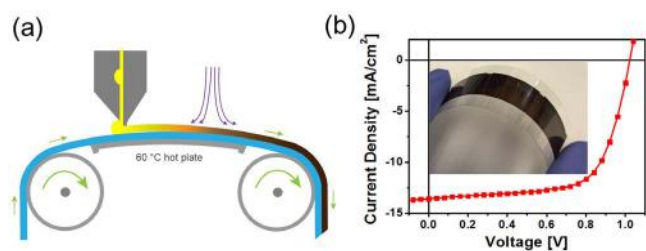


Figure F20.5: (a) R2R slot-die coating of a 2D-perovskite film. (b) Photographic image of the iso-BA-2D perovskite film prepared using the R2R process and the best J-V curve for a perovskite solar cell.

Table F20.1: Performance of "champion" 2D perovskite solar cells prepared using drop-casting and R2R slot-die deposition of a perovskite layer.

Method	V_{OC} [V]	J_{SC} [mAcm ⁻²]	FF [%]	PCE [%]
Drop-casting	1.15	-18.1	77.2	16.0
R2R	1.04	-13.6	66.0	9.3

Highlights

- A simple and slot-die compatible method was developed to prepare smooth, uniform and highly oriented 2D perovskite films, without spin-coating.
- A crystallisation control strategy was developed to improve film morphology, phase purity, and crystal orientation.
- PCEs of 16% and 9.3% were achieved for drop-cast and R2R slot-die processing, respectively.

Future Work

- Improve the PCE of perovskite solar cells using drop-cast perovskite layer.
- Improve the performance of semitransparent perovskite solar cells by optimising the perovskite layer and semitransparent electrode.
- Prepare four-terminal perovskite/silicon solar cells.

References

ZUO, C. T., SCULLY, A., YAK, D., TAN, W. L., JIAO, X. C., MCNEILL, C. R., ANGMO, D. C., DING, L. M. & GAO, M. 2019. Self-Assembled 2D Perovskite Layers for Efficient Printable Solar Cells. *Advanced Energy Materials*, 9.

Acknowledgements

Chuantian Zuo would like to acknowledge Wen Liang Tan and Christopher R. McNeill from Monash University, Fei Zheng and Kenneth P. Ghiggino from The University of Melbourne for GIWAX and PL measurements.



UNSW
SYDNEY

**AUSTRALIAN CENTRE
FOR ADVANCED PHOTOVOLTAICS**

UNSW SYDNEY NSW 2052 AUSTRALIA

Tel: +61 2 9385 4018

Fax: +61 2 9662 4240

Email: acap@unsw.edu.au

Website: acap.net.au

Director: Scientia Professor Martin Green